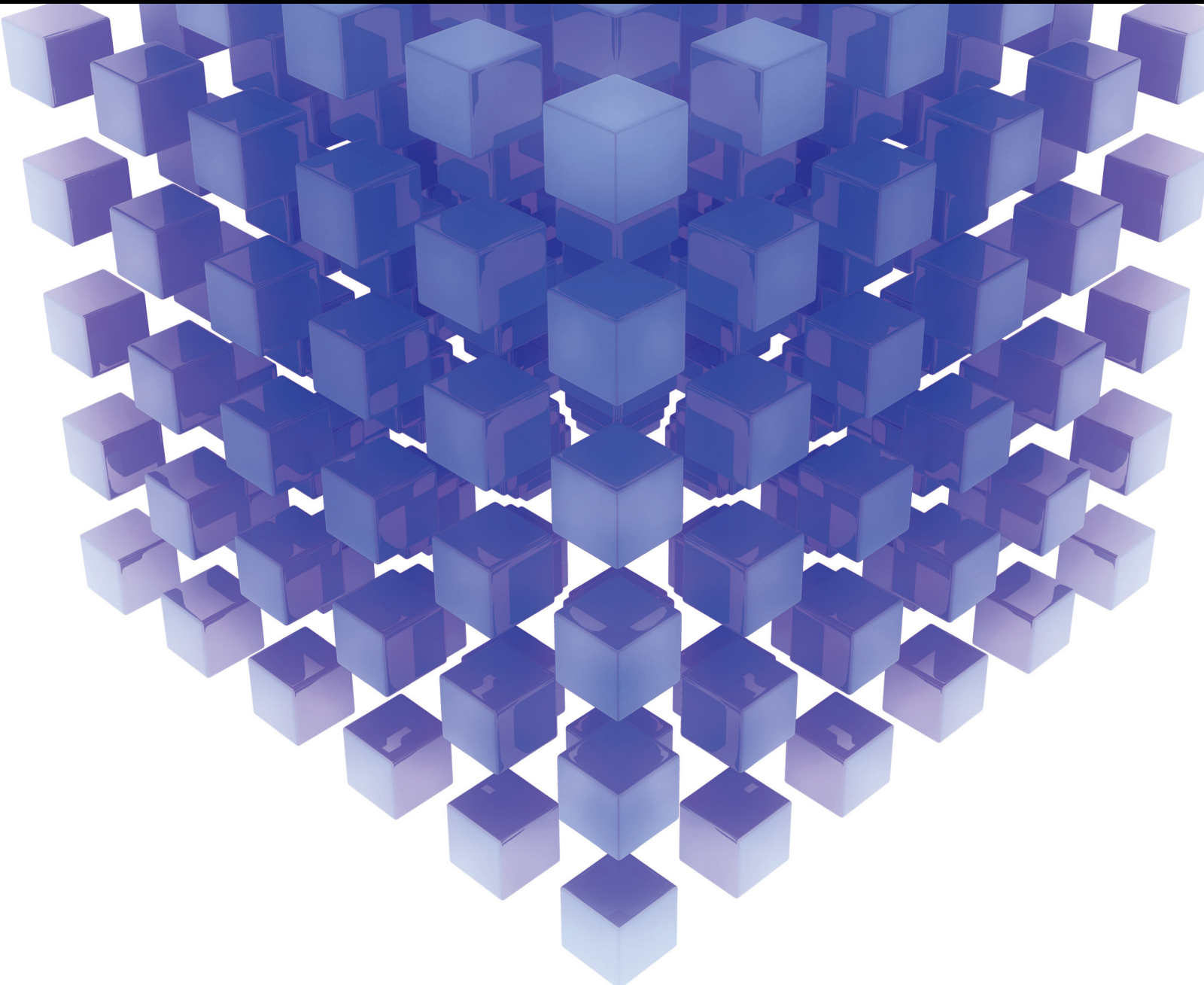


# Multi-Criteria Models to Evaluate Maintenance Strategy

Lead Guest Editor: Gianpaolo Di Bona

Guest Editors: Antonio Forcina, Filippo De Carlo, and Mohammad Mahdi Abaei





---

# **Multi-Criteria Models to Evaluate Maintenance Strategy**



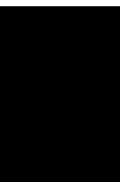
Mathematical Problems in Engineering

---

## **Multi-Criteria Models to Evaluate Maintenance Strategy**

Lead Guest Editor: Gianpaolo Di Bona

Guest Editors: Antonio Forcina, Filippo De Carlo,  
and Mohammad Mahdi Abaei




---

Copyright © 2021 Hindawi Limited. All rights reserved.

This is a special issue published in “Mathematical Problems in Engineering.” All articles are open access articles distributed under the Creative Commons Attribution License, which permits unrestricted use, distribution, and reproduction in any medium, provided the original work is properly cited.

# Chief Editor

Guangming Xie , China

## Academic Editors

Kumaravel A , India  
Waqas Abbasi, Pakistan  
Mohamed Abd El Aziz , Egypt  
Mahmoud Abdel-Aty , Egypt  
Mohammed S. Abdo, Yemen  
Mohammad Yaghoub Abdollahzadeh  
Jamalabadi , Republic of Korea  
Rahib Abiyev , Turkey  
Leonardo Acho , Spain  
Daniela Addessi , Italy  
Arooj Adeel , Pakistan  
Waleed Adel , Egypt  
Ramesh Agarwal , USA  
Francesco Aggogeri , Italy  
Ricardo Aguilar-Lopez , Mexico  
Afaq Ahmad , Pakistan  
Naveed Ahmed , Pakistan  
Elias Aifantis , USA  
Akif Akgul , Turkey  
Tareq Al-shami , Yemen  
Guido Ala, Italy  
Andrea Alaimo , Italy  
Reza Alam, USA  
Osamah Albahri , Malaysia  
Nicholas Alexander , United Kingdom  
Salvatore Alfonzetti, Italy  
Ghous Ali , Pakistan  
Nouman Ali , Pakistan  
Mohammad D. Aliyu , Canada  
Juan A. Almendral , Spain  
A.K. Alomari, Jordan  
José Domingo Álvarez , Spain  
Cláudio Alves , Portugal  
Juan P. Amezcua-Sanchez, Mexico  
Mukherjee Amitava, India  
Lionel Amodeo, France  
Sebastian Anita, Romania  
Costanza Arico , Italy  
Sabri Arik, Turkey  
Fausto Arpino , Italy  
Rashad Asharabi , Saudi Arabia  
Farhad Aslani , Australia  
Mohsen Asle Zaem , USA

Andrea Avanzini , Italy  
Richard I. Avery , USA  
Viktor Avrutin , Germany  
Mohammed A. Awadallah , Malaysia  
Francesco Aymerich , Italy  
Sajad Azizi , Belgium  
Michele Bacciocchi , Italy  
Seungik Baek , USA  
Khaled Bahlali, France  
M.V.A Raju Bahubalendruni, India  
Pedro Balaguer , Spain  
P. Balasubramaniam, India  
Stefan Balint , Romania  
Ines Tejado Balsera , Spain  
Alfonso Banos , Spain  
Jerzy Baranowski , Poland  
Tudor Barbu , Romania  
Andrzej Bartoszewicz , Poland  
Sergio Baselga , Spain  
S. Caglar Baslamisli , Turkey  
David Bassir , France  
Chiara Bedon , Italy  
Azeddine Beghdadi, France  
Andriette Bekker , South Africa  
Francisco Beltran-Carbajal , Mexico  
Abdellatif Ben Makhlof , Saudi Arabia  
Denis Benasciutti , Italy  
Ivano Benedetti , Italy  
Rosa M. Benito , Spain  
Elena Benvenuti , Italy  
Giovanni Berselli, Italy  
Michele Betti , Italy  
Pietro Bia , Italy  
Carlo Bianca , France  
Simone Bianco , Italy  
Vincenzo Bianco, Italy  
Vittorio Bianco, Italy  
David Bigaud , France  
Sardar Muhammad Bilal , Pakistan  
Antonio Bilotta , Italy  
Sylvio R. Bistafa, Brazil  
Chiara Boccaletti , Italy  
Rodolfo Bontempo , Italy  
Alberto Borboni , Italy  
Marco Bortolini, Italy

Paolo Boscariol, Italy  
Daniela Boso , Italy  
Guillermo Botella-Juan, Spain  
Abdesselem Boulkroune , Algeria  
Boulaïd Boulkroune, Belgium  
Fabio Bovenga , Italy  
Francesco Braghin , Italy  
Ricardo Branco, Portugal  
Julien Bruchon , France  
Matteo Bruggi , Italy  
Michele Brun , Italy  
Maria Elena Bruni, Italy  
Maria Angela Butturi , Italy  
Bartłomiej Błachowski , Poland  
Dhanamjayulu C , India  
Raquel Caballero-Águila , Spain  
Filippo Cacace , Italy  
Salvatore Caddemi , Italy  
Zuowei Cai , China  
Roberto Caldelli , Italy  
Francesco Cannizzaro , Italy  
Maosen Cao , China  
Ana Carpio, Spain  
Rodrigo Carvajal , Chile  
Caterina Casavola, Italy  
Sara Casciati, Italy  
Federica Caselli , Italy  
Carmen Castillo , Spain  
Inmaculada T. Castro , Spain  
Miguel Castro , Portugal  
Giuseppe Catalanotti , United Kingdom  
Alberto Cavallo , Italy  
Gabriele Cazzulani , Italy  
Fatih Vehbi Celebi, Turkey  
Miguel Cerrolaza , Venezuela  
Gregory Chagnon , France  
Ching-Ter Chang , Taiwan  
Kuei-Lun Chang , Taiwan  
Qing Chang , USA  
Xiaoheng Chang , China  
Prasenjit Chatterjee , Lithuania  
Kacem Chehdi, France  
Peter N. Cheimets, USA  
Chih-Chiang Chen , Taiwan  
He Chen , China

Kebing Chen , China  
Mengxin Chen , China  
Shyi-Ming Chen , Taiwan  
Xizhong Chen , Ireland  
Xue-Bo Chen , China  
Zhiwen Chen , China  
Qiang Cheng, USA  
Zeyang Cheng, China  
Luca Chiapponi , Italy  
Francisco Chicano , Spain  
Tirivanhu Chinyoka , South Africa  
Adrian Chmielewski , Poland  
Seongim Choi , USA  
Gautam Choubey , India  
Hung-Yuan Chung , Taiwan  
Yusheng Ci, China  
Simone Cinquemani , Italy  
Roberto G. Citarella , Italy  
Joaquim Ciurana , Spain  
John D. Clayton , USA  
Piero Colajanni , Italy  
Giuseppina Colicchio, Italy  
Vassilios Constantoudis , Greece  
Enrico Conte, Italy  
Alessandro Contento , USA  
Mario Cools , Belgium  
Gino Cortellessa, Italy  
Carlo Cosentino , Italy  
Paolo Crippa , Italy  
Erik Cuevas , Mexico  
Guozeng Cui , China  
Mehmet Cunkas , Turkey  
Giuseppe D'Aniello , Italy  
Peter Dabnichki, Australia  
Weizhong Dai , USA  
Zhifeng Dai , China  
Purushothaman Damodaran , USA  
Sergey Dashkovskiy, Germany  
Adiel T. De Almeida-Filho , Brazil  
Fabio De Angelis , Italy  
Samuele De Bartolo , Italy  
Stefano De Miranda , Italy  
Filippo De Monte , Italy



































José António Fonseca De Oliveira  
Correia , Portugal  
Jose Renato De Sousa , Brazil  
Michael Defoort, France  
Alessandro Della Corte, Italy  
Laurent Dewasme , Belgium  
Sanku Dey , India  
Gianpaolo Di Bona , Italy  
Roberta Di Pace , Italy  
Francesca Di Puccio , Italy  
Ramón I. Diego , Spain  
Yannis Dimakopoulos , Greece  
Hasan Dinçer , Turkey  
José M. Domínguez , Spain  
Georgios Dounias, Greece  
Bo Du , China  
Emil Dumic, Croatia  
Madalina Dumitriu , United Kingdom  
Premraj Durairaj , India  
Saeed Eftekhari Azam, USA  
Said El Kafhali , Morocco  
Antonio Elipse , Spain  
R. Emre Erkmen, Canada  
John Escobar , Colombia  
Leandro F. F. Miguel , Brazil  
FRANCESCO FOTI , Italy  
Andrea L. Facci , Italy  
Shahla Faisal , Pakistan  
Giovanni Falsone , Italy  
Hua Fan, China  
Jianguang Fang, Australia  
Nicholas Fantuzzi , Italy  
Muhammad Shahid Farid , Pakistan  
Hamed Faruqi, Iran  
Yann Favennec, France  
Fiorenzo A. Fazzolari , United Kingdom  
Giuseppe Fedele , Italy  
Roberto Fedele , Italy  
Baowei Feng , China  
Mohammad Ferdows , Bangladesh  
Arturo J. Fernández , Spain  
Jesus M. Fernandez Oro, Spain  
Francesco Ferrise, Italy  
Eric Feulvarch , France  
Thierry Floquet, France

Eric Florentin , France  
Gerardo Flores, Mexico  
Antonio Forcina , Italy  
Alessandro Formisano, Italy  
Francesco Franco , Italy  
Elisa Francomano , Italy  
Juan Frausto-Solis, Mexico  
Shujun Fu , China  
Juan C. G. Prada , Spain  
HECTOR GOMEZ , Chile  
Matteo Gaeta , Italy  
Mauro Gaggero , Italy  
Zoran Gajic , USA  
Jaime Gallardo-Alvarado , Mexico  
Mosè Gallo , Italy  
Akemi Gálvez , Spain  
Maria L. Gandarias , Spain  
Hao Gao , Hong Kong  
Xingbao Gao , China  
Yan Gao , China  
Zhiwei Gao , United Kingdom  
Giovanni Garcea , Italy  
José García , Chile  
Harish Garg , India  
Alessandro Gasparetto , Italy  
Stylianos Georgantzinou, Greece  
Fotios Georgiades , India  
Parviz Ghadimi , Iran  
Ştefan Cristian Gherghina , Romania  
Georgios I. Giannopoulos , Greece  
Agathoklis Giaralis , United Kingdom  
Anna M. Gil-Lafuente , Spain  
Ivan Giorgio , Italy  
Gaetano Giunta , Luxembourg  
Jefferson L.M.A. Gomes , United Kingdom  
Emilio Gómez-Déniz , Spain  
Antonio M. Gonçalves de Lima , Brazil  
Qunxi Gong , China  
Chris Goodrich, USA  
Rama S. R. Gorla, USA  
Veena Goswami , India  
Xunjie Gou , Spain  
Jakub Grabski , Poland











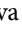
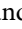

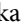






Antoine Grall , France  
George A. Gravvanis , Greece  
Fabrizio Greco , Italy  
David Greiner , Spain  
Jason Gu , Canada  
Federico Guarracino , Italy  
Michele Guida , Italy  
Muhammet Gul , Turkey  
Dong-Sheng Guo , China  
Hu Guo , China  
Zhaoxia Guo, China  
Yusuf Gurefe, Turkey  
Salim HEDDAM , Algeria  
ABID HUSSANAN, China  
Quang Phuc Ha, Australia  
Li Haitao , China  
Petr Hájek , Czech Republic  
Mohamed Hamdy , Egypt  
Muhammad Hamid , United Kingdom  
Renke Han , United Kingdom  
Weimin Han , USA  
Xingsi Han, China  
Zhen-Lai Han , China  
Thomas Hanne , Switzerland  
Xinan Hao , China  
Mohammad A. Hariri-Ardebili , USA  
Khalid Hattaf , Morocco  
Defeng He , China  
Xiao-Qiao He, China  
Yanchao He, China  
Yu-Ling He , China  
Ramdane Hedjar , Saudi Arabia  
Jude Hemanth , India  
Reza Hemmati, Iran  
Nicolae Herisanu , Romania  
Alfredo G. Hernández-Díaz , Spain  
M.I. Herreros , Spain  
Eckhard Hitzer , Japan  
Paul Honeine , France  
Jaromir Horacek , Czech Republic  
Lei Hou , China  
Yingkun Hou , China  
Yu-Chen Hu , Taiwan  
Yunfeng Hu, China  
Can Huang , China  
Gordon Huang , Canada  
Linsheng Huo , China  
Sajid Hussain, Canada  
Asier Ibeas , Spain  
Orest V. Iftime , The Netherlands  
Przemyslaw Ignaciuk , Poland  
Giacomo Innocenti , Italy  
Emilio Insfran Pelozo , Spain  
Azeem Irshad, Pakistan  
Alessio Ishizaka, France  
Benjamin Ivorra , Spain  
Breno Jacob , Brazil  
Reema Jain , India  
Tushar Jain , India  
Amin Jajarmi , Iran  
Chiranjibe Jana , India  
Łukasz Jankowski , Poland  
Samuel N. Jator , USA  
Juan Carlos Jáuregui-Correa , Mexico  
Kandasamy Jayakrishna, India  
Reza Jazar, Australia  
Khalide Jbilou, France  
Isabel S. Jesus , Portugal  
Chao Ji , China  
Qing-Chao Jiang , China  
Peng-fei Jiao , China  
Ricardo Fabricio Escobar Jiménez , Mexico  
Emilio Jiménez Macías , Spain  
Maolin Jin, Republic of Korea  
Zhuo Jin, Australia  
Ramash Kumar K , India  
BHABEN KALITA , USA  
MOHAMMAD REZA KHEDMATI , Iran  
Viacheslav Kalashnikov , Mexico  
Mathiyalagan Kalidass , India  
Tamas Kalmar-Nagy , Hungary  
Rajesh Kaluri , India  
Jyotheeswara Reddy Kalvakurthi, India  
Zhao Kang , China  
Ramani Kannan , Malaysia  
Tomasz Kapitaniak , Poland  
Julius Kaplunov, United Kingdom  
Konstantinos Karamanos, Belgium  
Michal Kawulok, Poland

Irfan Kaymaz , Turkey  
Vahid Kayvanfar , Qatar  
Krzysztof Kecik , Poland  
Mohamed Khader , Egypt  
Chaudry M. Khalique , South Africa  
Mukhtaj Khan , Pakistan  
Shahid Khan , Pakistan  
Nam-Il Kim, Republic of Korea  
Philipp V. Kiryukhantsev-Korneev ,  
Russia  
P.V.V Kishore , India  
Jan Koci , Czech Republic  
Ioannis Kostavelis , Greece  
Sotiris B. Kotsiantis , Greece  
Frederic Kratz , France  
Vamsi Krishna , India  
Edyta Kucharska, Poland  
Krzysztof S. Kulpa , Poland  
Kamal Kumar, India  
Prof. Ashwani Kumar , India  
Michal Kunicki , Poland  
Cedrick A. K. Kwuimy , USA  
Kyandoghere Kyamakya, Austria  
Ivan Kyrchei , Ukraine  
Márcio J. Lacerda , Brazil  
Eduardo Lalla , The Netherlands  
Giovanni Lancioni , Italy  
Jaroslaw Latalski , Poland  
Hervé Laurent , France  
Agostino Lauria , Italy  
Aimé Lay-Ekuakille , Italy  
Nicolas J. Leconte , France  
Kun-Chou Lee , Taiwan  
Dimitri Lefebvre , France  
Eric Lefevre , France  
Marek Lefik, Poland  
Yaguo Lei , China  
Kauko Leiviskä , Finland  
Ervin Lenzi , Brazil  
ChenFeng Li , China  
Jian Li , USA  
Jun Li , China  
Yueyang Li , China  
Zhao Li , China






























Zhen Li , China  
En-Qiang Lin, USA  
Jian Lin , China  
Qibin Lin, China  
Yao-Jin Lin, China  
Zhiyun Lin , China  
Bin Liu , China  
Bo Liu , China  
Heng Liu , China  
Jianxu Liu , Thailand  
Lei Liu , China  
Sixin Liu , China  
Wanquan Liu , China  
Yu Liu , China  
Yuanchang Liu , United Kingdom  
Bonifacio Llamazares , Spain  
Alessandro Lo Schiavo , Italy  
Jean Jacques Loiseau , France  
Francesco Lolli , Italy  
Paolo Lonetti , Italy  
António M. Lopes , Portugal  
Sebastian López, Spain  
Luis M. López-Ochoa , Spain  
Vassilios C. Loukopoulos, Greece  
Gabriele Maria Lozito , Italy  
Zhiguo Luo , China  
Gabriel Luque , Spain  
Valentin Lychagin, Norway  
YUE MEI, China  
Junwei Ma , China  
Xuanlong Ma , China  
Antonio Madeo , Italy  
Alessandro Magnani , Belgium  
Toqeer Mahmood , Pakistan  
Fazal M. Mahomed , South Africa  
Arunava Majumder , India  
Sarfranz Nawaz Malik, Pakistan  
Paolo Manfredi , Italy  
Adnan Maqsood , Pakistan  
Muazzam Maqsood, Pakistan  
Giuseppe Carlo Marano , Italy  
Damijan Markovic, France  
Filipe J. Marques , Portugal  
Luca Martinelli , Italy  
Denizar Cruz Martins, Brazil

Francisco J. Martos , Spain  
Elio Masciari , Italy  
Paolo Massioni , France  
Alessandro Mauro , Italy  
Jonathan Mayo-Maldonado , Mexico  
Pier Luigi Mazzeo , Italy  
Laura Mazzola, Italy  
Driss Mehdi , France  
Zahid Mehmood , Pakistan  
Roderick Melnik , Canada  
Xiangyu Meng , USA  
Jose Merodio , Spain  
Alessio Merola , Italy  
Mahmoud Mesbah , Iran  
Luciano Mescia , Italy  
Laurent Mevel , France  
Constantine Michailides , Cyprus  
Mariusz Michta , Poland  
Prankul Middha, Norway  
Aki Mikkola , Finland  
Giovanni Minafò , Italy  
Edmondo Minisci , United Kingdom  
Hiroyuki Mino , Japan  
Dimitrios Mitsotakis , New Zealand  
Ardashir Mohammadzadeh , Iran  
Francisco J. Montáns , Spain  
Francesco Montefusco , Italy  
Gisele Mophou , France  
Rafael Morales , Spain  
Marco Morandini , Italy  
Javier Moreno-Valenzuela , Mexico  
Simone Morganti , Italy  
Caroline Mota , Brazil  
Aziz Moukrim , France  
Shen Mouquan , China  
Dimitris Mourtzis , Greece  
Emiliano Mucchi , Italy  
Taseer Muhammad, Saudi Arabia  
Ghulam Muhiuddin, Saudi Arabia  
Amitava Mukherjee , India  
Josefa Mula , Spain  
Jose J. Muñoz , Spain  
Giuseppe Muscolino, Italy  
Marco Mussetta , Italy

Hariharan Muthusamy, India  
Alessandro Naddeo , Italy  
Raj Nandkeolyar, India  
Keivan Navaie , United Kingdom  
Soumya Nayak, India  
Adrian Neagu , USA  
Erivelton Geraldo Nepomuceno , Brazil  
AMA Neves, Portugal  
Ha Quang Thinh Ngo , Vietnam  
Nhon Nguyen-Thanh, Singapore  
Papakostas Nikolaos , Ireland  
Jelena Nikolic , Serbia  
Tatsushi Nishi, Japan  
Shanzhou Niu , China  
Ben T. Nohara , Japan  
Mohammed Nouari , France  
Mustapha Nourelfath, Canada  
Kazem Nouri , Iran  
Ciro Núñez-Gutiérrez , Mexico  
Włodzimierz Ogryczak, Poland  
Roger Ohayon, France  
Krzysztof Okarma , Poland  
Mitsuhiro Okayasu, Japan  
Murat Olgun , Turkey  
Diego Oliva, Mexico  
Alberto Olivares , Spain  
Enrique Onieva , Spain  
Calogero Orlando , Italy  
Susana Ortega-Cisneros , Mexico  
Sergio Ortobelli, Italy  
Naohisa Otsuka , Japan  
Sid Ahmed Ould Ahmed Mahmoud , Saudi Arabia  
Taoreed Owolabi , Nigeria  
EUGENIA PETROPOULOU , Greece  
Arturo Pagano, Italy  
Madhumangal Pal, India  
Pasquale Palumbo , Italy  
Dragan Pamučar, Serbia  
Weifeng Pan , China  
Chandan Pandey, India  
Rui Pang, United Kingdom  
Jürgen Pannek , Germany  
Elena Panteley, France  
Achille Paolone, Italy

George A. Papakostas , Greece  
Xosé M. Pardo , Spain  
You-Jin Park, Taiwan  
Manuel Pastor, Spain  
Pubudu N. Pathirana , Australia  
Surajit Kumar Paul , India  
Luis Payá , Spain  
Igor Pažanin , Croatia  
Libor Pekař , Czech Republic  
Francesco Pellicano , Italy  
Marcello Pellicciari , Italy  
Jian Peng , China  
Mingshu Peng, China  
Xiang Peng , China  
Xindong Peng, China  
Yuexing Peng, China  
Marzio Pennisi , Italy  
Maria Patrizia Pera , Italy  
Matjaz Perc , Slovenia  
A. M. Bastos Pereira , Portugal  
Wesley Peres, Brazil  
F. Javier Pérez-Pinal , Mexico  
Michele Perrella, Italy  
Francesco Pesavento , Italy  
Francesco Petrini , Italy  
Hoang Vu Phan, Republic of Korea  
Lukasz Pieczonka , Poland  
Dario Piga , Switzerland  
Marco Pizzarelli , Italy  
Javier Plaza , Spain  
Goutam Pohit , India  
Dragan Poljak , Croatia  
Jorge Pomares , Spain  
Hiram Ponce , Mexico  
Sébastien Poncet , Canada  
Volodymyr Ponomaryov , Mexico  
Jean-Christophe Ponsart , France  
Mauro Pontani , Italy  
Sivakumar Poruran, India  
Francesc Pozo , Spain  
Aditya Rio Prabowo , Indonesia  
Anchasa Pramuanjaroenkij , Thailand  
Leonardo Primavera , Italy  
B Rajanarayan Prusty, India

Krzysztof Puszynski , Poland  
Chuan Qin , China  
Dongdong Qin, China  
Jianlong Qiu , China  
Giuseppe Quaranta , Italy  
DR. RITU RAJ , India  
Vitomir Racic , Italy  
Carlo Rainieri , Italy  
Kumbakonam Ramamani Rajagopal, USA  
Ali Ramazani , USA  
Angel Manuel Ramos , Spain  
Higinio Ramos , Spain  
Muhammad Afzal Rana , Pakistan  
Muhammad Rashid, Saudi Arabia  
Manoj Rastogi, India  
Alessandro Rasulo , Italy  
S.S. Ravindran , USA  
Abdolrahman Razani , Iran  
Alessandro Reali , Italy  
Jose A. Reinoso , Spain  
Oscar Reinoso , Spain  
Haijun Ren , China  
Carlo Renno , Italy  
Fabrizio Renno , Italy  
Shahram Rezapour , Iran  
Ricardo Rianza , Spain  
Francesco Riganti-Fulginei , Italy  
Gerasimos Rigatos , Greece  
Francesco Ripamonti , Italy  
Jorge Rivera , Mexico  
Eugenio Roanes-Lozano , Spain  
Ana Maria A. C. Rocha , Portugal  
Luigi Rodino , Italy  
Francisco Rodríguez , Spain  
Rosana Rodríguez López, Spain  
Francisco Rossomando , Argentina  
Jose de Jesus Rubio , Mexico  
Weiguo Rui , China  
Rubén Ruiz , Spain  
Ivan D. Rukhlenko , Australia  
Dr. Eswaramoorthi S. , India  
Weichao SHI , United Kingdom  
Chaman Lal Sabharwal , USA  
Andrés Sáez , Spain

Bekir Sahin, Turkey  
Laxminarayan Sahoo , India  
John S. Sakellariou , Greece  
Michael Sakellariou , Greece  
Salvatore Salamone, USA  
Jose Vicente Salcedo , Spain  
Alejandro Salcido , Mexico  
Alejandro Salcido, Mexico  
Nunzio Salerno , Italy  
Rohit Salgotra , India  
Miguel A. Salido , Spain  
Sinan Salih , Iraq  
Alessandro Salvini , Italy  
Abdus Samad , India  
Sovan Samanta, India  
Nikolaos Samaras , Greece  
Ramon Sancibrian , Spain  
Giuseppe Sanfilippo , Italy  
Omar-Jacobo Santos, Mexico  
J Santos-Reyes , Mexico  
José A. Sanz-Herrera , Spain  
Musavarah Sarwar, Pakistan  
Shahzad Sarwar, Saudi Arabia  
Marcelo A. Savi , Brazil  
Andrey V. Savkin, Australia  
Tadeusz Sawik , Poland  
Roberta Sburlati, Italy  
Gustavo Scaglia , Argentina  
Thomas Schuster , Germany  
Hamid M. Sedighi , Iran  
Mijanur Rahaman Seikh, India  
Tapan Senapati , China  
Lotfi Senhadji , France  
Junwon Seo, USA  
Michele Serpilli, Italy  
Silvestar Šesnić , Croatia  
Gerardo Severino, Italy  
Ruben Sevilla , United Kingdom  
Stefano Sfarra , Italy  
Dr. Ismail Shah , Pakistan  
Leonid Shaikhet , Israel  
Vimal Shanmuganathan , India  
Prayas Sharma, India  
Bo Shen , Germany  
Hang Shen, China

Xin Pu Shen, China  
Dimitri O. Shepelsky, Ukraine  
Jian Shi , China  
Amin Shokrollahi, Australia  
Suzanne M. Shontz , USA  
Babak Shotorban , USA  
Zhan Shu , Canada  
Angelo Sifaleras , Greece  
Nuno Simões , Portugal  
Mehakpreet Singh , Ireland  
Piyush Pratap Singh , India  
Rajiv Singh, India  
Seralathan Sivamani , India  
S. Sivasankaran , Malaysia  
Christos H. Skiadas, Greece  
Konstantina Skouri , Greece  
Neale R. Smith , Mexico  
Bogdan Smolka, Poland  
Delfim Soares Jr. , Brazil  
Alba Sofi , Italy  
Francesco Soldovieri , Italy  
Raffaele Solimene , Italy  
Yang Song , Norway  
Jussi Sopanen , Finland  
Marco Spadini , Italy  
Paolo Spagnolo , Italy  
Ruben Specogna , Italy  
Vasilios Spitas , Greece  
Ivanka Stamova , USA  
Rafał Stanisławski , Poland  
Miladin Stefanović , Serbia  
Salvatore Strano , Italy  
Yakov Strelniker, Israel  
Kangkang Sun , China  
Qiuqin Sun , China  
Shuaishuai Sun, Australia  
Yanchao Sun , China  
Zong-Yao Sun , China  
Kumarasamy Suresh , India  
Sergey A. Suslov , Australia  
D.L. Suthar, Ethiopia  
D.L. Suthar , Ethiopia  
Andrzej Swierniak, Poland  
Andras Szekrenyes , Hungary  
Kumar K. Tamma, USA



Yong (Aaron) Tan, United Kingdom  
Marco Antonio Taneco-Hernández , Mexico  
Lu Tang , China  
Tianyou Tao, China  
Hafez Tari , USA  
Alessandro Tasora , Italy  
Sergio Teggi , Italy  
Adriana del Carmen Téllez-Anguiano , Mexico  
Ana C. Teodoro , Portugal  
Efstathios E. Theotokoglou , Greece  
Jing-Feng Tian, China  
Alexander Timokha , Norway  
Stefania Tomasiello , Italy  
Gisella Tomasini , Italy  
Isabella Torcicollo , Italy  
Francesco Tornabene , Italy  
Mariano Torrisi , Italy  
Thang nguyen Trung, Vietnam  
George Tsiatas , Greece  
Le Anh Tuan , Vietnam  
Nerio Tullini , Italy  
Emilio Turco , Italy  
Ilhan Tuzcu , USA  
Efstratios Tzirtzilakis , Greece  
FRANCISCO UREÑA , Spain  
Filippo Ubertini , Italy  
Mohammad Uddin , Australia  
Mohammad Safi Ullah , Bangladesh  
Serdar Ulubeyli , Turkey  
Mati Ur Rahman , Pakistan  
Panayiotis Vafeas , Greece  
Giuseppe Vairo , Italy  
Jesus Valdez-Resendiz , Mexico  
Eusebio Valero, Spain  
Stefano Valvano , Italy  
Carlos-Renato Vázquez , Mexico  
Martin Velasco Villa , Mexico  
Franck J. Vernerey, USA  
Georgios Veronis , USA  
Vincenzo Vespri , Italy  
Renato Vidoni , Italy  
Venkatesh Vijayaraghavan, Australia




Anna Vila, Spain  
Francisco R. Villatoro , Spain  
Francesca Vipiana , Italy  
Stanislav Vitek , Czech Republic  
Jan Vorel , Czech Republic  
Michael Vynnycky , Sweden  
Mohammad W. Alomari, Jordan  
Roman Wan-Wendner , Austria  
Bingchang Wang, China  
C. H. Wang , Taiwan  
Dagang Wang, China  
Guoqiang Wang , China  
Huaiyu Wang, China  
Hui Wang , China  
J.G. Wang, China  
Ji Wang , China  
Kang-Jia Wang , China  
Lei Wang , China  
Qiang Wang, China  
Qingling Wang , China  
Weiwei Wang , China  
Xinyu Wang , China  
Yong Wang , China  
Yung-Chung Wang , Taiwan  
Zhenbo Wang , USA  
Zhibo Wang, China  
Waldemar T. Wójcik, Poland  
Chi Wu , Australia  
Qihong Wu, China  
Yuqiang Wu, China  
Zhibin Wu , China  
Zhizheng Wu , China  
Michalis Xenos , Greece  
Hao Xiao , China  
Xiao Ping Xie , China  
Qingzheng Xu , China  
Binghan Xue , China  
Yi Xue , China  
Joseph J. Yame , France  
Chuanliang Yan , China  
Xinggang Yan , United Kingdom  
Hongtai Yang , China  
Jixiang Yang , China  
Mijia Yang, USA  
Ray-Yeng Yang, Taiwan

Zaoli Yang , China  
Jun Ye , China  
Min Ye , China  
Luis J. Yebra , Spain  
Peng-Yeng Yin , Taiwan  
Muhammad Haroon Yousaf , Pakistan  
Yuan Yuan, United Kingdom  
Qin Yuming, China  
Elena Zaitseva , Slovakia  
Arkadiusz Zak , Poland  
Mohammad Zakwan , India  
Ernesto Zambrano-Serrano , Mexico  
Francesco Zammori , Italy  
Jessica Zangari , Italy  
Rafal Zdunek , Poland  
Ibrahim Zeid, USA  
Nianyin Zeng , China  
Junyong Zhai , China  
Hao Zhang , China  
Haopeng Zhang , USA  
Jian Zhang , China  
Kai Zhang, China  
Lingfan Zhang , China  
Mingjie Zhang , Norway  
Qian Zhang , China  
Tianwei Zhang , China  
Tongqian Zhang , China  
Wenyu Zhang , China  
Xianming Zhang , Australia  
Xuping Zhang , Denmark  
Yinyan Zhang, China  
Yifan Zhao , United Kingdom  
Debao Zhou, USA  
Heng Zhou , China  
Jian G. Zhou , United Kingdom  
Junyong Zhou , China  
Xueqian Zhou , United Kingdom  
Zhe Zhou , China  
Wu-Le Zhu, China  
Gaetano Zizzo , Italy  
Mingcheng Zuo, China



# Contents

---





**Empowered Hybrid Parent Selection for Improving Network Lifetime, PDR, and Latency in Smart Grid**

Kanabadee Srisomboon , Tinnaphob Dindam , and Wilaiporn Lee   
Research Article (19 pages), Article ID 5551152, Volume 2021 (2021)

**Reliability Estimation under Scarcity of Data: A Comparison of Three Approaches**

Leonardo Leoni , Alessandra Cantini, Farshad BahooToroody, Saeed Khalaj, Filippo De Carlo ,  
Mohammad Mahdi Abaei, and Ahmad BahooToroody  
Research Article (15 pages), Article ID 5592325, Volume 2021 (2021)

**Health Indicator for Predictive Maintenance Based on Fuzzy Cognitive Maps, Grey Wolf, and K-Nearest Neighbors Algorithms**

G. Mazzuto , S. Antomarioni , F. E. Ciarapica , and M. Bevilacqua   
Research Article (21 pages), Article ID 8832011, Volume 2021 (2021)

**Gear Fault Diagnosis Based on VMD Sample Entropy and Discrete Hopfield Neural Network**

Jiakai Ding, Dongming Xiao , Liangpei Huang, and Xuejun Li  
Research Article (13 pages), Article ID 8882653, Volume 2020 (2020)

**Multisensor Prognostic of RUL Based on EMD-ESN**

Jiaxin Pei  and Jian Wang  
Research Article (12 pages), Article ID 6639171, Volume 2020 (2020)

**A Generalized Chart-Based Decision-Making Tool for Optimal Preventive Maintenance Time under Perfect Renewal Process Modeling**

Pablo Viveros Gunckel , Fredy Kristjanpoller , and René Tapia Peñaloza  
Research Article (28 pages), Article ID 3078041, Volume 2020 (2020)

## Research Article

# Empowered Hybrid Parent Selection for Improving Network Lifetime, PDR, and Latency in Smart Grid

**Kanabadee Srisomboon** , **Tinnaphob Dindam** , and **Wilaiporn Lee** 

*Communication and Computer Network Research Group (C2NRG), Electrical Engineering,  
Department of Electrical and Computer Engineering, Faculty of Engineering,  
King Mongkut's University of Technology North Bangkok, Bangkok, Thailand*

Correspondence should be addressed to Wilaiporn Lee; [wilaiporn.l@eng.kmutnb.ac.th](mailto:wilaiporn.l@eng.kmutnb.ac.th)

Received 20 January 2021; Accepted 13 May 2021; Published 25 May 2021

Academic Editor: Mohammad Mahdi Abaei

Copyright © 2021 Kanabadee Srisomboon et al. This is an open access article distributed under the Creative Commons Attribution License, which permits unrestricted use, distribution, and reproduction in any medium, provided the original work is properly cited.

To support the constraints of smart meters—low power and memory—of AMI network, RPL is considered as the most suitable routing protocol to be implemented in practice. Network lifetime, PDR, and latency are the critical issues to be focused on and addressed. Generally, single parent selection scheme cannot satisfy all expected performance requirements of RPL based on AMI network due to tradeoff between workload balancing and transmission performance, PDR and latency. Moreover, the single parent also suffers from the package size and transmission range. Then, multiparent solution is proposed to overcome these demerits using multipath transmission strategy. Although the existing multiparent solutions, MELT and MAHP, overcome the issue of transmission performance, they present low network lifetime since multiparent solution consumes high energy in data transmission. In this paper, we propose an “empowered hybrid parent selection (EHPS)” that exploits the merits of multiparent solution and the single parent with cognitive radio technology in a hybridizing scheme. To split the data packet efficiently under multipath transmission strategy, a fuzzy AHP (FAHP) is adopted; therefore, EHPS balances the workload effectively and maximizes the network lifetime over long transmission range and large data size. Moreover, by exploiting cognitive radio, EHPS is flexible to the transmission range and data size since it achieves the highest transmission performance, highest PDR, and lowest latency among others, while maintaining high network lifetime.

## 1. Introduction

With increasing electrical demands, the electrical grid shows a tendency to be managed more efficiently, which cannot be achieved by the conventional strategy based on a centralized and manual management system. To alleviate the impairment of conventional grid, a smart grid is being recognized as the next generation of electrical grid which corroborates communication and data processing technology with the electrical grid. Therefore, smart grid achieves system efficiency, reliability, and robustness of electrical generation and distribution system. The advanced metering infrastructure (AMI) [1–5] is the crucial application of the smart grid which manages information between utility and clients, e.g., smart meters, through a local access point (data concentrator unit: DCU) using the two-way communication

method. Once the information can be exchanged between smart meters and the DCU in both directions and in real time, the smart grid is recognized as the self-monitoring and self-healing system since simple troubleshooting and repairing can be performed automatically without technician intervention.

In an AMI network, a number of low power and memory devices, smart meters, are interconnected in a multihop manner through modern communication technology. The routing protocol is considered as a crucial function in the AMI network that is used to ensure high communication performance in terms of packet delivery ratio (PDR) and latency. The routing protocol for low power and lossy networks (RPL) [6–13] is considered as the most suitable routing protocol for AMI network according to its characteristics as it has the ability to deal with lossy links, support

communication in a point-to-multipoint and multipoint-to-point manner, and provide a low energy consumption and low bandwidth usage due to low signaling overheads [7]. Once the battery and memory are the limitation of the smart meters [8], not only PDR and latency are determined, but also the meter workload should be taken into account to prolong a network lifetime and prevent information loss due to a fast battery depletion issue.

Based on the RPL routing scheme, a smart meter forwards the data to the DCU through several relay nodes, i.e., the neighbor smart meters advertised by lower rank level. In RPL, the relay node is known as a parent. If the workload is not considered, the smart meter with a high workload will deplete fast and before the maintenance session is performed, which refers to an early depletion node. Generally, the network lifetime is determined by the early depletion node. Therefore, the utility loses the information to be used for the electrical production planning and electricity billing application. Then, each meter lifetime needs to be monitored carefully and individually. On the other hand, to achieve the objective of smart grid, a high transmission performance, i.e., PDR and latency, is required.

PDR, the success data transmission rate, should be high while the latency should be low to achieve a real-time application [14]. These two metrics are affected by the quality of the selected link of parent meters. If the link quality of parent meter is low, the data packets may drop during the transmission; then, the data retransmission is required. Therefore, the smart meter must consume extra energy for the data retransmission.

Parent selection is the vital function of the RPL that plays an important role in avoiding the early depletion node while maintaining the performance of the transmission. Currently, the parent selection can be categorized into single selection [15–23] and multiparent solution scheme [24–26]. Traditionally, parent selection of RPL determines the single immediate parent by considering only a single metric, i.e., residual energy or expected transmission count (ETX). By considering only the ETX [15–18], only the parent with the highest quality is selected; then, it achieves a high PDR and low latency. However, the batteries of the high quality parents deplete much faster than the others. Therefore, the early depletion node occurs. On the other hand, although the parent selection based on residual energy [19, 20] balances the workload perfectly, high PDR and low latency cannot be met since the low quality parent is selected. Later, several techniques [21–23] are proposed to address the issues by taking energy into account. However, they cannot satisfy overall performance.

On the contrary, the rate of PDR is affected by two important factors: link quality and data package size. The link quality degrades on the transmission channel characteristic and the transmission range. On the other hand, the data package size depends on the application of AMI; i.e., the package size for energy usage of household is much smaller than that for energy usage of manufacturing, which causes a decrease in the PDR rate and an increase in the latency. As stated in RFC standard [13], once the single parent suffers from the low rate of PDR, the multiple parent needs to be

considered to address the issue. Moreover, depending on convergecast traffic of single parent scheme, there is always a tradeoff between the transmission performance and the load balancing ability since all of the data from a single node will be transmitted to the immediate parent. Multiparent solution is proposed to address this tradeoff issue by splitting the data into small packets and forwarding them to a number of parents. The multiparent based on ELT (MELT) [26] is proposed by splitting the parents' workload on an estimated the expected lifetime (ELT) [23] according to the ELT of bottleneck parents. However, the workload of MELT splits on the fixed step; therefore, the workload of each parent is not balanced comprehensively and effectively. Later, an analytic hierarchy process (AHP) [27–31] is utilized for multiparent selection (MAHP) [32] to improve the performance of MELT by considering ETX, node remaining energy, and hop count (HC) as the main criteria. However, under fixed influence weights of criteria, MAHP cannot achieve high network lifetime since the meters with different rank have different workloads. Therefore, the influence weight of energy-efficient criteria should be varied on the ranking.

In this paper, we propose the empowered hybrid parent selection (EHPS) algorithm of RPL for AMI network. The multiparent solution with fuzzy analytic hierarchy process (FAHP) [33–35] and the cognitive radio [36, 37] are exploited under hybridizing scheme to achieve high performance of the three crucial metrics: network lifetime, PDR, and latency. Cognitive radio is the advanced communication technology that is proposed to deal with the underutilization of spectrum resources. The unlicensed user is permitted to utilize the available licensed channel while causing unnoticeable interference to the licensed user. Therefore, the meter should be considered as the cognitive device that can monitor the status of surrounding communication channels and can adapt its parameter for using on the selected channel.

The contribution of this paper is threefold. First, network lifetime is maximized through hybrid parent selection algorithm. The quality of parents is comprehensively analyzed through the FAHP, which is an extended scheme of an analytic hierarchy process (AHP) with the weight adapting scheme where ETX, ELT, and expected transmission time (ETT) are determined as the main criteria. The meter's ranking is considered in adapting the influence of the energy efficiency since the meters advertised by the lower rank come at a cost of high workload; i.e., the lower rank meters have to forward the data from their children. Then, the appropriate size of data package is forwarded to each parent on its quality. Therefore, the workload of each parent is balanced effectively, and the network lifetime is prolonged.

Second, the issue of low PDR under long transmission range is addressed by hybridizing the merits of multiple parents and single parent with cognitive radio technology. Through multiparent solution, the PDR is improved by forwarding a number of small packets to  $k$  parents since the transmission error rate is affected by the size of transmitted data. Moreover, under long transmission range, multiple parents cannot achieve high performance of PDR and energy



efficiency because the transmission error rate also increases on the distance. Therefore, we exploit the cognitive radio technology on the single parent scheme to address the transmission range issue. Under cognitive radio technology, the meter forwards data on available licensed channels opportunistically. Although the meters should consume higher transmission power as compared to the original Zigbee [38] technology of RPL, we achieve high energy efficiency and high PDR since the meter on Zigbee channel wastes the energy on performing retransmission which also gives low PDR. It should be noted that the single parent with cognitive radio cannot achieve high energy-efficient performance under short transmission range since multiple parents can present high PDR at short transmission range. Once the single parent with cognitive radio consumes the energy usefully, the EHPS presents the highest network lifetime under long transmission range.

Third, the EHPS achieves the lowest latency since it presents high PDR under hybridizing scheme. Under low transmission range, a low latency is achieved by using multiparent solution while the EHPS maintains low latency under long transmission range using the cognitive radio.

The remainder of this paper is organized as follows. In Section 2, the details of RPL and parent selection methods are introduced. The issues of parent selection are described in Section 3. In Section 4, EHPS algorithm is proposed and described in detail. The simulation results and the performance evaluation are presented in Section 5. Conclusion is presented in the final section.

## 2. Related Works

*2.1. IPv6 Routing Protocol for Low Power and Lossy Networks (RPL).* RPL [6–13] is the routing standard for the lossy network comprising low power and memory devices. It is considered as the most suitable routing protocol to be implemented with the smart meters of AMI network since the RPL has the ability to deal with lossy links, support communication in a point-to-multipoint and multipoint-to-point manner, and provide a low energy consumption and low bandwidth usage due to low signaling overheads [9].

The key characteristic of RPL is the interconnection with loop avoiding of RPL network—directed acyclic graphs (DAG). Through distance vector base routing, the RPL constructs a rooted  $k$ -ary tree routing topology, destination-oriented directed acyclic graphs (DODAG), according to distance vector where the role of each node is advertised by the rank. In  $k$ -ary tree topology,  $k$  is the number of children for each parent. As illustrated in Figure 1,  $k$  is set to 3, so each parent has 3 children.

In the DODAG construction and maintenance process, a root node—border router or data concentrator (DCU) of AMI network—broadcasts the DAG information option (DIO) message, which contains DODAG identifier, current rank of the node, objective function (OF), and additional information for path computation to neighbors. The neighbors who receive the broadcasted DIO message use the received information to update their rank level, select the immediate parent, and join the DODAG. Therefore, the

neighbor who selects the broadcasted DIO message as the immediate parent is considered as the child node. Then, the child node sends the feedback to its immediate parent using destination advertisement object (DAO) message.

As illustrated in Figure 2, firstly, the root node broadcasts DIO message to node 2, node 3, and node 4. Then, these nodes update their rank level to “rank 1” and they select the route node as the immediate parent by sending the DAO message to the route node. Once node 2, node 3, and node 4 complete their DODAG joining process, they will broadcast the DIO message to other neighbors, node 5 to node 9, for further DODAG construction. On the other hand, if a node needs to join the DODAG or needs to perform local route maintenance when batteries of all candidate parents deplete, the node exploits DODAG information solicitation (DIS) to request route maintenance. Therefore, the nodes who receive DIS message will broadcast DIO message to neighbors and the requested node. It can be noticed that the level of rank of a node is assigned according to the distance vector to the root node. The nodes with highest rank can transmit their information to the root node in upward direction. To avoid information looping, the node in the topology is not allowed to transmit the DAO message to neighbors with the same rank.

RPL also supports data transmission in an upward direction; therefore, the smart meters can forward the information, such as energy usage, to the DCU via ancestor meters. In the upward data transmission process, the child meter exploits DAO message to transmit its information to the DCU in a unicast manner. The DAO message contains the generated information and the target parents. The immediate parent who receives the DAO message will send an acknowledgment message to the child node, generate a new DAO message, and send the new DAO message containing the message generated by the child to its parent. The process is repeated until the generated message reaches the target parent. Therefore, the framework of RPL is suitable to be implemented in the smart meters of AMI network. Once the memory and battery are considered as the limitation of the meters [8], not only the packet delivery ratio (PDR) and latency are determined, but also the energy efficiency must be taken into account.

*2.2. Parent Selection.* Parent selection plays the important role in achieving a high requirement of data transmission of AMI application where the PDR should be as high as 0.98 [14]. Generally, parent selections can be categorized into single parent and multiparent method. Traditionally, the first standard of RPL selects the parent based on a single metric, expected transmission count (ETX) or residual energy. In this paper, we consider that the parent selection based on ETX is called “RPL.” The RPL selects the parent by determining the ETX metric where ETX is given as

$$ETX = \frac{1}{(D_f \times D_r)} = \frac{1}{1 - p}, \quad (1)$$

where  $D_f$  is the probability that the packets are received by the neighbor,  $D_r$  is the probability that the acknowledgment

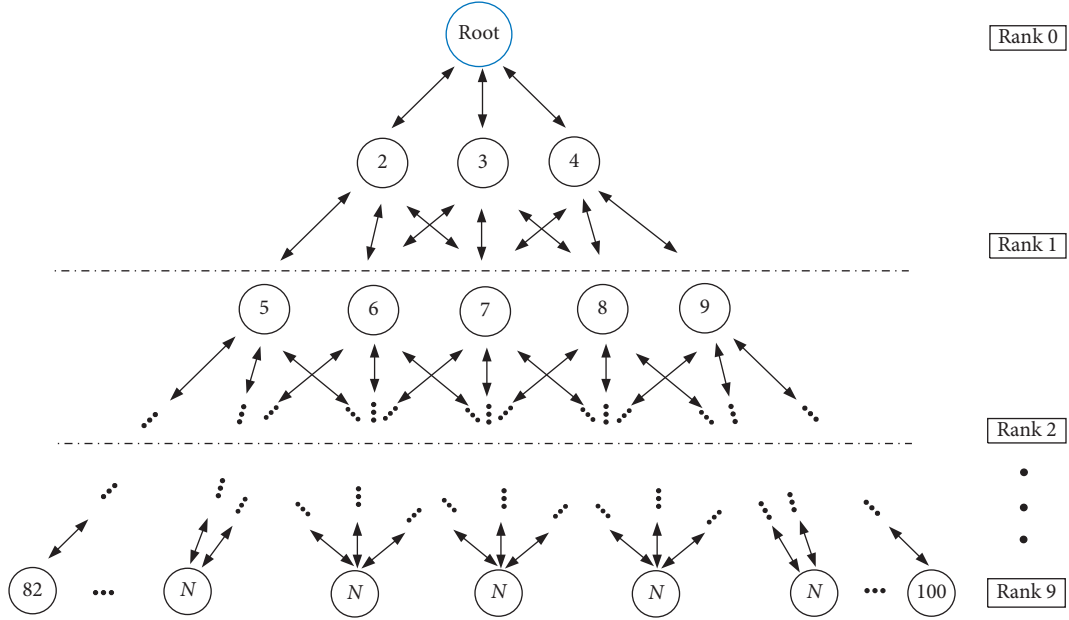


FIGURE 1: 3-ary tree topology of RPL network.

packet is successfully received, and  $p$  is the error data transmission rate.

It can be noticed that ETX is used to determine the quality of parents from the perspective of the PDR. The parent will be declared to be of high quality if the ETX is as low as 1. If the ETX is greater than 1, the quality of the parent becomes worse. Even if the RPL achieves high PDR, it does not take the workload balancing into account since the child selects only the highest quality parent to be the immediate parent. The parent selection of the RPL is illustrated in Figure 3 where the immediate parent is selected based on the lowest ETX.

Later, the alternative metrics are considered for single parent selection scheme. However, they cannot overcome the tradeoff between the transmission performance and the energy consumption. Moreover, they cannot achieve high transmission performance affected by the data package size and transmission range. Therefore, RFC standard [13] stated that multiparent, multipath routing scheme should be considered to address the single parent issues. The multipath routing scheme splits the data into small packets and forwards them to a number of parents. Multiparent solution based on ELT (MELT) [26] is proposed to improve the workload balancing while maintaining the PDR at high rate by considering the expected lifetime of child node according to the ELT of bottleneck parents. The bottleneck meter has a noticeably high workload and seems to be the first node whose battery depletes. The expected lifetime (ELT) of a node ( $N$ ) is considered as

$$\text{ELT}(N) = \frac{E_{\text{res}}(N)}{(T_N \times \text{ETX}(N, P) / \text{DATA\_RATE}) \times P_{\text{RadioTX}}(N)}, \quad (2)$$

where  $T_N$  is the traffic generated by a considered meter and its children,  $\text{ETX}(N, P)$  is the ETX of the meter and its

considered parent ( $P$ ), and  $\text{DATA\_RATE}$  is the transmission rate.

It should be mentioned that the residual energy ( $E_{\text{res}}(N)$ ) can be calculated by

$$E_{\text{res}}(N) = \text{Battery} - E_{\text{cons}}(N), \quad (3)$$

where the energy consumption ( $E_{\text{cons}}(N)$ ) is given as

$$E_{\text{cons}}(N) = T_{\text{CPU}} \times P_{\text{CPU}} + T_{\text{RadioRX}}(N) \times P_{\text{RadioRX}}(N) + T_{\text{RadioTX}}(N) \times P_{\text{RadioTX}}(N), \quad (4)$$

where  $T_{\text{CPU}}$  is the CPU processing time,  $P_{\text{CPU}}$  is the power consumption of CPU,  $T_{\text{RadioRX}}(N)$  is the receiver processing time,  $P_{\text{RadioRX}}(N)$  is the power consumption of receiver,  $T_{\text{RadioTX}}(N)$  is the transmitter processing time, and  $P_{\text{RadioTX}}(N)$  is the power consumption of transmitter.

Therefore, parents' workload is balanced according to the expected lifetime of the node and the bottlenecks through the traffic ratio ( $\alpha_p$ ). Generally, the bottleneck nodes are the nodes at rank 1. The load balancing algorithm of MELT is shown in Algorithm 1.

To determine the traffic ratio ( $\alpha_p$ ), node  $N$  determines the best parent iteratively to assign the highest traffic ratio. Firstly, the minimum ELT of node  $N$  and bottlenecks are estimated by increasing  $\alpha_p$  of considered parent individually with the load balancing step ( $\gamma$ ). Secondly, the best parent with the maximum expected lifetime (ELT) is determined. Thirdly, node  $N$  decreases  $\alpha_p$  of considered parent and increases  $\alpha_p$  of other parents to investigate the expected lifetime (ELT). Finally, the parent  $P$  with the maximum ELT will be assigned the highest  $\alpha_p$ . Then, the illustration of workload balancing of MELT is shown in Figure 4. MELT benefits from the transmission of small packets, so it achieves high transmission performance, PDR and latency.

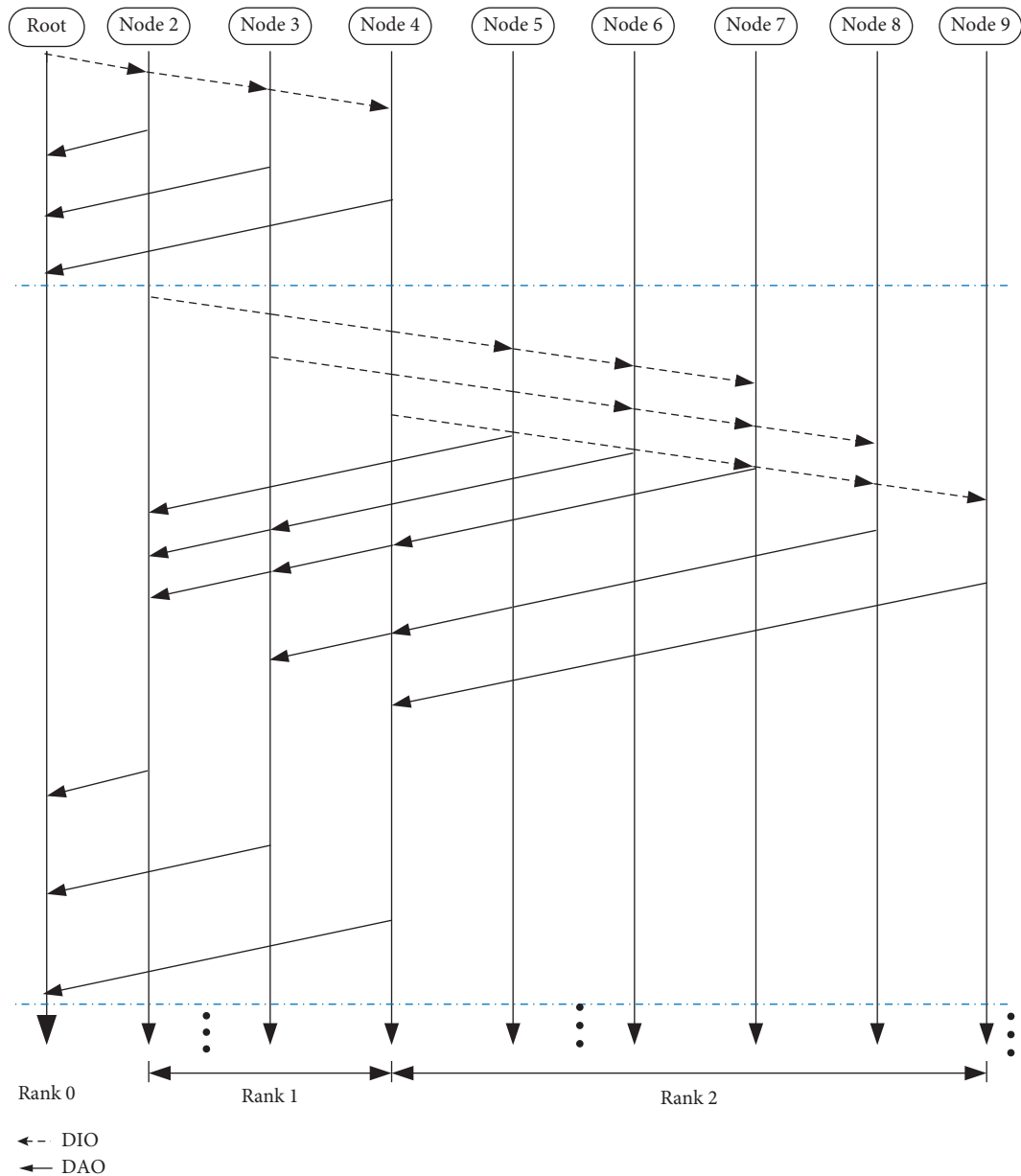


FIGURE 2: Route construction of RPL.

Moreover, MELT addresses the instability of a single parent scheme since all parents are utilized.

Multiparent selection adopts an analytic hierarchy process (MAHP) [32] to assign the split data packets to each parent based on its performance. Based on AHP algorithm, firstly the main criteria must be defined, and then each criterion undergoes a pairwise comparison according to the assigned importance weights. In MAHP, ETX, node remaining energy, and hop count (HC) are determined as the main criteria. Then, the pairwise comparison matrix of main criteria is constructed, and the weights of main criteria are calculated using a normalized eigenvector. To generate the traffic ratio of MAHP, the values of each main criterion are determined as subcriteria, and the weights are calculated. Then, the traffic ratio is generated by determining the expected performance of the main criteria weight

corresponding to subcriteria weight of each parent. By comprehensive determining of parents' quality, MAHP improves the performance of MELT. The illustration of MAHP parent selections is depicted in Figure 5.

### 3. Problem Statement

Being associated with the application of the smart grid, network lifetime, packet delivery ratio (PDR), and latency are the major concerns of low power devices, such as smart meter, of the network. The network lifetime refers to the early depletion node whose battery runs out faster than others and before the maintenance session is performed.

Once the early depletion node occurs, the root node loses the information from the early depletion node. Therefore, the DCU cannot utilize the data to perform the further

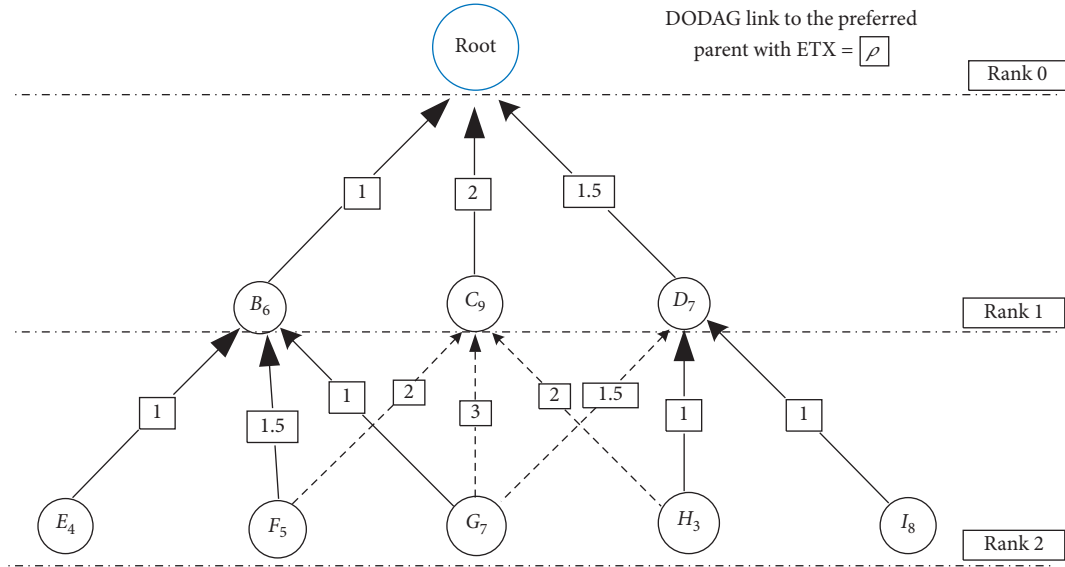


FIGURE 3: Illustration of traditional RPL parent selection.

```

Data:  $N$ ,  $\gamma$ —the step of the load increase
Result: compute  $\{\alpha_p\}_{p \in \text{Parents}(N)}$ 
for  $i = 1$  to  $\gamma^{-1}$  do
   $\text{max\_elt} \leftarrow 0$ ;
  for  $P \in \text{Parents}(N)$  do
    //test this parent  $P$  with its new weight
     $\alpha_p \leftarrow \alpha_p + \gamma$ ;
    //track the min ELT with this new weight
     $\text{min\_elt} \leftarrow \min_{B \in \text{Bottlenecks}(P)} \{\text{ELT}(B)\}$ ;
     $\text{min\_elt} \leftarrow \min\{\text{min\_elt}, \text{ELT}(N)\}$ ;
    //is this parent the best one?
    if  $\text{max\_elt} < \text{min\_elt}$  then
       $\text{max\_elt} \leftarrow \text{min\_elt}$ ;
       $\text{preferred\_parent} \leftarrow P$ ;
    end
  //test each parent before taking a decision
   $\alpha_p \leftarrow \alpha_p - \gamma$ ;
  end
   $\alpha_{\text{parent\_max}} \leftarrow \alpha_{\text{parent\_max}} + \gamma$ ;
end

```

ALGORITHM 1: Load balancing algorithm of MELT [26].

operation. On the other hand, based on a single parent scheme, the transmission performance—PDR and latency—is affected by the quality of the immediate parent affected by the surrounding environment. Then, the parent selection function of the RPL plays an important role in avoiding the early depletion node while maintaining the reliability and latency.

**3.1. Network Lifetime.** Depending on the tree structure of RPL, each node is ranked according to the distance vector between the node and the root node. The node can only forward the data to the neighbors who are advertised by the different number of rank. By considering the traditional parent

selection scheme with a nonconsidering workload balancing concept, the node selects the parent with the highest quality to be the immediate parent which is selected during route construction and maintenance session. Based on 3-ary tree structure, as illustrated in Figure 1, each parent has three children. For example, node 2 is considered as the parent of node 5 and node 6, and it is considered as the candidate parent of node 7. Node 3 is considered as the parent of node 7, and it is considered as the candidate parent of node 6 and node 8. Node 4 is considered as the parent of node 8 and node 9, and it is considered as the candidate parent of node 7.

It can be mentioned that, without taking into account the nonbalancing concept, the node only forwards its data to the best parent until the immediate parent is disabled due to battery depletion. As depicted in Figure 6(a), by considering node 2 and node 3, it can be noticed that node 2 consumes the battery faster than node 3 because it has more children. With the passing of time, node 2 will deplete faster than node 3 due to battery depletion. Then, the local route maintenance is performed, where the DIS message is broadcasted to neighbors, as illustrated in Figure 6(b), by node 6 and it will select node 3 as the immediate parent. The dataflow of each node and the loss of information from node 2 are shown in Figure 7. Based on this scenario, the root node loses the information from node 2 since node 2 does not have the power to transmit its data. Moreover, node 5 wastes the battery usage for performing the local route maintenance request, and node 6 will have more workload since it has to forward the data from node 5 to its immediate parent. Once node 6 gains its workload, its battery will deplete faster than others and the root node will also lose the information from node 6.

Since the workload balancing scheme is not taken into account, the depleted node will occur before the network maintenance session. Then, the utility will lose the information from the early depletion nodes. Therefore, the workload balancing scheme plays an important function for the low power device network.

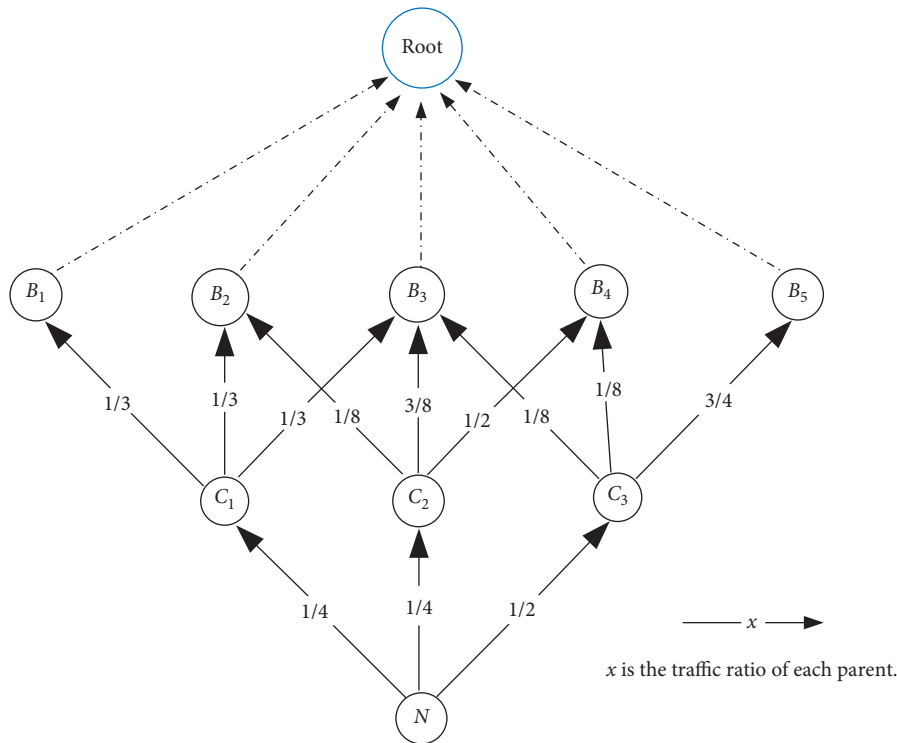


FIGURE 4: Illustration of MELT load balancing scheme.

3.2. *Transmission Performance.* In practice, the smart meters are considered as the static nodes; however, the quality of data transmission—PDR and latency—is affected by the surrounding environment, such as noise, distance between the child meter and the immediate parent, and data size. In general, PDR and latency are the two factors that relate to the surrounding environment directly. The environment between a child and a parent is bad; i.e., the noise is high and the child node is far from the parent. Therefore, the quality of received data by the parent will be low, and the received data will be neglected since its quality is too low to be utilized.

The packet delivery ratio (PDR) is the major factor that is used to evaluate transmission performance. PDR refers to the success transmission rate which is the ratio between the data packets transmitted by the transmitter and the packets received by the receiver. PDR should be high while latency should be low to achieve a real-time application. Generally, the transmission range and the size of data are the two major factors that degrade the PDR and increase the latency.

Once the distance between the child meter and parent is far, the transmitted package drops during the transmission and then the PDR decreases. Therefore, the retransmission is required, which increases the latency, and the child meter and parent meter must consume extra energy. This extra energy consumption refers to the energy inefficiency. On the other hand, the data package size affects transmission performance. Once the package size is high, the probability of package drop during transmission increases. Therefore, the PDR noticeably decreases on increasing package size while latency increases.

As stated by RFC standard [13], since the single parent scheme cannot meet the requirement of the transmission performance for the long transmission range and large data package size, the multiparent solution should be considered.

Although the multiparent solution presents higher transmission performance with high workload balancing than the single parent at long transmission range, a high energy consumption and low network lifetime are considered as the major demerits. Moreover, over noticeably long transmission range, the multiparent solution cannot satisfy the requirements of a high PDR and low latency due to the limited transmission channel, presents a low network lifetime, and cannot achieve high energy efficiency.

Therefore, in this paper, we proposed a hybrid solution that adapts the parameter to transmit the data packet between the multiparent solution and the single parent with cognitive radio based on the expected performance determined by the advanced multicriteria ranking method.

#### 4. Empowered Hybrid Parent Selection

In this paper, we propose the empowered hybrid parent selection (EHPS) algorithm to maximize the network lifetime and achieve a high packet delivery ratio (PDR) and low latency using hybridizing scheme of the multiparent solution and the single parent with cognitive radio. The fuzzy analytic hierarchy process (FAHP) [33–35] is exploited where the expected transmission count (ETX), expected lifetime (ELT), and expected transmission time (ETT) [22] are determined as the main criteria, to analyze the quality of



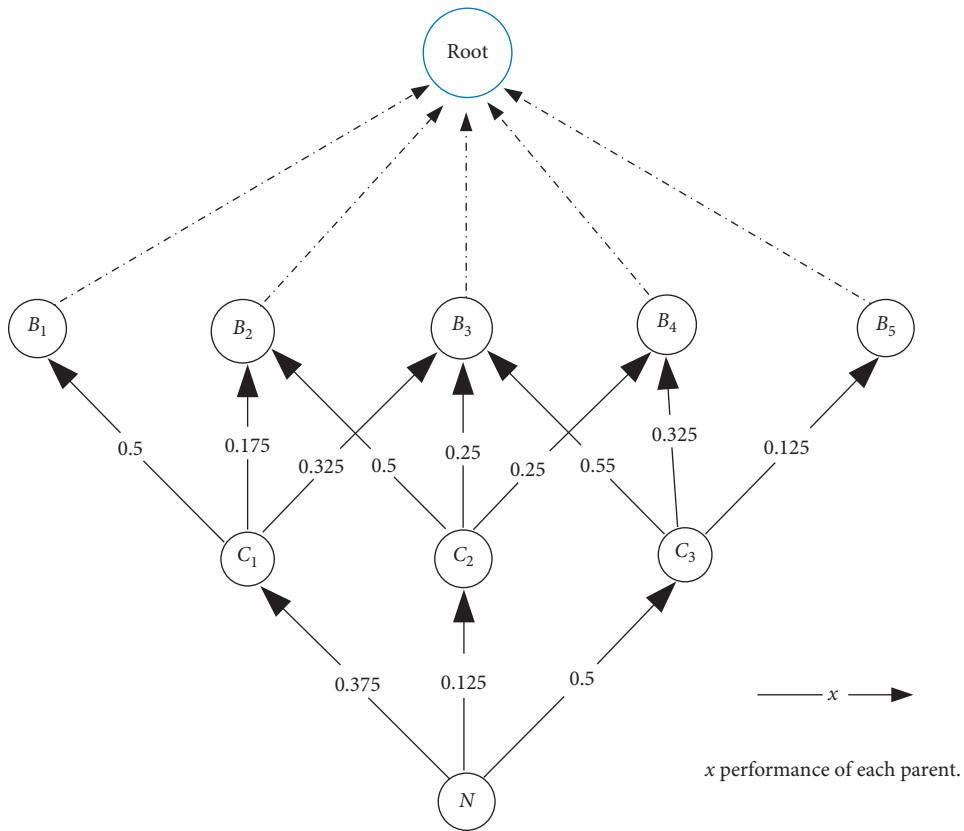
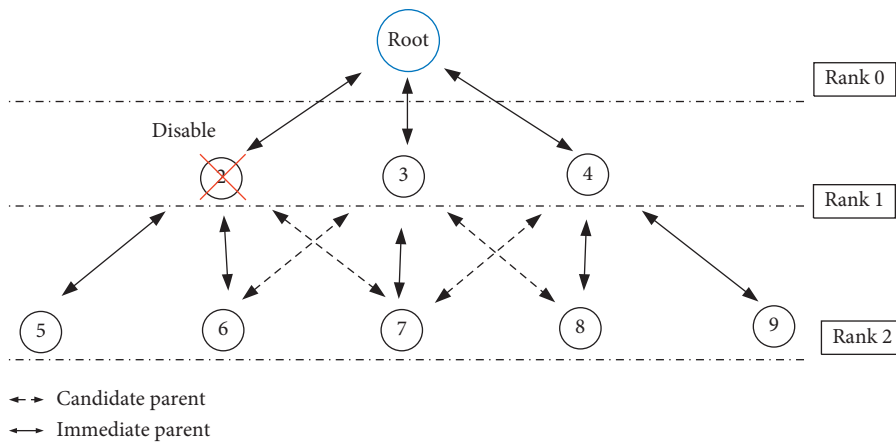


FIGURE 5: Illustration of MAHP load balancing scheme.



(a)

FIGURE 6: Continued.

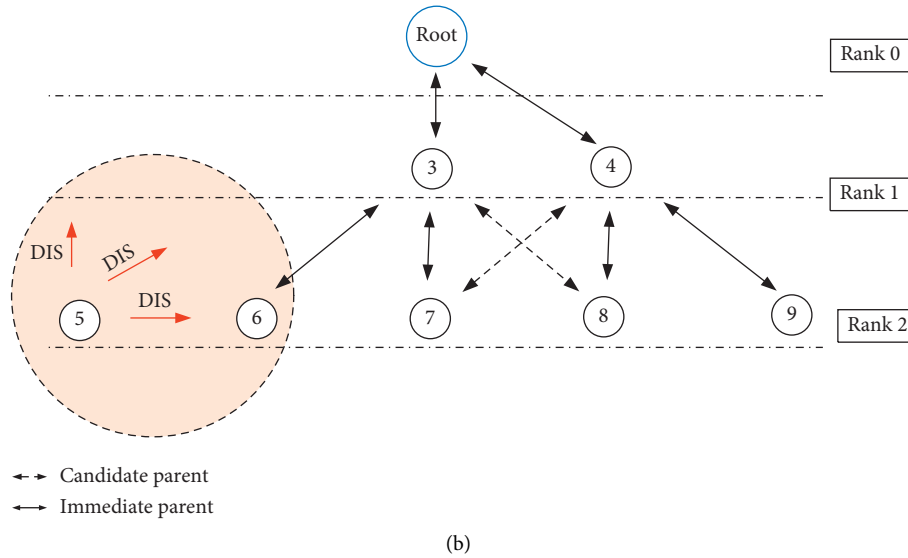
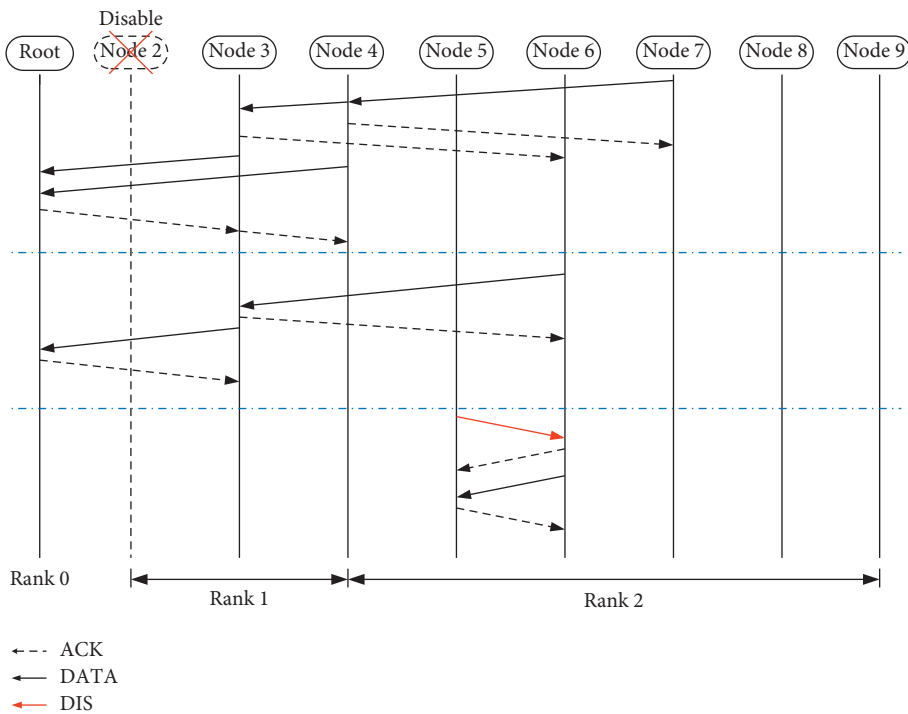


FIGURE 6: Occurrence of early depletion node: (a) 3-ary tree structure of RPL network with node 2 disabled; (b) local route maintenance session performed by node 5.



parent meters comprehensively. In FAHP, the fuzzy set is exploited with the traditional AHP to address the unbalance judgment scaling of traditional version. To achieve high network lifetime, the workload balancing capability is improved by using influence weight adapting scheme. From our study, the energy consumption increases on decreasing meter’s ranking in an exponential manner. Therefore, our algorithm adapts the influence of energy efficiency through ELT criteria

exponentially. Moreover, the single parent with cognitive radio is adopted in a hybridizing scheme with multi-parent solution to achieve a high PDR rate, high energy efficiency, and low latency under a long transmission range.

The framework of EHPS is shown in Figure 8 which can be categorized into offline and online mode. In an offline mode, once the algorithm is activated, the three main criteria—ETX, ELT, and ETT—are pairwise compared

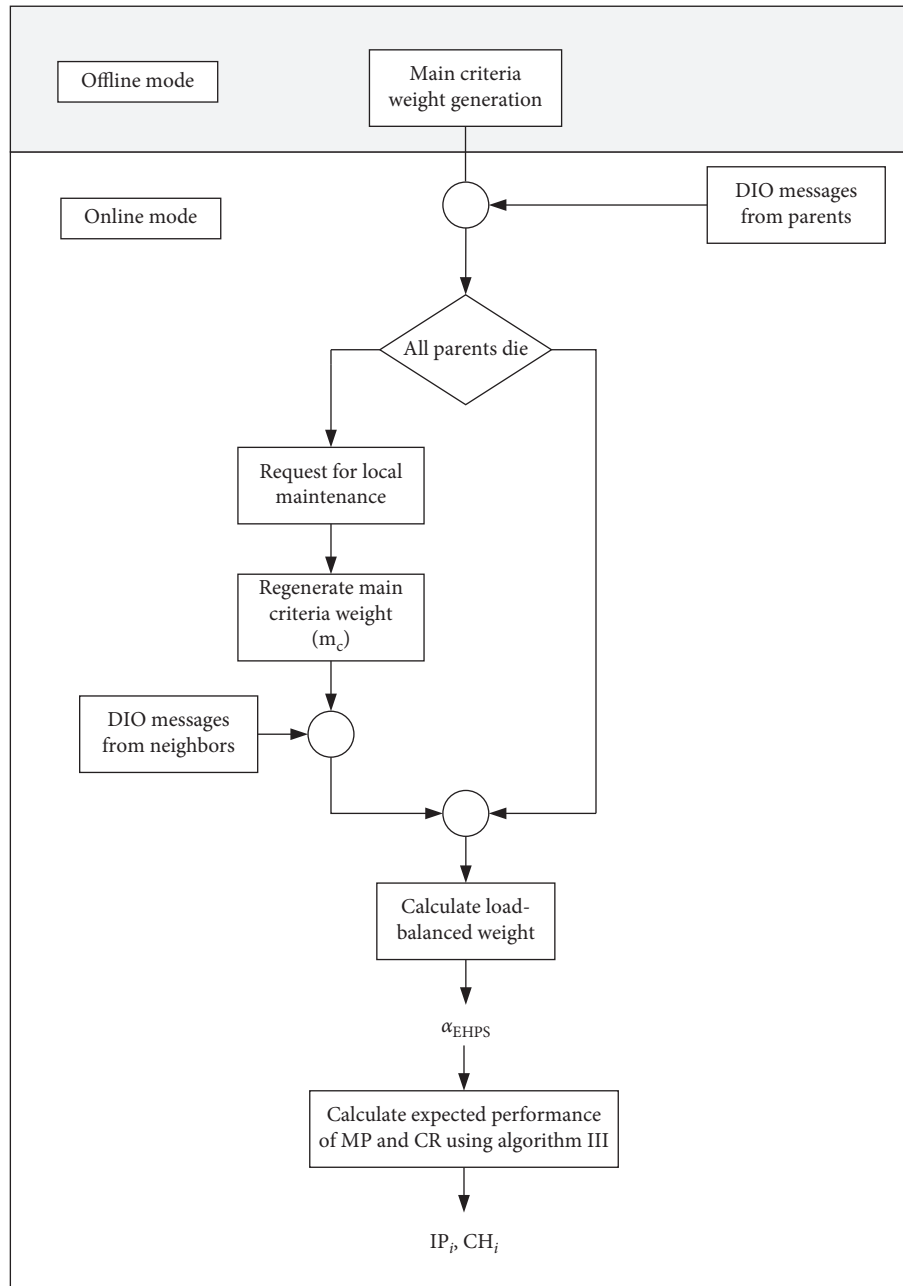


FIGURE 8: Framework of EHPS.

according to FAHP theorem to generate the main criteria weight ( $m_c$ ). Depending on tree topology, the level of energy consumption in each rank is different according to the number of children; then, the requirement of workload balancing in each rank should be different. Therefore, in our algorithm, we determine the effect of network ranking as the factor for performing a pairwise comparison in multicriteria ranking process. Then, the pairwise comparison between ETX and ELT is varied based on the number of rank; e.g., ELT factor in rank 4 should be more important than ELT factor in rank 5 because a parent in rank 4 has a higher number of children than a parent in rank 5.

In an online mode, firstly, the node receives the DIO messages from a number of candidate parents, where the message contains its ELT. Secondly, the node performs the ELT calculation of those candidate parents by adding its traffic to determine the actual ELT when the traffic of the node is taken into account. If all candidate parents die, the node will broadcast DIS message to request the local maintenance process. Once the neighbors receive the DIS message, they will transmit DIO message to the node. Then, the node will calculate the load-balanced weight through FAHP procedure.

To calculate ELT, firstly, the data traffic from the node to be transmitted to the parents is determined, where the data traffic ( $T$ ) is given by

$$T = T_{\text{node}} + \sum_{i \in \text{Children}(\text{node})} T_i. \quad (5)$$

Secondly, the energy consumption ( $E$ ) of the node included with the retransmission factor is calculated, which can be expressed as

$$E(N) = \frac{T \times (\sum_{i \in \text{Children}(\text{node})} \alpha_i) \times \text{ETX}(\text{node}, C)}{\text{Data\_rate}} \times P_{\text{TX}}, \quad (6)$$

where  $\alpha_i$  is the traffic ratio in which the children forward the packets to the node,  $P_{\text{TX}}$  is the transmission power, and  $\text{Data\_rate}$  is the data transmission rate.

Finally, the expected lifetime (ELT) of node  $N$  is given as

$$\text{ELT}(N) = \frac{E_{\text{res}}(N)}{E(N)}. \quad (7)$$

By exploiting FAHP theorem [35], firstly, pairwise comparison is made on each main criterion; therefore, weight of importance between criteria should be assigned. As mentioned earlier, the effect of meter's ranking where the energy consumption changes exponentially is taken into account, and it is determined as the multiplication factor (mf) to be used in the pairwise comparison process. Then, the mf can be derived as follows. The exponential change of energy consumption can be expressed as

$$y = Ce^{bx}, \quad (8)$$

where  $C$  is the constant value,  $b$  is the growth rate of exponential function, and energy consumption is considered as the input data ( $x$ ).

Then, the decaying exponential function can be rewritten as

$$\ln y = \ln C + bx. \quad (9)$$

Therefore, the fitting values can be given as

$$b = \frac{n \sum_{i=1}^n x_i \ln y_i - \sum_{i=1}^n x_i \sum_{i=1}^n \ln y_i}{n \sum_{i=1}^n x_i^2 - (\sum_{i=1}^n x_i)^2}, \quad (10)$$

where  $n$  is the amount of data.

In our algorithm, we utilize the exponential function with the growth rate where influence of rank is taken into account. Therefore, the multiplication factor (mf) is given as

$$\text{mf} = e^{b(\text{Rank}_{\text{max}} - \text{Rank}_{\text{current}})}, \quad (11)$$

where  $\text{Rank}_{\text{max}}$  is the maximum rank of the network and  $\text{Rank}_{\text{current}}$  is the current rank.

Therefore, to determine the load-balanced weight of EHPS ( $\alpha_{\text{EHPS}} = [\alpha_{\text{EHPS}_1}, \alpha_{\text{EHPS}_2}, \dots, \alpha_{\text{EHPS}_k}]$ ), the structure of multicriteria ranking according to FAHP algorithm is constructed as depicted in Figure 9. In our proposed algorithm, ETX, ELT, and ETT are determined as the main criteria. The actual values of each main criterion are determined as the input of subcriteria.

The framework of EHPS is illustrated in Algorithm 2. Once the objective, main criteria, and subcriteria are defined,

firstly, each main criterion is pairwise compared to others by constructing the  $M \times M$  of pairwise comparison matrix ( $\mathbf{A}$ ), where  $M$  is the number of main criteria. As mentioned earlier, by taking mf into account, the pairwise comparison matrix ( $\mathbf{A}$ ) can be given by

$$\mathbf{A} = \begin{bmatrix} 1 & \text{mf} \times a_{12} & a_{13} \\ \frac{1}{\text{mf}} & 1 & a_{23} \\ a_{31} & a_{32} & 1 \end{bmatrix}, \quad (12)$$

where  $a_{12}$  represents the weight of importance between ETX and ELT,  $a_{13}$  represents the weight of importance between ETX and ETT, and  $a_{23}$  represents the weight of importance between ELT and ETT. In general,  $a_{ji}$  is the comparison of importance between criteria where  $a_{ji}$  is equal to  $1/a_{ij}$ . The scale of importance comparison is in the range of 9 to  $1/9$ . For example, if  $a_{12}$  is 1, ETX is as important as ELT. By taking the multiplication factor (mf) into account, the importance of ETX is changed based on the effect of rank level.

Secondly, the fuzzy comparison matrix ( $\tilde{\mathbf{A}}$ ) is generated according to the pairwise comparison matrix ( $\mathbf{A}$ ) with respect to the fuzzy triangular number which is shown in Table 1.

$$\tilde{\mathbf{A}} = \begin{bmatrix} \tilde{a}_{11} & \cdots & \tilde{a}_{1n} \\ \vdots & \ddots & \vdots \\ \tilde{a}_{m1} & \cdots & \tilde{a}_{mm} \end{bmatrix}, \quad (13)$$

where  $n$  is three times the number of the main criteria which is based on the fuzzy rule.

Thirdly, the fuzzy comparison matrix ( $\tilde{\mathbf{A}}$ ) performs geometric means calculation ( $\tilde{r}_i$ ) which can be given as

$$\tilde{r}_i = \left( \prod_{j=1}^n \tilde{a}_{ij} \right)^{1/n}, \quad i = 1, 2, \dots, n. \quad (14)$$

Fourthly, the fuzzy weights are generated by performing the vector summation of each  $\tilde{r}_i$  and inverting each summation vector. Therefore, the maximum order ( $uw_i$ ), average order ( $mw_i$ ), and minimum order ( $lw_i$ ) are obtained. Then, the fuzzy weights ( $\tilde{w}_i$ ) can be obtained by

$$\tilde{w}_i = \tilde{r}_i \otimes (\tilde{r}_1 \oplus \tilde{r}_2 \oplus \cdots \oplus \tilde{r}_n)^{-1}, \quad (15)$$

where  $\oplus$  is a direct sum and  $\otimes$  is a dyadic product.

Then, the fuzzy weights are defuzzified by

$$dw_i = \frac{lw_i + mw_i + uw_i}{3}. \quad (16)$$

Finally, the main criteria weight ( $\mathbf{m}_c = [m_{c_1}, m_{c_2}, \dots, m_{c_M}]$ ) is generated by normalizing the defuzzified vector ( $\mathbf{dw}$ ) when the normalized defuzzified vector ( $\mathbf{dw}$ ) can be expressed as

$$m_{c_i} = \frac{dw_i}{\sum_{i=1}^M dw_i}. \quad (17)$$

After the main criteria weight is calculated, the subcriteria weights ( $s_c^C = [s_{c_1}^C, s_{c_2}^C, \dots, s_{c_m}^C]$ ) of each main

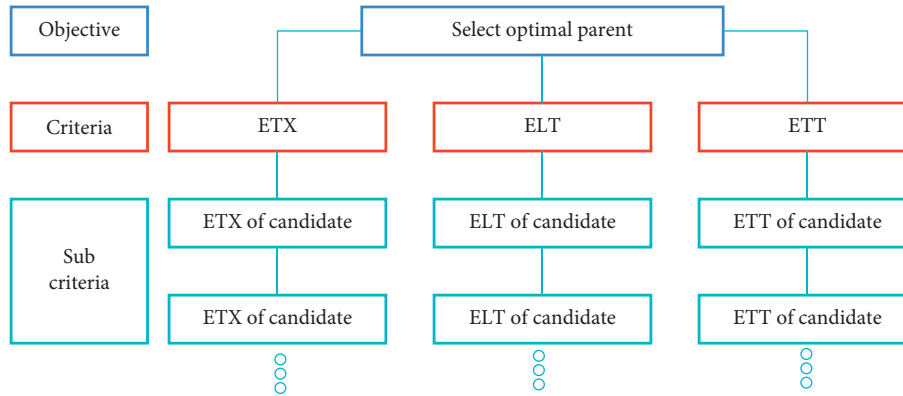


FIGURE 9: Structure of multicriteria ranking according to FAHP algorithm.

```

Input  $k$ ,  $ELT$ ,  $ETX$  and  $ETT$ 
Output Load-balanced weight  $\{\alpha_{EHPS}\}$ 
if All candidate parents die then
  Broadcast DIS message to perform local maintenance;
  Increase the rank number of the node;
end
Calculate the multiplication factor (mf) according to the rank;
Calculate weight of main criteria  $\{m_c\}$  according to mf;
Calculate weight of subcriteria  $\{s_c^C\}$ ;
for  $i \in k$ 
   $\alpha_{EHPS_i} \leftarrow 0$ ;
  for  $j \in N$ 
     $\alpha_{EHPS_i} \leftarrow \alpha_{EHPS_i} + (s_c^j \times m_{c_j})$ 
  end
end
Generate  $\alpha_{EHPS}$  by calculating  $s_c$  according to  $\mathbf{m}_c$ ;

```

ALGORITHM 2: Multicriteria load balancing algorithm.

TABLE 1: Interpretation of the significance of influence in triangular fuzzy scale [35].

Influence in a numeric scale	Definition	Triangular fuzzy scale
1	Equal significance	(1, 1, 1)
3	Moderate significance	(2, 3, 4)
5	Strong significance	(4, 5, 6)
7	Very strong significance	(6, 7, 8)
9	Extreme significance	(9, 9, 9)
2		(1, 2, 3)
4		(3, 4, 5)
6	Intermediate values between two adjacent judgments	(5, 6, 7)
8		(7, 8, 9)

criterion are calculated as the main criteria procedures. Therefore, the load-balanced weight ( $\alpha_{EHPS} = [\alpha_{EHPS_1}, \alpha_{EHPS_2}, \dots, \alpha_{EHPS_k}]$ ) is generated by computing  $s_c$  according to  $\mathbf{m}_c$ .

It should be mentioned that the load-balanced weight of EHPS ( $\alpha_{EHPS}$ ) can be expressed the quality of each parent. Then, we select the lowest quality parent and estimate its performance according to the cognitive radio environment. Then, the expected quality of the selected

parent on cognitive radio is  $ELT_{CR}$ ,  $ETX_{CR}$ , and  $ETT_{CR}$ . To compare the performance of multiparent solution and the single parent with cognitive radio, the expected quality of the multiparent solution— $ELT_{MP}$ ,  $ETX_{MP}$ , and  $ETT_{MP}$ —is calculated according to  $\alpha_{EHPS}$ . Therefore, the expected quality of the selected parent on cognitive radio and multiparent solution is considered as the input of hybrid parent selection algorithm and used as the subcriteria.

As shown in Algorithm 3, the main criteria weight from multicriteria load balancing algorithm is used as the main criteria weight of hybrid parent selection. Then, subcriteria weights ( $s_h^C = [s_{h_{MP}}^C, s_{h_{CR}}^C]$ ) are calculated, where  $s_{h_{MP}}^C$  is the subcriteria weight of multiparent solution and  $s_{h_{CR}}^C$  is the subcriteria weight of single parent with cognitive radio. Therefore, the performance weight ( $\mathbf{Per} = [\text{Per}_1, \text{Per}_2]$ ) is calculated, where  $\text{Per}_1$  is the expected performance of multiparent solution and  $\text{Per}_2$  is the expected performance of selected parent on cognitive radio. If the performance of the multiparent solution is higher than the single parent with cognitive radio, then the multiparent solution is activated and the child meter forwards the data to multiple parents according to  $\alpha_{\text{EHPS}}$ . Otherwise, the child meter transmits the DIS message to the selected parent to inform it about changing of communication channel to the cognitive radio. The output of Algorithm 3 presents the selected parent and the transmission technology as shown in Table 2.

## 5. Simulation Results

In this section, we simulate the performance of the empowered hybrid parent selection (EHPS) algorithm under 3-ary tree topology of AMI network. The performance of EHPS is evaluated as compared to 3 former parent selection methods: traditional RPL, multiparent selection based on expected lifetime (MELT) [26], and multiparent selection based on an analytic hierarchy process (MAHP) [32]. The three critical network performance metrics, packet delivery ratio (PDR), latency, and network lifetime, are determined. The PDR and latency are used to determine the transmission performance where PDR is the ratio of the packets transmitted by the child meter to the packets received by the parent meter. Latency is defined as the data transmission time. As stated in [14], the required PDR, data reliability, for transmitting the energy usage information is as high as 0.98.

**5.1. Simulation Setup.** To simulate the performance of parent selection, based on 3-ary tree topology, the quality of the middle parent is set to be the best where the distance of the middle parent to the child is set to be less than that of other parents. For example, as depicted in Figure 1, node 3 is considered as the middle parent. Therefore, the distance of node 3 to node 7 is less than the distance of node 2 and node 4 to node 7. To investigate the effect of path loss, the distance between the middle parent and the child ranges between 10 and 80 meters. The specification of transmitter and receiver is based on Zigbee module CC2500 [38]. All simulations are performed on MATLAB. Other parameters are shown in Table 3.

As described earlier, to generate the load-balanced weight ( $\alpha_{\text{EHPS}}$ ) of EHPS, firstly the pairwise comparison between performance metrics is performed. In this paper, we set the influence of each metric equally and adapt the influence of energy efficiency through the multiplication factor (mf). The mf is gathered by using (11), where  $b$  is estimated from the meter lifetime when the workload of multiparent is

perfectly balanced; i.e., all parents share data packets equally. Then,  $b$  is set to  $-0.5443$ . Therefore, the pairwise comparison matrix ( $\mathbf{A}$ ) is given as

$$\mathbf{A} = \begin{bmatrix} 1 & \text{mf} & 1 \\ \frac{1}{\text{mf}} & 1 & 1 \\ 1 & 1 & 1 \end{bmatrix}, \quad (18)$$

where

$$\text{mf} = e^{-0.5443(\text{Rank}_{\max} - \text{Rank}_{\text{current}})}. \quad (19)$$

**5.2. Performance Evaluation.** Firstly, we determine the network lifetime presented by each parent selection algorithm as a function of the rank number and the distance between child meter and parents. As depicted in Table 4, for a single parent based on RPL algorithm, the number of rank affects the decrease in network lifetime noticeably since the number of forwarded packets by the parent node is corresponding to the rank number. The lower the rank advertised by a node is, the higher the number of data packets from the children and grandchildren meters is determined. On the other hand, the transmission range also affects the network lifetime. If the distance between a meter and parent meter increases, the times of required data retransmission increase due to the packet loss. Therefore, for RPL algorithm, the network lifetime decreases when the distance is higher than 50 m. When the distance is greater than 65 m, the meter wastes the energy for retransmission, so the network lifetime is noticeably low.

As depicted in Tables 5 and 6, the network lifetimes of MELT and MAHP are determined, respectively. Although the multiparent solutions have the merits of efficient workload balancing and high PDR, they also have the demerit of high energy consumption since the information needs to be split and forwarded to a number of parents. On the contrary, as shown in Table 7, EHPS algorithm considers the quality of parents comprehensively through a fuzzy AHP (FAHP) algorithm and through activating the cognitive radio technology on the single parent scheme; therefore, it overcomes the tradeoff between high energy consumption and high transmission performance of multiparent solution effectively. Therefore, the EHPS can maximize the network lifetime under long transmission range environment.

Consequently, RPL algorithm presents the highest network lifetime when the distance is lower than 50 m. It should be noted that retransmission is not performed at those distances since the PDR is as high as 1. When the distance increases, the data retransmission is required; therefore, the network lifetime for RPL is noticeably low. Although, the multiparent solutions—MELT and MAHP—present better workload balancing performance by activating all candidate parents when the data transmission is performed, they present a lower network lifetime than the RPL algorithm since they consume more energy in transmitting a number

```

Input  $ELT_{CR}$ ,  $ETX_{CR}$ ,  $ETT_{CR}$ ,  $ELT_{MP}$ ,  $ETX_{MP}$  and  $ETT_{MP}$ 
Output Parent ( $IP_i$ ) and transmission channel ( $CH_i$ )
  Calculate weight of subcriteria  $\{s_h^C\}$ ;
  for  $i \in \text{Channel}$ 
     $Per_i \leftarrow 0$ ;
    for  $j \in N$ 
       $Per_i \leftarrow Per_i + (s_{h_i}^j \times m_{e_j})$ 
    end
  end
  if  $Per_1 > Per_2$  then
    return  $IP_i \leftarrow 1$ ;  $CH_i \leftarrow 1$ ; //
  else
    return  $IP_i \leftarrow 2$ ;  $CH_i \leftarrow 2$ ; //
  end

```

ALGORITHM 3: Hybrid parent selection algorithm.

TABLE 2: Interpretation of the outputs of Algorithm 3.

Subscripted number (i)	1	2
$CH_i$	Zigbee	CR
$IP_i$	All candidate parents	Selected single parent

TABLE 3: Simulated parameters [38].

Parameters	Value
Tx power	76.3 mW
CR Tx power	100 mW
Rx power	47.9 mW
Idle power	900 nW
Sleep power	400 nW
Spectrum sensing power	65.83 mW
DIO interval before data transmitting	90 seconds
Household data transmitting interval	15 min
Manufacturer data transmitting interval	60 min
Household data packet	318 bytes
Manufacturer data packet	1200 bytes
DIO message size	64 bytes
DAO message size	46 bytes
DIS message size	2 bytes
Transmission time of data packet	192 $\mu$ s
Transition time from sleep to active mode	970 $\mu$ s
Simulation time	3600 min
Load balancing step of MELT	1/3

of small packets to multiple parents. On the other hand, EHPS presents a network lifetime close to that of the RPL algorithm when the distance is lower than 50 m by hybridizing the multiparent solution and the single parent with cognitive radio technology. Moreover, with the merit of cognitive radio, EHPS presents the highest network lifetime when the transmission range is greater than 50 m.

Secondly, we evaluate the PDR and latency of EHPS as compared to RPL, MELT, and MAHP as a function of distance at rank 9 during household data transmission. As shown in Figure 10, the comparison of PDR is determined. As a result, all algorithms present PDR as high as 1 when the

distance between meter and parent meters is lower than 50 m. When the distance increases, the PDR of the RPL algorithm is the worst since its performance suffers from packet loss according to the package size and distance. On the other hand, MELT, MAHP, and EHPS present higher PDR since the data is split into small packets based on the multiparent solution. Moreover, by our proposed cognitive radio hybridizing scheme, EHPS presents the highest PDR among others since it utilizes better transmission channel opportunistically. The single parent based on cognitive radio is activated by the performance comparison to multiparent solution through the proposed hybrid parent selection algorithm.

As shown in Figure 11, the latency values of RPL, MELT, MAHP, and EHPS are compared. The simulation results show that EHPS presents the lowest latency as compared to others. By utilizing the cognitive radio continually, EHPS can present efficient data transmission performance, high PDR and low latency, while maximizing the network lifetime since the quality of parents is determined comprehensively. Moreover, by adapting the influence of energy-efficient criteria on the rank number, the workload can be balanced effectively.

Thirdly, we evaluate the PDR and latency of EHPS as compared to RPL, MELT, and MAHP as a function of distance at rank 9 during manufacturer data transmission. It should be mentioned that the interval of the energy usage of manufacturer data transmission is 60 min, and the data package size is 1200 bytes which is much higher than the size of household energy usage. As mentioned earlier, the data package size affects the PDR, latency, and required retransmission. As shown in Figure 12, the PDR of the RPL algorithm decreases when the distance is 45 m. Its PDR noticeably decreases when the distance increases and reaches 0 at 80 m. Although MELT and MAHP present much better PDRs than the RPL, their PDRs are also noticeably low on increasing distance due to the limited communication channel. In addition, the PDRs of MELT and MAHP are 0 at 80 m, the same as RPL algorithm.

As a result, EHPS overcomes the limited performance of Zigbee communication channel by hybridizing the multiparent solution and the single parent with cognitive radio

TABLE 4: Network lifetime of RPL.

Distance (m)	Rank							
	2	3	4	5	6	7	8	9
10	8245	4620	2915	1990	1425	1100	860	695
15	8245	4620	2915	1990	1425	1100	860	695
20	8245	4620	2915	1990	1425	1100	860	695
25	8245	4620	2915	1990	1425	1100	860	695
30	8245	4620	2915	1990	1425	1100	860	695
35	8245	4620	2915	1990	1425	1100	860	695
40	8245	4620	2915	1990	1425	1100	860	695
45	8240	4620	2915	1990	1425	1100	860	695
50	8225	4605	2905	1985	1425	1095	860	695
55	8120	4540	2865	1960	1425	1080	845	680
60	7655	4230	2650	1805	1320	995	785	630
65	6170	3305	2040	1385	995	750	590	475
70	2525	1265	725	480	310	245	185	140
75	125	65	65	65	65	65	65	65
80	65	65	65	65	50	40	30	25

TABLE 5: Network lifetime of MELT.

Distance (m)	Rank							
	2	3	4	5	6	7	8	9
10	6930	3725	2230	1485	1060	795	630	515
15	6930	3725	2230	1485	1060	795	630	515
20	6930	3725	2230	1485	1060	795	630	515
25	6930	3725	2230	1485	1060	795	630	515
30	6930	3545	2100	1385	975	725	570	450
35	6930	3545	2100	1385	975	725	570	450
40	6930	3545	2100	1385	975	725	570	450
45	6930	3545	2100	1385	975	725	570	450
50	6920	3535	2095	1385	975	725	565	450
55	6845	3485	2065	1365	965	720	555	440
60	6545	3305	1955	1285	905	665	530	420
65	5405	2645	1555	1005	705	535	400	305
70	1545	905	545	305	215	185	125	95
75	65	65	65	65	65	65	65	65
80	65	65	65	65	55	40	30	25

TABLE 6: Network lifetime of MAHP.

Distance (m)	Rank							
	2	3	4	5	6	7	8	9
10	7760	4240	2610	1750	1255	935	725	580
15	7760	4240	2610	1750	1255	935	725	580
20	7760	4240	2610	1750	1255	935	725	580
25	7760	4240	2610	1750	1255	935	725	580
30	7770	4250	2610	1750	1255	935	725	580
35	7770	4250	2610	1750	1255	935	725	580
40	7770	4250	2610	1750	1255	935	725	580
45	7770	4250	2610	1745	1255	935	725	580
50	7745	4240	2610	1720	1255	935	725	580
55	7645	4175	2575	1720	1230	915	720	570
60	7120	3890	2395	1605	1145	845	665	535
65	5400	2945	1805	1205	860	650	490	400
70	1565	905	605	420	305	235	185	125
75	65	65	65	65	65	65	65	65
80	65	65	65	65	65	60	45	35



TABLE 7: Network lifetime of EHPS.

Distance (m)	Rank							
	2	3	4	5	6	7	8	9
10	7845	4385	2640	1785	1350	1015	835	665
15	7845	4385	2640	1785	1350	1015	835	665
20	7845	4385	2640	1785	1350	1015	835	665
25	7845	4385	2640	1785	1350	1015	835	665
30	7810	4265	2660	1855	1385	1025	820	665
35	7810	4265	2660	1855	1385	1025	820	665
40	7810	4265	2660	1855	1385	1025	820	665
45	7810	4265	2660	1855	1385	1025	820	665
50	7805	4255	2660	1855	1385	1025	830	675
55	7685	4205	2620	1830	1375	1025	830	670
60	7165	3960	2470	1685	1335	1000	780	665
65	5455	3355	2105	1440	1190	905	750	665
70	2705	1385	785	545	545	365	305	305
75	65	65	65	65	65	65	65	65
80	65	65	65	65	65	65	65	65

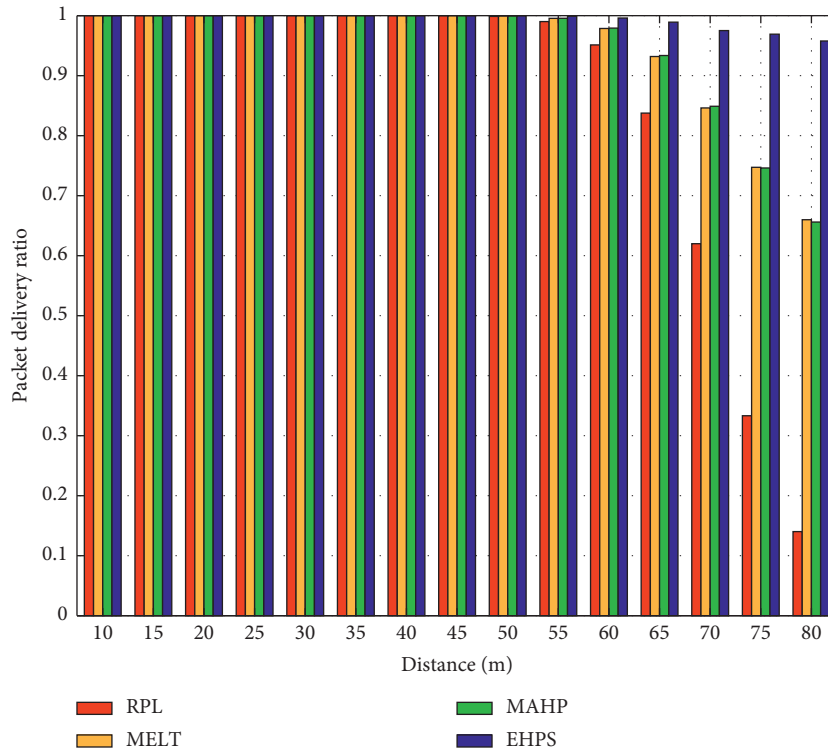


FIGURE 10: Comparison of PDR as a function of distance of household energy usage.

technology. When the distance is lower than 55 m, the multiparent scheme is frequently activated since it consumes less energy than the single parent with cognitive radio. When the distance increases, the expected overall performance of multiparent solution determined by FAHP is lower than that using the cognitive radio. Therefore, the single parent with cognitive radio is more activated. Then, the high PDR can be maintained as much higher than others. As shown in Figure 13, EHPS presents the lowest latency as compared to others for all transmission distance while other techniques can perform data transmission when the distance is lower

than 75 m. At 80 m, RPL, MELT, and MAHP cannot forward the data to the parent meter since the PDR is 0, so their latency values are noticeably high.

From the simulation results, the empowered hybrid parent selection (EHPS) algorithm is flexible to be used under various sizes of data packages and distances. By hybridizing usage of multiparent solution and the single parent with cognitive radio, EHPS maximizes the network lifetime under long data transmission range and presents the highest PDR and lowest latency among others. In our proposed algorithm, we follow the information exchange

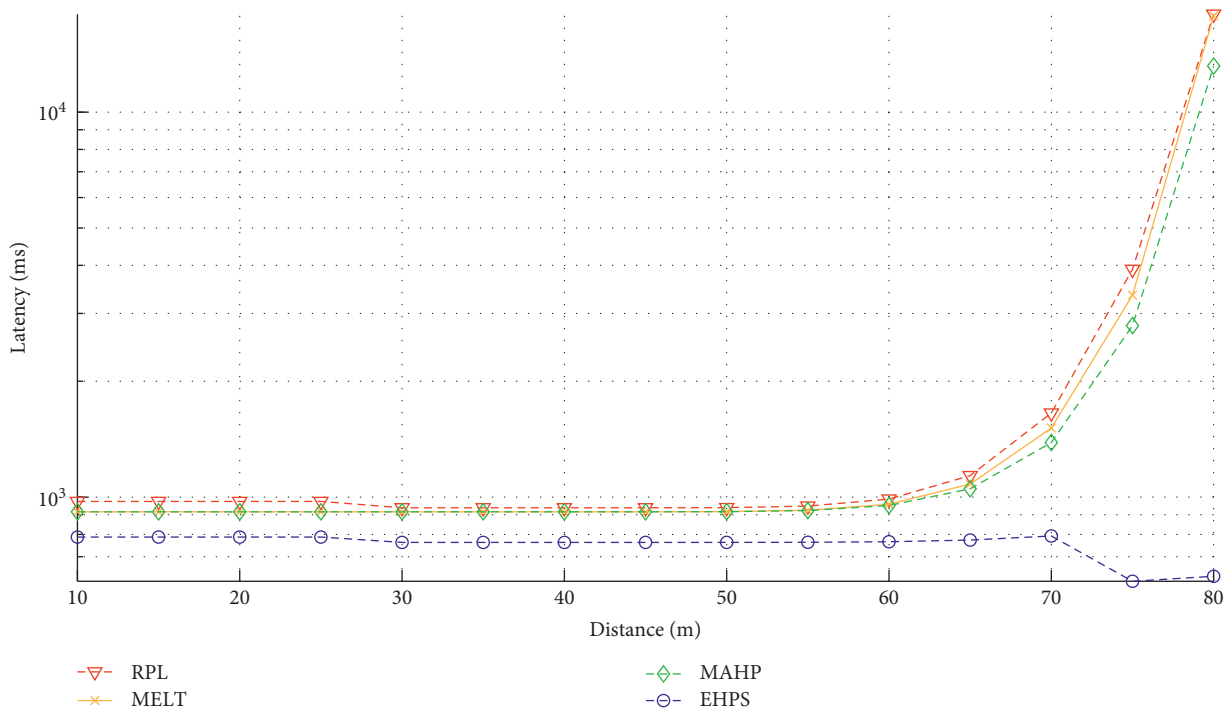


FIGURE 11: Comparison of latency as a function of distance of household energy usage.

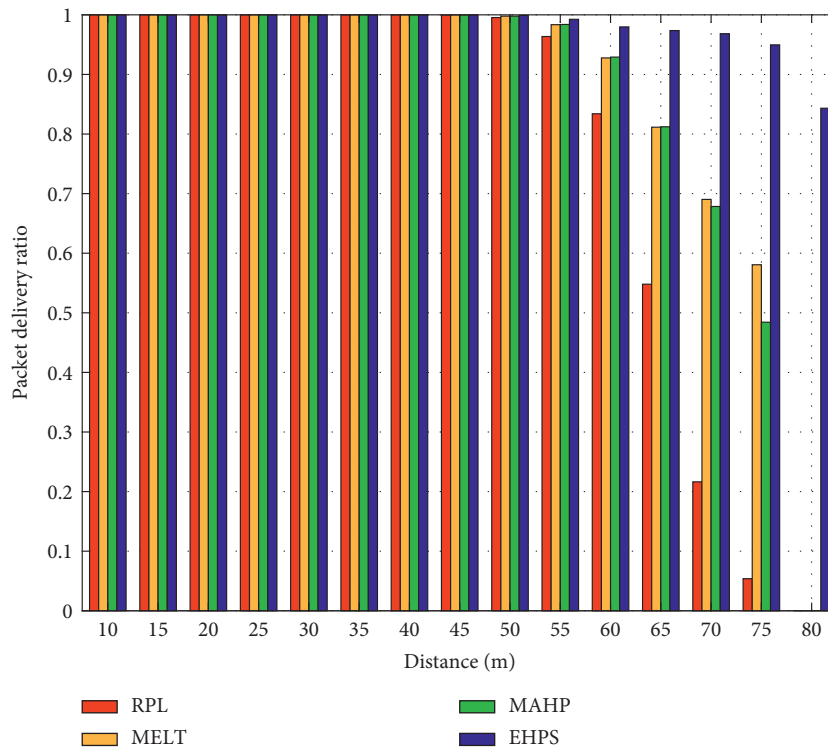


FIGURE 12: Comparison of PDR as a function of distance of manufacturing energy usage.

according to the RPL mechanism where the message—DIO, DAO, and DIS—for route construction and maintenance is exchanged between nodes periodically. Therefore, the extra overhead is not required. On the other hand, the complexity of EHPS is bound at  $O(n^3)$  where  $n$  is number of candidate

parents. Moreover, the EHPS does not suffer from a high complexity of FAHP since the numbers of main criteria and alternatives are low. Moreover, by determining the parents' quality comprehensively through an adaptive FAHP scheme, the workload can be balanced; then, it is facilitated for the

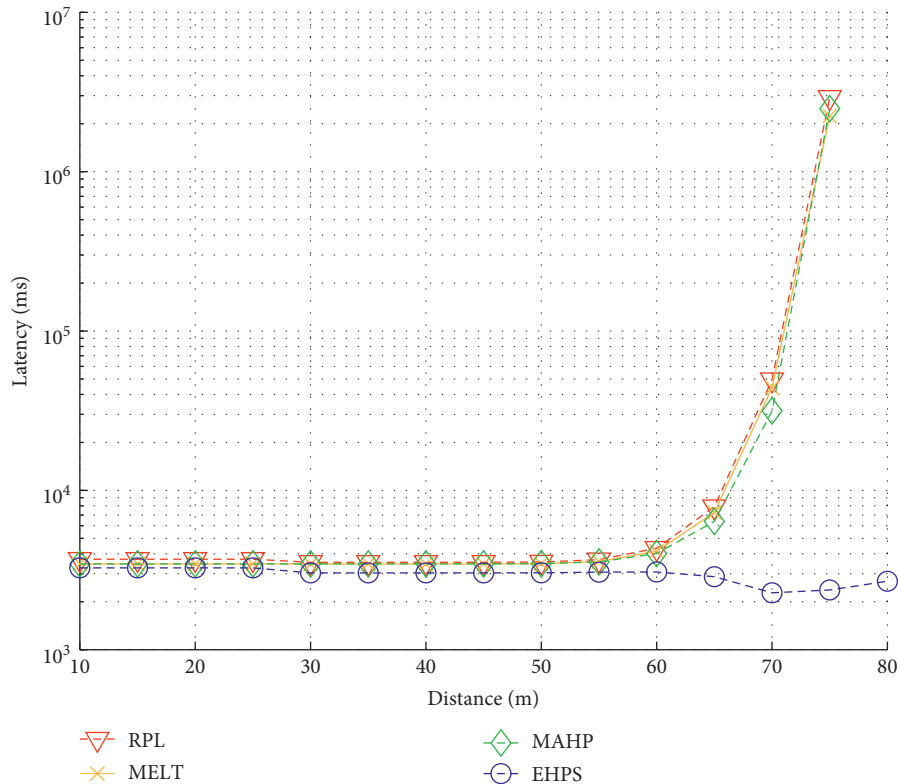


FIGURE 13: Comparison of latency as a function of distance of manufacturing energy usage.

electrical production planning and electricity billing application.

## 6. Conclusion

In this paper, an “empowered hybrid parent selection (EHPS)” is proposed to overcome the issues of the parent selections of RPL for AMI network. In general, single parent and multiparent solutions suffer from the tradeoff between the network lifetime and transmission performance. Even if the single parent selection presents higher network lifetime than multiparent solutions, it gives worse transmission performance under long transmission range and large data size. On the other hand, multiparent solutions meet high transmission performance but give low network lifetime due to the energy consumption based on multipath strategy. By hybridizing the merits of multiple parents and single parent with cognitive radio technology, EHPS maximizes the network lifetime over long transmission range and large data size. Through the proposed hybrid scheme with adaptive fuzzy analytic hierarchy process (FAHP), EHPS balances the meter workload effectively and is flexible with respect to the transmission range and data size.

## Data Availability

No data were used to support this study.

## Conflicts of Interest

The authors declare that they have no conflicts of interest.

## References

- [1] V. C. Gungor, D. Sahin, T. Kocak et al., “Smart grid technologies: communication technologies and standards,” *IEEE Transactions on Industrial Informatics*, vol. 7, no. 4, pp. 529–539, 2011.
- [2] V. C. Gungor, D. Sahin, T. Kocak et al., “A survey on smart grid potential applications and communication requirements,” *IEEE Transactions on Industrial Informatics*, vol. 9, no. 1, pp. 28–42, 2013.
- [3] U. Ozgur, S. Tonyali, K. Akkaya, and F. Senel, “Comparative evaluation of smart grid AMI networks: performance under privacy,” in *Proceedings of the 2016 IEEE Symposium on Computers and Communication (ISCC)*, pp. 1–3, Messina, Italy, June 2016.
- [4] S. Nimbargi, S. Mhaisne, S. Nangare, and M. Sinha, “Review on AMI technology for smart meter,” in *Proceedings of the IEEE International Conference on Advances in Electronics, Communication and Computer Technology (ICAECCT)*, pp. 21–27, Pune, India, December 2016.
- [5] Z. Fan, P. Kulkarni, S. Gormus et al., “Smart grid communications: overview of research challenges, solutions, and standardization activities,” *IEEE Communications Surveys & Tutorials*, vol. 15, no. 1, pp. 21–38, 2013.
- [6] T. Winter, *RPL: IPv6 Routing Protocol for Low-Power and Lossy Networks*, IETF, Fremont, CA, USA, 2012.
- [7] E. Ancilolotti, R. Bruno, and M. Conti, *RPL Routing Protocol in Advanced Metering Infrastructure: An Analysis of the Unreliability Problems*, IFIP, Laxenburg, Austria, 2012.
- [8] I. F. Akyildiz, W. Su, Y. Sankarasubramaniam, and E. Cayirci, “Wireless sensor networks: a survey,” *Computer Networks*, vol. 38, no. 4, pp. 393–422, 2002.

- [9] D. Wang, Z. Tao, J. Zhang, and A. Abouzeid, "RPL based routing for advanced metering infrastructure in smart grid," in *Proceedings of the 2010 IEEE International Conference on Communications Workshops (ICC)*, pp. 1–6, Cape Town, South Africa, May 2010.
- [10] X. Yang, "The application of RPL routing protocol in low power wireless sensor and lossy networks," *Sensors & Transducers*, vol. 170, no. 5, pp. 107–111, 2014.
- [11] A. Kheaksong, K. Srisomboon, and W. Lee, "A comparative study of various routing protocols for smart grid communication," *ECTI E-Magazine*, vol. 10, no. 1, 2016.
- [12] A. R. Parnian, M. R. Kharazmi, and R. Javidan, "RPL routing protocol in smart grid communication," *ARN Journal of Systems and Software*, vol. 4, no. 5, pp. 128–132, 2014.
- [13] J. Tripathi, *Performance Evaluation of the Routing Protocol for Low-Power and Lossy Networks (RPL)*, Cisco Systems, San Jose, CA, USA, 2012.
- [14] M. Kuzlu, M. Pipattanasomporn, and S. Rahman, "Communication network requirements for major smart grid applications in HAN, NAN and WAN," *Computer Networks*, vol. 67, pp. 74–88, 2014.
- [15] W. Zhang, G. Han, Y. Feng, and J. Lloret, "IRPL: an energy efficient routing protocol for wireless sensor networks," *Journal of Systems Architecture*, vol. 75, pp. 35–49, 2017.
- [16] P. Thubert, *Objective Function Zero for RPL*, Cisco Systems, San Jose, CA, USA, 2012.
- [17] S. A. Abdel Hakeem, A. A. Hady, and H.W. Kim, "RPL routing protocol performance in smart grid applications based wireless sensors: experimental and simulated analysis," *Electronics*, vol. 8, no. 2, 2019.
- [18] O. Gnawali and P. Levis, *RFC 6719-the Minimum Rank with Hysteresis Objective Function*, Internet Engineering Task Force (IETF), Fremont, CA, USA, 2012.
- [19] A.-L. Kampen, K. Øvsthus, and Ø. Kure, "Energy balancing algorithms in wireless sensor networks," in *Proceedings of the 2015 Federated Conference on Computer Science and Information Systems (FedCSIS)*, vol. 5, pp. 1223–1231, Lodz, Poland, September 2015.
- [20] P. Kamgueu, E. Nataf, T. D. Ndie, and O. Faster, *Energy-Based Routing Metric for RPL*, INRIA, Domaine de Voluceau, France, 2013.
- [21] L.-H. Chang, T.-H. Lee, S.-J. Chen, and C.-Y. Liao, "Energy-efficient oriented routing algorithm in wireless sensor networks," in *Proceedings of the 2013 IEEE International Conference on Systems, Man, and Cybernetics*, pp. 3813–3818, Manchester, UK, October 2013.
- [22] P. M. Esposito, M. E. M. Campista, I. M. Moraes, L. H. M. K. Costa, O. C. M. B. Duarte, and M. G. Rubinstein, "Implementing the expected transmission time metric for OLSR wireless mesh networks," in *Proceedings of the 2008 1st IFIP Wireless Days*, Dubai, United Arab Emirates, November 2008.
- [23] O. Iova, F. Theoleyre, and T. Noel, "Improving the network lifetime with energy-balancing routing: application to RPL," in *Proceedings of the 2014 7th IFIP Wireless and Mobile Networking Conference (WMNC)*, pp. 1–8, Vilamoura, Portugal, May 2014.
- [24] P. Thulasiraman, "RPL routing for multigateway AMI networks under interference constraints," in *Proceedings of the 2013 IEEE International Conference on Communications (ICC)*, Budapest, Hungary, June 2013.
- [25] M. Ali Lodhi, A. Rehman, M. M. Khan, and F. B. Hussain, "Multiple path RPL for low power lossy networks," in *Proceedings of the 2015 IEEE Asia Pacific Conference on Wireless and Mobile (APWiMob)*, Bandung, Indonesia, August 2015.
- [26] O. Iova, F. Theoleyre, and T. Noel, "Using multiparent routing in RPL to increase the stability and the lifetime of the network," *Ad Hoc Networks*, vol. 29, 2015.
- [27] A. H. Process, "The analytic hierarchy process," *Computing*, vol. 18, no. 2, 1980.
- [28] K. Teknomo, "Analytic hierarchy process (AHP) tutorial," 2006, <http://people.revoledu.com/kardi/tutorial/AHP/AHP.htm>.
- [29] Y. Min, L. T. Yang, F. Wang, and W. Wang, "Dynamic sleeping algorithm based on AHP for wireless sensor networks," in *Proceedings of the 2008 Second International Conference on Future Generation Communication and Networking*, pp. 387–392, Hainan, China, December 2008.
- [30] G. Di Bona and A. Forcina, "Analytic critical flow method (ACFM): a reliability allocation method based on analytic hierarchy process," *Journal of Failure Analysis and Prevention Volume*, vol. 17, no. 1, pp. 1–15, 2017.
- [31] G. Di Bona, D. Falcone, A. Forcina, A. Silvestri, and L. Silvestri, "A new model for maintenance strategy based on failure analysis and multicriteria approach," *International Journal of Information Systems in the Service Sector (IJISSS)*, vol. 12, no. 4, pp. 60–90, 2020.
- [32] W. Alayed, L. Mackenzie, and D. Pezaros, "Analytical hierarchy process multi-metric objective function for RPL," in *Proceedings of the IEEE 17th International Symposium on Network Computing and Applications (NCA)*, Cambridge, MA, USA, November 2018.
- [33] G. Kabir and M. Ahsan Akhtar Hasin, "Comparative analysis of AHP and Fuzzy AHP models for multicriteria inventory classification," *International Journal of Fuzzy Logic Systems (IJFLS)*, vol. 1, 2011.
- [34] S. Paul, A. Chakraborty, and J. S. Banerjee, "A fuzzy AHP-based relay node selection protocol for wireless body area networks (WBAN)," in *Proceedings of the 2017 4th International Conference on Opto-Electronics and Applied Optics (Optronix)*, Kolkata, India, November 2017.
- [35] M. Imran Tariq, "Prioritization of information security controls through fuzzy AHP for cloud computing networks and wireless sensor networks," *Sensors*, vol. 20, no. 5, pp. 1–39, 2020.
- [36] Y.-C. Liang, K.-C. Chen, G. Y. Li, and P. Mähönen, "Cognitive radio networking and communications: an overview," *IEEE Transactions on Vehicular Technology*, vol. 60, no. 7, 2011.
- [37] Z. Qin, "20 years of evolution from cognitive to intelligent communications," *IEEE Transactions on Cognitive Communication and Networking*, vol. 6, no. 1, 2020.
- [38] CC2500, "Errata Notes (Rev. E)," 2013, <https://www.ti.com/lit/er/swrz002e/swrz002e.pdf>.

## Research Article

# Reliability Estimation under Scarcity of Data: A Comparison of Three Approaches

Leonardo Leoni <sup>1</sup>, Alessandra Cantini,<sup>1</sup> Farshad BahooToroody,<sup>2</sup> Saeed Khalaj,<sup>2</sup> Filippo De Carlo <sup>1</sup>, Mohammad Mahdi Abaei,<sup>3</sup> and Ahmad BahooToroody<sup>4</sup>

<sup>1</sup>Department of Industrial Engineering (DIEF), University of Florence, Florence 50123, Italy

<sup>2</sup>Department of Civil Engineering, University of Parsian, Qazvin 3176795591, Iran

<sup>3</sup>Department of Maritime and Transport Technology, Delft University of Technology, Delft 2628 CD, Netherlands

<sup>4</sup>Marine and Arctic Technology Group, Department of Mechanical Engineering, Aalto University, Espoo 11000, Finland

Correspondence should be addressed to Filippo De Carlo; [filippo.decarlo@unifi.it](mailto:filippo.decarlo@unifi.it)

Received 13 January 2021; Revised 27 February 2021; Accepted 11 March 2021; Published 20 March 2021

Academic Editor: Vahid Kayvanfar

Copyright © 2021 Leonardo Leoni et al. This is an open access article distributed under the Creative Commons Attribution License, which permits unrestricted use, distribution, and reproduction in any medium, provided the original work is properly cited.

During the last decades, the optimization of the maintenance plan in process plants has lured the attention of many researchers due to its vital role in assuring the safety of operations. Within the process of scheduling maintenance activities, one of the most significant challenges is estimating the reliability of the involved systems, especially in case of data scarcity. Overestimating the average time between two consecutive failures of an individual component could compromise safety, while an underestimate leads to an increase of operational costs. Thus, a reliable tool able to determine the parameters of failure modelling with high accuracy when few data are available would be welcome. For this purpose, this paper aims at comparing the implementation of three practical estimation frameworks in case of sparse data to point out the most efficient approach. Hierarchical Bayesian modelling (HBM), maximum likelihood estimation (MLE), and least square estimation (LSE) are applied on data generated by a simulated stochastic process of a natural gas regulating and metering station (NGRMS), which was adopted as a case of study. The results identify the Bayesian methodology as the most accurate for predicting the failure rate of the considered devices, especially for the equipment characterized by less data available. The outcomes of this research will assist maintenance engineers and asset managers in choosing the optimal approach to conduct reliability analysis either when sufficient data or limited data are observed.

## 1. Introduction

Several hazardous substances are handled inside process plants; therefore, unforeseen events could produce fires, explosions, and chemical releases that could generate enormous financial loss and injuries or deaths of nearby employees and civilians [1]. Among the potential causes, asset failure is often regarded as the primary source of the aforementioned dangerous phenomena [2]; hence, the equipment involved in process industries should be adequately maintained to guarantee appropriate standards of safety and reliability, while generating a profit from the operations.

Over the past decades, safety and reliability requirements have progressively increased [3], leading to significant deployment of resources in maintenance activities [4]. This fundamental vision has resulted in the development of many maintenance policies such as reliability-centered maintenance (RCM) [5–11], risk-based maintenance (RBM) [12–16], and condition-based maintenance (CBM) [8–11]. Within the development of a CBM plan, failure prognosis is of prominent importance; thus, there is an ongoing effort on condition monitoring and calculation of the remaining useful life [17–19]. Zeng and Zio [18] developed a dynamic risk assessment framework based on a Bayesian model to

update the reliability of safety barriers as soon as new data are collected. After updating the reliabilities, the risk indexes are determined through an event-tree (ET). Another relevant work by Chen et al. [19] proposes an integration between neuro-fuzzy systems (NFSs) and Bayesian algorithm to predict the evolution of the operating condition of a given system. The approach is tested on two case studies, and the results reveal a greater accuracy than other conventional predictors (e.g., recurrent neural networks, NFSs, and recurrent NFSs).

To implement a proper maintenance plan based on preventive actions, a crucial task is represented by the estimation of the probabilities of failure. During this phase, the accuracy of the prediction is essential since overestimating the failure rates could lead to greater resource consumption. By contrast, an underestimation may delay the maintenance actions, resulting in a riskier state of the operations. Consequently, a great deal of research studies has been made to provide accurate estimation procedures adopting different tools such as fault tree analysis (FTA) [20], probability graph paper [21], support vector machines [22], FORM (first-order reliability method) [23], SORM (second-order reliability method) [24], and Bayesian network (BN) [25]. To prove the advantages and limitations of the estimation methodologies, many researchers have also focused their efforts on comparing the results arising from the application of distinct approaches [26–28]. Musleh and Helu [27] applied Bayesian inference, MLE, and LSE to censored data samples. The results of this study pointed out the Bayesian estimator as the best in terms of bias, mean squared error, and Pitman nearness probability. A more recent work by BahooToroodi et al. [28] presented the comparison between the MLE and the HBM in case of perfect repair and minimal repair. The authors tested the two approaches on an NGRMS, proving that the Bayesian inference provides more precision in failure modelling than the MLE. The proposed frameworks operate under condition of availability of sufficient data, while the challenges arising from sparse and limited data have not been addressed.

Within probability and reliability applications, data scarcity is regarded as one of the main issues. Indeed, lack of available data increases the uncertainties related to the estimation process [29], causing sometimes the inability to find the probability distributions [30]. Sparse data could be generated from many sources, such as the rarity of an event, limited knowledge, missing data, and inappropriate data collection. Moreover, the implementation of maintenance strategies also contributes reducing available data since maintenance actions are performed to prevent failures from happening [31]. Quite recently, a BN-based quantitative risk assessment methodology was developed by Yang et al. [32]. In this work, a BN along with precursors are adopted to cope with data scarcity, while the consequences are evaluated through loss functions. The classic Bayesian approaches can partially compensate for limited data by incorporating prior knowledge and expert judgments. However, under the primary assumption of the work, they neglected the effect of source-to-source variability of failure data in the process

model [33]. To overcome this limitation and simultaneously deal with sparse data, HBM, along with precursor data, has been extensively exploited by many academics [34–38]. Li et al. [39] integrated the BN and the HBM for a dynamic risk assessment of a submerged pipeline. In their study, the classical BN is used to model the conditional dependencies among primary events, while the hierarchical approach is developed for predicting the probabilities associated with basic events and the safety barriers. The proposed methodology can be updated as soon as new information becomes available, by including them into the prior distribution characterizing the HBM.

During the last years, the adoption of HBM has spread to a broader audience thanks to the advances in open-source Markov chain Monte Carlo (MCMC) sampling software such as OpenBugs [40]. Examples of applications include RBM planning [41, 42], condition monitoring [43, 44], and probabilistic risk assessment [45, 46]. Recently, Abaei et al. [47] presented an HBM-based methodology able to predict the probability of failure of a tidal energy converter assuming a homogeneous Poisson process (HPP) for the failure modelling.

Despite all the ongoing efforts, there is still a need for a sound tool able to deal with the uncertainties arising from the lack of data in maintenance applications. Indeed, while the literature provides many comparison studies among distinct statistical methodologies when sufficient data are observed, less interest has been devoted to the comparison of estimation tools under the assumption of limited data available. To this end, the main objective of this paper is to provide a comparison between the Bayesian inference and two classic estimation approaches (i.e., MLE and LSE) in the event of data scarcity arising from frequent preventive maintenance actions. The methods are evaluated based on their accuracy in the estimation process for the failure rate of the components belonging to an NGRMS, which is chosen as a case study.

*1.1. Hierarchical Bayesian Modelling.* The first step required to conduct a statistical inference is collecting “Data,” which are defined as the observed values of a given process. Next, “Information” is obtained by manipulating, evaluating, and organizing “Data.” The process of gathering “Information” leads to acquire “Knowledge,” which is subsequently exploited to perform “Inference” [48]. As stated by El-Gheriani et al. [29], the HBM allows to carry out the inference tasks through Bayes’ theorem, shown by

$$\pi_1(\theta|x) = \frac{f(x|\theta)\pi_0(\theta)}{\int_{\theta} f(x|\theta)\pi_0(\theta)d\theta} \quad (1)$$

Bayes’ theorem relies on the proportionality between the posterior distribution, denoted by  $\pi_1(\theta|x)$ , and the product of the likelihood function and the prior distribution, respectively, identified by  $f(x|\theta)$  and  $\pi_0(\theta)$ . The prior distribution is usually named informative when it conceals relevant information about the unknown parameter of interest ( $\theta$ ), while it is regarded as noninformative when little



or no information about  $\theta$  is considered [49]. It is worth mentioning that the HBM owes its name to the adoption of a multistage or hierarchical prior distributions [50], given by [51]

$$\pi_0(\theta) = \int_{\varnothing} \pi_1(\theta|\varphi)\pi_2(\varphi)d\varphi, \quad (2)$$

where  $\varphi$  is a vector whose components are called hyperparameters, while  $\pi_2(\varphi)$  is the hyperprior distributions, representing the uncertainty of  $\varphi$ . Finally,  $\pi_1(\theta|\varphi)$  is referred as first-stage prior distribution, which considers the variability of  $\theta$  given a certain value of  $\varphi$ .

**1.2. Maximum Likelihood Estimation.** Given a random sample  $y = (y_1, y_2, \dots, y_n)$  arising from a stochastic process, the objective of MLE is to determine the probability distribution from which the sample is most likely to have been generated. For this purpose, it is required to specify a proper distribution for the sample data and its characterizing parameters. Assuming that  $\theta = (\theta_1, \theta_2, \dots, \theta_n)$  is a vector that lies within the parameter space, the most probable parameters that define the probability distribution of the observed data are obtained by maximising the likelihood function, illustrated by [28]

$$f(\theta_1, \theta_2, \dots, \theta_n|y) = f_1(\theta_1|y)f_2(\theta_2|y), \dots, f_n(\theta_n|y). \quad (3)$$

**1.3. Least Square Estimation.** As stated by Myung [52], the LSE method is exploited primarily for descriptive purposes. Its main goal is to define the parameters that generate the most accurate description of the observed data. Let  $y = (y_1, y_2, \dots, y_n)$  be a sample of  $n$  observations and  $\theta = (\theta_1, \theta_2, \dots, \theta_m)$  a vector of parameters. After choosing a proper distribution for the model, the parameters that best fit the data are found by minimizing the sum of squares error (SSE), shown by

$$\text{SSE}(\theta) = \sum_{i=1}^n (y_i - \text{prd}_i(\theta))^2, \quad (4)$$

where  $y_i$  is the  $i$ th observation, while  $\text{prd}_i(\theta)$  is the prediction of the model associated to the  $i$ th observation.

The remainder of the paper is organized as follows: Section 2 describes the steps of the proposed study. Section 3 illustrates the implementation of the methodologies to the NGRMS, while Section 4 provides the discussion of the results. At last, in Section 5, conclusions are presented.

## 2. Methodology

Within the reliability analysis process, the exploitation of different estimation tools could lead to distinct results, which may affect the adopted maintenance strategy. To this end, the main goal of this paper is to investigate the application of three estimation methodologies in case of few data available, focusing mainly on the comparison between the Bayesian approach and the classic approaches (i.e., MLE

and LSE). A brief overview of the framework is represented in Figure 1.

The first step (1) of the methodology is to collect failure data generated by the considered process. Since the majority of industrial equipment undergoes substantial preventive maintenance, both Times To Failure (TTFs) and Censored Times To Failure (CTTFs) are taken into account for the study (1.1); moreover, the number of failures observed during a specified time span is also considered (1.2). CTTFs arise when preventive maintenance is performed or a given component survives longer than the exposure time.

During the second phase (2), the failure model is specified. In the present work, the HPP is adopted for modelling the failure behaviour of the considered devices. The HPP describes a scenario where the interarrival times between failures are independent and identically distributed according to an exponential distribution. Due to the frequent preventive measures that completely restore the life of the active components, the assumption of constant failure rate (i.e., number of failures independent upon a time) is regarded as appropriate for this study.

Next, the third part (3) consists of selecting the desired estimation tool, which is used to compute the failure rate of each apparatus (4). Three estimation methodologies are evaluated in this paper: (i) HBM (3.1), (ii) MLE (3.2), and (iii) LSE (3.3). The results arising from the different methods are then compared (5) to point out the most accurate and precise estimator. A special focus on the comparison between the more recent Bayesian inference and the classic approaches is presented.

**2.1. Hierarchical Bayesian Modelling.** Assuming an HPP for the failure events of a given system, the number of failures  $x$ , experienced during a timeframe equal to  $t$ , can be obtained via

$$f(x|\lambda) = \frac{(\lambda t)^x e^{-\lambda t}}{x!}, \quad x = 0, 1, \dots, \quad (5)$$

where  $\lambda$  is the intensity characterizing the Poisson distribution, i.e., the unknown parameter of interest. As suggested by Siu and Kelly [49], the first-stage prior representing the variability of  $\lambda$  among different sources should be a beta distribution, given by

$$\pi_1(\lambda|\alpha, \beta) = \frac{\beta^\alpha \lambda^{\alpha-1} e^{-\beta\lambda}}{\Gamma(\alpha)}, \quad (6)$$

where  $\alpha$  and  $\beta$  are the hyperparameters, which are considered as independent before including any observations into the analysis [48]. After choosing the likelihood and the prior distributions, the MCMC simulations are performed to determine the posterior distributions of the hyperparameters. As a result, the posterior distribution of  $\lambda$  is also obtained through the sampling procedure.

**2.2. Maximum Likelihood Estimation.** Under the hypothesis of HPP, the probability distribution of failure interarrival times, denoted by  $T$ , is given by the following equations:

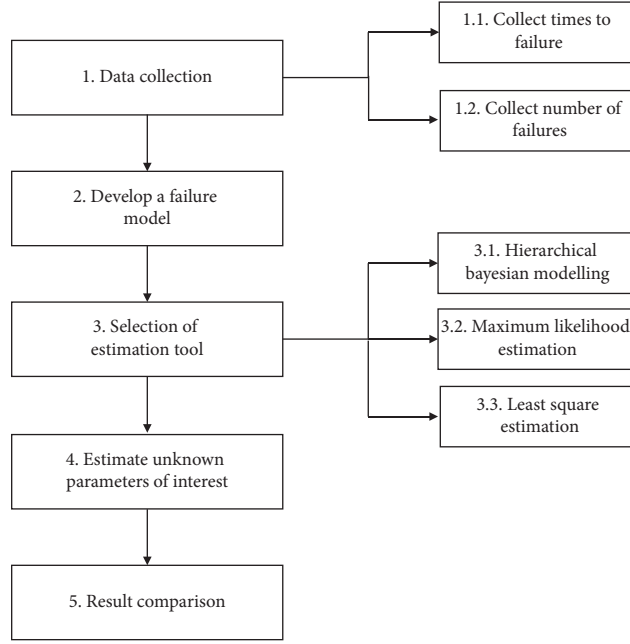


FIGURE 1: Flowchart representing the steps of the presented study.

$$F(t) = 1 - e^{-\lambda t}, \quad (7)$$

$$f(t) = \lambda e^{-\lambda t}, \quad (8)$$

where  $\lambda$  represents the rate of arrival. As previously discussed, the MLE determines the parameters of the considered distribution by maximising the likelihood function, which in case of exponential distribution is expressed by

$$L(\lambda) = \prod_{i=1}^n \lambda e^{-\lambda T_i} = \lambda^n e^{-\lambda \sum_{i=1}^n T_i} = \lambda^n e^{-\lambda n \bar{T}}, \quad (9)$$

where  $n$  indicates the total number of failures, while  $\bar{T}$  is addressed as the mean of the interarrival times. The estimator of  $\lambda$  is then found via [28, 53]

$$\hat{\lambda} = \frac{1}{\bar{T}} = \frac{n}{\sum_{i=1}^n T_i}. \quad (10)$$

**2.3. Least Square Estimation.** Let the interarrival time of failures follow a negative exponential distribution, described by equations (7) and (8). The LSE estimates the unknown parameters by defining a straight line that minimizes the sum of squared distances between the observed data and the line itself. Therefore, the exponential distribution should be rewritten in the form shown by

$$y = ax + b. \quad (11)$$

After applying the logarithm to both sides of equation (7) and some simplification, the following equation is obtained:

$$t = \frac{-\ln[1 - F(t)]}{\lambda}, \quad (12)$$

which represents a straight line with  $a = -1/\lambda$  and  $b = 0$ , while  $y = t$  and  $x = \ln[F(t)]$ . Let  $t = (t_1, t_2, \dots, t_n)$  be a sample of TTFs, and the estimation of  $\lambda$  is found by minimizing the SSE reported by

$$\text{SSE}(\lambda) = \sum_{i=1}^n \left( t_i - \frac{-\ln[1 - F(t_i)]}{\lambda} \right)^2, \quad (13)$$

where  $t_i$  stands for the  $i$ th observed TTF, while  $F(t_i)$  is replaced by the median rank, expressed by [54]

$$F(t_i) = \frac{i - 0.3}{n + 0.4}, \quad t_i, i = 1, 2, \dots, n (t_1 < t_2 < \dots < t_n). \quad (14)$$

### 3. Application of the Methodology to NGRMS

To show a practical application of the three approaches and compare their results, an NGRMS (Figure 2) is chosen as a case study. A generic NGRMS is divided into four groups and twelve main components, listed in Table 1.

The natural gas distribution network is a complex infrastructure formed by pipes and apparatuses able to withstand high-pressure values. Thus, before distributing the methane to the final users, the gas pressure must be reduced to be suitable for the various utilities. To fulfill this task, NGRMSs are usually installed along with additional subsequent pressure reduction units. The core of the plant is the reduction group, in which the pressure regulator and the pilot are tasked with reducing the pressure. During standard



TABLE 1: NGRMS' main groups and components.

Group	Component
Reduction	Pressure regulator (PR) Pilot Filter
Measuring	Pressure and temperature gauge (PTG) Calculator Meter
Odorization	Remote control system (RCS) THT tank THT pipelines
Preheating	Pump Boiler Water pipe (WP)

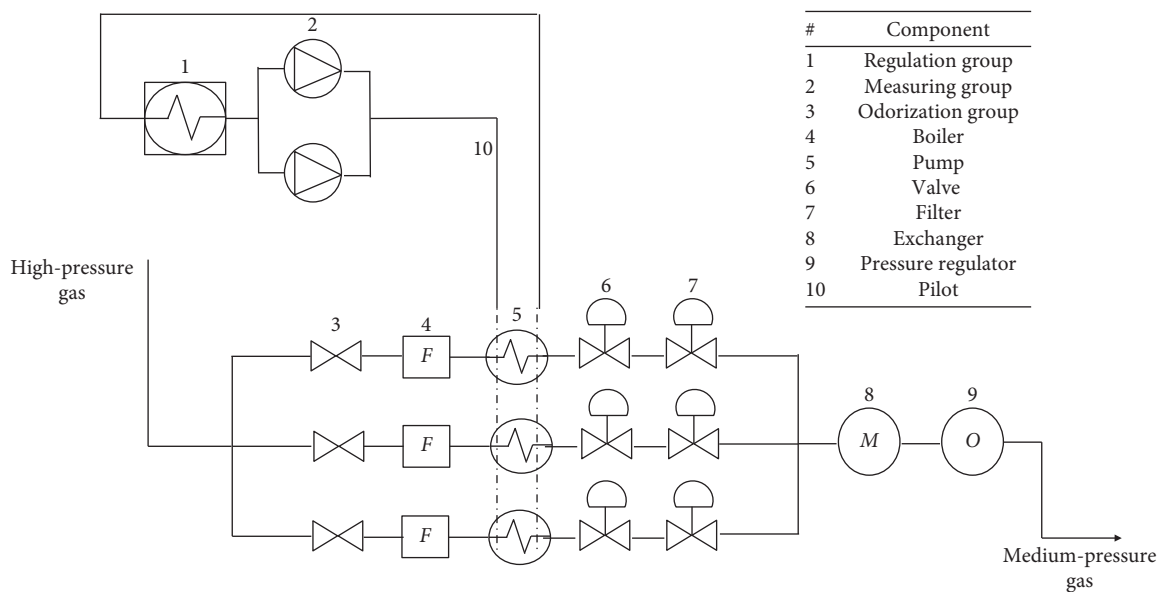


FIGURE 2: Schematic representation of an NGRMS.

conditions, the pressure is decreased by varying the cross-sectional flow area of the pressure regulator, while the downstream pilot is activated just in case a faster or more accurate pressure reduction is required. The solid and liquid impurities that could be present in the gas flow are removed by the filter, which is located upstream of the pressure regulator. Since decreasing the pressure is always accompanied by a temperature reduction, the gas must be heated before entering the pressure regulator to avoid the formation of ice. To this end, a water flow is preheated by a boiler, and subsequently, it is sent to an exchanger in which flows the methane gas. At last, the measuring group evaluates the natural gas's most relevant parameters (e.g., pressure, temperature, and mass flow), while the odorization group is required to add a precise quantity of odorizer, usually tetrahydrothiophene (THT), to the gas flow.

3.1. Data Collection. To implement the approaches, the operations of a real-life NGRMS were reproduced through the AnyLogic simulation software (developed by The

AnyLogic Company, <http://www.xjtek.com>), focusing on the stochastic failure generation process. The developed model has an NGRMS located in Tuscany near Arezzo Town and a maintenance centre in Prato Town (Figure 3), served by two maintenance teams available 24/7. The first maintenance squad is tasked with preventive actions, while the second one is in charge of the corrective actions. Agent-based modelling and fifteen simulation run were adopted for this study. From each run, the TTFs, the CTTFs, and the number of failures were extracted to conduct the subsequent analysis (step 1 of Figure 1). It is worthwhile mentioning that the failure rates adopted for the simulation are chosen based on real experience; therefore, from now on, they are considered as "real" parameters. As a result, such failure rates are also exploited as reference values to compare the precision of the three estimation approaches.

For the sake of conciseness, the estimation methods will be presented in detail for the pressure regulator; however, a summary reporting the obtained results for all the considered components will be discussed later through this study. Table 2 shows the observed number of failures and the

number of preventive maintenance actions arising from each simulation run for the pressure regulator. Each simulation run is considered as a different source of the failure rate of the components for the HBM. After this brief introduction, step 4 of Figure 1 will be implemented in the next sections.

**3.2. Hierarchical Bayesian Modelling.** The BN illustrated by Figure 4 was adopted to predict the posterior distribution of  $\lambda$ . The aforementioned number of failures observed in each source (Table 2) is denoted by  $X_i$ , while  $\lambda_i$  refers to the failure rate of the  $i$ -th run. The calculation of posterior distribution in Bayesian will be carried out by MCMC simulation. Three chains, each starting from a distinct point in the parameter space, were used to assure the convergence. The sampling from the likelihood and the prior distribution was conducted with 105 iterations for each chain, preceded by 1,000 burn-in iterations. The estimated posterior distribution of  $\alpha$  and  $\beta$  along with their respective mean values is shown in Figure 5. Furthermore, the correlation between the two parameters is represented in Figure 6.

The MCMC sampling process revealed a mean value of  $\alpha$  equal to 0.3863, with a 95% credible interval of (0.1156, 0.9065), while the mean of the posterior predicted distribution for  $\beta$  is  $1.68E+4$  hours with the following 95% credible interval: ( $2.12E+3$ ,  $4.52E+4$ ).

The caterpillar plot representing the 95% credible interval for the failure rate of each source is illustrated in Figure 7. As shown in Figure 7, the computed mean value (red vertical line) of the posterior predictive distribution for  $\lambda$  is  $1.68E-05$  (per hour). Table 3 reports a summary of the posterior distribution of every  $\lambda_i$ .

Due to the different number of failures and distinct exposure time observed in each source, the mean failure rate varies significantly from source-to-source. For instance, the first source is characterized by the highest mean failure rate of  $5.69E-05$  (per hour) since it has experienced the highest number of failures (3) in the shortest timespan (44,300 hours). By contrast, the tenth pressure regulator owns the lowest mean failure rate equal to  $3.59E-06$  (per hour), because no failure has been detected for a decade. The source-to-source variability is incorporated within the aforementioned mean value of  $1.68E-05$  (per hour).

Considering an exponential distribution for the inter-arrival time of failures, the MTTF is given by the reciprocal of the failure rate, as shown in

$$\text{MTTF} = \frac{1}{\lambda}. \quad (15)$$

Following equation (15), the MTTF of the pressure regulator is estimated. It emerged that the average time between two subsequent failure states is 59,524 hours (about six and a half years).

**3.3. Maximum Likelihood Estimation.** To perform this step of the analysis, the statistical software called Minitab was exploited. Minitab allows considering both the TTFs and the CTTFs for the estimation of  $\lambda$ . The MLE application provides a failure rate of  $1.22E-05$  (per hour), which

corresponds to an MTTF equal to 82,060 hours (more than nine years). The resulting probability density function is reported in Figure 8.

**3.4. Least Square Estimation.** As in the previous step, Minitab was adopted for the LSE as well. The intensity of the Poisson process estimated by the LSE method is slightly higher than the rate calculated via the MLE. The calculation depicted a  $\lambda$  equal to  $1.28E-05$  (per hour), equivalent to an MTTF of 78,219 hours (slightly less than nine years). The exponential probability density function of failure inter-arrival time corresponding to the estimated failure rate is illustrated in Figure 9.

## 4. Discussion

In this section, step 5 of Figure 1 is presented. As described by the previous section, applying the three approaches with the same input data provided three different values for the failure rate of the pressure regulator. The HBM yields a failure rate of  $\lambda_{\text{HBM}} = 1.68E-05$ , which results in an MTTF equal to 59,524 hours. On the other hand, it emerged that the MTTFs calculated by the MLE and LSE approaches are much higher than the Bayesian ones. Indeed, the MLE and the LSE quantified an average time between two subsequent failures of 82,060 and 78,219 hours, respectively.

The real failure rate (i.e., the one adopted during the simulation process) is  $\lambda_{\text{REAL}} = 1.64E-05$ , corresponds to a MTTF of 60,882 hours. Accordingly, the calculation revealed a much accurate and precise Bayesian estimator with respect to the other ones. Indeed, the real value is underestimated by the HBM for 1,300 hours (about 54 days), while the other estimations are more than 2 years longer compared to  $\text{MTTF}_{\text{REAL}}$ .

A summary of the Bayesian results and the other approaches is listed in Tables 4 and 5. The comparison will be discussed further for each group in the following sections.

The estimated MTTFs are transformed into dimensionless values through the average time between two consecutive failures adopted for the simulation (i.e.,  $\text{MTTF}_{\text{REAL}}$ ). The results are shown in Table 6 and Figure 10.

**4.1. Reduction Group.** To illustrate the differences arising from the three estimation methodologies, the cumulative distribution functions (CDFs) of each approach were developed for the reduction devices (Figures 11 and 12). As depicted by Tables 4–6, the HBM provided the most accurate estimation for the failure rate of the pilot, while the MLE and the LSE of the MTTF are, respectively, 129 days longer and 154 days shorter than the real value. Considering the filter, the difference between  $\text{MTTF}_{\text{REAL}}$  and  $\text{MTTF}_{\text{HBM}}$  is just 17 hours, while both the MLE and the LSE overestimate the average time between two consecutive failures. The MLE yields an MTTF which is 20 days longer compared to  $\text{MTTF}_{\text{REAL}}$ , whereas the mean time span between two failure states is estimated by the LSE as 25 days longer than the real one.



FIGURE 3: Map of the location of the simulated case.

TABLE 2: Number of failures, preventive actions, and exposure time for the pressure regulator in each source (simulation run).

Source	Number of failures	Number of preventive actions	Exposure time (hours)
1	3	0	44,300
2	1	0	44,300
3	2	0	44,300
4	0	1	78,840
5	0	1	78,840
6	0	1	78,840
7	0	0	54,000
8	1	0	54,000
9	0	0	54,000
10	0	1	87,600
11	2	0	87,600
12	2	0	87,600
13	1	0	61,320
14	1	0	61,320
15	0	0	61,320

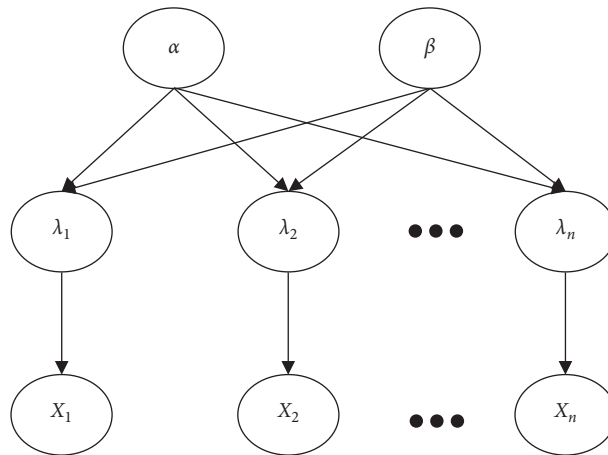


FIGURE 4: Developed HBM for estimating the failure rate of each device.

4.2. *Measuring Group.* For the calculator, the HBM yields a posterior mean interarrival time of failure equal to 68,027 hours, while the MLE and the LSE of MTTF are estimated at 88,825 and 80,837 hours, respectively. Given the real value of 73,233 hours, the HBM is the most accurate estimation tool once again. The Bayesian approach manifested its advantages over the other methodologies for the PTG as well. Indeed, the difference between  $MTTF_{HBM}$  and  $MTTF_{REAL}$  is

128 hours (about five days), while both the MLE and the LSE overestimate the real mean time between two contiguous failures by approximately 1,000 hours (41 days). On the contrary, the application of LSE emerged as the most precise for both the meter and the RCS. However, the Bayesian inference demonstrated greater accuracy than the MLE for these two devices. The  $MTTF_{HBM}$  of the meter is just 14 days longer than the MTTF estimated by the LSE, while the

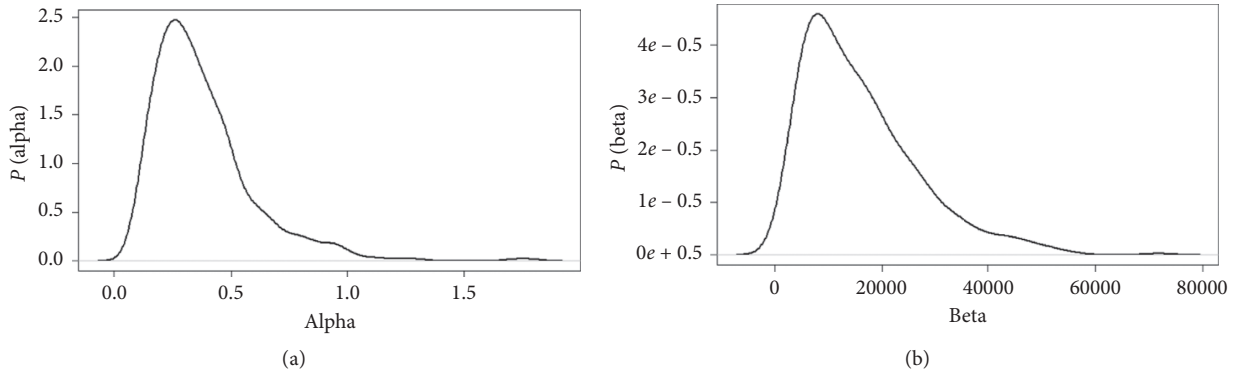


FIGURE 5: The posterior probability density function for alpha (on the left) and beta (on the right).

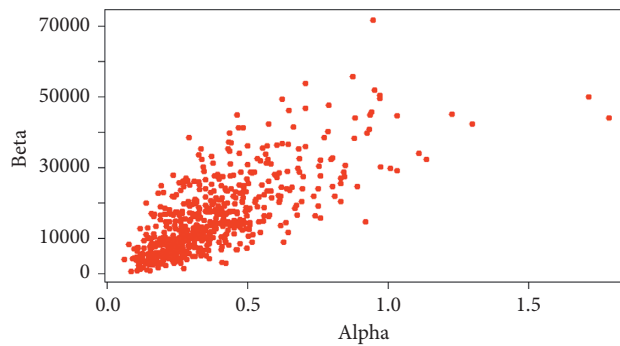


FIGURE 6: Correlation between alpha and beta.

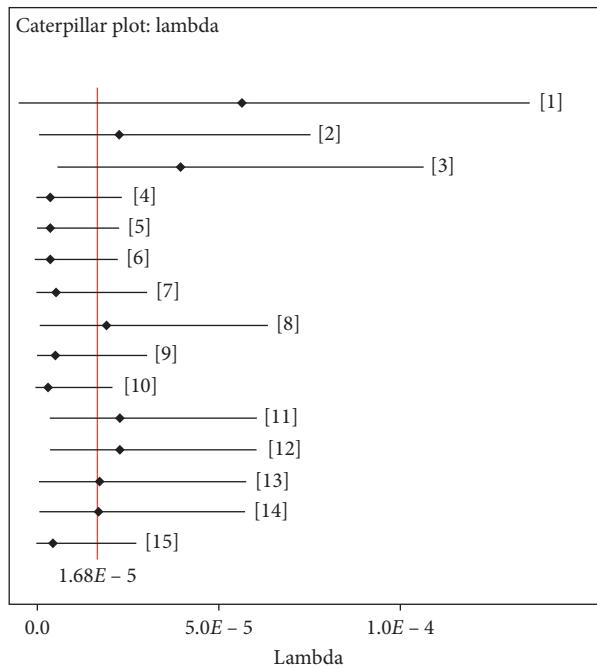


FIGURE 7: Predicted 95% credible interval for the failure rate of the pressure regulator in each source. The black dots are the posterior means of each source, while the red line represents the average of posterior means.

discrepancy between the Bayesian prediction and the LSE estimator for the RCS is equal to 12 days. Both the HBM and the LSE showed an estimation error of about 5,000 hours

(208 days) and 1,500 hours (62 days) for the meter and the RCS, respectively. The CDFs of the measuring components are represented in Figures 13 and 14.

TABLE 3: Statistical properties of the failure rate for each source of the pressure regulator.

HBM parameter	Mean	2.5 percentile	97.5 percentile
$\lambda_1$	$5.69E-05$	$1.29E-05$	$1.36E-04$
$\lambda_2$	$2.30E-05$	$1.29E-06$	$7.53E-05$
$\lambda_3$	$3.98E-05$	$6.07E-06$	$1.07E-04$
$\lambda_4$	$3.91E-06$	$1.57E-12$	$2.33E-05$
$\lambda_5$	$3.92E-06$	$1.61E-12$	$2.30E-05$
$\lambda_6$	$3.95E-06$	$1.80E-12$	$2.32E-05$
$\lambda_7$	$5.28E-06$	$2.06E-12$	$3.10E-05$
$\lambda_8$	$1.97E-05$	$1.10E-06$	$6.40E-05$
$\lambda_9$	$5.27E-06$	$2.60E-12$	$3.09E-05$
$\lambda_{10}$	$3.59E-06$	$1.56E-12$	$2.12E-05$
$\lambda_{11}$	$2.29E-05$	$3.49E-06$	$6.05E-05$
$\lambda_{12}$	$2.30E-05$	$3.50E-06$	$6.04E-05$
$\lambda_{13}$	$1.78E-05$	$9.91E-07$	$5.82E-05$
$\lambda_{14}$	$1.78E-05$	$9.78E-07$	$5.82E-05$
$\lambda_{15}$	$4.77E-06$	$2.16E-12$	$2.79E-05$

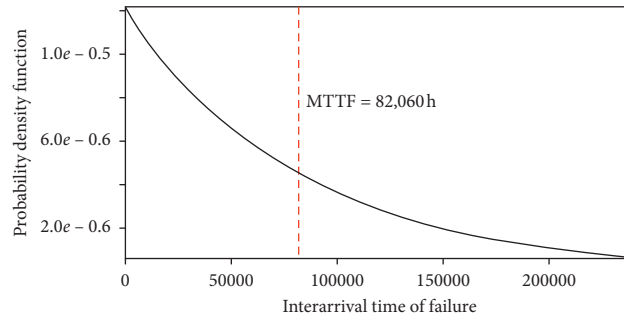


FIGURE 8: Interarrival time of failure distribution for the pressure regulator obtained via MLE.

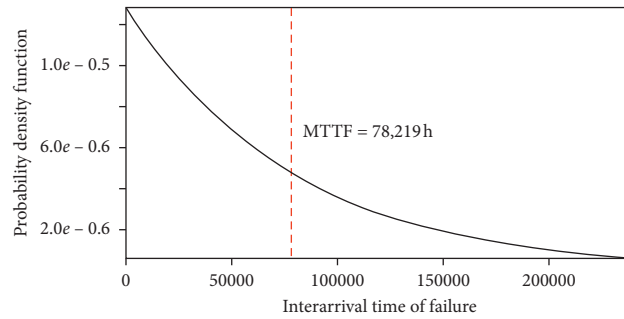


FIGURE 9: Interarrival time of failure distribution for the pressure regulator obtained via LSE.

TABLE 4: Real failure rate and failure rates estimated through the three approaches.

Component	Real $\lambda$	$\lambda$ HBM	$\lambda$ MLE	$\lambda$ LSE
Pressure regulator	$1.64E-05$	$1.68E-05$	$1.22E-05$	$1.28E-05$
Pilot	$2.18E-05$	$2.18E-05$	$2.04E-05$	$2.37E-05$
Filter	$9.67E-05$	$9.69E-05$	$9.26E-05$	$9.15E-05$
PTG	$5.17E-05$	$5.20E-05$	$4.91E-05$	$4.96E-05$
Calculator	$1.37E-05$	$1.47E-05$	$1.12E-05$	$1.24E-05$
Meter	$2.26E-05$	$2.01E-05$	$1.84E-05$	$2.02E-05$
RCS	$2.67E-05$	$2.55E-05$	$2.54E-05$	$2.57E-05$
THT tank	$1.08E-05$	$1.02E-05$	$8.18E-06$	$9.42E-06$
THT pipeline	$7.55E-06$	$7.79E-06$	$6.17E-06$	$9.76E-06$
Pump	$4.80E-05$	$4.82E-05$	$4.50E-05$	$4.31E-05$
Boiler	$3.16E-05$	$3.24E-05$	$3.19E-05$	$3.25E-05$
Water pipe	$7.40E-06$	$5.49E-06$	$4.11E-06$	$4.48E-06$

TABLE 5: Real MTTF and MTTFs estimated through the three approaches.

Component	Real MTTF	MTTF HBM	MTTF MLE	MTTF LSE
Pressure regulator	60,882	59,524	82,060	78,219
Pilot	45,815	45,872	48,909	42,123
Filter	10,337	10,320	10,800	10,934
PTG	19,359	19,231	20,379	20,151
Calculator	73,233	68,027	88,825	80,837
Meter	44,248	49,751	54,343	49,400
RCS	37,492	39,216	39,392	38,928
THT tank	92,593	98,039	122,272	106,137
THT pipeline	132,363	128,370	162,050	102,454
Pump	20,848	20,747	22,231	23,219
Boiler	31,623	30,864	31,362	30,741
Water pipe	135,166	182,149	243,075	223,270

TABLE 6: Dimensionless mean time to failure (D-MTTF) for each estimation approach.

Component	D-MTTF HBM	D-MTTF MLE	D-MTTF LSE
Pressure regulator	0.978	1.348	1.285
Pilot	1.001	1.068	0.919
Filter	0.998	1.045	1.058
PTG	0.993	1.053	1.041
Calculator	0.929	1.213	1.104
Meter	1.124	1.228	1.116
RCS	1.046	1.051	1.038
THT tank	1.059	1.321	1.146
THT pipeline	0.970	1.224	0.774
Pump	0.995	1.066	1.114
Boiler	0.976	0.992	0.972
Water pipe	1.348	1.798	1.652

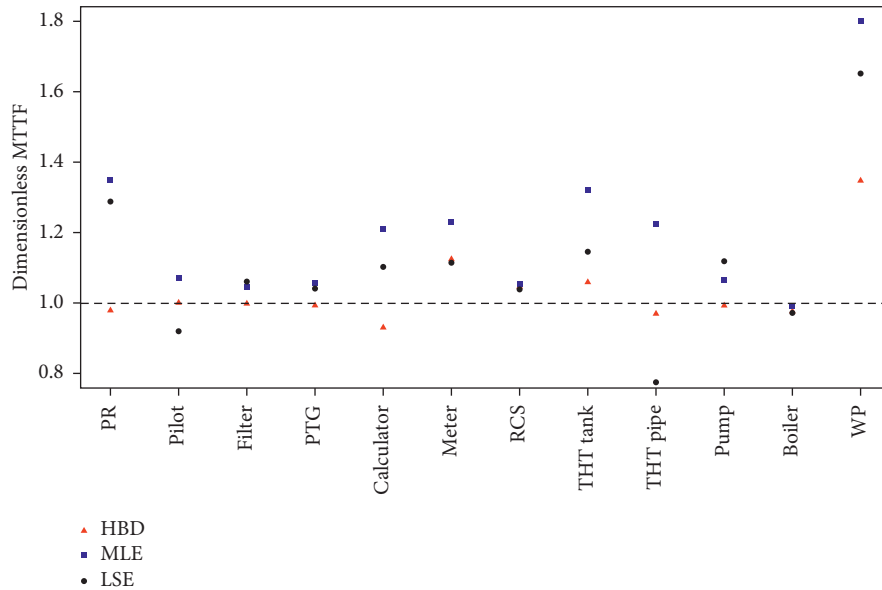


FIGURE 10: Developed dotplot of the D-MTTFs for each methodology. The black dashed line represents the real MTTF.

4.3. *Odorization Group.* The CDFs built for the THT tank and THT pipe are illustrated in Figure 15. The Bayesian approach proved its higher performance also for the components belonging to the odorization group. The  $MTTF_{HBM}$

of the THT tank is estimated at 98,039 hours, which is about 5,500 hours (about 230 days) shorter than  $MTTF_{REAL}$ . The MLE model resulted in an average interarrival time of 13.9 years, while the LSE yields an MTTF of 12.1 years. Compared

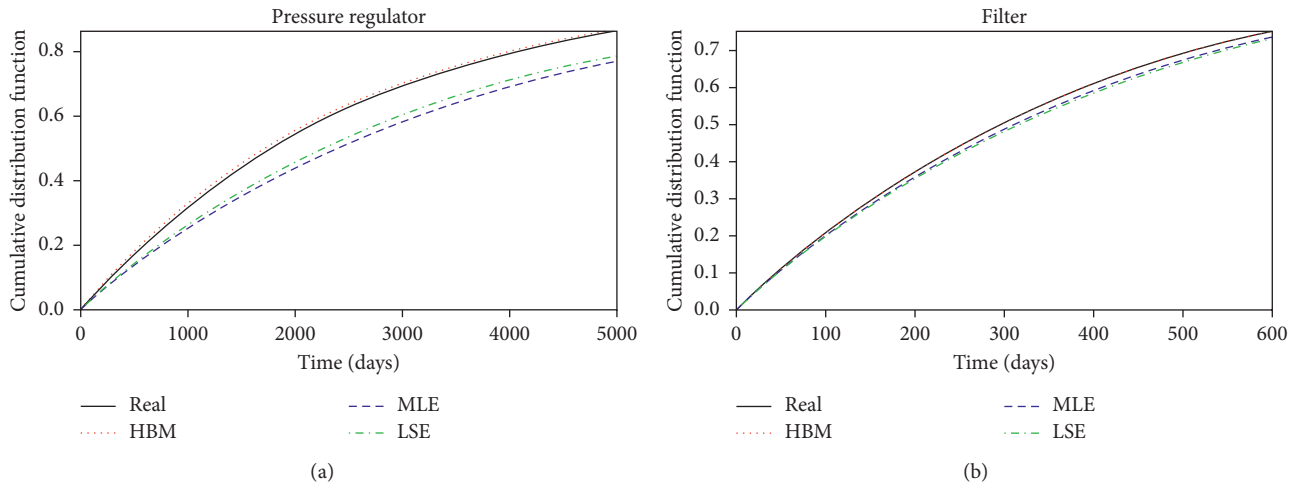


FIGURE 11: Developed CDFs for the pressure regulator and the filter.

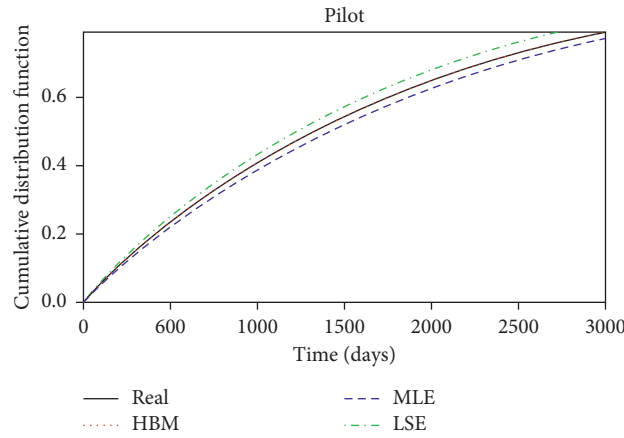


FIGURE 12: Developed CDF for the pilot.

to the real value, the ML and the LSE estimators showed a gap of about 30,000 hours (more than three years) and 13,000 hours (about 1.5 years), respectively. For the THT pipe, a similar scenario is seen. Indeed, both the ML and LS of MTTFs are about 30,000 hours longer than the real average time expected before experiencing a failure. By contrast, the HBM predicted a posterior mean value of 128,370 hours, which is close to the real mean interarrival time to failure of 132,363 hours.

**4.4. Preheating Group.** The water pipe is the component associated with the worst estimations due to extreme data scarcity (Figures 16 and 17). The HBM yields a posterior MTTF of 182,149 hours, which is five years longer than  $MTTF_{REAL}$ . The MLE and the LSE also overestimated the real average time between two consecutive failures by 12 and 10 years, respectively. Considering the boiler, the MLE estimator is the most accurate, with a discrepancy of just 300 hours (almost 13 days) compared to  $MTTF_{REAL}$ . Nevertheless, the application of the HBM is more precise than LSE. At last, the Bayesian inference emerged as the best estimator

for the pump, presenting a gap of 100 hours (four days) with respect to the mean interarrival time of failure adopted for the simulation. On the other side, an overestimation of 58 and 99 days is observed, respectively, for the MLE and the LSE of the MTTF related to the pump.

**4.5. Discussion: Maintenance Application.** The HBM has proven itself as the most reliable estimator under limited data, which concerns particularly the pressure regulator, the calculator, the THT tank, the THT pipe, and the water pipe. Indeed, these components are characterized by a longer MTTF than the other apparatuses; therefore, fewer failures are observed during the same time interval. The Bayesian predictions of the failure parameter for the aforementioned devices show a better precision than the other estimation methodologies. Moreover, the accuracy showed by the HBM is also higher than the other approaches for most of the devices. The root mean square error (RMSE) is calculated for each method to demonstrate the last statements, as shown by equation (18):

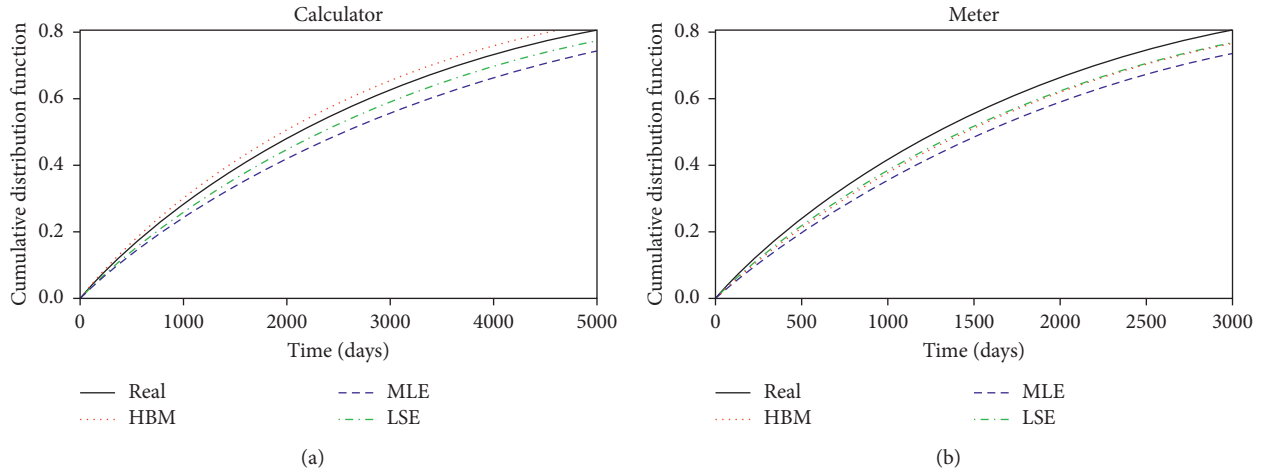


FIGURE 13: Developed CDFs for the calculator and the meter.

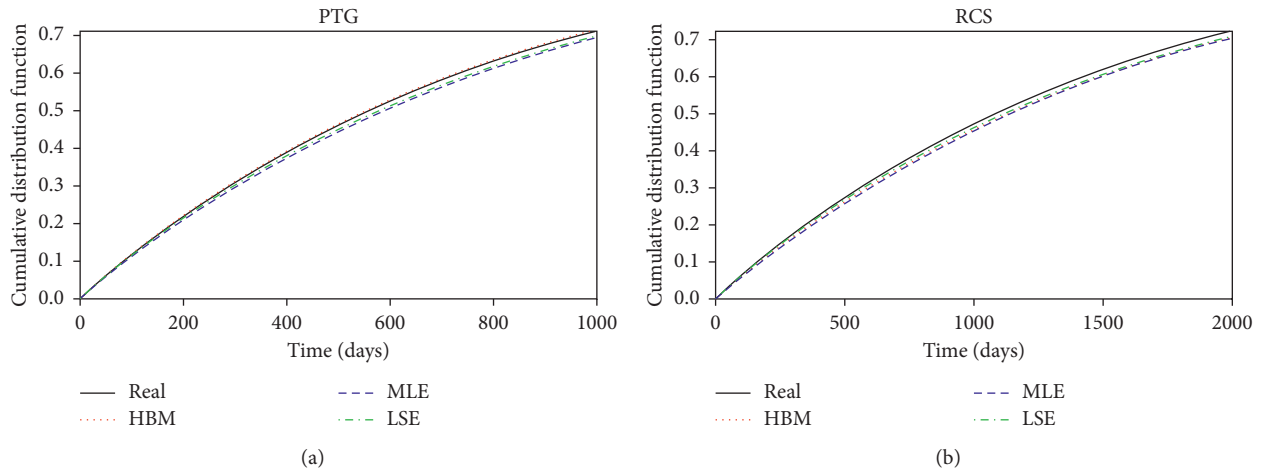


FIGURE 14: Developed CDFs for the PTG and the RCS.

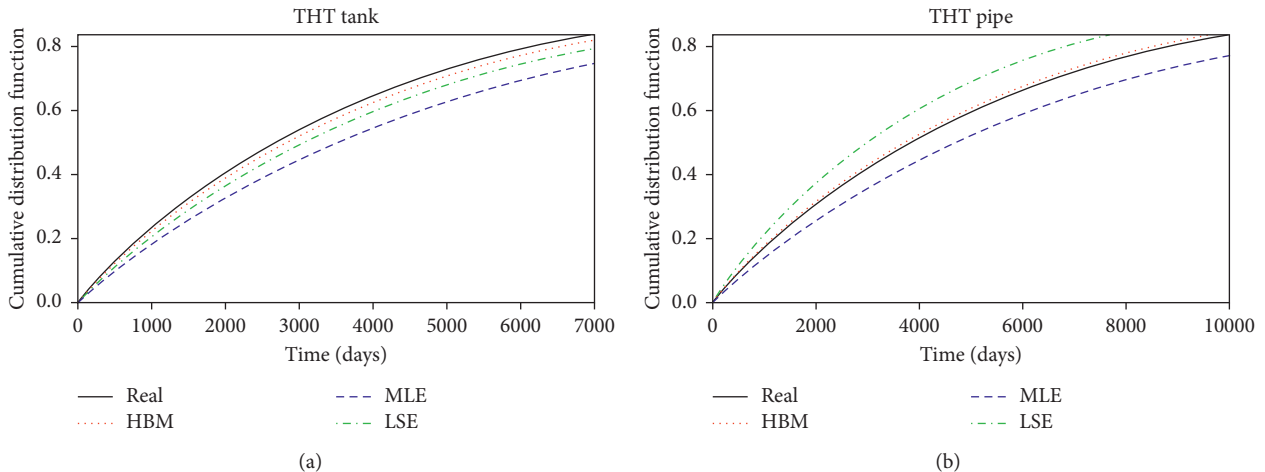


FIGURE 15: Developed CDFs for the THT tank and the THT pipe.



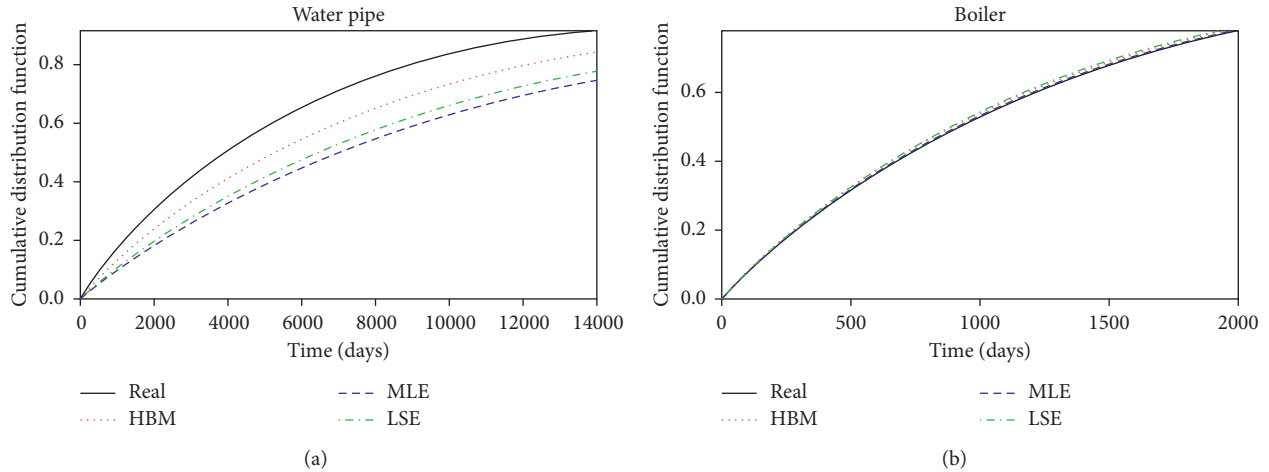


FIGURE 16: Developed CDFs for the water pipe and the boiler.

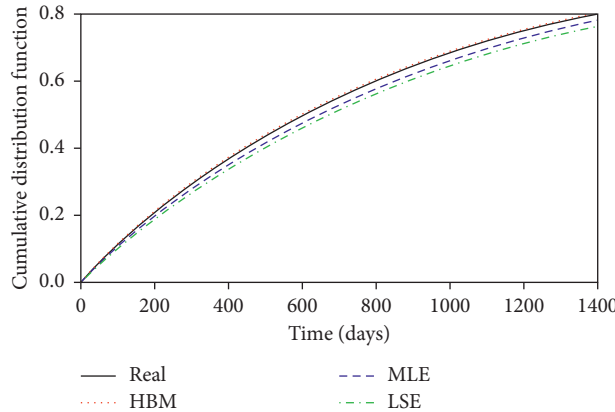


FIGURE 17: Developed CDF for the pump.

$$RMSE = \sqrt{\frac{\sum_{i=1}^n (MTTF_i - MTTF_{REAL,i})^2}{n}}, \quad (16)$$

where  $n$  denotes the number of components, while  $MTTF_i$  is the estimated average time between two consecutive failures for the  $i$ th device. At last,  $MTTF_{REAL,i}$  is the mean inter-arrival time between failures adopted for the  $i$ th equipment during the simulation. The RMSE computed for the HBM through equation (16) is equal to 13,892 hours, while the RMSE of the MLE and LSE is estimated, respectively, at 34,420 and 27,761 hours. Accordingly, the exploitation of the Bayesian method will result in a much safer maintenance strategy without overlooking economic aspects by avoiding premature maintenance actions.

### 5. Conclusions

Any maintenance policy is deeply affected by the previous failure rate estimation process, which often suffers from limited data. Thus, one of the most significant challenges associated with the reliability analysis is selecting a proper estimation approach capable of producing accurate and

precise results in case of limited data. To this end, the application of three estimation tools is investigated in this paper, with a particular focus on the comparison between the Bayesian inference and two common estimation methodologies: the MLE and the LSE. The three analyses were tested on twelve components of an NGRMS, whose operations were simulated through a simulation model to extract failure data (i.e., TTF, CTTF, and the number of failures). Under the assumption of HPP, the results highlighted a greater accuracy of the HBM, which emerged as the most precise estimator for nine devices out of twelve. The advantages of the Bayesian estimator are especially evident in the event of data shortage, associated with the devices with greater MTTF. Indeed, the lack of data is partially compensated by the HBM through the consideration of source-to-source variability, which is disregarded by the MLE and the LSE. On the other side, the MLE and LSE precision improves for the equipment characterized by more data available, up to taking the upper hand over the Bayesian inference for the meter, the RCS, and the boiler. However, the discrepancy between the Bayesian predictions and the other estimations for these components are negligible since almost no difference can be seen from their respective CDFs.

Considering all the above, adopting a Bayesian approach for the reliability analysis will help to deal with sparse data, resulting in a more efficient and effective maintenance plan. Further developments can include the application of weakly-informative kind of prior to the Bayesian model to incorporate some prior knowledge into the estimation framework.

## Data Availability

The data used to support the findings of this study are included within the article.

## Conflicts of Interest

The authors declare that they have no conflicts of interest.

## References

- [1] H.-m. Kwon, "The effectiveness of process safety management (PSM) regulation for chemical industry in Korea," *Journal of Loss Prevention in the Process Industries*, vol. 19, no. 1, pp. 13–16, 2006.
- [2] F. Jaderi, Z. Z. Ibrahim, and M. R. Zahiri, "Criticality analysis of petrochemical assets using risk based maintenance and the fuzzy inference system," *Process Safety and Environmental Protection*, vol. 121, pp. 312–325, 2019.
- [3] H. Soltanali, A. Rohani, M. H. Abbaspour-Fard, A. Parida, and J. T. Farinha, "Development of a risk-based maintenance decision making approach for automotive production line," *International Journal of System Assurance Engineering and Management*, vol. 11, no. 1, pp. 236–251, 2020.
- [4] Y. Wang, G. Cheng, H. Hu, and W. Wu, "Development of a risk-based maintenance strategy using FMEA for a continuous catalytic reforming plant," *Journal of Loss Prevention in the Process Industries*, vol. 25, no. 6, pp. 958–965, 2012.
- [5] D. Li and J. Gao, "Study and application of reliability-centered maintenance considering radical maintenance," *Journal of Loss Prevention in the Process Industries*, vol. 23, no. 5, pp. 622–629, 2010.
- [6] H. Islam, "Reliability-centered maintenance methodology and application: a case study," *Engineering*, vol. 2, no. 11, 2010.
- [7] B. Yssaad and A. Abene, "Rational reliability centered maintenance optimization for power distribution systems," *International Journal of Electrical Power & Energy Systems*, vol. 73, pp. 350–360, 2015.
- [8] G. Zou, K. Banisoleiman, A. González, and M. H. Faber, "Probabilistic investigations into the value of information: a comparison of condition-based and time-based maintenance strategies," *Ocean Engineering*, vol. 188, Article ID 106181, 2019.
- [9] C. Duan, Z. Li, and F. Liu, "Condition-based maintenance for ship pumps subject to competing risks under stochastic maintenance quality," *Ocean Engineering*, vol. 218, Article ID 108180, 2020.
- [10] Z. Liang, B. Liu, M. Xie, and A. K. Parlikad, "Condition-based maintenance for long-life assets with exposure to operational and environmental risks," *International Journal of Production Economics*, vol. 221, Article ID 107482, 2020.
- [11] J. Kang, Z. Wang, and C. Guedes Soares, "Condition-based maintenance for offshore wind turbines based on support vector machine," *Energies*, vol. 13, no. 14, p. 3518, 2020.
- [12] G. Pui, J. Bhandari, E. Arzaghi, R. Abbassi, and V. Garaniya, "Risk-based maintenance of offshore managed pressure drilling (MPD) operation," *Journal of Petroleum Science and Engineering*, vol. 159, pp. 513–521, 2017.
- [13] H. Hu, G. Cheng, Y. Li, and Y. Tang, "Risk-based maintenance strategy and its applications in a petrochemical reforming reaction system," *Journal of Loss Prevention in the Process Industries*, vol. 22, no. 4, pp. 392–397, 2009.
- [14] M. Florian and J. D. Sørensen, "Risk-based planning of operation and maintenance for offshore wind farms," *Energy Procedia*, vol. 137, pp. 261–272, 2017.
- [15] G. Kumar and J. Maiti, "Modeling risk based maintenance using fuzzy analytic network process," *Expert Systems with Applications*, vol. 39, no. 11, pp. 9946–9954, 2012.
- [16] A. BahooToroody, M. M. Abaei, E. Arzaghi, F. BahooToroody, F. De Carlo, and R. Abbassi, "Multi-level optimization of maintenance plan for natural gas system exposed to deterioration process," *Journal of Hazardous Materials*, vol. 362, pp. 412–423, 2019.
- [17] D. Zhang, A. D. Bailey, and D. Djurdjanovic, "Bayesian identification of hidden Markov models and their use for condition-based monitoring," *IEEE Transactions on Reliability*, vol. 65, no. 3, pp. 1471–1482, 2016.
- [18] Z. Zeng and E. Zio, "Dynamic risk assessment based on statistical failure data and condition-monitoring degradation data," *IEEE Transactions on Reliability*, vol. 67, no. 2, pp. 609–622, 2018.
- [19] C. Chen, B. Zhang, and G. Vachtsevanos, "Prediction of machine health condition using neuro-fuzzy and Bayesian algorithms," *IEEE Transactions on Instrumentation and Measurement*, vol. 61, no. 2, pp. 297–306, 2011.
- [20] D. Yuhua and Y. Datao, "Estimation of failure probability of oil and gas transmission pipelines by fuzzy fault tree analysis," *Journal of Loss Prevention in the Process Industries*, vol. 18, no. 2, pp. 83–88, 2005.
- [21] T. Zhang and R. Dwight, "Choosing an optimal model for failure data analysis by graphical approach," *Reliability Engineering & System Safety*, vol. 115, pp. 111–123, 2013.
- [22] J.-M. Bourinet, F. Deheeger, and M. Lemaire, "Assessing small failure probabilities by combined subset simulation and support vector machines," *Structural Safety*, vol. 33, no. 6, pp. 343–353, 2011.
- [23] A. P. Teixeira, C. Guedes Soares, T. A. Netto, and S. F. Estefen, "Reliability of pipelines with corrosion defects," *International Journal of Pressure Vessels and Piping*, vol. 85, no. 4, pp. 228–237, 2008.
- [24] J. Zhang and X. Du, "A second-order reliability method with first-order efficiency," *Journal of Mechanical Design*, vol. 132, no. 10, 2010.
- [25] J. Wu, R. Zhou, S. Xu, and Z. Wu, "Probabilistic analysis of natural gas pipeline network accident based on Bayesian network," *Journal of Loss Prevention in the Process Industries*, vol. 46, pp. 126–136, 2017.
- [26] R. Calabria and G. Pulcini, "On the maximum likelihood and least-squares estimation in the inverse Weibull distribution," *Statistica Applicata*, vol. 2, no. 1, pp. 53–66, 1990.
- [27] R. M. Musleh and A. Helu, "Estimation of the inverse Weibull distribution based on progressively censored data: comparative study," *Reliability Engineering & System Safety*, vol. 131, pp. 216–227, 2014.
- [28] A. BahooToroody, M. M. Abaei, E. Arzaghi et al., "On reliability challenges of repairable systems using hierarchical bayesian inference and maximum likelihood estimation,"

- Process Safety and Environmental Protection*, vol. 135, pp. 157–165, 2020.
- [29] M. El-Gheriani, F. Khan, D. Chen, and R. Abbassi, “Major accident modelling using spare data,” *Process Safety and Environmental Protection*, vol. 106, pp. 52–59, 2017.
- [30] N. Khakzad, “System safety assessment under epistemic uncertainty: using imprecise probabilities in Bayesian network,” *Safety Science*, vol. 116, pp. 149–160, 2019.
- [31] D. F. Percy, “Maintenance based on limited data,” in *Complex System Maintenance Handbook*, pp. 133–154, Springer, Berlin, Germany, 2008.
- [32] M. Yang, F. Khan, and P. Amyotte, “Operational risk assessment: a case of the Bhopal disaster,” *Process Safety and Environmental Protection*, vol. 97, pp. 70–79, 2015.
- [33] P. Kumari, D. Lee, Q. Wang, M. N. Karim, and J. S.-I. Kwon, “Root cause analysis of key process variable deviation for rare events in the chemical process industry,” *Industrial & Engineering Chemistry Research*, vol. 59, no. 23, 2020.
- [34] N. Khakzad, F. Khan, and N. Paltrinieri, “On the application of near accident data to risk analysis of major accidents,” *Reliability Engineering & System Safety*, vol. 126, pp. 116–125, 2014.
- [35] N. Khakzad, S. Khakzad, and F. Khan, “Probabilistic risk assessment of major accidents: application to offshore blowouts in the Gulf of Mexico,” *Natural Hazards*, vol. 74, no. 3, pp. 1759–1771, 2014.
- [36] M. Yang, F. I. Khan, and L. Lye, “Precursor-based hierarchical Bayesian approach for rare event frequency estimation: a case of oil spill accidents,” *Process Safety and Environmental Protection*, vol. 91, no. 5, pp. 333–342, 2013.
- [37] M. Yang, F. Khan, L. Lye, and P. Amyotte, “Risk assessment of rare events,” *Process Safety and Environmental Protection*, vol. 98, pp. 102–108, 2015.
- [38] H. Yu, F. Khan, and B. Veitch, “A flexible hierarchical Bayesian modeling technique for risk analysis of major accidents,” *Risk Analysis*, vol. 37, no. 9, pp. 1668–1682, 2017.
- [39] X. Li, G. Chen, F. Khan, and C. Xu, “Dynamic risk assessment of subsea pipelines leak using precursor data,” *Ocean Engineering*, vol. 178, pp. 156–169, 2019.
- [40] D. Spiegelhalter, A. Thomas, N. Best, and D. Lunn, *OpenBUGS User Manual, Version 3.0. 2*, MRC Biostatistics Unit, Cambridge, UK, 2007.
- [41] L. Leoni, A. BahooToroody, M. M. Abaei et al., “On hierarchical bayesian based predictive maintenance of autonomous natural gas regulating operations,” *Process Safety and Environmental Protection*, vol. 147, pp. 115–124, 2021.
- [42] L. Leoni, F. De Carlo, F. Sgarbossa, and N. Paltrinieri, “Comparison of risk-based maintenance approaches applied to a natural gas regulating and metering station,” *Chemical Engineering Transactions*, vol. 82, pp. 115–120, 2020.
- [43] A. BahooToroody, F. De Carlo, N. Paltrinieri, M. Tucci, and P. H. A. J. M. Van Gelder, “Bayesian regression based condition monitoring approach for effective reliability prediction of random processes in autonomous energy supply operation,” *Reliability Engineering & System Safety*, vol. 201, Article ID 106966, 2020.
- [44] A. BahooToroody, M. M. Abaei, F. BahooToroody, F. De Carlo, R. Abbassi, and S. Khalaj, “A condition monitoring based signal filtering approach for dynamic time dependent safety assessment of natural gas distribution process,” *Process Safety and Environmental Protection*, vol. 123, pp. 335–343, 2019.
- [45] L. Niu, P. H. A. J. M. Van Gelder, Y. Guan, C. Zhang, and J. K. Vrijling, “Probabilistic analysis of phytoplankton biomass at the Frisian Inlet (NL),” *Estuarine, Coastal and Shelf Science*, vol. 155, pp. 29–37, 2015.
- [46] M. Yang, F. Khan, V. Garaniya, and S. Chai, “Multimedia fate modeling of oil spills in ice-infested waters: an exploration of the feasibility of fugacity-based approach,” *Process Safety and Environmental Protection*, vol. 93, pp. 206–217, 2015.
- [47] M. M. Abaei, N. R. Arini, P. R. Thies, and J. Lars, “Failure estimation of offshore renewable energy devices based on hierarchical bayesian approach,” in *Proceedings of the International Conference on Offshore Mechanics and Arctic Engineering*, Prague, Czech, June 2019.
- [48] D. L. Kelly and C. L. Smith, “Bayesian inference in probabilistic risk assessment-The current state of the art,” *Reliability Engineering & System Safety*, vol. 94, no. 2, pp. 628–643, 2009.
- [49] N. O. Siu and D. L. Kelly, “Bayesian parameter estimation in probabilistic risk assessment,” *Reliability Engineering & System Safety*, vol. 62, no. 1-2, pp. 89–116, 1998.
- [50] D. Kelly and C. Smith, *Bayesian Inference for Probabilistic Risk Assessment: A Practitioner’s Guidebook*, Springer Science & Business Media, Berlin, Germany, 2011.
- [51] M. M. Abaei, E. Arzaghi, R. Abbassi, V. Garaniya, M. Javanmardi, and S. Chai, “Dynamic reliability assessment of ship grounding using Bayesian Inference,” *Ocean Engineering*, vol. 159, pp. 47–55, 2018.
- [52] I. J. Myung, “Tutorial on maximum likelihood estimation,” *Journal of Mathematical Psychology*, vol. 47, no. 1, pp. 90–100, 2003.
- [53] S. M. Ross, *Introduction to Probability Models*, Academic Press, Cambridge, MA, USA, 2014.
- [54] M. Z. Rashid and A. S. Akhter, “Estimation accuracy of exponential distribution parameters,” *Pakistan Journal of Statistics and Operation Research*, vol. 7, no. 2, 2011.

## Research Article

# Health Indicator for Predictive Maintenance Based on Fuzzy Cognitive Maps, Grey Wolf, and K-Nearest Neighbors Algorithms

G. Mazzuto , S. Antomarioni , F. E. Ciarapica , and M. Bevilacqua 

*Dipartimento Ingegneria Industriale e Scienze Matematiche, Università Politecnica Delle Marche, Via Brecce Bianche, Ancona 60131, Italy*

Correspondence should be addressed to G. Mazzuto; [g.mazzuto@univpm.it](mailto:g.mazzuto@univpm.it)

Received 22 September 2020; Revised 8 October 2020; Accepted 20 January 2021; Published 17 February 2021

Academic Editor: Filippo De Carlo

Copyright © 2021 G. Mazzuto et al. This is an open access article distributed under the Creative Commons Attribution License, which permits unrestricted use, distribution, and reproduction in any medium, provided the original work is properly cited.

An essential step in the implementation of predictive maintenance involves the health state analysis of productive equipment in order to provide company managers with performance and degradation indicators which help to predict component condition. In this paper, a supervised approach for health indicator calculation is provided combining the Grey Wolf Optimisation method, Swarm Intelligence algorithm, and Fuzzy Cognitive Maps. The k-neighbors algorithms is used to predict the Remaining Useful Life of an item, since, in addition to its simplicity, they produce good results in a large number of domains. The approach aims to solve the problem that frequently occurs in interpolation procedures: the approximation of functions belonging to a chosen class of functions of which we have no knowledge. The proposed algorithm allows maintenance managers to distinguish different degradation profiles in depth with a consequently more precise estimate of the Remaining Useful Life of an item and, in addition, an in-depth understanding of the degradation process. Specifically, in order to show its suitability for predictive maintenance, a dataset on NASA aircraft engines has been used and results have been compared to those obtained with a neural network approach. Results highlight how all of the degradation profiles, obtained using the proposed approach, are modelled in a more detailed manner, allowing one to significantly distinguish different situations. Moreover, the physical core speed and the corrected fan speed have been identified as the main critical factors to the engine degradation.

## 1. Introduction

Although predictive maintenance practices have existed for many years, only recently, thanks to the emerging Industry 4.0 technologies with increasingly reliable and affordable smart systems, it has become widely accessible [1]. It has several advantages, including machine life increase by 3–5%, reduced maintenance costs by up to 40%, and returns on investment up to 10 times [2].

One of the most relevant steps in the prediction process is the choice of the best approach for the item behaviour assessment, such as data-driven or model-driven approach [3]. In particular, according to the platform developed by Patel et al. [4] for the application of Industry 4.0 principles to the industrial reality, the data-analytic layer is crucial to understand a plant functioning. Moreover, if properly designed, it allows users to identify the presence of invisible

relations among data provided by the application layer [5]. It is also true that, according to the “no free lunch” theorems, a standard procedure for predictive maintenance does not exist. Still, it must be chosen among those that best suit the reality under analysis [6]. In any case, regardless of the adopted process, for a more accurate and optimal prediction, it is necessary to gather and analyse appropriately large amounts of data within a time frame [7, 8] with consequent problems deriving from the identification of the most accurate health indicators. The health of a system can be defined as the deviation or degradation of an item behaviour from its regular operating performance [9].

The calculation of a suitable health indicator (HI) is fundamental to establish a link between the deviation or degradation of an item and its Remaining Useful Life (RUL). Thus, an accurate HI is a key for a more precise prediction tool, guaranteeing its reproducibility [10, 11]. This



observation is the reason why many researchers focus their activity on this issue ranging from supervised and unsupervised algorithms [12, 13] to physical [14] and virtual [15] HIs.

The HI assessment needs the monitored parameters provided by the physical data from sensors to be transformed into information represented as indicators. The potential benefits include not only the reduction of the quantity of data examined but also the maximisation of the useful information content [16].

In this context, the proposed paper lays its foundations. An approach for HI definition and calculation is provided combining the Grey Wolf Optimisation (GWO) approach, belonging to the set of Swarm Intelligence algorithms, and Fuzzy Cognitive Maps (FCMs). Subsequently, the *k*-neighbors algorithms are used to predict the item RULs.

The proposed approach, in comparison to previous studies presented in the literature, does not require knowledge about the gradients of the cost function and constrained functions, guaranteeing both reliable and robust performance and easy implementation. Moreover, it ensures extreme flexibility and adaptability to a given domain. It allows an in-depth understanding of a specific issue; thanks to the possibility of symbolically representing the relationships among all the involved variables.

To present the methodology and analyse its performance, the rest of the paper is organised as follows. Section 2 briefly describes the analysed literature on Swarm Intelligence algorithms and FCMs application to predictive maintenance. Section 3, divided into three sections, focuses on the explanation of the FCMs theory and GWO algorithm functioning. It then explains the proposed algorithm steps, underlining its benefits. Section 4 shows the results obtained using a dataset provided by NASA regarding the RUL prediction for aircraft engines and compares the results with an Artificial Neural Network approach. Conclusions have been drawn in Section 5.

## 2. Literature Review

As mentioned, research on predictive maintenance has grown in recent years due to the development of Industry 4.0 technology. Hence, to gather the most relevant contributions dealing with maintenance in general and FCMs and Swarm Intelligence applications in particular, a systematical approach has been adopted. The Scopus scientific database has been selected, considering that all the papers have an available full text written in English. All articles have been read to assess their relevance and pertinence to the theme developed in this study. In Table 1, the combination of the keywords selected, the number of papers retrieved by Scopus, and the ones chosen for this literature review are reported.

In recent literature, several contributions deal with the development of HIs aiming at predicting the need for maintenance interventions. For example, some authors propose the implementation of dashboards for the monitoring of the equipment health status in the semiconductor manufacturing industry [17, 18], while others

focus on structural vibrations analysis [19] and RUL prediction [20, 21]. Various techniques and methodologies can be found in the literary contributions: for instance, Baraldi et al. [22] develop a differential evolution-based multiobjective model aiming at defining the health status of the system and adopting maintenance strategies; other authors, instead, apply artificial neural networks [23] or genetic algorithms [24] to model the health status of the system.

To the best of the authors' knowledge, there is no evidence of scientific papers dealing with predictive maintenance through the application of FCMs and Swarm Intelligence (SI) approaches. At the same time, a contribution can be found only through the application of SI methods. Li et al. [25], indeed, applied a multiclass relevant vector machine—optimised through the application of the SI dragonfly algorithm—to predict the failures of a diesel engine. Other SI applications to the maintenance field can be found in existing literature, for example, Zheng et al. [26] use the particle swarm optimisation to predict the performance degradation of aeroengines, considering aspects such as fuel consumption, rotor vibration, and thrust loss. A similar perspective is adopted by Hu et al. [27], in diagnosing the failures of a gearbox, through the particle swarm optimisation and the kernel extreme learning machine, and by Zhao and Liu [28] who solved the same class of problems through the rough set theory. Several further SI applications to the maintenance field instead focus on the definition of the maintenance scheduling [29–32]; R. [33].

Going into detail regarding the GWO algorithm, some applications in the maintenance field can be found in the literature: the majority of them focus on the cost efficiency of the maintenance processes. For example, it is applied to optimise the design and maintenance of photovoltaic power plants [34] or to minimise maintenance costs of heat and power systems [35–38]. Kumar et al. [39] focus on both the reliability and the costs of a Space Shuttle, through the implementation of a multiobjective GWO. Dalla Vedova et al. [40], instead, compare different algorithms, among which the GWO is for the RUL estimation of an aircraft actuator, while Abdelghafar et al. [41] optimise a support vector machine through the GWO to improve the detection of satellite sensor failures. Some works focus on the scheduling through the implementation of the GWO Algorithm: it can be applied to solve job shop and maintenance scheduling problems [42] as well as to block flow shop scheduling, considering fuzzy processing times and dynamic maintenance strategies [43, 44].

FCMs have proved to be useful tools in supporting the decision-making processes in the maintenance field. For instance, they can be applied to verify the impact of maintenance activities on a building's energy efficiency [37] or to identify the factors affecting human reliability during the maintenance operations [45]. According to Gupta and Gandhi [46], data coming from maintenance work orders can be used to detect possible improvement areas in terms of component design. Dynamic risk modelling is also

TABLE 1: Summary of the selected literary contributions.

Keywords	# of papers	# of relevant papers
“Predictive maintenance” and “health indicator”	25	21
“Predictive maintenance” and “Fuzzy Cognitive Map(s)” and “Swarm Intelligence”	—	—
“Predictive maintenance” and “Fuzzy Cognitive Map(s)”	—	—
“Maintenance” and “Fuzzy Cognitive Map(s)”	42	10
“Predictive maintenance” and “Swarm Intelligence”	2	1
“Maintenance” and “Swarm Intelligence”	135	9
“Predictive maintenance” and “Grey Wolf”	1	—
“Maintenance” and “Grey Wolf”	33	10

performed through the FMCs: in Lopez and Salmeron study [47], an FCM is built to assess the risk during the enterprise resource planning of maintenance processes, while in Jamshidi et al. [48], it is used to study the critical factors related to the maintenance outsourcing. Damage detection can also be performed through the FMCs. For instance, Senniappan et al. [49] propose an application for the early detection of damages in civil structures’ elements of support based on an FCM, modelling both the knowledge obtained from the domain experts and the existing literature. Instead, Lee et al. [50] use rule-based FCMs based on the experts’ knowledge and experience to identify the factors accelerating the deterioration of rubber components in order to predict the maintenance timing and structure a diagnostic process. In the work of Azadeh et al. [51], the FCM is used to assess which factors among cognitive and temporal ones have a more relevant impact on the execution of the maintenance interventions. Similarly, maintenance errors can be analysed through FCMs in order to highlight which are the most critical and repetitive ones and recommend modifications in the maintenance process or training [52]. Zhang et al. [53], instead, develop a robot dedicated to live maintenance whose behaviour is predicted through an FCM.

According to the existing contributions, there is no evidence of the joint implementation of FCMs and GWO, even though both the methodologies have been successfully applied to the maintenance field. Among the benefits harboured by the GWO, its ability to work in a dynamic environment is one of the most useful in this application field. In parallel, the FCMs are useful for the qualitative simulation of a modelled system. To sum up, the benefits harboured by the joint implementation of the two techniques proposed in this research approach are the flexibility and adaptability, as well as the reliability and robustness of the performance.

### 3. The Research Approach

The general scheme of a predictive maintenance procedure proposed in this work is shown in Figure 1 and described below.

- (i) *Preprocessing Data*. Preprocessing means the preparation of the dataset for analysis; it incorporates all the steps for dataset preparation. In this part of the process, it is essential to get as much information and indications as possible from the dataset.

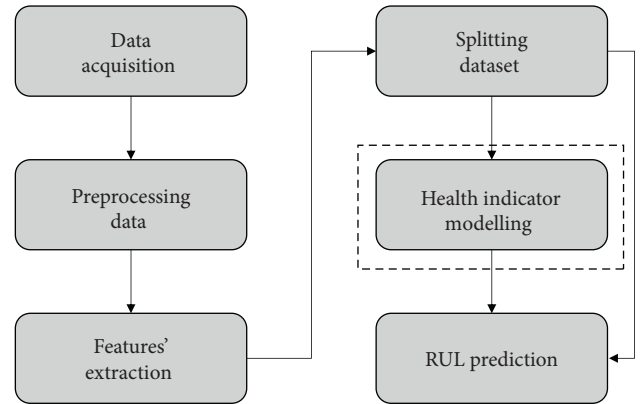


FIGURE 1: General scheme for a predictive maintenance procedure.

- (ii) *Features' Extraction*. It is the step in which variables are selected and/or the amount of data to be processed is reduced, ensuring an accurate and complete description of the original dataset.
- (iii) *Splitting Data*. This is an analytical step to understand how to train the machine learning system in the best way. As a matter of fact, within machine learning systems, there are two parts: the first is the training that, as the name may indicate, trains the course and teaches it how to act. After this step, the system is ready to perform what it has learned and to test if the training completed in the previous step was successful. This is done through the score or test. Given the significance that these two steps assume, it is of fundamental importance to understand the best way to divide the available data package in the right proportions.
- (iv) *Health Indicator Modelling*. The sensor readings, reworked in the previous steps, are combined into a single parameter called health indicator to be used in the prediction of the adverse event.
- (v) *RUL Prediction*. The RUL equipment is carried out in this work through the K-nearest neighbors classifier [54] and Weibull fitting [55].

The core activities of this work are the HI definition and RUL Prediction. The innovative proposed methodology to develop these activities will be described in depth in Section 3.1.

**3.1. The HI Modelling.** The proposed approach for the HI modelling is performed by the combined use of FCM and a Swarm Intelligence algorithm such as the GWO. Before describing the proposed approach, the FCM and GWO theories are briefly described in the following two sections.

**3.1.1. The FCMs' Modelling.** A cognitive map (CM) can be thought of as a concept map reflecting mental processing, comprised of collected information and several cognitive abstractions, individually filtered, about regarding physical phenomena and experiences [56]. Cognitive maps are visual representations of an individual's mental model constructs, analogous to concept maps for representing human reasoning and knowledge or beliefs [7]. Thus, a generic problem is considered, and an expert panel of experts is formed for its in-depth analysis, since different individuals may face the same question differently. According to their area of expertise through fuzzy logic, they model collective FCM identifying concepts and relationships about regarding the considered problem. In particular, concepts, in number of  $N$ , are the FCM key elements that stand for the main characteristics of the abstract mental model for whichever complex system [57]. Once concepts are identified, experts are asked to assign a numerical value  $w_{ij}$  (the weight of the relation between concept  $i$ th and  $j$ th) for the  $W$  matrix, which represents the influence of concept  $C_i$  on concept  $C_j$ . According to equation (1),  $w_{ij}$  ranges in  $[-1, 1]$ . Specifically,  $w_{ij} = 0$  indicates no causality between concepts,  $w_{ij} > 0$  indicates causal  $C_j$  increases as  $C_i$  increases (or  $C_j$  decreases as  $C_i$  decreases), and  $w_{ij} < 0$  shows causal decrease or negative causality ( $C_j$  decreases as  $C_i$  increases or  $C_j$  increases as  $C_i$  decreases):

$$\text{FCM} = \begin{bmatrix} w_{1,1} & \cdots & w_{1,N} \\ \vdots & \ddots & \vdots \\ w_{N,1} & \cdots & w_{N,N} \end{bmatrix}. \quad (1)$$

Although many studies exist concerning the dynamical representation of an FCM, generally, the experts' opinion aggregation of expert opinions for the collective weight matrix modelling is performed using the SUM method [58]. Then, overall linguistic weight is evaluated using the centre of gravity (COG) defuzzification method [59]. Some examples are presented by Bevilacqua et al. [7, 60, 61] and Stylios et al. [62] where a unique credibility value is assigned to each expert and a threshold function is used in the aggregation. On the contrary, a modification of the approach mentioned above has been provided by Stylios and Groumpos [63] and Stylios and Groumpos [64], introducing a corrective factor for the experts' credibility evaluation. However, this approach does not take into consideration the fact that, in a complex multidisciplinary problem, most experts have in-depth knowledge of only parts of the problem and not the entire issue [65].

Once the total weights' matrix,  $W$ , has been designed, it is possible to analyse the system behaviour through simulations. Thus, if  $A_i$  defines the instantaneous value of concept

$C_i$ , its evolution over time can be evaluated computing the influence of the related concepts  $C_j$  on the specific concept  $C_i$  according to

$$A_i^{k+1} = f \left( A_i^k + \sum_{\substack{j=1 \\ j \neq i}}^n A_j^k w_{i,j} \right), \quad (2)$$

where  $A_i^{k+1}$  is the value of concept  $C_i$  at simulation step  $k+1$  and  $A_j^k$  is the value of concept  $C_j$  at simulation step  $k$ . Also,  $w_{ij}$  is the weight of the interconnection from concept  $C_j$  to concept  $C_i$  and  $f$  is an appropriate threshold function used to force the concept value to be monotonically mapped into a normalised range [66]. Other equations can be used in place of equation (2) as suggested by Mazzuto et al. [67] and Osoba and Kosko [68].

An important topic in the FCM analysis is the indirect and total causal effect evaluation (Axelrod, 1976), whose knowledge allows an in-depth map analysis. The indirect effect  $I_k$  of  $C_i$  concept on  $C_j$  concept can be defined as shown in

$$I_k(C_i, C_j) = \min \{w(C_p, C_{p+1})\}. \quad (3)$$

$I_k$  is defined as the minimum numerical of the  $w_{ij}$  weight along a single path between concepts  $i$ th to  $j$ th. At the same time, the total causal effect  $T(C_i, C_j)$  (equation (4)) is the maximum of the indirect effect of concept  $C_i$  on concept  $C_j$ :

$$T(C_i, C_j) = \max \{I_k(C_p, C_{p+1})\}. \quad (4)$$

According to Bevilacqua et al. [7], equation (3) can be described using the "weak ring in the chain" metaphor. Indeed, it is necessary for the identification of ATO identify concept concatenation as a chain where the weight  $w_{ij}$  is the hardness of each chain ring. In the presence of a weak ring into the chain, it is not possible to consider it as a "resistant chain," and its total hardness is quantified with the hardness of the weak ring. Therefore, once derived the value of hardness is derived from by equation (3), and equation (4) allows defining the more resistant chain to be defined. Finally, the chain hardness highlights the relevance of the first concept in the concatenations affecting the top event.

In the proposed approach, the concepts of the FCM represent the working conditions of the component to be analysed, the sensor signals installed on the components, and the HI of the component. The FCM takes the advantage of the situation to identify the relationships among all the involved concepts in a matrix form to be used to calculate the health indicator for the RUL prediction.

**3.1.2. The GWO Algorithm.** Mirjalili et al. [69] introduced the GWO, which mimics the hierarchy of leadership and the mechanism for hunting grey wolf packs in the wild. The algorithm divides the agents (grey wolves) into four different hierarchical categories called alpha ( $\alpha$ ), beta ( $\beta$ ), delta ( $\delta$ ), and omega ( $\omega$ ), in the descending order.

Each hierarchy has different roles to find solutions, which in this case correspond to the prey. The leaders of the packs are the wolves called alphas. The alpha is primarily responsible for decisions about hunting, where to sleep, and so on. The alpha wolf is the dominant one, and the pack must follow his orders. The beta wolves identify the second level in the hierarchy. They are subordinate wolves that help the alpha in decision-making or other pack activities. Moreover, a beta wolf must not only respect the alpha but also command other lower level wolves.

The lower level grey wolf is the omega. The  $\omega$  plays the role of scapegoat, and it helps to satisfy the entire pack and maintain the dominant structure. Omega wolves must always submit themselves to all other dominant wolves. It may seem that the omega is not an essential individual in the pack, but it is also true that the entire pack faces internal struggles and problems if the omega is lost. If a wolf is not an alpha, beta, or omega, it is called a subordinate (or delta in some references). Delta wolves must submit themselves to alphas and betas, but dominate omegas. Scouts and hunters, for example, belong to this category. They are responsible for guarding the boundaries of the territory and warning the pack in case of danger. Hunters help the alphas and betas to hunt prey and provide food.

To mathematically model the social hierarchy of wolves in the GWO design,  $\alpha$  is therefore considered the most suitable (optimal) solution. Consequently, the second- and third-best solutions are named  $\beta$  and  $\delta$ , respectively. The remaining candidate solutions are the  $\omega$  ones.

In the GWO algorithm,  $\alpha$ ,  $\beta$ , and  $\delta$  wolves impose the rules of hunting and the  $\omega$  ones follow them. In particular, the hunt is composed of three main phases such as (i) searching and chasing prey, (ii) surrounding and harassing the victim until it stops moving, and, finally, (iii) attacking the prey.

After spotting the possible prey, the wolves begin to surround it and then move on to the attack. Equations (5) and (6) model mathematically encirclement behaviour:

$$D = |C \cdot x_p(t) - x(t)|, \quad (5)$$

$$x(t+1) = x_p(t) - A \cdot D, \quad (6)$$

where  $D$  represents the difference between the position of the prey and the predator,  $t$  denotes the current iteration,  $x_p$  specifies the location of the victim, and  $x$  indicates the wolf location. Equations (7) and (8) allow one to calculate the  $A$  and  $C$  values:

$$A = 2 \cdot a \cdot r_1 - a, \quad (7)$$

$$C = 2 \cdot r_2, \quad (8)$$

where the components of  $a$  linearly decrease from 2 to 0 during each iteration and  $r_1$  and  $r_2$  are random arrays with ranging in  $[0, 1]$ , and they allow wolves to reach any position between the points, as illustrated in Figure 2.

As shown in Figure 2(a), a wolf in position  $(X, Y)$  can update its location according to the prey's position  $(X^*, Y^*)$ , and the same consideration is possible in 3D space (Figure 2(b)), or in  $n$  dimension space.

It is assumed that alpha (best candidate solution), beta, and delta have a better knowledge of the potential position of the prey to simulate the hunting behaviour of wolves mathematically. Therefore, the first three best solutions are considered, and the other search agents (omega wolves) are obliged to update their positions according to the location of the best search agent [70].

As mentioned above, wolves end the hunt by attacking their prey when it stops moving. If  $|A| < 1$ , the wolves begin the attack phase by moving towards the victim. Wolves look for prey mainly based on alpha, beta, and delta positions. In this phase of research (exploration), the wolves move away from each other to identify the different places of the prey (solutions). The vector  $A$  assumes values higher than one or less than  $-1$  and forces the research agent to diverge from the victim. This emphasises the exploration and allows the GWO algorithm to search globally to find better prey. Thus, once  $\alpha$ ,  $\beta$ , and  $\delta$  wolves are identified, all of the members' pack positions are updated according to

$$\begin{aligned} D_\alpha &= |C_1 \cdot x_\alpha(t) - x(t)|, \quad D_\beta = |C_2 \cdot x_\beta(t) - x(t)|, \\ D_\delta &= |C_3 \cdot x_\delta(t) - x(t)|, \end{aligned} \quad (9)$$

$$\begin{aligned} x_1(t+1) &= x_\alpha(t) - A_1 \cdot D_\alpha, \quad x_2(t+1) = x_\beta(t) - A_2 \\ &\cdot D_\beta, \quad x_3(t+1) = x_\delta(t) - A_3 \cdot D_\delta, \end{aligned} \quad (10)$$

$$x(t+1) = \frac{x_1(t+1) + x_2(t+1) + x_3(t+1)}{3}. \quad (11)$$

Figure 3 describes the step to implement the GWO according to the mentioned equations.

The GWO has the advantage of having few parameters to initialise and be a flexible algorithm, so it can adapt to various practical engineering problems. Indeed, only the number of wolves in the pack ( $nPop$ ) and the maximum number of iteration ( $MaxIt$ ) must be initialised. In Figure 3,  $Iter$  is the current iteration. Moreover, the GWO can be easily implemented, and thanks to its hierarchical structure, which guarantees high accuracy in the solution.

Although recently introduced, the GWO has been used in various fields of application. Das et al. [71] have tested the GWO to optimise the parameters of a PID controller used for speed control of a DC motor system. Komaki and Kayvanfar [72] proposed the application of GWO to program the optimal machining and assembly sequence to minimise the completion time. The results obtained with this algorithm were then compared with other methods. This comparison revealed that the GWO provided better performance. Nguyen et al. [73] used a multiobjective GWO to solve the problem of node location in a wireless sensor network. Various constraints were considered in the



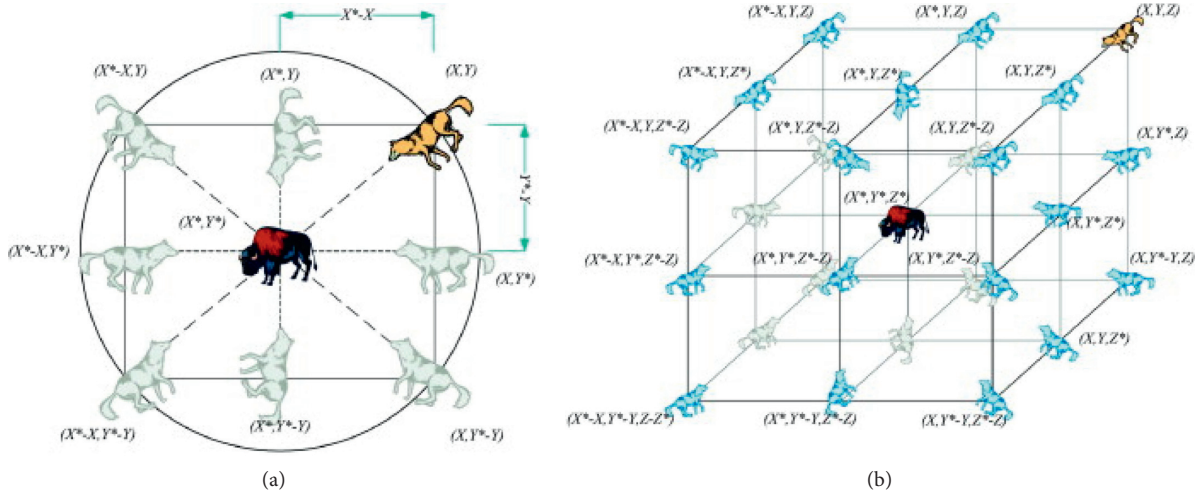


FIGURE 2: The pack hunting scheme [69].

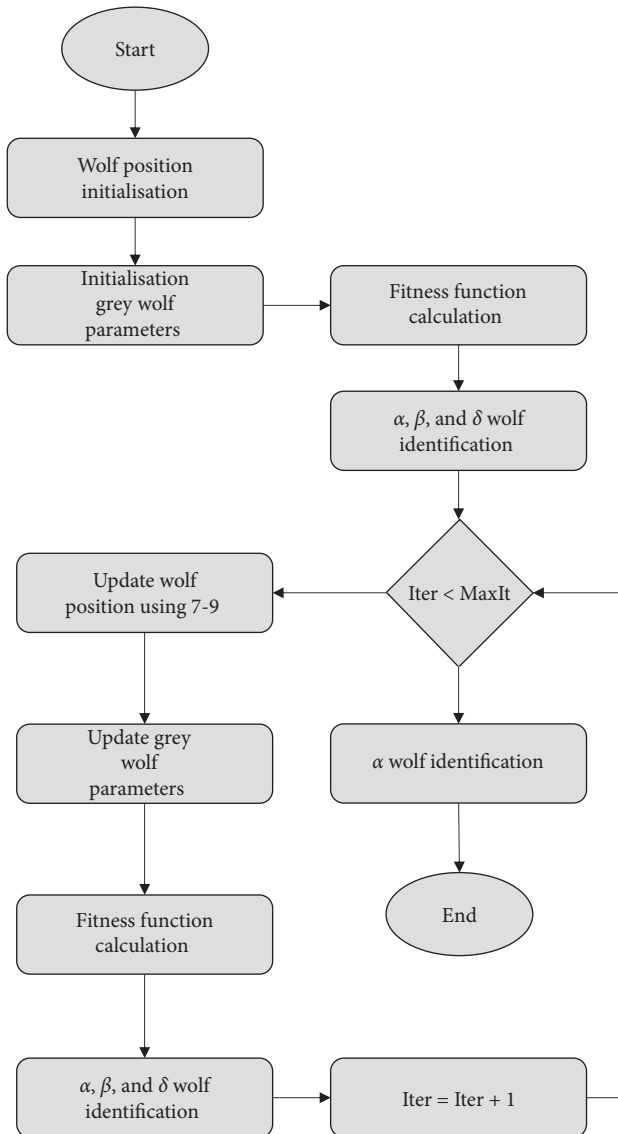


FIGURE 3: The Grey Wolf flowchart.

localisation model, including the limitation of spatial distance between nodes and the restriction of topology. The results of the simulations show significant improvements in terms of localisation accuracy and rate of convergence to the optimal solution, compared to those obtained with other methods. Song et al. [74] used GWO to estimate the parameters of Rayleigh Waves (a type of elastic surface wave).

However, the research and development activities for this algorithm are still at an early stage [75]. As previously stated, the GWO has a strong exploration capacity, which can avoid convergence in excellent premises. This feature may lead the algorithm to slow convergence and indeed led us to try GWO to define the  $w_{ij}$  values of the FCM.

**3.1.3. The K-Nearest Neighbors Algorithm.** An in-depth analysis of the k-nearest neighbors (KNN) algorithm allows underlining as it is simple and easy-to-implement supervised machine learning algorithm used to solve both classification and regression problems. Its functioning is based on the similarity of the characteristics: the closer an instance is to a data point, the more KNN will consider them similar [76].

Once the HIs have been defined for each training unit, they can be used as models representing the degradation profile, from normal functioning to disruption. At this point, a set of models  $M_i$  (with  $i = 1$  to the number of items composing the training dataset) is available and usable to predict the RUL. Therefore, to find the most similar element, it is necessary to measure the distance between the model  $M_i$  and  $Y = y_1, y_2, \dots, y_r$ , which represents the HI of the test unit obtained through consecutive observations. The distance is calculated by the Euclidean distance (depending on the problem under examination) or by the mean value of the absolute residual (used in the proposed approach), as described by equations (11) and (12). Thus, the smaller the distance, the greater the similarity between the data point and the instance to be predicted:

$$d(x_i, x_l) = \sqrt{(x_{i1} - x_{l1})^2 + (x_{i2} - x_{l2})^2 + \dots + (x_{ip} - x_{lp})^2}, \quad (12)$$

$$d(x_i, x_l) = \text{mean}(|y_i - y_l|), \quad (13)$$

where  $y_i$  is  $i$ th training model and  $y_l$  is the  $l$  th testing one, and each of them is composed of  $x_i$  and  $x_l$  components.

Then, the calculated distances are used as the argument to evaluate the similarity weight,  $sw_{i,l}$ , between the testing HI and all of the training ones considering

$$sw_{i,l} = \exp(-d(x_i, x_l)^2). \quad (14)$$

Once obtaining the similarity weights among the testing unit and training ones, it is possible to rank them in descending order and identify the number of similar unit SU as described in

$$SU = \min(k, N), \quad (15)$$

where  $N$  is the number of training units and  $k$  is an initial fixed value. In particular, when  $k$  is small, it is limiting the prediction region, forcing the classifier to be “more blind” than the general distribution. On the contrary, a large  $k$  reduces the impact of the variance caused by a random error but runs the risk of ignoring small details that might be relevant. For the proposed approach, initially,  $k$  is fixed equal to 50. Thus, having similar units, it is possible, considering the relative end dates updated to the number of test samples, to fit a Weibull distribution to find the RUL.

**3.1.4. The Procedure for HI Assessment.** Figure 4 shows the framework used to esteem the aircraft engine HIs and, subsequently, to predict the RUL of the engine. The proposed algorithm can be classified within the condition monitoring techniques. It consists of a general framework and can be applied to any equipment. The dataset, both training and testing, are composed of the sensor readings of the considered items.

In the “*Time Indicator Modelling*” phase, a lifetime indicator (*LTI*) is defined. The sample number of each piece of equipment (that corresponds to the number of rows of the dataset) represents its life duration.

The main idea of *LTI* is to model a degradation profile considering that, at the beginning of sampling, an item has the maximum reliability value (equal to 1), and when the disruption occurs, the item reliability has a minimum amount (equal to 0). The first value of *LTI* is equal to 1, and the last one is equal to zero, according to

$$TI_m' = [DU R_m - 1 \quad DU R_m - 2 \quad \dots \quad 0], \quad (16)$$

$$TI_m(t)' = \frac{TI_m(t)}{DU R_m}, \quad (17)$$

$$LTI_m(t) = TI_m(t)'' + (1 - TI_m(t = 1)''), \quad (18)$$

where  $DUR_m$  is the dataset length for the  $m$ th equipment. Each element of  $TI_m$  indicates the remaining cycle times to the relative disruption at time  $t$  (then normalised in  $TI_m$ ). Hence, each value of  $LTI_m$  decreases from 1 to 0.  $LTI_m$  represents the parameter to be esteemed and used in the algorithm for the HI estimation. Table 2 shows an example of *LTI* calculation.

The “*FCM Modelling*” phase is the core of the proposed approach to identify the HI. Figure 5 describes the iterative phase for the HI calculation reviewing the general GWO algorithm shown in Figure 3. In particular, the GWO algorithm is used for defining the weight of the relation between concept  $i$ th and  $j$ th ( $w_{ij}$  values) of the FCM matrix. The concepts of the FCM represent the working conditions of the equipment to be analysed, the sensor signals installed on the equipment, and the last concept which is the HI. In particular, since the purpose of the approach is the HI estimation using the FCM theory, the number of concepts (*NC*) to be used is equal to the number of reduced dataset variables' number plus the HI (the algorithm output). This means that if the reduced dataset variables number is  $n$ ,  $NC = n + 1$ .

The iterative phase, shown in Figure 5, is executed for each equipment belonging to the training dataset. In each iteration, the final  $\alpha$  wolf position is assumed as the temporary  $FCM_j$  and used as initial  $FCM$  for the next one. When the terminal equipment has been analysed, the relative  $FCM$  is considered as the optimal solution.

The GWO algorithm is used to define the  $w_{ij}$  values of FCM. These values randomly in the range  $[-1 \ 1]$  or  $[0 \ 1]$ , as required by the FCM theory, for each pack member. Then, equation (1) calculates the relative cost. By analysing Figure 5, it is possible to highlight how the lifetime indicator and the reduced dataset are used as input for the fitness function calculation.

Assuming to have a reduced training dataset related to  $M$  equipment, with  $n$  main variables, it is divided in  $M$  reduced subdataset, each one related to a specific equipment. Thus, a reduced subdataset  $RD_m$  (the sensors' readings of equipment  $m$  with  $m = 1, 2, \dots, M$ ) is available with the relative  $LTI_m$ , in the form expressed in

$$RD_m = \begin{bmatrix} Var_{1,1}^m & \dots & Var_{n,1}^m \\ \vdots & \ddots & \vdots \\ Var_{1,f}^m & \dots & Var_{n,f}^m \end{bmatrix}, \quad LTI_m = [lti_1 \quad \dots \quad lti_f]. \quad (19)$$

The term  $f$  identifies the instant in which the fault occurred;  $n$  represents the progressive number of the main reduced variables, and  $m$  is the number of considered equipment.

The pack members' position, obtained through the GWO application for a specific device, is given in the form of

$$FCM_{p,m}^{iter} = \begin{bmatrix} w_{1,1} & \dots & w_{1,NC} \\ \vdots & \ddots & \vdots \\ w_{NC,1} & \dots & w_{NC,NC} \end{bmatrix}, \quad (20)$$

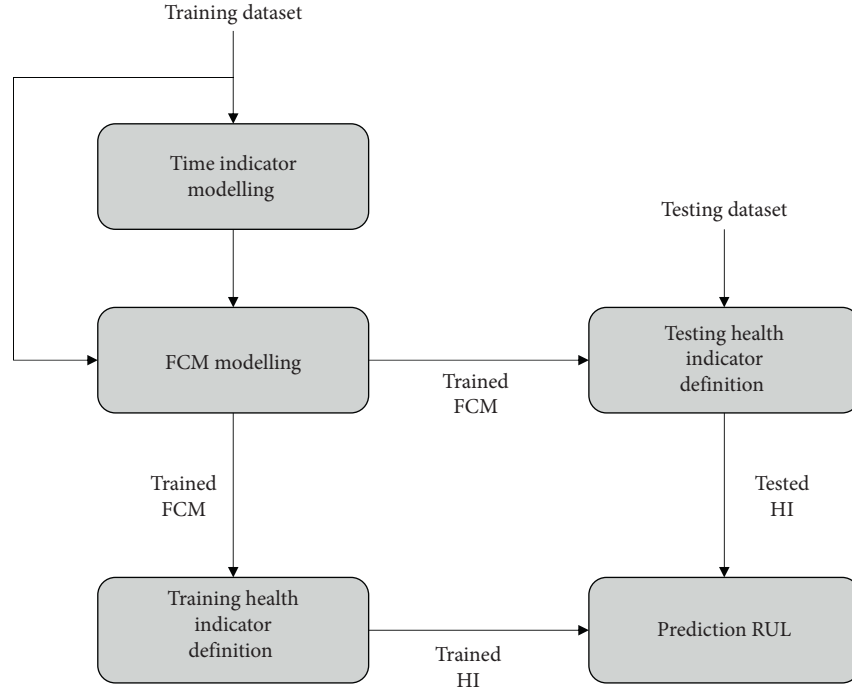


FIGURE 4: The proposed framework approach.

TABLE 2: An example of equations (16)–(18) application.

Steps description	Equation application
Suppose machine 1 breaks after 10 sampling cycles; it follows that $DU R_1 = 10$ , according to equation (16)	$TI'_1 = [9 \ 8 \ 7 \ 6 \ 5 \ 4 \ 3 \ 2 \ 1 \ 0]$
According to equation (17), the relative normalised value	$TI^s_1 = [0.9 \ 0.8 \ 0.7 \ 0.6 \ 0.5 \ 0.4 \ 0.3 \ 0.2 \ 0.1 \ 0]$
According to equation (18), the lifetime indicator	$LTI_1 = [1 \ 0.9 \ 0.8 \ 0.7 \ 0.6 \ 0.5 \ 0.4 \ 0.3 \ 0.2 \ 0.1]$

where  $p$  is the  $p$ th member of the pack ( $p = 1, 2, \dots, nPop$ ),  $iter$  is the current iteration with  $iter \leq MaxIt$ , and  $NC$  is the concepts number for the FCM algorithm defined before. Thus,  $FCM^{iter}_{p,m}$  is the relative position of the  $p$ th pack member at the current iteration for the  $m$ th equipment.

By analysing Figure 5, it is possible to highlight the presence of two main “for loop.” The first one (external) is referred to the number of available equipment ( $M$ ) and the second one (internal) to the maximum iteration number for GWO ( $MaxIt$ ).

At each iteration of the external loop (the iteration is equal to the equipment number in the dataset), the LTI related to a specific item is used as the benchmark for the positional cost calculation (if the iteration is equal to one, the  $LTI_1$  is examined). This means that the external loop has the objective of identifying the best  $FCM_m$  for the  $m$ th equipment. In the internal loop, for the GWO application, all the pack members take a position within the domain space, updating it at each inner iteration. At the end of the inner loop, the best position for the considered

item is identified ( $FCM_m$ ). The obtained  $FCM_m$  is used as the initial position for the  $FCM_{m+1}$  identification (as long as  $m < M$ ) to improve its accuracy.

In the algorithm initialisation,  $FCM_1^0$  can be defined randomly if there is no knowledge of the involved equipment or a panel of experts cannot be established to model it, as described for the classical FCM design approach, according to the experience of each professional involved.

As mentioned before, equation (1) evaluates the fitness cost value for each  $FCM^{iter}_{p,m}$ . This step is the most critical in the whole algorithm, as highlighted by Mazzuto and Stylios [77]. Indeed, to calculate the cost connected to  $FCM^{iter}_{p,m}$ , it is necessary to consider all of the samples which make up  $RD_m$  and  $LTI_m$ . More accurately, if  $RD_m$  has  $f$  samples (as described above) as well as  $LTI_m$ , equation (1) has to be applied  $f$  times. Besides, since the number of iteration ( $k$ ) in equation (1) depends on the function convergence or the fixed amount of repetition ( $FCMiter$ ), the fitness cost evaluation requires an iteration number equal to  $(f \cdot FCM_{iter})$ . Considering  $nPop$  wolves and a maximum

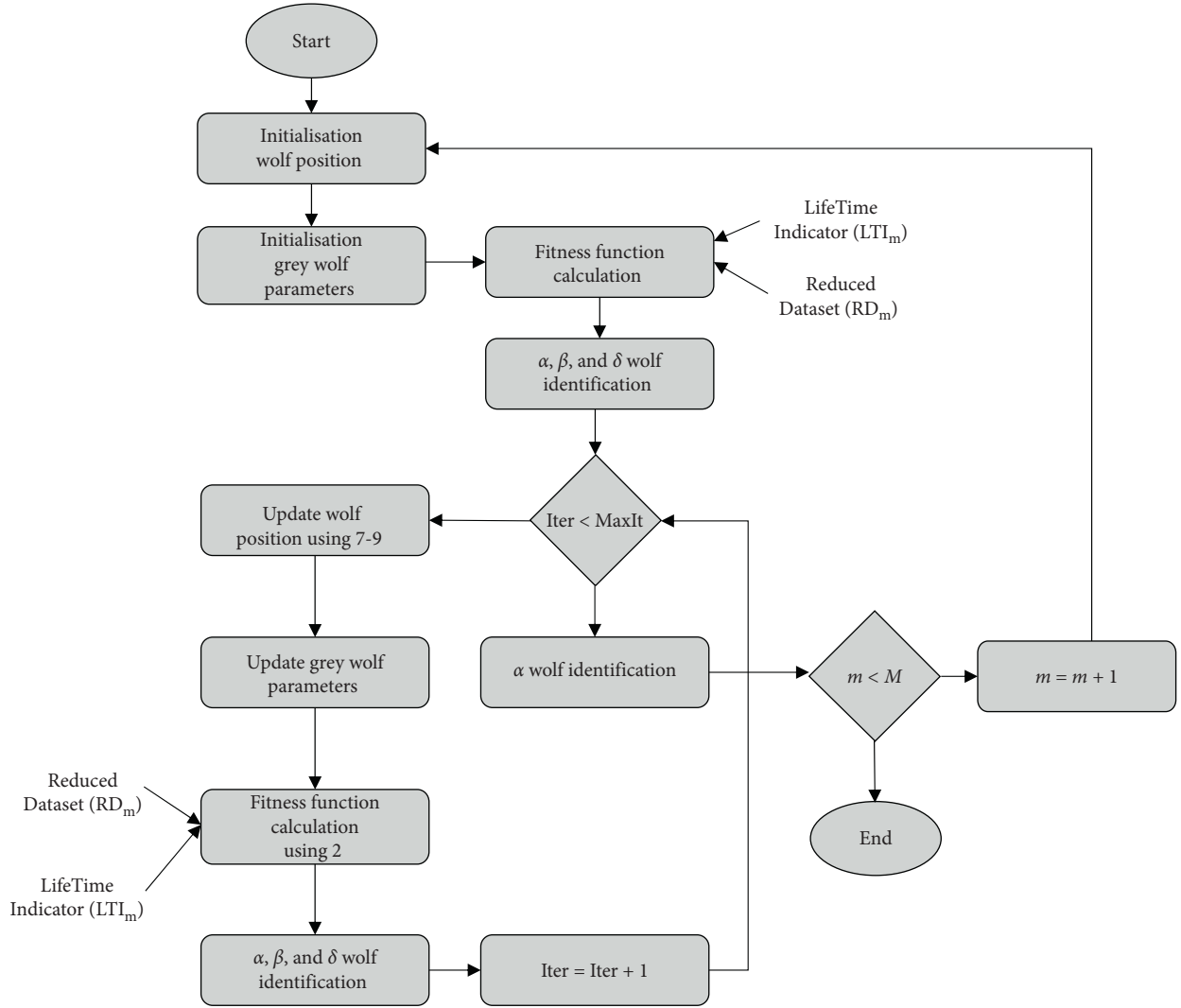


FIGURE 5: Framework of the proposed methodology.

iteration number for the GWO ( $MaxIt$ ), the total number of iterations for the identification of the optimal FCM is equal to  $(f \cdot FCM_{iter}) \cdot nPop \cdot MaxIt$ .

Considering the  $p$ th pack member, once its position is defined ( $FCM_{p,m}^{iter}$ ), its positional cost has to be calculated according to equation (1) for the best position identification.

The main idea is to consider each sample in the reduced dataset for a specific item ( $RD_m$ ) as the initial array  $A^0$  at the specified iteration according to

$$A_m^{0,j} = [\text{Var}_{1,j}^m \dots \text{Var}_{n,j}^m \ 0], \quad 4j = 1, 2 \dots f, \quad m = 1, 2 \dots M. \quad (21)$$

The null value is because the output is considered within the set of FCM concepts, but it is the variable that needs to be taken into consideration.

When the application of equation (1) reaches the convergent,  $A_m^{*,j}$  will be described by

$$A_m^{*,j} = [\widehat{\text{Var}}_{1,j}^m \dots \widehat{\text{Var}}_{n,j}^m \ HI_m^{*,j}], \quad (22)$$

$$j = 1, 2 \dots f, \quad m = 1, 2 \dots M,$$

where  $\widehat{\text{Var}}_{1,j}^m$  is the convergent value for the variable  $\text{Var}_{1,j}^m$  and  $HI_m^{*,j}$  is the esteemed output for the sample at time  $j$  for the  $m$ th engine.

Once all of the samples in  $RD_m$  have been processed, a final output array  $HI_{p,m}^*$  for the  $p$ th pack member, equation (23), will be available:

$$H_{p,m}^* = [HI_m^{*,1} \ HI_m^{*,2} \ \dots \ HI_m^{*,f}], \quad f, \quad m = 1, 2 \dots M. \quad (23)$$

Thus, the esteemed output  $HI_{p,m}^*$  and the connected  $LTI_m$  can be used to calculate the fitness cost value ( $C_{p,m}^{iter}$ ), for the  $p$ th pack member and the  $m$ th item and at iteration  $iter$ , using the root mean squared error formula, as shown in

$$C_{p,m}^{\text{iter}} = \sqrt{\frac{\sum_{j=1}^f (LTI_m^j - H_{p,m}^{*,j})^2}{f}} \quad (24)$$

The root mean square error has been chosen because it describes efficiently how concentrated the data is around the line of best fit [78].

Finally, once the optimal FCM to be used for the HI identification phases is identified, it is used to calculate the HIs in the “*Training Health Indicator definitions*” and “*Testing Health Indicator definitions*,” respectively.

#### 4. Research Approach Application

To explain the proposed approach and to test its accuracy for HI modelling, the Turbofan Engine Degradation Simulation Dataset has been used. It is available online on the NASA repository website (<https://ti.arc.nasa.gov/tech/dash/groups/pcoe/prognostic-data-repository/>, last access July 21, 2020).

The aircraft gas turbine engine has an integrated control system, which consists of a fan-speed controller and a set of controllers and limiters. In particular, it includes three high-limit regulators aimed at preventing the engine from exceeding its designed parameters [79].

Several categories of signals could be used, including temperature, pressure, speed, and air ratio to monitor the condition of the aircraft gas turbine engine. The dataset is composed of 21 sensors installed in the aircraft engine’s different components, allowing the health conditions of the aircraft engine to be monitored (see Figure 6). An excerpt of the used dataset is shown in Table 3. To have a complete view of the dataset, it is possible to refer to Saxena et al. [79] and Xu et al. [80].

The training dataset is made up of readings from 249 engines (for a total of 61249 rows and 26 columns), while the testing dataset is made up of data from 248 engines (for a total of 41214 rows and 26 columns). The approach evaluation has been carried out using Matlab 2019© installed on a Intel® Core™ i7-6700HQ CPU @ 2.60 GHz.

The results of the proposed approaches have been compared to those obtained using an artificial neural network, due to the similarity between the Artificial Neural Network (ANN) and FCM, in order to evaluate the performance of these approaches. In light of this, to have comparable results, the initial dataset has been standardised according to the working conditions and then reduced through the trendability analysis [21] to guarantee the impartiality of the data suitability obtained with the two approaches. The reduced dataset has been used as input for the proposed approach and the ANN. More specifically, according to Figure 6, the number of reduced sensors is equal to 8, such as 2, 3, 4, 8, 9, 11, 13, and 17 (see Table 4).

These sensors will be the concepts for the realised FCM and the input for the ANN. Table 5 shows the nomenclature used for each sensors, the concepts in FCM, and the input of the ANN.

**4.1. The Proposed Approach Results.** Once the training dataset has been reduced, for each engine, according to

Index	Symbol	Description	Units
1	T2	Total temperature at fan inlet	°R
2	T24	Total temperature at LPC outlet	°R
3	T30	Total temperature at HPC outlet	°R
4	T50	Total temperature at LPT outlet	°R
5	P2	Pressure at fan inlet	Psia
6	P15	Total pressure in bypass-duct	Psia
7	P30	Total pressure at HPC outlet	Psia
8	Nf	Physical fan speed	rpm
9	Nc	Physical core speed	rpm
10	Epr	Engine pressure ratio	—
11	Ps30	Static pressure at HPC outlet	Psia
12	Phi	Ratio of fuel flow to Ps30	pps/psi
13	NRf	Corrected fan speed	rpm
14	NRc	Corrected core speed	rpm
15	BPR	Bypass ratio	—
16	farB	Burner fuel-air ratio	—
17	htBleed	Bleed enthalpy	—
18	Nf_dmd	Demanded fan speed	rpm
19	PCNfr_dmd	Demanded corrected fan speed	rpm
20	W31	HPT coolant bleed	lbm/s
21	W32	LPT coolant bleed	lbm/s

°R	The Rankine temperature scale
Psia	Pounds per square inch absolute
rpm	Revolutions per minute
pps	Pulse per second
psi	Pounds per square inch
lbm/s	Pound mass per second

FIGURE 6: Sensors implemented in the aircraft engine [80].

equations (16)–(18), the relative LTI array has been calculated (see Figure 7) to be used as output in the proposed approach regarding the positional cost definition.

As far as the proposed approach is concerned, as mentioned in Section 3.1.3, it can be initialised either using an FCM design referring to the experience of an expert panel or with a random matrix to be iteratively corrected. Due to the lack of availability of the experts concerning the aircraft engine knowhow, for the examined case study, a random initial FCM has been adopted.

Since the training dataset is composed of 249 engines, the entire process has been carried out for 249 iterations during which the FCM obtained in the previous iteration is corrected. Figure 8 shows the convergence curves during the algorithm iterations and highlights the final value of the last curve that shows the minimum root mean square error equal to 1.6117. Moreover, concerning the application of equation (2), the hyperbolic tangent function has been chosen as the threshold function  $f()$  with slope factor equal to 1. The maximum number of iterations for the positional cost calculus has been fixed equal to 50 and an additional threshold value, equal to 10–3, has been defined to potentially arrest the algorithm. The required training time to identify the final FCM has been calculated to be equal to 15 minutes due to the large numbers of samples composing the dataset.

Table 6 shows the final  $w_{ij}$  values among the concepts of the optimal FCM and the output of the proposed algorithm. The last row shows all null values being the last concept C9, the HI, an output concept.

Analysing Table 6, it is possible to highlight the presence of some low values (less than 0.1). It would be possible to filter the final FCM so that these values could be considered null to facilitate the HI calculus. However, the additional filtering phase adds to the entire process a delay factor since the user



TABLE 3: An excerpt of the training dataset referring to Engine 1.

Id engine	Cycle	Working conditions			Sensors													
		1	2	3	1	2	3	4	5	6	7	8	9	...	19	20	21	
1	1	42.0	0.8	100.0	445.0	549.7	1343.4	1112.9	3.9	5.7	137.4	2211.9	8311.3	...	100.0	10.6	6.4	
1	2	20.0	0.7	100.0	491.2	606.1	1477.6	1237.5	9.4	13.6	332.1	2323.7	8713.6	...	100.0	24.4	14.7	
1	3	42.0	0.8	100.0	445.0	549.0	1343.1	1117.1	3.9	5.7	138.2	2211.9	8306.7	...	100.0	10.5	6.4	
1	4	42.0	0.8	100.0	445.0	548.7	1341.2	1118.0	3.9	5.7	138.0	2211.9	8312.4	...	100.0	10.5	6.4	
1	5	25.0	0.6	60.0	462.5	536.1	1255.2	1033.6	7.1	9.0	174.8	1915.2	7994.9	...	84.9	14.0	8.7	
1	6	35.0	0.8	100.0	449.4	554.8	1352.9	1117.0	5.5	8.0	193.8	2222.8	8340.0	...	100.0	14.9	8.9	
1	7	0.0	0.0	100.0	518.7	641.8	1583.5	1393.9	14.6	21.6	552.5	2387.9	9050.5	...	100.0	38.9	23.5	
1	8	42.0	0.8	100.0	445.0	549.1	1344.2	1110.8	3.9	5.7	137.1	2211.9	8307.3	...	100.0	10.6	6.3	
1	9	42.0	0.8	100.0	445.0	549.6	1342.9	1101.7	3.9	5.7	138.0	2211.9	8307.8	...	100.0	10.6	6.3	
1	10	25.0	0.6	60.0	462.5	536.4	1251.9	1041.4	7.1	9.0	174.7	1915.2	8005.8	...	84.9	14.3	8.6	
1	11	20.0	0.7	100.0	491.2	606.9	1478.0	1233.1	9.4	13.6	333.2	2323.7	8709.6	...	100.0	24.6	14.7	
1	12	35.0	0.8	100.0	449.4	554.5	1366.0	1122.7	5.5	8.0	193.7	2222.8	8337.5	...	100.0	14.7	8.9	
1	13	25.0	0.6	60.0	462.5	536.3	1257.8	1040.9	7.1	9.0	174.5	1915.3	8000.1	...	84.9	14.4	8.6	
1	14	20.0	0.7	100.0	491.2	607.3	1470.3	1242.4	9.4	13.6	333.7	2323.7	8714.4	...	100.0	24.3	14.7	
...	...	...	...	...	...	...	...	...	...	...	...	...	...	...	...	...	...	

TABLE 4: An excerpt of the reduced and normalised training dataset referred to Engine 1.

Id engine	Cycle	Sensors								
		2	3	4	8	9	11	13	17	
1	1	0.435	-1.385	-1.282	-0.608	-0.877	-1.207	-0.386	-0.327	
1	2	-2.472	-0.888	-1.357	-1.660	-0.878	-1.416	-1.907	-2.277	
1	3	-1.137	-1.432	-0.825	-0.357	-1.126	-1.311	-0.464	-0.929	
1	4	-1.675	-1.717	-0.716	-0.524	-0.821	-1.242	-0.270	-1.531	
1	5	-1.655	-0.935	-1.763	-0.911	-1.441	-0.861	-1.032	-1.272	
1	6	-1.637	-1.837	-1.298	-1.059	-0.894	-1.579	-0.976	-2.293	
1	7	-1.296	-0.753	-1.167	-1.106	-0.674	-1.691	-1.305	-0.970	
1	8	-0.922	-1.274	-1.521	-0.357	-1.095	-1.520	-0.464	-0.929	
1	9	0.155	-1.472	-2.530	-0.440	-1.066	-2.076	-0.347	-1.531	
1	10	-1.007	-1.506	-0.723	-0.863	-0.621	-1.856	-0.808	-1.272	
1	11	-0.879	-0.826	-1.855	-1.466	-1.102	-1.698	-1.433	-1.087	
1	12	-2.132	0.199	-0.637	-1.020	-1.037	-1.543	-1.012	-1.063	
1	13	-1.085	-0.487	-0.789	-0.626	-1.055	-1.110	-0.763	-1.272	
1	14	-0.013	-1.985	-0.805	-1.368	-0.836	-1.487	-1.338	-0.492	
1	15	-1.603	-0.284	-1.235	-0.863	-0.688	-1.069	-0.897	-1.969	
1	16	-2.315	-1.459	-0.353	-1.514	-0.689	-1.769	-1.291	-2.277	
1	17	-1.741	-2.353	-1.497	-1.383	-1.152	-1.489	-1.470	-0.721	
1	18	-0.125	-1.193	-1.179	-0.273	-1.001	-1.172	-0.425	-0.929	
1	19	-1.331	-1.684	-1.330	-1.612	-1.076	-1.275	-1.575	-1.087	
1	20	-1.705	-0.936	-1.622	-1.612	-0.877	-1.275	-1.670	-1.087	
1	21	-1.627	-1.728	-0.751	-5.281	-1.553	-1.015	-5.341	-1.550	
1	22	-0.348	-1.623	-1.684	-1.514	-1.505	-1.557	-1.670	-1.087	
1	23	-1.160	-1.553	-1.431	-1.039	-1.070	-1.319	-1.036	-1.550	
1	24	-1.707	-1.503	-1.862	-0.721	-1.158	-1.027	-0.763	-2.666	
1	25	-0.771	-1.574	-1.050	-0.566	-1.165	-1.172	-0.502	-0.929	
...	...	...	...	...	...	...	...	...	...	

TABLE 5: Sensors nomenclature for FCM and ANN approaches.

	Sensor 2	Sensor 3	Sensor 4	Sensor 8	Sensor 9	Sensor 11	Sensor 13	Sensor 17
FCM id	C1	C2	C3	C4	C5	C6	C7	C8
ANN id	I1	I2	I3	I4	I5	I6	I7	I8

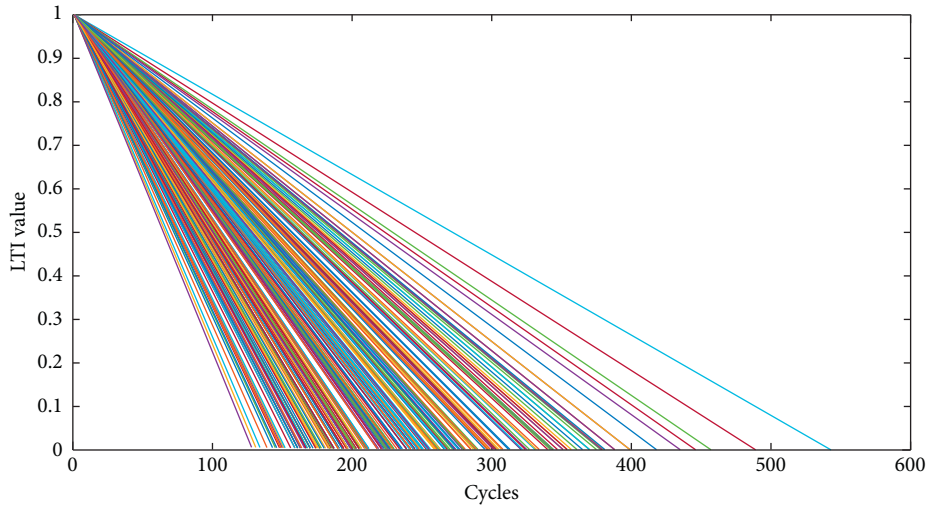


FIGURE 7: LTI curves for the reduced training dataset.

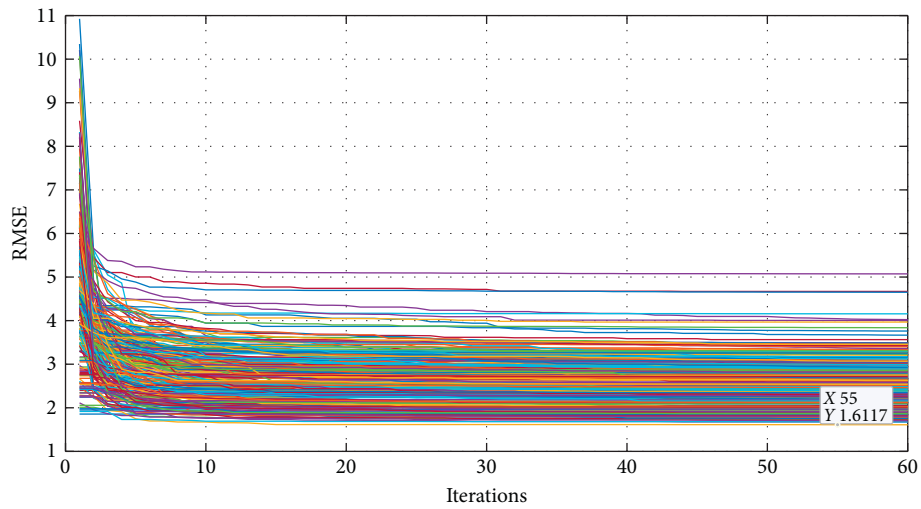


FIGURE 8: Convergence curves at each training iterations.

TABLE 6: The identified FCM.

	Concepts								
	C1	C2	C3	C4	C5	C6	C7	C8	C9
C1	—	0.090	0.016	-0.084	0.015	0.604	0.089	0.159	0.266
C2	0.106	—	0.405	0.509	-0.260	0.163	-0.255	0.069	-0.056
C3	0.091	0.045	—	0.173	0.029	0.420	0.322	0.749	0.022
C4	0.193	0.595	0.016	—	0.230	0.098	0.047	0.218	-0.042
C5	0.040	0.454	0.164	0.198	—	0.322	0.773	0.648	-0.998
C6	0.022	0.309	0.133	0.346	0.391	—	0.077	-0.892	-0.276
C7	0.320	0.293	0.166	0.770	1.000	0.555	—	0.790	-0.200
C8	0.171	0.122	-0.069	-0.156	0.239	0.153	0.329	—	-0.062
C9	—	—	—	—	—	—	—	—	—

should define the filter threshold value properly through specific algorithms, increasing the iteration time. Since the size of the FCM concepts set, for the examined case study, is not so big, the additional filter phase has been neglected.

The final FCM can be graphically represented to evaluate all the concatenations among concepts, as shown in Figure 9. Once the final FCM has been obtained, the strength of the concepts involved can be analysed so as to identify the

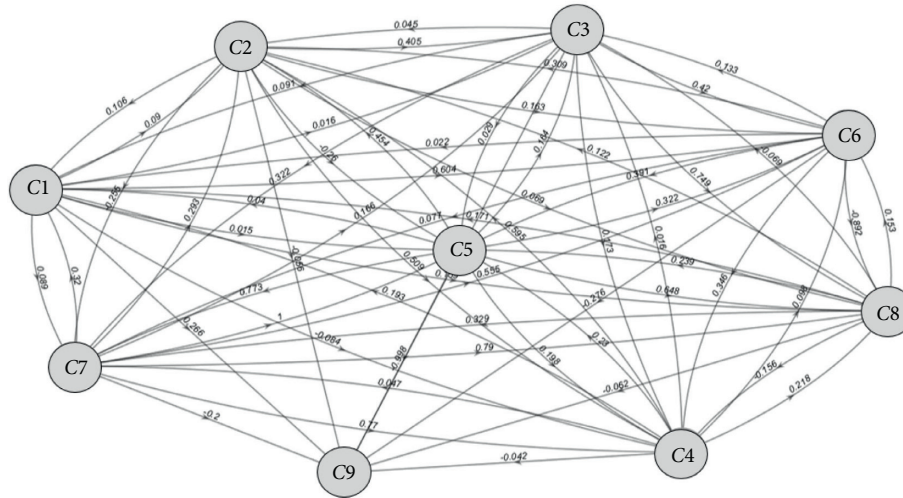


FIGURE 9: The final FCM in the symbolic form.

TABLE 7: TEs matrix among all of the involved concepts.

	Concepts								
	C1	C2	C3	C4	C5	C6	C7	C8	C9
C1	—	0.309	0.133	0.346	0.391	0.604	0.159	0.604	0.391
C2	-0.255	—	0.405	0.509	-0.260	0.405	0.322	0.405	-0.276
C3	0.320	0.309	—	0.346	0.391	0.420	0.329	0.749	0.391
C4	0.193	0.595	0.405	—	-0.260	0.230	-0.255	0.230	-0.260
C5	0.320	0.454	0.405	0.770	—	0.555	0.773	0.773	-0.998
C6	0.193	0.391	0.309	0.346	0.391	—	0.391	-0.892	0.391
C7	0.320	0.595	0.293	0.770	1.000	0.555	—	0.790	-0.998
C8	0.320	0.293	0.166	0.329	0.329	0.329	0.329	—	0.329
C9	—	—	—	—	—	—	—	—	—

main relevant ones and, through the critical path analysis, identify those concepts that can be considered the leading causes of the degradation profile for each engine.

Specifically, according to equation (3), Table 7 shows the Total Effects' matrix where the  $(i, j)$  values of this matrix represent how much the concept indicated in the rows affects the concept indicated in the columns.

The most significant influence is related to the relationship between concept C7 (sensor number 13) and C1 (sensor number 2) with the strength value equal to 1. This relation means that C7, the *Corrected fan speed*, is the main cause of the increase to C1 that is the *Total temperature at the LPC outlet*.

Focusing on the degradation profile, the HI concept C9, it is possible to highlight that concept C7, jointly with concept C5 (sensor number 9, *Physical core speed*) have the most significant weight since the strength value is equal to -0.998. This mean that the fan speed increasing is the relevant cause of aircraft engine degradation.

Analysing in depth all the critical paths (Table 8) starting from each concept of the FCM and ending in the concept C9, it is evident how the strength of the relationship between C7 and C9 is not a direct influence. This is because C7 indirectly affects C9 through the influence on C5. Thus, C5 can be

TABLE 8: Main paths affecting HI concept (C9).

Initial node	End node		TE	
C1	C6	C5	C9	0.391
C2	C3	C6	C9	-0.276
C3	C6	C5	C9	0.391
C4	C2	C5	C9	-0.260
C5			C9	-0.998
C6		C5	C9	0.391
C7		C5	C9	-0.998
C8	C7	C5	C9	0.329

considered the most relevant cause of aircraft engine degradation. This could be an important consideration for a proper maintenance plan design.

Once the FCM has been analysed, it can be used to calculate the HIs for each engine in the training dataset (the first 50 HIs are shown in Figure 10) and also for the testing dataset. In practical terms, the HI shape provides maintenance managers with the real RUL value.

4.2. The Comparison between the Proposed Approach with ANN. Results of the proposed approach have been compared to those obtained using an Artificial Neural Network.



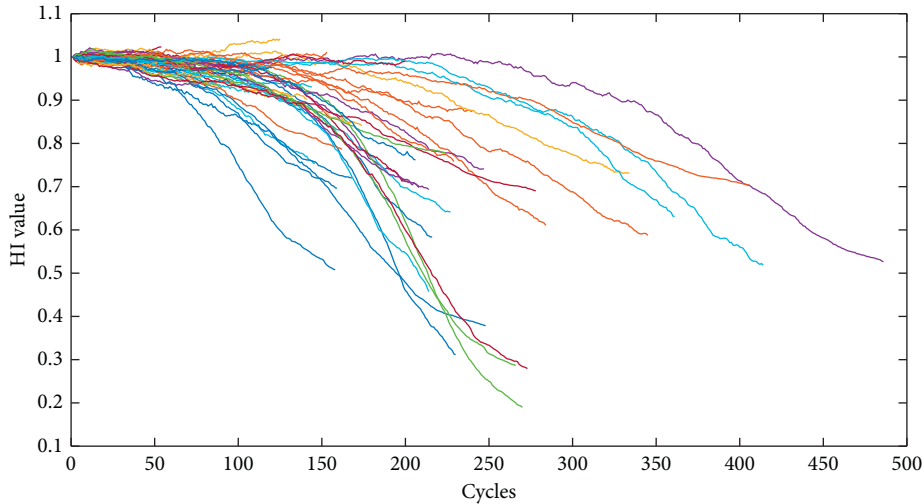


FIGURE 10: HIs’ curves for the first 50 engines of the training dataset through the proposed approach.

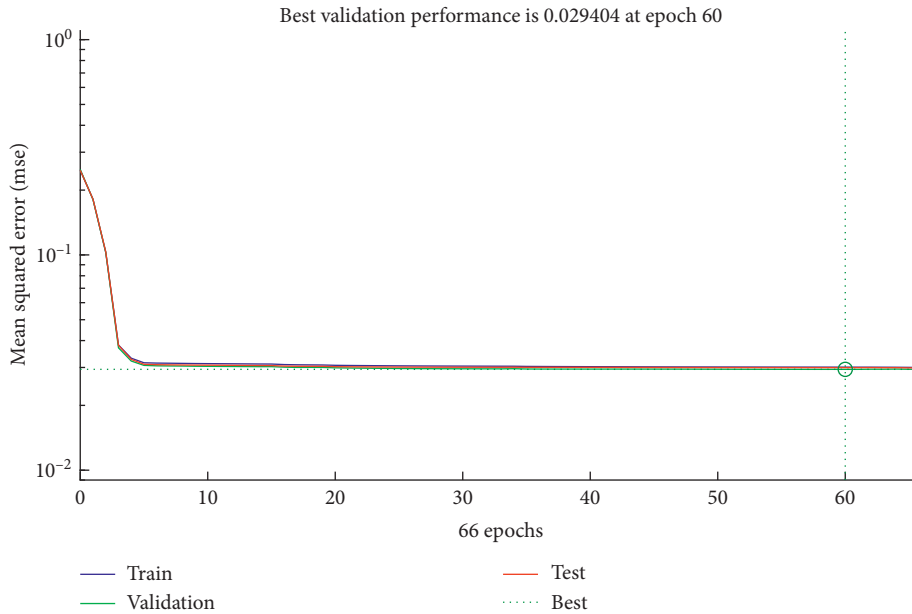


FIGURE 11: Best validation performance of the used ANN used.

The ANNs were chosen for the comparison as this methodology is one of the most used in literature for the evaluation of the HI and also due to the similarity with the FCM method. As far as the ANN is concerned, the best results have been obtained considering a two-level network composed of ten neurons, respectively. Referring to the Levenberg–Marquardt method [81] and using the mean squared error as a performance indicator, Figure 11 shows how the lower MSE is obtained at 60th epoch with a value ranging between  $[10^{-2} 10^{-1}]$ .

The LTI shown in Figure 7 have been used to train the ANN in order to obtain the HI estimation, as reported in Figure 12.

The HIs defined for the engines in the testing dataset have been used for the RUL prediction using k-neighbors

algorithm. Table 9 shows an excerpt of the results. Specifically, engines are reported in the ascending order in terms of the FCM percentage error ( $\%err_{FCM}$ ). The second column is the real RUL value for each machine (values provided by NASA).

The estimated RUL values by FCM and ANN (columns 3 and 4, respectively) underline how the proposed approach performances are better than those obtained using ANN.

Figures 13 and 14 compare the Weibull distributions derived from the similarity approach based on FCM and ANN for HIs. These figures show, as an example, the case of Engine 1. For all other engines, similar results have been obtained.

The RUL obtained by the ANN approach is affected by an overestimation with respect to the FCM one. Thus, few

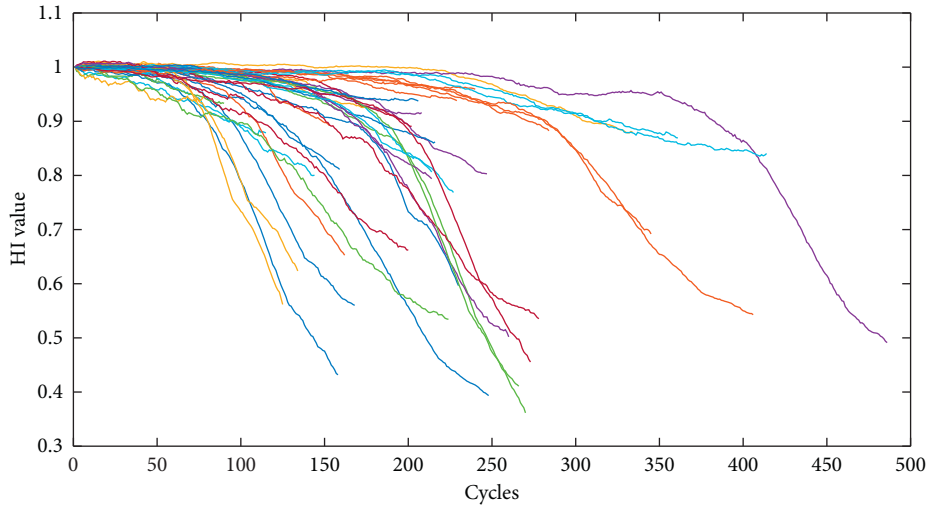


FIGURE 12: HIs' curves for the first 50 engines of the training dataset through the ANN approach.

TABLE 9: An excerpt of estimated RUL for the testing dataset.

Id engine	TrueRUL	EsFCM	EsANN	%Err FCM	%Err ANN
2	83	82.1	94.73	1.09%	14.13%
9	176	178.11	170.69	1.20%	3.02%
3	89	87.89	124.81	1.25%	40.24%
11	176	178.84	219.61	1.61%	24.78%
4	53	51.84	50.54	2.19%	4.64%
18	171	167.05	180.09	2.31%	5.32%
5	64	62.46	76.85	2.41%	20.08%
1	33	33.82	44.6	2.48%	35.15%
7	70	71.93	100.15	2.76%	43.07%
22	163	167.84	160.83	2.97%	1.33%
13	110	113.36	157.72	3.05%	43.38%
16	109	112.73	155.48	3.42%	42.64%
21	113	117.74	131.87	4.20%	16.70%
25	111	105.84	148.76	4.64%	34.02%
8	41	43.03	40.10	4.95%	2.20%
6	33	34.86	37.35	5.64%	13.18%
24	75	69.87	105.27	6.84%	40.36%
27	76	70.37	101.51	7.41%	33.57%
26	71	76.31	101.37	7.48%	42.77%
17	46	49.76	57.99	8.17%	26.07%
15	37	40.48	34.03	9.40%	8.03%
12	26	22.9	35.54	11.90%	36.69%
23	39	43.95	55.13	12.68%	41.36%
...	...	...	...	...	...

involved curves allow the reduction of the variability range for a likely prediction. This is a typical problem of ANN that has been overcome through the proposed method.

The HIs defined using the proposed approach are more accurate and, in addition, the algorithm provides significant discrimination of all the considered aircraft engines (see Figure 15). Thus, small variations in the sensor readings define quite distinct degradation profiles.

### 5. Discussion

The proposed approach has the ability to operate in a dynamic environment with no significant difference in the

operation of the algorithm in steady state or dynamic mode, guaranteeing a reliable and robust performance together with an easy implementation.

At the same time, it requires particular attention by users in defining all the involved parameters such as the size of the dataset, the number of agents to be used to find the final FCM, and the threshold values. Indeed, as discussed, the total number of iterations and therefore the total computational time to calculate HIs depends on them. However, the analysed case study has highlighted how this limitation can be overcome by applying, before the algorithm initialisation, a dataset reduction to minimise the involved variables number.

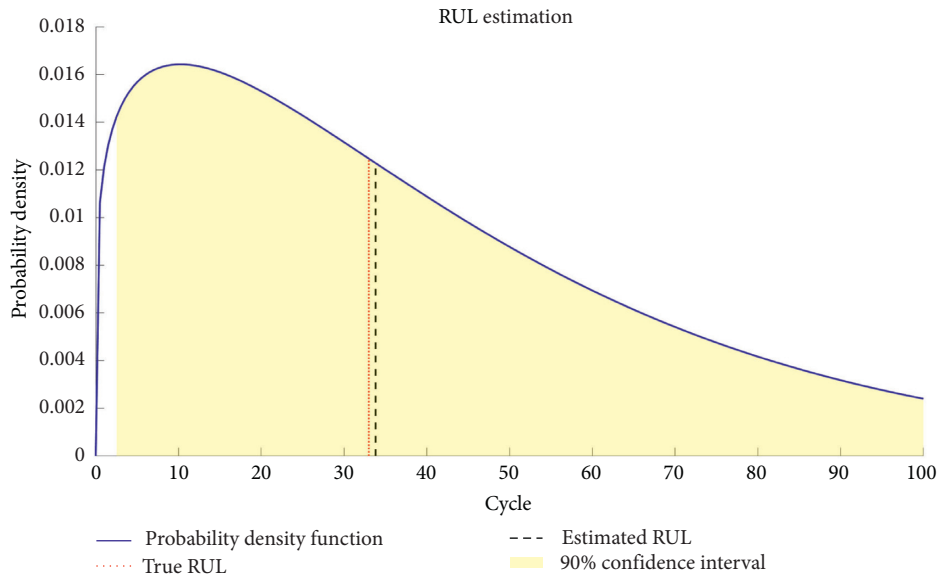


FIGURE 13: Engine 1, Probability Density Function, True RUL, and Estimated RUL with proposed approach (trueRUL=33 and estRUL=33.82).

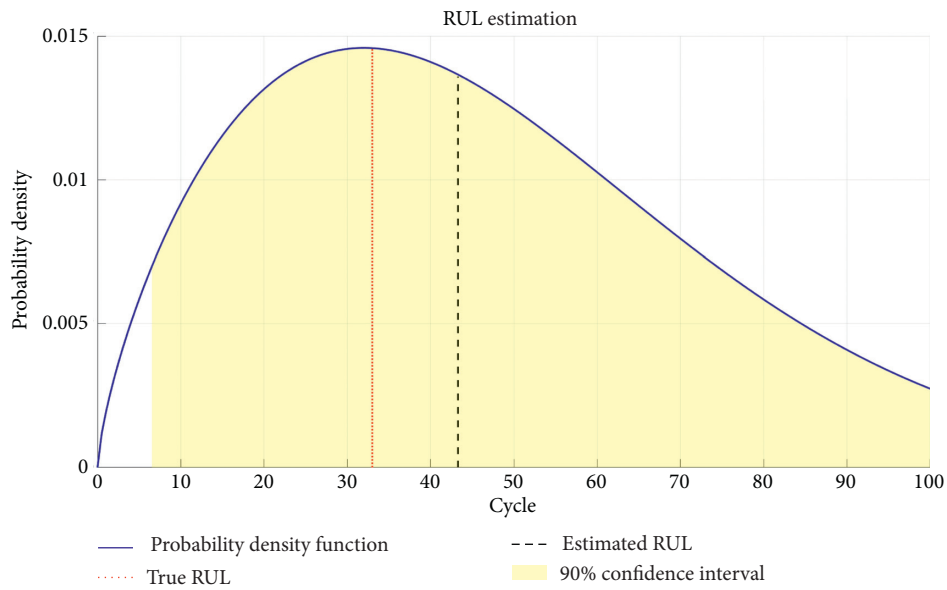
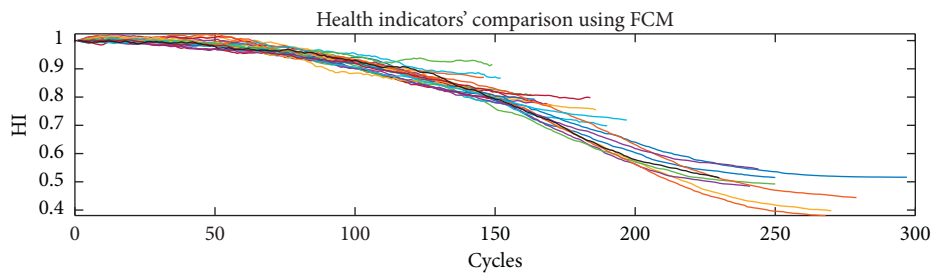


FIGURE 14: Engine 1, Probability Density Function, True RUL, and Estimated RUL with ANN (trueRUL = 33 and estRUL = 44.60).



(a)

FIGURE 15: Continued.

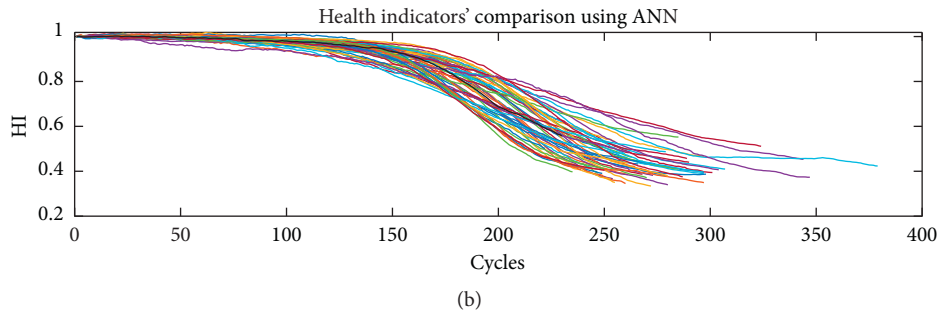


FIGURE 15: HIs' comparison using FCM and ANN for Engine 1.

Probably the most significant advantage of the swarm's intelligence is its ability to operate in a dynamic environment. The swarm can continuously follow the path even for rapidly evolving optimisation. In principle, there is no significant difference in the operation of the algorithm in steady state or dynamic mode [82]. Moreover, these algorithms do not require knowledge, for example, about the gradients of the cost function and constrained functions. They guarantee reliable and robust performance together with an easy implementation [83]. Specifically, as far as the GWO is concerned, the most important one refers to the small number of parameters needed for its implementation and adjustment [84, 85].

At the same time, regarding the utilisation of FCMs, among several advantages, the most important is their extreme flexibility and adaptability to a given domain, allowing qualitative simulation of a system once constructed. Furthermore, FCMs symbolically represent knowledge, converting the relations between the elements of a mental landscape to assess the impact of these elements [86, 87]. The use of FCMs demonstrates other additional benefits, including the use of fuzzy logic. Indeed, the fuzzy set theory allows the incorporation of uncertainty due to sparse and imprecise information [88]. A fuzzy value is a fuzzy representation of a specific property when it is not precisely known [89]. The fuzzy set theory and numbers are mainly used to quantify the grade to which a property can be connected with an object. It must not be confused with the concept of probability. Indeed, the causality among concepts is considered as a certainty, since the concept of causality is not used to try to identify or find relationships between factors such as structural equation model and/or Bayesian nets [90].

## 6. Conclusion

In this paper, an innovative supervised approach that combines a Swarm Intelligence algorithm, the GWO, and FCMs is proposed for HI analysis and calculation. This approach allows maintenance managers to predict the RUL of items through the use of  $k$ -neighbors algorithms as well as to have an in-depth understanding of the degradation process; thanks to the analysis of the main paths of concepts that affect the HI. In order to enhance the operating reliability and reduce maintenance costs, an integrated fault diagnosis and prognosis framework that analyse the machinery degradation process is necessary.

In the proposed approach, the working conditions of the engines and the sensor signals installed on engines become the concepts of the FCM, while the GWO, a Swarm Intelligence algorithm, has been used for defining the connection weight among these concepts and the HI concepts.

A dataset provided by NASA that concerns the data of aircraft engines has been used to test the proposed approach. The case used underlines a crucial aspect. Comparing the results with those obtained through neural networks, the proposed algorithm models, and all of the degradation profiles in a more detailed manner allows one to significantly distinguish different situations without imposing any specified mathematical functions. This consideration is reflected in fewer profiles that can be considered similar to the case in question and, consequently, give a more precise estimate of the RUL. Moreover, analysing the final FCM, the physical core speed and the corrected fan speed have been identified as the main critical factors to the engine degradation.

Furthermore, the use of the FCM approach allows the user to be able to analyse in an intuitive way the relationships between the variables involved and thus have a greater understanding of the degradation process, which is impossible for an ANN. Indeed, in an ANN, the variables involved are the inputs for the system and the neurons concatenation has no meaning to understand the process. On the contrary, in an FCM, the variables are simultaneous inputs and "neurons," so their concatenation gives more information about the process.

The performance of the proposed approach has been demonstrated using a NASA dataset, but it can also be applicable to the other fault diagnosis and prognosis equipment. A wide range of experiments will be performed to investigate the robustness of the proposed method in our next step research. At the same time, it is evident how the proposed approach can be based not only on a feature reduction but also on the determination of the most useful items for the training phase. Indeed, considering all the variables involved for the algorithm application (number of wolves, maximum iteration number for the GWO, thresholds etc.), the total number of iterations for the identification of the optimal FCM can be very huge and time-consuming. For this reason, as further development is crucial to design a preliminary step to be used after feature extraction step.

## Data Availability

To explain the proposed approach and to test its accuracy for Health Indicator modelling, the Turbofan Engine Degradation Simulation Data Set has been used. It is available online on the NASA repository website (<https://ti.arc.nasa.gov/tech/dash/groups/pcoe/prognostic-data-repository/>, last access July 21, 2020).

## Conflicts of Interest

The authors declare that they have no conflicts of interest.

## Acknowledgments

This research was funded by INAIL (Istituto Nazionale per l'Assicurazione Contro gli Infortuni sul Lavoro), the Italian National Institute for Insurance against Accidents at Work, under the BRIC 2018 project titled "Sviluppo di soluzioni smart attraverso metodologie Digital Twin per aumentare la sicurezza degli operatori durante i processi di manutenzione degli impianti produttivi" (BRIC ID12).

## References

- [1] Y. Ran, X. Zhou, P. Lin, Y. Wen, and R. Deng, "A survey of predictive maintenance: systems, purposes and approaches," 2019, <http://arxiv.org/abs/1912.07383>.
- [2] S. Selcuk, "Predictive maintenance, its implementation and latest trends," *Proceedings of the Institution of Mechanical Engineers, Part B: Journal of Engineering Manufacture*, vol. 231, no. 9, pp. 1670–1679, 2017.
- [3] T. Sutharssan, S. Stoyanov, C. Bailey, and C. Yin, "Prognostic and health management for engineering systems: a review of the data-driven approach and algorithms," *The Journal of Engineering*, vol. 2015, no. 7, pp. 215–222, 2015.
- [4] P. Patel, M. I. Ali, and A. Sheth, "From raw data to smart manufacturing: AI and semantic web of things for industry 4.0," *IEEE Intelligent Systems*, vol. 33, no. 4, pp. 79–86, 2018.
- [5] F. Ciarapica, M. Bevilacqua, and S. Antomarioni, "An approach based on association rules and social network analysis for managing environmental risk: a case study from a process industry," *Process Safety and Environmental Protection*, vol. 128, pp. 50–64, 2019.
- [6] A. J. Lockett, "No free lunch theorems," in *General-Purpose Optimization through Information Maximization*, A. J. Lockett and A. C. Di, Eds., Springer, New York, NY, USA, 2020.
- [7] M. Bevilacqua, F. E. Ciarapica, and G. Mazzuto, "Fuzzy cognitive maps for adverse drug event risk management," *Safety Science*, vol. 102, pp. 194–210, 2018.
- [8] R. Sahal, J. G. Breslin, and M. I. Ali, "Big data and stream processing platforms for Industry 4.0 requirements mapping for a predictive maintenance use case," *Journal of Manufacturing Systems*, vol. 54, pp. 138–151, 2020.
- [9] V. A. Sotiris, P. W. Tse, and M. G. Pecht, "Anomaly detection through a bayesian support vector machine," *IEEE Transactions on Reliability*, vol. 59, no. 2, pp. 277–286, 2010.
- [10] D. Azevedo, A. Cardoso, and B. Ribeiro, "Estimation of health indicators using advanced analytics for prediction of aircraft systems remaining useful lifetime," *PHM Society European Conference*, vol. 5, no. 1, p. 10, 2020.
- [11] H. Yang, Z. Sun, G. Jiang, F. Zhao, and X. Mei, "Remaining useful life prediction for machinery by establishing scaled-corrected health indicators," *Measurement*, vol. 163, Article ID 108035, 2020.
- [12] L. Guo, N. Li, F. Jia, Y. Lei, and J. Lin, "A recurrent neural network based health indicator for remaining useful life prediction of bearings," *Neurocomputing*, vol. 240, pp. 98–109, 2017.
- [13] L. Guo, Y. Lei, N. Li, T. Yan, and N. Li, "Machinery health indicator construction based on convolutional neural networks considering trend burr," *Neurocomputing*, vol. 292, pp. 142–150, 2018.
- [14] Y. Lei, N. Li, and J. Lin, "A new method based on stochastic process models for machine remaining useful life prediction," *IEEE Transactions on Instrumentation and Measurement*, vol. 65, no. 12, pp. 2671–2684, 2016.
- [15] M. Zhao, B. Tang, and Q. Tan, "Bearing remaining useful life estimation based on time-frequency representation and supervised dimensionality reduction," *Measurement*, vol. 86, pp. 41–55, 2016.
- [16] B. Abichou, A. Voisin, and B. Iung, "Choquet integral parameters inference for health indicators fusion within multi-levels industrial systems: application to components in series," *IFAC Proceedings Volumes*, vol. 45, no. 31, pp. 193–198, 2012.
- [17] M. Luo, Z. Xu, H. L. Chan, and M. Alavi, "Online predictive maintenance approach for semiconductor equipment," in *Proceedings of the IECON 2013-39th Annual Conference of the IEEE Industrial Electronics Society*, pp. 3662–3667, Vienna, Austria, 2013.
- [18] J. Moyne, J. Iskandar, P. Hawkins et al., "Deploying an equipment health monitoring dashboard and assessing predictive maintenance," in *Proceedings of the ASMC 2013 SEMI Advanced Semiconductor Manufacturing Conference*, Saratoga Springs, NY, USA, 2013.
- [19] T. Gerber, N. Martin, and C. Mailhes, "Time-Frequency tracking of spectral structures estimated by a data-driven method," *IEEE Transactions on Industrial Electronics*, vol. 62, no. 10, pp. 6616–6626, 2015.
- [20] F. Calabrese, A. Regattieri, L. Botti, C. Mora, and F. G. Galizia, "Unsupervised fault detection and prediction of remaining useful life for online prognostic health management of mechanical systems," *Applied Sciences*, vol. 10, no. 12, p. 4120, 2020.
- [21] Y. Lei, N. Li, S. Gontarz, J. Lin, S. Radkowski, and J. Dybala, "A model-based method for remaining useful life prediction of machinery," *IEEE Transactions on Reliability*, vol. 65, no. 3, pp. 1314–1326, 2016.
- [22] P. Baraldi, G. Bonfanti, and E. Zio, "Differential evolution-based multi-objective optimization for the definition of a health indicator for fault diagnostics and prognostics," *Mechanical Systems and Signal Processing*, vol. 102, pp. 382–400, 2018.
- [23] I. Amihai, M. Chioua, R. Gitzel et al., "Modeling machine health using gated recurrent units with entity embeddings and K-means clustering," in *Proceedings of the 2018 IEEE 16th International Conference On Industrial Informatics (INDIN)*, pp. 212–217, Porto, Portugal, 2018.
- [24] T. Laloix, B. Iung, A. Voisin, and E. Romagne, "Parameter identification of health indicator aggregation for decision-making in predictive maintenance: application to machine tool," *CIRP Annals*, vol. 68, no. 1, pp. 483–486, 2019.
- [25] Z. Li, Y. Jiang, Z. Duan, and Z. Peng, "A new swarm intelligence optimized multiclass multi-kernel relevant vector machine: an experimental analysis in failure diagnostics of



- diesel engines,” *Structural Health Monitoring*, vol. 17, no. 6, pp. 1503–1519, 2018.
- [26] B. Zheng, Y.-F. Li, J. Guo, and H.-Z. Huang, “Aeroengine performance prediction based on double-extremum learning particle swarm optimization,” *International Journal of Turbo & Jet-Engines*, vol. 37, no. 1, pp. 17–29, 2020.
- [27] W. Hu, H. Chang, and X. Gu, “A novel fault diagnosis technique for wind turbine gearbox,” *Applied Soft Computing*, vol. 82, p. 6, Article ID 10555, 2019.
- [28] F. Zhao and H. Liu, “A swarm-based multiple reduction approach for fault diagnosis,” *International Journal of Modelling, Identification and Control*, vol. 18, no. 3, p. 261, 2013.
- [29] I. P. Kougias and N. P. Theodossiou, “Multiobjective pump scheduling optimization using harmony search algorithm (HSA) and polyphonic HSA,” *Water Resources Management*, vol. 27, no. 5, pp. 1249–1261, 2013.
- [30] S. Lakshminarayanan and D. Kaur, “Optimal maintenance scheduling of generator units using discrete integer cuckoo search optimization algorithm,” *Swarm and Evolutionary Computation*, vol. 42, pp. 89–98, 2018.
- [31] R. Puzis, D. Shirtz, and Y. Elovici, “A particle swarm model for estimating reliability and scheduling system maintenance,” *Enterprise Information Systems*, vol. 10, no. 4, pp. 349–377, 2016.
- [32] X. Ye and L. Zhou, “Using SCADA data fusion by swarm intelligence for wind turbine condition monitoring,” in *Proceedings of the 2013 Fourth Global Congress on Intelligent Systems*, pp. 210–215, Hong Kong, China, 2013.
- [33] R. Zhang, S. Song, and C. Wu, “A simulation-based differential evolution algorithm for stochastic parallel machine scheduling with operational considerations,” *International Transactions in Operational Research*, vol. 20, no. 4, pp. 533–557, 2013.
- [34] T. E. K. Zidane, M. R. Adzman, M. F. N. Tajuddin, S. M. Zali, A. Durusu, and S. Mekhilef, “Optimal design of photovoltaic power plant using hybrid optimisation: a case of south Algeria,” *Energies*, vol. 13, no. 11, p. 2776, 2020.
- [35] L. Jing, B. Song, Y. Zhu, B. Yang, and H. Shu, “Grey wolf optimizer based MPPT control of centralized thermoelectric generator applied in thermal power stations,” in *Proceedings of the 2020 Asia Energy And Electrical Engineering Symposium (AEEES)*, pp. 127–132, Chengdu, China, 2020.
- [36] E. Martinez de Salazar and J. García Sanz-Calcedo, “Study on the influence of maintenance operations on energy consumption and emissions in healthcare centres by fuzzy cognitive maps,” *Journal of Building Performance Simulation*, vol. 12, no. 4, pp. 420–432, 2019.
- [37] O. Mahian, M. Javidmehr, A. Kasaeian, S. Mohasseb, and M. Panahi, “Optimal sizing and performance assessment of a hybrid combined heat and power system with energy storage for residential buildings,” *Energy Conversion and Management*, vol. 211, Article ID 112751, 2020.
- [38] V. B. Pamshetti, S. Singh, and S. P. Singh, “Reduction of energy demand via conservation voltage reduction considering network reconfiguration and soft open point,” *International Transactions on Electrical Energy Systems*, vol. 30, no. 1, Article ID e12147, 2020.
- [39] A. Kumar, S. Pant, M. Ram, and S. Chaube, “Multi-objective grey wolf optimizer approach to the reliability-cost optimization of life support system in space capsule,” *International Journal of System Assurance Engineering and Management*, vol. 10, no. 2, pp. 276–284, 2019.
- [40] M. D. L. Dalla Vedova, P. C. Berri, and S. Re, “A comparison of bio-inspired meta-heuristic algorithms for aircraft actuator prognostics,” in *Proceedings of the 29th European Safety And Reliability Conference (ESREL)*, pp. 1064–1071, Hannover, Germany, 2019.
- [41] S. Abdelghafar, A. Darwish, and A. E. Hassanien, “Cube satellite failure detection and recovery using optimized support vector machine,” in *Proceedings Of the International Conference On Advanced Intelligent Systems And Informatics 2018*, A. E. Hassanien, M. F. Tolba, K. Shaalan, A. T. Azar, and A. c. Di, Eds., , 2019.
- [42] S. Mousavipour, H. Farughi, and F. Ahmadizar, “A job shop scheduling problem with sequence-dependent setup times considering position-based learning effects and availability constraints,” *International Journal of Industrial Engineering*, vol. 30, no. 3, p. 12, 2019.
- [43] Z. Yang, C. Liu, and W. Qian, “An Improved Multi-Objective Grey Wolf Optimization Algorithm for Fuzzy Blocking Flow Shop Scheduling Problem,” in *Proceedings Of the 2017 IEEE 2nd Advanced Information Technology, Electronic and Automation Control Conference (IAEAC)*, pp. 661–667, Chongqing, China, 2017.
- [44] Z. Yang and C. Liu, “A hybrid multi-objective gray wolf optimization algorithm for a fuzzy blocking flow shop scheduling problem,” *Advances in Mechanical Engineering*, 2018.
- [45] V. N. Aju kumar, M. S. Gandhi, and O. P. Gandhi, “Identification and assessment of factors influencing human reliability in maintenance using fuzzy cognitive maps,” *Quality and Reliability Engineering International*, vol. 31, no. 2, pp. 169–181, 2015.
- [46] P. Gupta and O. P. Gandhi, “Equipment redesign feasibility through maintenance-work-order records using fuzzy cognitive maps,” *International Journal of System Assurance Engineering and Management*, vol. 5, no. 1, pp. 21–31, 2014.
- [47] C. Lopez and J. L. Salmeron, “Dynamic risks modelling in ERP maintenance projects with FCM,” *Information Sciences*, vol. 256, pp. 25–45, 2014.
- [48] A. Jamshidi, S. A. Rahimi, D. Ait-kadi, and A. Ruiz, “Dynamic risk modeling and assessing in maintenance outsourcing with FCM,” in *Proceedings of the 2015 International Conference on Industrial Engineering and Systems Management (IESM)*, pp. 209–215, IEEE, Seville, Spain, 2015.
- [49] V. Senniappan, J. Subramanian, E. I. Papageorgiou, and S. Mohan, “Application of fuzzy cognitive maps for crack categorization in columns of reinforced concrete structures,” *Neural Computing and Applications*, vol. 28, no. S1, pp. 107–117, 2017.
- [50] S. Lee, S.-U. Cheon, and J. Yang, “Development of a fuzzy rule-based decision-making system for evaluating the lifetime of a rubber fender,” *Quality and Reliability Engineering International*, vol. 31, no. 5, pp. 811–828, 2015.
- [51] A. Azadeh, S. F. Ghaderi, S. Pashapour, A. Keramati, M. R. Malek, and M. Esmizadeh, “A unique fuzzy multivariate modeling approach for performance optimization of maintenance workshops with cognitive factors,” *The International Journal of Advanced Manufacturing Technology*, vol. 90, no. 1–4, pp. 499–525, 2017.
- [52] A. T. James, O. P. Gandhi, and S. G. Deshmukh, “Assessment of failures in automobiles due to maintenance errors,” *International Journal of System Assurance Engineering and Management*, 2017.
- [53] Y. Zhang, Y. Tian, and S. Lu, “Design of a Live Maintenance Mobile Robot System for Power Substation Equipment,” in *Proceedings of the 2017 Chinese Automation Congress (CAC)*, pp. 882–887, IEEE, Jinan, China, 2017.

- [54] H. Saadatfar, S. Khosravi, J. H. Joloudari, A. Mosavi, and S. Shamshirband, "A new K-nearest neighbors classifier for big data based on efficient data pruning," *Mathematics*, vol. 8, no. 2, p. 286, 2020.
- [55] L. Wu, W. Krijgsman, J. Liu, C. Li, R. Wang, and W. Xiao, "CFLab: a MATLAB GUI program for decomposing sediment grain size distribution using Weibull functions," *Sedimentary Geology*, vol. 398, Article ID 105590, 2020.
- [56] A. J. Miller, "Structure of decision: the cognitive maps of political Elites Robert Axelrod, ed. Princeton: Princeton University Press, 1976, pp. xvi, 404 - perception and misperception in international Politics Robert Jervis Princeton: Princeton University Press, 1976, pp. xi, 445," *Canadian Journal of Political Science*, vol. 12, no. 1, pp. 177–179, 1979.
- [57] G. Mazzuto, C. Stylios, and M. Bevilacqua, "Hybrid decision support system based on DEMATEL and fuzzy cognitive maps," *IFAC-PapersOnLine*, vol. 51, no. 11, pp. 1636–1642, 2018c.
- [58] J. Fang, "Sums of L-fuzzy topological spaces," *Fuzzy Sets and Systems*, vol. 157, no. 6, pp. 739–754, 2006.
- [59] L. H. Tsoukalas and R. E. Uhrig, *Fuzzy and Neural Approaches in Engineering*, John Wiley & Sons, Hoboken, NJ, USA, 1st ed. edition, 1996.
- [60] M. Bevilacqua, F. E. Ciarapica, and G. Mazzuto, "Analysis of injury events with fuzzy cognitive maps," *Journal of Loss Prevention in the Process Industries*, vol. 25, no. 4, pp. 677–685, 2012.
- [61] M. Bevilacqua, F. E. Ciarapica, and G. Mazzuto, "A fuzzy cognitive maps tool for developing a RBI&M model," *Quality and Reliability Engineering International*, vol. 32, no. 2, pp. 373–390, 2014.
- [62] C. D. Stylios, P. P. Groumpos, and V. C. Georgopoulos, "Fuzzy cognitive maps modelling supervisory large scale control systems," *IFAC Proceedings Volumes*, vol. 31, no. 20, pp. 93–98, 1998.
- [63] C. D. Stylios and P. P. Groumpos, "Modeling complex systems using fuzzy cognitive maps," *IEEE Transactions on Systems, Man, and Cybernetics - Part A: Systems and Humans*, vol. 34, no. 1, pp. 155–162, 2004.
- [64] C. D. Stylios and P. P. Groumpos, "Fuzzy Cognitive Maps in modeling supervisory control systems," *Journal of Intelligent & Fuzzy Systems*, vol. 8, no. 1, pp. 83–98, 2000.
- [65] G. Mazzuto, M. Bevilacqua, C. Stylios, and V. C. Georgopoulos, "Aggregate experts knowledge in fuzzy cognitive maps," in *Proceedings of the 2018 IEEE International Conference On Fuzzy Systems (FUZZ-IEEE)*, pp. 1–6, Rio de Janeiro, Brazil, 2018a.
- [66] S. Bueno and J. L. Salmeron, "Benchmarking main activation functions in fuzzy cognitive maps," *Expert Systems with Applications*, vol. 36, no. 3, pp. 5221–5229, 2009.
- [67] G. Mazzuto, F. E. Ciarapica, C. Stylios, and V. C. Georgopoulos, "Fuzzy Cognitive Maps designing through large dataset and experts' knowledge balancing," in *Proceedings of the 2018 IEEE International Conference On Fuzzy Systems (FUZZ-IEEE)*, pp. 1–6, Rio de Janeiro, Brazil, 2018b.
- [68] O. A. Osoba and B. Kosko, "Fuzzy cognitive maps of public support for insurgency and terrorism," *The Journal of Defense Modeling and Simulation: Applications, Methodology, Technology*, vol. 14, no. 1, pp. 17–32, 2017.
- [69] S. Mirjalili, S. M. Mirjalili, and A. Lewis, "Grey wolf optimizer," *Advances in Engineering Software*, vol. 69, pp. 46–61, 2014.
- [70] D. Guha, P. K. Roy, and S. Banerjee, "Load frequency control of large scale power system using quasi-oppositional grey wolf optimization algorithm," *Engineering Science and Technology, an International Journal*, vol. 19, no. 4, pp. 1693–1713, 2016.
- [71] K. R. Das, D. Das, and J. Das, "Optimal Tuning of PID Controller using GWO Algorithm for Speed Control in DC motor," in *Proceedings of the 2015 International Conference on Soft Computing Techniques and Implementations (ICSCTI)*, pp. 108–112, IEEE, Faridabad, India, 2015.
- [72] G. M. Komaki and V. Kayvanfar, "Grey Wolf Optimizer algorithm for the two-stage assembly flow shop scheduling problem with release time," *Journal of Computational Science*, vol. 8, pp. 109–120, 2015.
- [73] T.-T. Nguyen, H. T. H. Thom, and T.-K. Dao, "Estimation localization in wireless sensor network based on multi-objective grey wolf optimizer," in *Advances in Information and Communication Technology*, M. Akagi, T.-T. Nguyen, D.-T. Vu, T.-N. Phung, V.-N. Huynh, and A. c. Di, Eds., vol. 538, pp. 228–237, Springer International Publishing, New York, NY, USA, 2017.
- [74] X. Song, L. Tang, S. Zhao et al., "Grey Wolf Optimizer for parameter estimation in surface waves," *Soil Dynamics and Earthquake Engineering*, vol. 75, pp. 147–157, 2015.
- [75] P. Niu, S. Niu, N. Liu, and L. Chang, "The defect of the Grey Wolf optimization algorithm and its verification method," *Knowledge-Based Systems*, vol. 171, pp. 37–43, 2019.
- [76] S. A. Dudani, "The distance-weighted k-nearest-neighbor rule," *IEEE Transactions on Systems, Man, and Cybernetics*, vol. SMC-6, no. 4, pp. 325–327, 1976.
- [77] G. Mazzuto and C. Stylios, "Empower fuzzy cognitive maps decision making abilities with swarm intelligence algorithms," in *Proceedings of the 2019 IEEE International Conference on Systems, Man and Cybernetics (SMC)*, pp. 2602–2607, Bari, Italy, 2019.
- [78] R. J. Hyndman and A. B. Koehler, "Another look at measures of forecast accuracy," *International Journal of Forecasting*, vol. 22, no. 4, pp. 679–688, 2006.
- [79] A. Saxena, K. Goebel, D. Simon, and N. Eklund, "Damage propagation modeling for aircraft engine run-to-failure simulation," in *Proceedings of the 2008 International Conference on Prognostics and Health Management*, Denver, CO, USA, 2008.
- [80] J. Xu, Y. Wang, and L. Xu, "PHM-oriented integrated fusion prognostics for aircraft engines based on sensor data," *IEEE Sensors Journal*, vol. 14, no. 4, pp. 1124–1132, 2014.
- [81] G. Lera and M. Pinzolas, "Neighborhood based Levenberg-Marquardt algorithm for neural network training," *IEEE Transactions on Neural Networks*, vol. 13, no. 5, pp. 1200–1203, 2002.
- [82] A. K. Kordon, "Swarm intelligence: the benefits of swarms," in *Applying Computational Intelligence: How To Create Value*, A. Kordon and A. c. Di, Eds., Springer, New York, NY, 2010.
- [83] M. M. Ali and W. X. Zhu, "A penalty function-based differential evolution algorithm for constrained global optimization," *Computational Optimization and Applications*, vol. 54, no. 3, pp. 707–739, 2013.
- [84] W. Long, X. Liang, S. Cai, J. Jiao, and W. Zhang, "A modified augmented Lagrangian with improved grey wolf optimization to constrained optimization problems," *Neural Computing and Applications*, vol. 28, no. 1, pp. 421–438, 2017.
- [85] S. Saremi, S. Z. Mirjalili, and S. M. Mirjalili, "Evolutionary population dynamics and grey wolf optimizer," *Neural Computing and Applications*, vol. 26, no. 5, pp. 1257–1263, 2015.

- [86] J. Aguilar, "A survey about fuzzy cognitive maps papers," *International Journal of Computational Cognition*, vol. 3, no. 2, pp. 27–33, 2005.
- [87] R. Taber, R. R. Yager, and C. M. Helgason, "Quantization effects on the equilibrium behavior of combined fuzzy cognitive maps," *International Journal of Intelligent Systems*, vol. 22, no. 2, pp. 181–202, 2007.
- [88] N. S. Arunraj, S. Mandal, and J. Maiti, "Modeling uncertainty in risk assessment: an integrated approach with fuzzy set theory and Monte Carlo simulation," *Accident Analysis & Prevention*, vol. 55, pp. 242–255, 2013.
- [89] A. Gonzalez, O. Pons, and M. A. Vila, "Dealing with uncertainty and imprecision by means of fuzzy numbers," *International Journal of Approximate Reasoning*, vol. 21, no. 3, pp. 233–256, 1999.
- [90] J. P. Carvalho, "On the semantics and the use of fuzzy cognitive maps and dynamic cognitive maps in social sciences," *Fuzzy Sets and Systems*, vol. 214, pp. 6–19, 2013.



## Research Article

# Gear Fault Diagnosis Based on VMD Sample Entropy and Discrete Hopfield Neural Network

Jiakai Ding,<sup>1,2</sup> Dongming Xiao ,<sup>1,2</sup> Liangpei Huang,<sup>1</sup> and Xuejun Li<sup>2</sup>

<sup>1</sup>Hunan Provincial Key Laboratory of Health Maintenance for Mechanical Equipment, Hunan University of Science and Technology, Xiangtan 411201, China

<sup>2</sup>School of Mechatronics Engineering, Foshan University, Foshan 528225, China

Correspondence should be addressed to Dongming Xiao; [dongming.xiao@outlook.com](mailto:dongming.xiao@outlook.com)

Received 17 September 2020; Revised 28 October 2020; Accepted 30 November 2020; Published 18 December 2020

Academic Editor: Antonio Forcina

Copyright © 2020 Jiakai Ding et al. This is an open access article distributed under the Creative Commons Attribution License, which permits unrestricted use, distribution, and reproduction in any medium, provided the original work is properly cited.

The gear fault signal has some defects such as nonstationary nonlinearity. In order to increase the operating life of the gear, the gear operation is monitored. A gear fault diagnosis method based on variational mode decomposition (VMD) sample entropy and discrete Hopfield neural network (DHNN) is proposed. Firstly, the optimal VMD decomposition number is selected by the instantaneous frequency mean value. Then, the sample entropy value of each intrinsic mode function (IMF) is extracted to form the gear feature vectors. The gear feature vectors are coded and used as the memory prototype and memory starting point of DHNN, respectively. Finally, the coding vector is input into DHNN to realize fault pattern recognition. The newly defined coding rules have a significant impact on the accuracy of gear fault diagnosis. Driven by self-associative memory, the coding of gear fault is accurately classified by DHNN. The superiority of the VMD-DHNN method in gear fault diagnosis is verified by comparing with an advanced signal processing algorithm. The results show that the accuracy based on VMD sample entropy and DHNN is 91.67% of the gear fault diagnosis method. The experimental results show that the VMD method is better than the complete ensemble empirical mode decomposition with adaptive noise (CEEMDAN) and empirical mode decomposition (EMD), and the effect of it in the diagnosis of gear fault diagnosis is emphasized.

## 1. Introduction

Gears are widely used in modern industrial machines and play a key role. When the gear is damaged, the transmission machinery will cause huge economic losses. The corresponding vibration signal will be generated when the gear runs under normal, wear, cracked, and broken teeth, which contains abundant fault information [1]. Therefore, it plays an important role to monitor the running state of the gear, which can be detected and replaced when the early weak fault occurs.

The most mature gear monitoring technology is based on the vibration signal. When the gear is damaged, the corresponding vibration signal will change. Therefore, it is only necessary to collect the vibration signal of gear under the corresponding fault state and extract the corresponding feature, and then, the fault diagnosis of gear can be carried

out. The innovation of gear fault diagnosis technology is based on the signal method. Traditional gear fault diagnosis methods include time-frequency domain analysis. Classical signal processing methods such as wavelet packet transform (WPT), Hilbert–Huang transform (HHT), and short-time Fourier transform (STFT) have been widely used in the field of fault diagnosis [2]. Mohammed et al. [3] utilized the vibration signal for gear fault diagnosis. Rafiee [4] utilized autocorrelation of continuous wavelet coefficients (CWCs) for gear fault diagnosis. These traditional time-frequency transforms are still insufficient in time-frequency resolution. Empirical mode decomposition (EMD), local mode decomposition (LMD), and other modern signal processing methods have also been applied [5–7]. Rafiee et al. [8] introduced an automatic feature extraction system for gear and bearing fault diagnosis using wavelet-based signal processing. However, EMD and LMD methods have

problems such as mode-mixing and endpoint effect [9, 10]. In order to effectively solve the mode-mixing and endpoint effect of the EMD and the LMD, variational mode decomposition (VMD) came into being [11]. VMD overcomes the shortcomings of the traditional signal adaptive decomposition methods of EMD and LMD, which converts the signal adaptive decomposition into a variational problem and solves the signal adaptive decomposition by seeking the optimal solution of the problem. However, the parameter combination of the penalty factors and the number of decomposition should be determined before VMD decomposition, which brings great difficulties to the accurate decomposition of signals. Some researchers used an optimization algorithm to optimize the parameter combination of the penalty factors and the number of decomposition in the VMD decomposition process. The genetic mutation particle swarm optimization (GMPPO) algorithm to optimize the VMD algorithm parameters is utilized by Ding [12, 13]. Experimental results show that the GMPPO-VMD algorithm has a good decomposition effect on the gear fault signal. The optimal adaptive VMD decomposition algorithm can adaptively determine the penalty factor and decomposition number in the VMD algorithm according to the time-frequency characteristics of different fault signals [14]. A variational mode decomposition method based on a cuckoo search algorithm to adjust the changes in internal parameters in VMD decomposition is utilized by Yan and Jia [15], and the multicomponent signal could be adaptively decomposed into a subsignal superposition of inherent mode function. The VMD adaptive decomposition algorithm [16] can be realized by adaptively adjusting the parameters of vibration signals of rotating machinery under VMD decomposition, such as the optimal number of mode decomposition and frequency bandwidth control.

The intrinsic mode functions (IMFs) of the original fault signal were decomposed by the VMD algorithm, the IMFs contain abundant characteristic parameters, and different characteristic parameters represent different physical meanings. Therefore, selecting more effective feature parameters can increase the recognition accuracy for subsequent fault diagnoses. The vibration signal of rotating machinery is usually nonlinear and nonstationary, which makes it very difficult to extract fault features. Entropy value can be used as a very effective parameter to extract fault features [17]. In order to improve the fault identification accuracy of rolling bearing, Chen applied the rapid sample entropy [18] and the improved multiscale amplitude-aware permutation entropy (IMAAPE) [19] to the feature extraction of rolling bearing diagnosis signal and achieved good results. A milling flutter detection method based on VMD and energy entropy is proposed by Liu et al. [20]. In order to automatically detect the flutter frequency band better, a flutter detection method based on energy entropy was proposed. The energy entropy value is taken as the fault feature parameter to extract, and it is verified that the energy entropy value can effectively express the flutter characteristics. Therefore, according to the advantages of simple sample entropy calculation and fast calculation speed, this paper selects it to extract the vibration signal feature of gear fault.

The feature vectors after feature extraction can be used as the input vectors in the fault diagnosis model. As a classifier, support vector machine (SVM) has been studied by

researchers for a long time. VMD is used to extract features from signals, and SVM is used for fault diagnosis. The results show that, under complex conditions, the proposed method can also perform fault diagnosis more accurately [21, 22]. However, in the process of SVM classification, kernel functions need to be solved according to specific problems and are not self-adaptive. In addition, there are many deep learning algorithms for fault diagnosis research, such as deep belief network (DBN) [23], long short-term memory (LSTM), deep self-encoder (DSE), deep convolution neural network (DCNN), and other deep learning algorithms [24–28] in recent years. However, the training time of the deep learning algorithm is too long to make fault diagnosis in time. The discrete Hopfield neural network (DHNN) is a recursive neural network, which was first proposed by JJ Hopfield [29]. Its operating mode is a binary system, and the value of the network node is only 1 or  $-1$ . It is a neural network model that can simulate human memory. In the field of mechanical fault diagnosis, DHNN has not been applied to gear fault diagnosis. So it is a new attempt to apply DHNN to gear fault diagnosis.

Based on the shortcomings of the EMD and the LMD, the optimized VMD is utilized to decompose the gear fault vibration signal. The sample entropy value is extracted as the characteristic parameter. Because the sample entropy is sensitive to the change of signal chaos, the sample entropy as the signal feature parameter is extracted by this paper. Based on the above literature on deep neural network algorithms, it is concluded that the deep neural network algorithm has too long training time in fault diagnosis and cannot quickly make fault diagnosis. Therefore, this paper synthesizes the shortcomings of the above literature. In order to quickly and accurately diagnose faults, a gear fault diagnosis based on VMD sample entropy and DHNN is proposed.

## 2. Experimental System and Methods

**2.1. Experimental System.** This section verifies the gear fault diagnosis capability of the VMD-DHNN method under different working conditions. This method mainly analyzes the fault signals collected from the gear experimental test rig. The gear experimental test rig is shown in Figure 1. The active and slave gears are all bevel gears, and the vibration acceleration signals from the gearbox are collected by using B&K data collector. Meanwhile, the sampling frequency and sampling time of the experiment were 8192 Hz and 0.25 s, respectively. The test rig includes an electromagnetic speed control motor controller, a three-phase asynchronous motor, two couplings, a reducer, an acceleration sensor, a B&K data acquisition analyzer, and a laptop. The gear fault parts are shown in Figure 2.

**2.2. VMD Sample Entropy and DHNN Fault Diagnosis Method.** As mentioned in Introduction, the VMD is selected in this paper to avoid the endpoint effect and mode confusion of the EMD and the LMD. The VMD has the advantage of high accuracy of the center frequency of each IMF and fast calculation speed, while DHNN has the

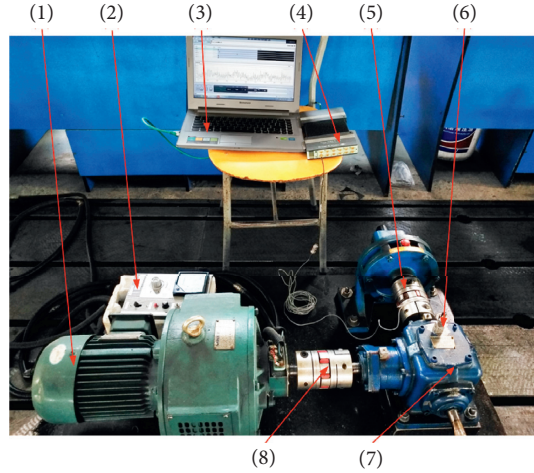


FIGURE 1: Gear experimental test rig: (1) three-phase induction motor; (2) electromagnetic speed control motor controller; (3) laptop; (4) B&K data acquisition analyzer; (5) coupling; (6) acceleration sensor; (7) reducer; (8) coupling.

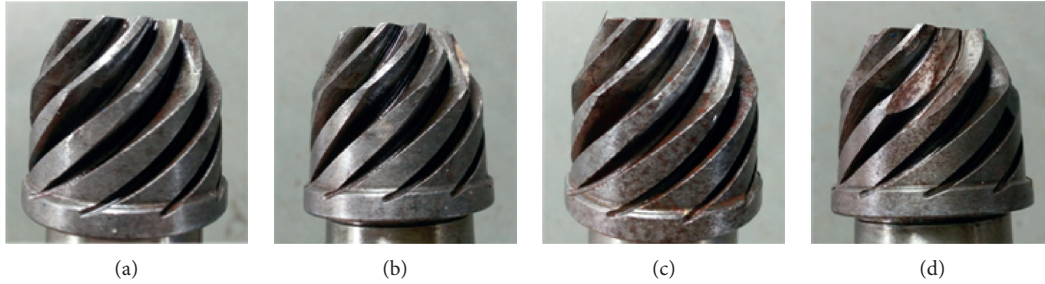


FIGURE 2: Gear fault parts: (a) normal gear; (b) gear with tooth crack; (c) gear with tooth wear; (d) gear with tooth break.

advantage of associative memory to speed up the calculation speed and improve the accuracy. The effectiveness of the method is verified by the measured gear fault diagnosis experiment. The implementation steps of the VMD-DHNN method are shown in Figure 3.

The detailed steps of the VMD-DHNN method are as follows:

- (i) Step 1. The optimal number of the VMD decomposition algorithm is selected.
- (ii) Step 2. The optimized VMD algorithm is utilized to decompose the gear fault signal.
- (iii) Step 3. The sample entropy value is extracted from each IMF, which form the feature vector of gear fault.
- (iv) Step 4. The gear fault feature vectors are encoded.
- (v) Step 5. The encoded fault feature vectors are input to DHNN for gear fault diagnosis.
- (vi) Step 6. Output results.

### 3. Gear Fault Feature Extraction of VMD Sample Entropy

**3.1. VMD Method.** Dragomiretskiy and Zosso proposed the VMD algorithm [11] in 2014. The original gear signal  $f(t)$  is decomposed into  $k$  IMFs  $x_k(t)$  by the VMD algorithm. The core of VMD is to construct an L2 norm equation, whose formula is expressed as

$$\min_{\{u_k\}, \{\omega_k\}} \left\{ \sum_k \left\| \partial_t \left[ \left( \delta(t) + \frac{j}{\pi t} \right) \times x_k(t) \right] e^{-j\omega_k t} \right\|_2^2 \right\}, \quad (1)$$

$$\text{s.t. } \sum_{k=1} u_k = f(t),$$

$$L(\{x_k\}, \{\omega_k\}, \{\lambda\}) = \alpha \sum_k \left\| \partial_t \left[ \left( \delta(t) + \frac{j}{\pi t} \right) \times x_k(t) \right] e^{-j\omega_k t} \right\|_2^2 + \left\| f(t) - \sum_k x_k(t) \right\|_2^2 + \langle \lambda(t), f(t) - \sum_k x_k(t) \rangle, \quad (2)$$

where  $\omega_k$  is the center frequency of the IMFs and  $\partial_t$  is the differential symbol.

The alternate direction method of multipliers (ADMM) is used to calculate equation (2), and the optimal solution is expressed as

$$\hat{x}_k^{n+1}(\omega) = \frac{\hat{f}(\omega) - \sum_{i \neq k} \hat{x}_i(\omega) + (\hat{\lambda}_i(\omega)/2)}{1 + 2\alpha(\omega - \omega_k)^2}, \quad (3)$$

$$\hat{\omega}_k^{n+1} = \frac{\int_0^\infty \omega |u(\omega)|^2 d\omega}{\int_0^\infty |u_k(\omega)|^2 d\omega},$$

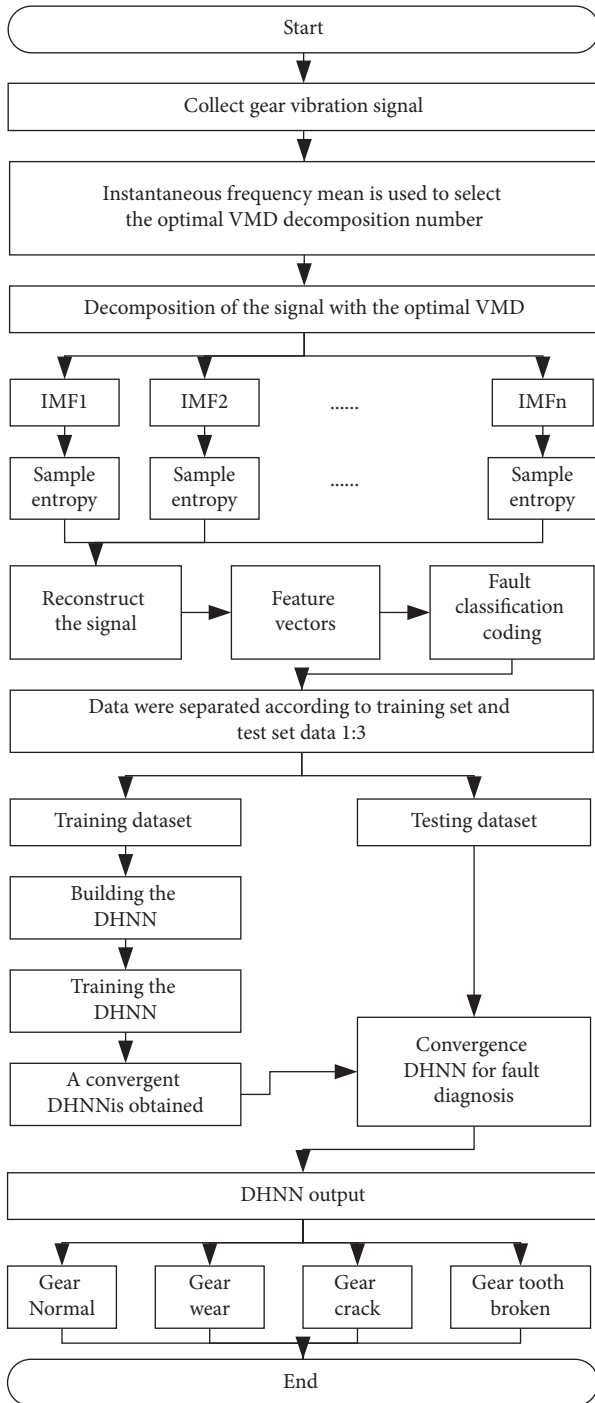


FIGURE 3: The flow chart of VMD sample entropy and DHNN gear fault diagnosis.

where  $\hat{f}(\omega)$ ,  $\hat{x}_i(\omega)$ , and  $\hat{\lambda}(\omega)$  represent the Fourier transform of  $f(\omega)$ ,  $x_i(\omega)$ , and  $\lambda(\omega)$ , respectively, and  $\varepsilon$  represents the discriminant accuracy.

According to reference [30], the optimal decomposition number of the VMD is selected through the change in instantaneous frequency mean value. This paper also selects the optimal decomposition number of the VMD by the same method. According to literature [11], the penalty factor  $\alpha$  and discriminant accuracy  $\varepsilon$  of the VMD algorithm are 2000

and 10-7, respectively. After repeated experimental analysis, the optimal decomposition number  $k = 4$ .

**3.2. Sample Entropy Method.** Sample entropy is an indicator to measure the complexity of time series signals. The higher the sample entropy value of the signal, the more complex the signal. The sample entropy is calculated as follows:

- (i) Step 1. A vector sequence with dimension  $m$  by ordinal number is formed,  $X_m(1), \dots, X_m(N - m + 1)$ , where  $x_m(i) = (x_m(i), x_m(i + 1), \dots, x_m(i + m - 1))$ . These vectors represent  $m$  consecutive values of  $x$  starting at the point  $i$ .
- (ii) Step 2. The distance between vector  $X_m(i)$  and  $X_m(j)$  is defined, and  $d[X_m(i), X_m(j)]$  is the absolute value of the maximum difference between the corresponding elements, that is,

$$d[X_m(i), X_m(j)] = \max_{k=0,1,\dots,m-1} (|x(i+k) - x(j+k)|). \quad (4)$$

- (iii) Step 3. For a given  $X_m(i)$ , the number of  $j(1 \leq j \leq N - m, j \neq i)$  is counted whose distance between  $X_m(i)$  and  $X_m(j)$  is less than or equal to threshold  $r$ , and it is called  $B_i$ . For  $1 \leq i \leq N - m$ ,  $B_i^m(r)$  is defined as

$$B_i^m(r) = \frac{B_i}{N - m + 1}. \quad (5)$$

- (iv) Step 4. The average value of the  $B_i^m(r)$  is defined as

$$B^m(r) = \frac{1}{N - m} \sum_{i=1}^{N-m} B_i^m(r). \quad (6)$$

- (v) Step 5. The dimension to  $m + 1$  is increased, the number of  $j(1 \leq j \leq N - m, j \neq i)$  is counted whose distance between  $X_{m+1}(i)$  and  $X_{m+1}(j)$  is less than or equal to threshold  $r$ , and it is called as  $A_i$ .  $A_i^m(r)$  and is defined as

$$A_i^m(r) = \frac{A_i}{N - m + 1}. \quad (7)$$

- (vi) Step 6. The average value of the  $A_i^m(r)$  is defined as

$$A^m(r) = \frac{1}{N - m} \sum_{i=1}^{N-m} A_i^m(r). \quad (8)$$

So the sample entropy is defined as

$$\text{SampEn}(m, r, N) = -\ln \left[ \frac{A^m(r)}{B^m(r)} \right]. \quad (9)$$



The 16 sets of data in the four states were separately decomposed by VMD. Through the previous analysis, the original gear fault signal is decomposed into 4 IMFs, and then, the sample entropy value of each IMF is extracted to form the gear fault feature vector. G1 represents the normal gear, G2 represents the gear with tooth wear, G3 represents the gear with tooth crack, and G4 represents the gear with tooth break. SampEn1 represents the sample entropy value of the component IMF1, SampEn2 represents the sample entropy value of the component IMF2, SampEn3 represents the sample entropy value of the component IMF3, and SampEn4 represents the sample entropy value of the component IMF4. Table 1 shows the sample entropy values of the IMFs.

In order to obtain a better classification effect, it is preliminarily classified from the size range of the overall sample entropy. The distribution of the size range of the overall sample entropy is shown in Table 2.

Then, the entropy value range of the samples of normal gear, gear with tooth wear, gear with tooth crack, and gear with tooth break is divided from SE1–SE4 (see Table 3 for details).

## 4. DHNN Fault Diagnosis Model

**4.1. DHNN Method.** This paper attempts to find a new method of gear fault diagnosis and establishes a new diagnosis model for gear fault diagnosis. Therefore, a new method of discrete Hopfield neural network (DHNN) was proposed to diagnose the entropy characteristics of gear fault samples, so as to solve the problems of low fault diagnosis accuracy and slow diagnosis speed of traditional methods. Through testing the established model, the results showed that the algorithm had better detection and diagnosis results.

Due to its network structure and activation function settings, DHNN has the functions of associative memory and nonlinear mapping of information, classification, and recognition. It has been widely used in the field of fault diagnosis.

After the VMD decomposition of the gear vibration signal, the sample entropy value is extracted from each IMF to form the feature vectors. Then, it encodes the feature vectors as the memory prototype and memory starting point of the associative memory, respectively. Then, the coding vectors are input to DHNN for fault diagnosis.

The design steps of this fault diagnosis model mainly include the following eight steps, as shown in Figure 4.

**4.2. Structure of DHNN.** The DHNN is a binary input and output binary neural network. Taking the DHNN network structure model composed of 3 neurons as an example, as shown in Figure 5, two layers of neurons are set, but only the first layer of neurons is the actual neurons. The first layer of neurons reads the input signal of layer 0, and after weighted cumulative summation, and then activates the  $\text{sgn}$  function to discriminate and outputs the signal to the next step until the network reaches steady state. The structure of DHNN is shown in Figure 6

Layer 0 is only the input layer of the DHNN, and it is not the actual neuron, so layer 0 has no computing power. The

layer 1 is the actual neuron, whose function is to sum the product of the input information and the weight coefficient and produces the output information after the processing of the nonlinear function  $\text{sgn}$ , where the original information  $SE_i$  is input from layer 1 to layer 0 for operation.

The entropy value of the gear fault sample  $SE = (SE_1, SE_2, \dots, SE_i)$  and the neuron node state of DHNN are 1 or  $-1$ ; 1 means that the neuron is activated, and  $-1$  means that the neuron is inhibited.  $h_i(t)$  is the weighted cumulant input by the neuron at the moment. As calculated by the following equation,

$$h_i(t) = \sum_{j=1}^n \omega_{ij} - q_i, \quad j = 1, 2, 3, \quad (10)$$

where  $\omega_{ij}$  is the connection weight between neuron  $i$  and neuron  $j$ ,  $q_i$  is the threshold of neuron  $i$ , and then, the next state  $y_i(t+1)$  of neuron  $i$  is calculated as shown in the following equation:

$$y_i(t+1) = \text{sgn}(h_i(t)) = \begin{cases} 1, & h_i(t) \geq 0, \\ -1, & h_i(t) < 0. \end{cases} \quad (11)$$

Let  $y_i(t)$  be the output value of neuron  $i$  at time  $t$ , and the network feeds  $y_i(t)$  back to the input terminal to become the input value of neuron  $i$  at the next moment, thus obtaining the output value of the network at the next moment  $y_i(t+1)$ , as shown in equation (12). After a certain number of iterations of the network according to the calculation method shown in equation (12), the network will converge to a steady state. In this case, the output value of the network should be the same as the output value at the previous moment, as shown in equation (13):

$$y_i(t+1) = \text{sgn}(h_i(t)), \quad (12)$$

$$y_i(t+1) = y_i(t). \quad (13)$$

As it can be seen from the above equation, the output value of DHNN is only 1 or  $-1$ , where 1 represents that the neural network node is activated, and  $-1$  represents that the neural network node is suppressed.

**4.3. DHNN Encoding Rules.** Firstly, the standard data set was input into the DHNN for binary coding, and then, the coding vectors were input into the DHNN for training. The state of neurons in DHNN neural network is only 1 and  $-1$ , and the coding of DHNN neural network needs to change the state of neurons. So, it is necessary to code the evaluation index when mapping to the state of the neuron. Coding rule: when greater than or equal to the index value of a certain level, the corresponding neuron state is set to “1;” otherwise, it is set to “ $-1$ .” The four-grade evaluation indexes of gear fault state are encoded as shown in the following table: • represents the neuron state as “1,” which means greater than or equal to the ideal evaluation index value of the corresponding grade; otherwise, it is denoted by  $\circ$ .

The standard vector value of normal gear is defined here as 1, the standard vector value of gear with tooth wear is 2,

TABLE 1: Sample entropy values of each IMF.

State of the gear	Signal sequence	SampEn1	SampEn2	SampEn3	SampEn4
G1	1	0.6542	0.7433	0.8416	0.8176
	2	0.7151	0.7666	0.8174	0.7689
	3	0.7224	0.7483	0.7932	0.8600
	4	0.7105	0.7698	1.1610	0.8194
G2	1	0.6871	0.7919	0.9700	1.0353
	2	0.6903	0.7964	0.9545	0.9600
	3	0.6847	0.8094	0.9436	0.9389
	4	0.7001	0.7999	0.8822	0.9433
G3	1	0.7307	0.8161	0.9177	0.8973
	2	0.7500	0.7711	0.8560	0.8839
	3	0.7377	0.8300	0.8618	0.8748
	4	0.7186	0.8232	0.8580	0.8604
G4	1	0.6514	0.8357	0.9759	0.7661
	2	0.6679	0.8478	1.0348	0.8100
	3	0.6622	0.8590	1.1180	0.7844
	4	0.6198	0.7533	0.9809	0.8218

TABLE 2: Distribution of the size range and the mean value of the overall sample entropy value.

Sample entropy	SampEn1	SampEn2	SampEn3	SampEn4
Numerical range	0.65–0.75	0.74–0.86	0.79–1.03	0.76–0.96
Mean value of the sample entropy	0.7	0.8	0.91	0.86

TABLE 3: Numerical range and the mean value of SE1, SE2, SE3, and SE4 sample entropy values in various gear states.

State of the gear	G1	G2	G3	G4
Numerical range of SampEn1	0.70–0.72	0.67–0.70	0.72–0.75	0.65–0.67
Mean value of SampEn1	0.71	0.685	0.735	0.66
Numerical range of SampEn2	0.74–0.77	0.77–0.8	0.8–0.83	0.83–0.86
Mean value of SampEn2	0.755	0.785	0.815	0.845
Numerical range of SampEn3	0.79–0.85	0.97–0.97	0.85–0.91	0.97–1.03
Mean value of SampEn3	0.82	0.97	0.88	1
Numerical range of SampEn4	0.81–0.86	0.91–0.96	0.86–0.91	0.76–0.81
Mean value of SampEn4	0.835	0.935	0.885	0.785

the standard vector value of gear with tooth crack is 3, and the standard vector value of gear broken tooth is 4. The standard vector value represents the position of the number of columns where the state of the DHNN neuron is 1 in the following binarization matrix: 1 represents the number of 1 in the first column and 2 represents the number of 1 in the second column. The data of normal, wear, crack, and broken teeth of four groups of standard gears are selected for encoding vectors, and the coding vectors is as follows:

$$\text{Normal gear: sim}_1 = [1 \ 1 \ 1 \ 1].$$

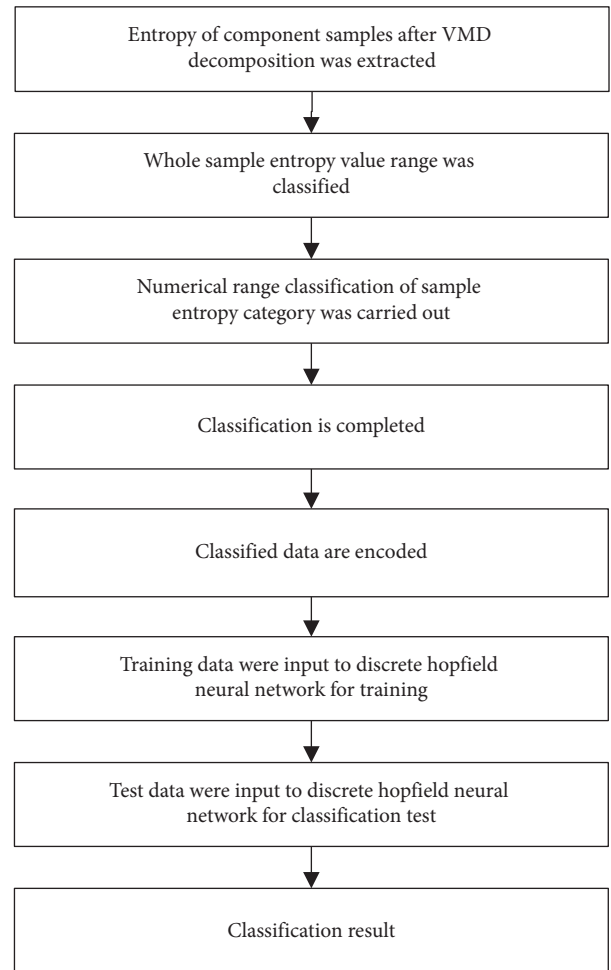
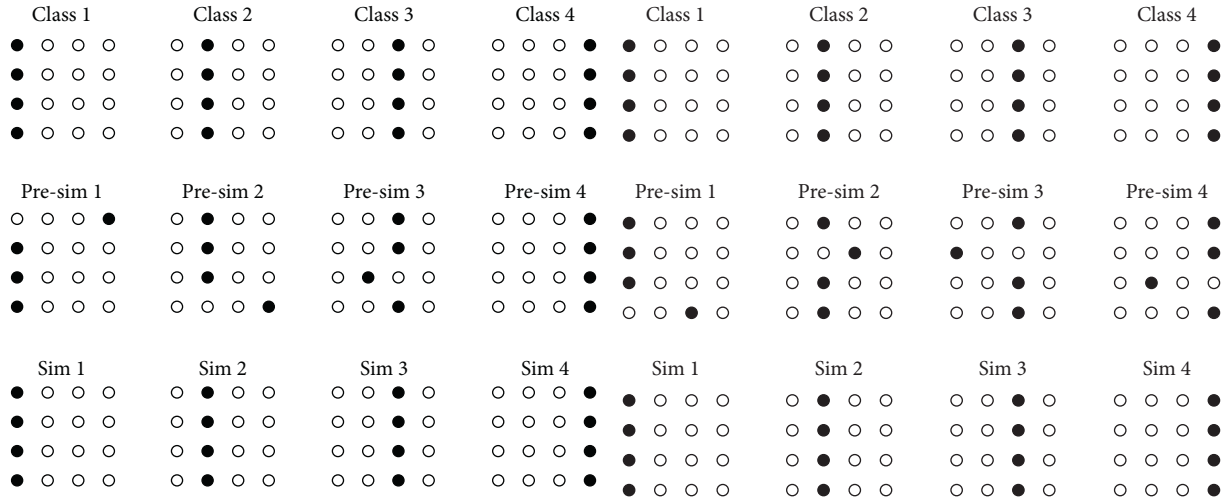
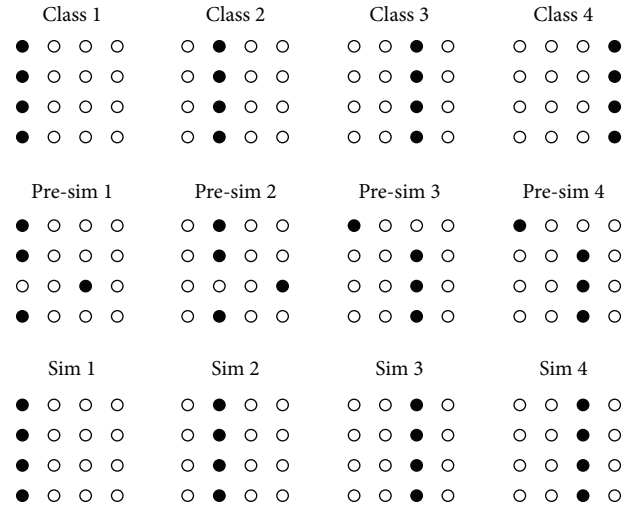


FIGURE 4: DHNN step diagram.



(a)

(b)



(c)

FIGURE 5: CEEMDAN-DHNN gear fault diagnosis and identification results.

Gear with tooth wear:  $sim\_2 = [2 \ 2 \ 2 \ 2]$ .

Gear with tooth crack:  $sim\_3 = [3 \ 3 \ 3 \ 3]$ .

Gear with tooth break:  $sim\_4 = [4 \ 4 \ 4 \ 4]$ .

Next, binarization of the coding vectors:

$$\text{Normal gear: } sim\_1 = \begin{bmatrix} 1 & -1 & -1 & -1 \\ 1 & -1 & -1 & -1 \\ 1 & -1 & -1 & -1 \\ 1 & -1 & -1 & -1 \end{bmatrix}$$

$$\text{Gear with tooth wear: } sim\_2 = \begin{bmatrix} -1 & 1 & -1 & -1 \\ -1 & 1 & -1 & -1 \\ -1 & 1 & -1 & -1 \\ -1 & 1 & -1 & -1 \end{bmatrix}$$

$$\text{Gear with tooth crack: } sim\_3 = \begin{bmatrix} -1 & -1 & 1 & -1 \\ -1 & -1 & 1 & -1 \\ -1 & -1 & 1 & -1 \\ -1 & -1 & 1 & -1 \end{bmatrix}$$

$$\text{Gear with tooth break: } sim\_4 = \begin{bmatrix} -1 & -1 & -1 & 1 \\ -1 & -1 & -1 & 1 \\ -1 & -1 & -1 & 1 \\ -1 & -1 & -1 & 1 \end{bmatrix}$$

The remaining 16 groups of data were randomly divided into three groups for gear fault status identification. Each group of data contained 4 sample entropy vectors. The following is the result of binarization of the remaining data:

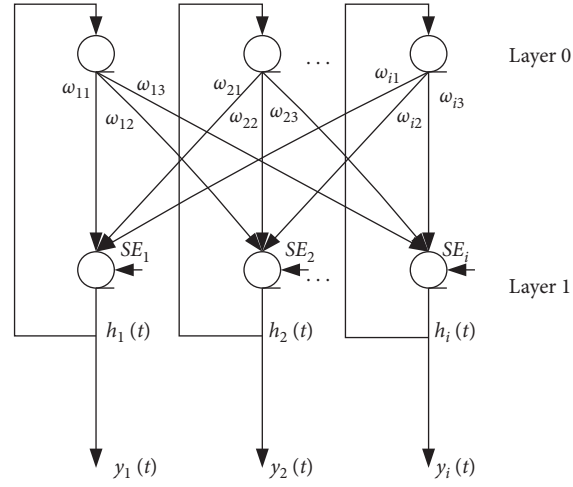


FIGURE 6: DHNN structure.

$$\begin{aligned}
 \text{sim\_1} &= \begin{bmatrix} -1 & -1 & -1 & 1 \\ 1 & -1 & -1 & -1 \\ 1 & -1 & -1 & -1 \\ 1 & -1 & -1 & -1 \end{bmatrix}, & \text{sim\_7} &= \begin{bmatrix} -1 & -1 & 1 & -1 \\ -1 & -1 & 1 & -1 \\ -1 & 1 & -1 & -1 \\ -1 & -1 & 1 & -1 \end{bmatrix}, \\
 \text{sim\_2} &= \begin{bmatrix} 1 & -1 & -1 & -1 \\ 1 & -1 & -1 & -1 \\ 1 & -1 & -1 & -1 \\ -1 & -1 & 1 & -1 \end{bmatrix}, & \text{sim\_8} &= \begin{bmatrix} -1 & -1 & 1 & -1 \\ 1 & -1 & -1 & -1 \\ -1 & -1 & 1 & -1 \\ -1 & -1 & 1 & -1 \end{bmatrix}, \\
 \text{sim\_3} &= \begin{bmatrix} 1 & -1 & -1 & -1 \\ 1 & -1 & -1 & -1 \\ -1 & -1 & 1 & -1 \\ 1 & -1 & -1 & -1 \end{bmatrix}, & \text{sim\_9} &= \begin{bmatrix} 1 & -1 & -1 & -1 \\ -1 & -1 & 1 & -1 \\ -1 & -1 & 1 & -1 \\ -1 & -1 & 1 & -1 \end{bmatrix}, \\
 \text{sim\_4} &= \begin{bmatrix} -1 & 1 & -1 & -1 \\ -1 & 1 & -1 & -1 \\ -1 & 1 & -1 & -1 \\ -1 & -1 & -1 & 1 \end{bmatrix}, & \text{sim\_10} &= \begin{bmatrix} -1 & -1 & -1 & 1 \\ -1 & -1 & -1 & 1 \\ -1 & -1 & -1 & 1 \\ -1 & -1 & -1 & 1 \end{bmatrix}, \\
 \text{sim\_5} &= \begin{bmatrix} -1 & 1 & -1 & -1 \\ -1 & -1 & 1 & -1 \\ -1 & 1 & -1 & -1 \\ -1 & 1 & -1 & -1 \end{bmatrix}, & \text{sim\_11} &= \begin{bmatrix} -1 & -1 & -1 & 1 \\ -1 & -1 & -1 & 1 \\ -1 & 1 & -1 & -1 \\ -1 & -1 & -1 & 1 \end{bmatrix}, \\
 \text{sim\_6} &= \begin{bmatrix} -1 & 1 & -1 & -1 \\ -1 & 1 & -1 & -1 \\ -1 & -1 & -1 & 1 \\ -1 & 1 & -1 & -1 \end{bmatrix}, & \text{sim\_12} &= \begin{bmatrix} 1 & -1 & -1 & -1 \\ -1 & 1 & -1 & -1 \\ -1 & -1 & -1 & 1 \\ -1 & -1 & 1 & -1 \end{bmatrix}.
 \end{aligned} \tag{14}$$

Selection standard of training samples of each component of the entropy, which were selected from Table 1, is



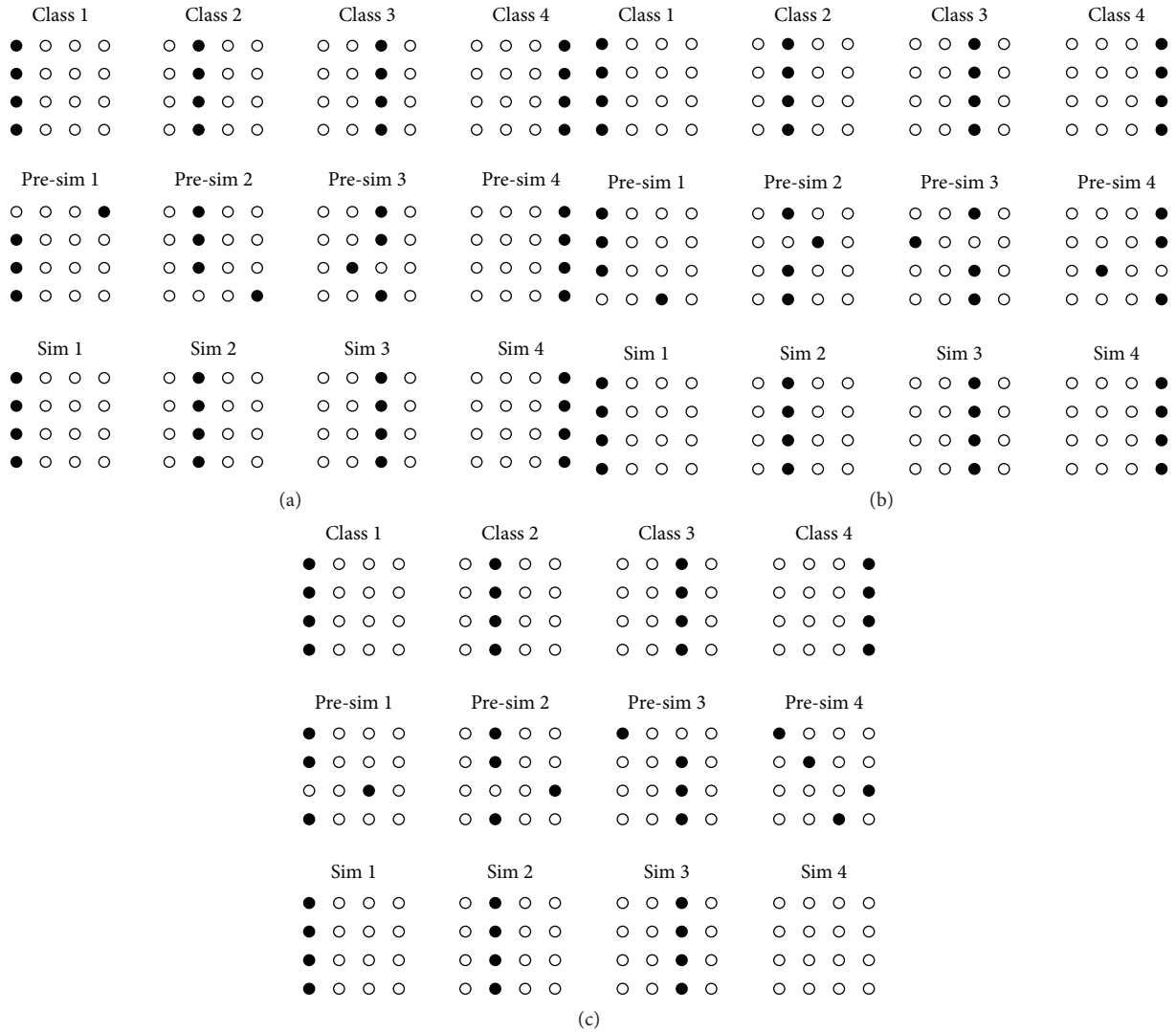


FIGURE 7: VMD-DHNN gear fault diagnosis and identification results.

the sample entropy of the signal sequence SampEn3 normal gear, the gear with tooth wear and tear of sample entropy SampEn2 signal sequence, the gear with tooth crack sample entropy SampEn3 signal sequence, and the gear tooth broken sample entropy SampEn1 input signal sequence to the DHNN training, after waiting for neural network training, and then, the remaining 12 group gears as the unknown state data were input into the trained neural network to identify the state. Before the sample entropy value is input to the DHNN, the standard data group is firstly binary coded, and then, the coding vectors are input to the DHNN for training.

### 5. Gear Fault Diagnosis Based on the VMD Sample Entropy and DHNN

The 16 sets of sample entropy value data were binarized and input to DHNN for network training as a standard sample. Then, the remaining 12 sets of sample entropy values were

tested as the test data group. The above binarization matrix was input into DHNN for classification and identification, and the VMD-DHNN recognition results are shown in Figures 7(a)–7(c).

Among them, class1 represents normal gear standard data, class2 represents gear with tooth wear standard data, class3 represents gear with tooth crack standard data, and class4 represents gear with tooth break standard data. Pre-sim1 represents the first test data, pre-sim2 represents the second test data, pre-sim3 represents the third test data, and pre-sim4 represents the fourth test data. Sim1 represents the first test data classification result, sim2 represents the second test data classification result, sim3 represents the third test data classification result, and sim4 represents the fourth test data classification result.

As shown in Figures 7(a)–7(c), 11 of the 12 test samples of the DHNN model classifier correspond to the fault features, and one of them is not recognized due to the unclear features but is not recognized incorrectly.

True class	Gear with tooth break	2			
	Gear with tooth crack		3		
	Gear with tooth wear			3	
	Normal gear				3
		Gear with tooth break	Gear with tooth crack	Gear with tooth wear	Normal gear
		Predicted class			

FIGURE 8: Confusion matrix of the VMD-DHNN classification results.

In order to get the accuracy of gear fault identification more clearly, the confusion matrix of VMD-DHNN classification results is made below. According to Figure 8, normal gear, gear with tooth wear, and gear with tooth crack faults are correctly classified, and there is a classification error in the gear with tooth break fault. However, the failure classification of gear with tooth break fault is not identified as other gear fault types.

In order to verify the superiority of the VMD-DHNN algorithm, the VMD-DHNN algorithm is compared with complete ensemble empirical mode decomposition adaptive noise (CEEMDAN)-DHNN algorithm and empirical mode decomposition (EMD)-DHNN algorithm in the accuracy of gear fault diagnosis. Firstly, the training gear fault feature vectors are input into CEEMDAN-DHNN and EMD-DHNN to obtain the gear fault identification result. Then, the test gear fault feature vectors are input into the trained CEEMDAN-DHNN and EMD-DHNN, and the classification result of gear fault is obtained.

The CEEMDAN-DHNN recognition results are shown in Figures 5(a)–5(c).

As shown in Figure 5(c), the gear with tooth break fault is identified as gear with tooth crack fault. The best recognition rate of 91.67% was obtained using CEEMDAN-DHNN.

In order to get the accuracy of gear fault identification more clearly, the confusion matrix of CEEMDAN-DHNN classification results is made below. According to Figure 9, normal gear, gear with tooth wear, and gear with tooth crack faults are correctly classified, and there is a classification error in the gear with tooth break fault.

The EMD-DHNN recognition results are shown in Figures 10(a)–10(c). It can be seen from Figure 10(c) that the gear with tooth break fault is identified as gear with tooth crack fault, the gear with tooth wear fault is identified as normal gear, and the gear with tooth crack fault is identified as the gear with tooth wear fault. The best recognition rate of 75% was obtained using EMD-DHNN.

In order to get the accuracy of gear fault identification more clearly, the confusion matrix of EMD-DHNN classification results is given in Figure 11.

Table 4 shows the gear fault diagnosis accuracy of different signal decomposition algorithms combined with DHNN and SVM.

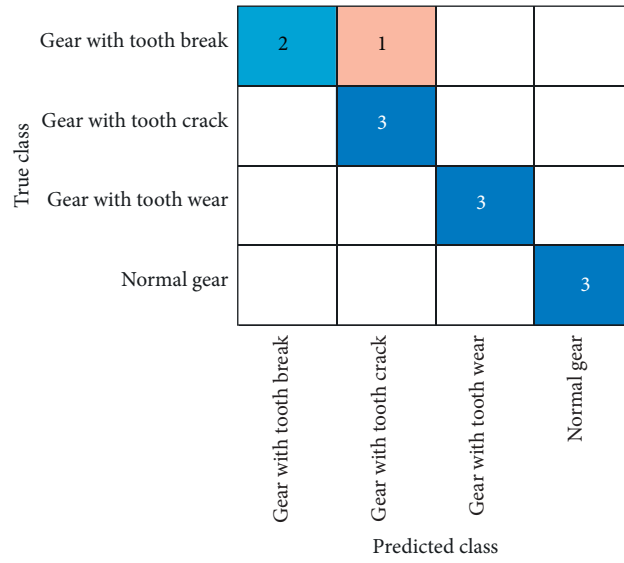


FIGURE 9: Confusion matrix of the CEEMDAN-DHNN classification results.

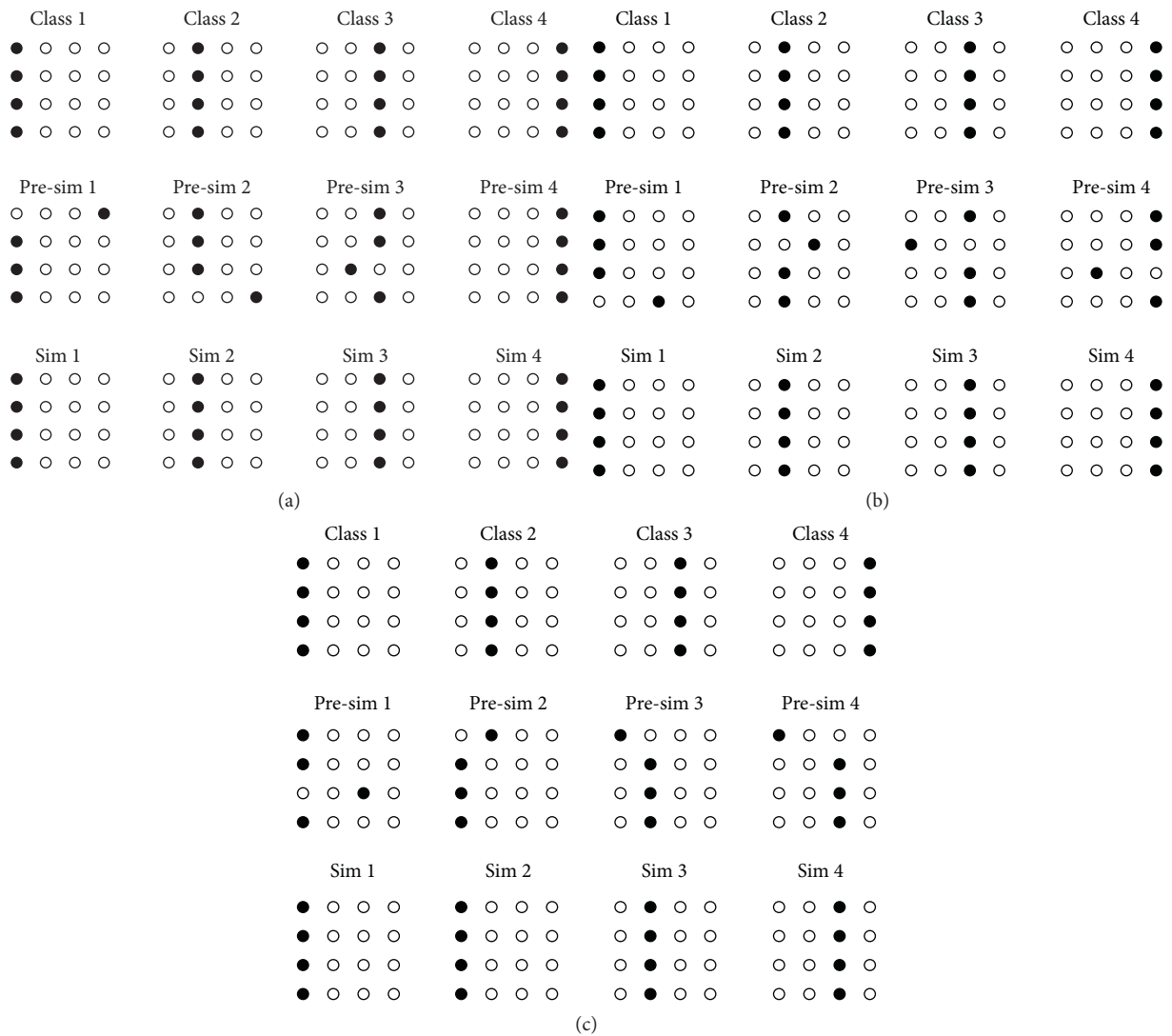


FIGURE 10: EMD-DHNN gear fault diagnosis and identification results.

True Class	Gear with tooth break	2	1		
	Gear with tooth crack		2	1	
	Gear with tooth wear			2	1
	Normal gear				3
		Gear with tooth break	Gear with tooth crack	Gear with tooth wear	Normal gear
		Predicted Class			

FIGURE 11: Confusion matrix of the EMD-DHNN classification results.

TABLE 4: Gear fault diagnosis accuracy of different signal decomposition algorithms combined with DHNN.

Signal decomposition algorithm	Classification algorithm	Accuracy (%)
EMD	DHNN	75
CEEMDAN	DHNN	91.67
VMD	DHNN	91.67
EMD	SVM	50
CEEMDAN	SVM	66.67
VMD	SVM	75

## 6. Conclusions

In this paper, a VMD-DHNN method is proposed and applied to nonstationary signal decomposition. Firstly, the vibration signals of nonstationary gear fault are decomposed by the VMD, and their center frequencies are accurately separated. Then, each decomposed IMF is an extracted sample entropy value, and the extracted feature value is formed into the feature vector. Finally, the gear fault feature vector is input to DHNN for fault diagnosis.

The optimized VMD algorithm can avoid the disadvantages of the EMD algorithm, and VMD has the advantages of fast operation speed and high-frequency accuracy of separated IMFs center. The DHNN has the advantage of associative memory and can further shorten the operation time. The combination of VMD-DHNN can improve the fault diagnosis time of gear and reduce the damage.

The VMD-DHNN is more accurate in identifying faults such as normal gear, gear with tooth wear, and gear with tooth crack. This method can be further applied to defect detection in additive manufacturing and welding. Moreover, the intelligent optimization algorithm can be utilized to optimize the parameters of VMD so that it can be adaptive to decompose the signal.

The limitation of this article is that we need to encode the signal in advance and then diagnose the fault in the input to DHNN, which may increase the complexity of the method.

## Data Availability

The data used to support the findings of this study are available from the corresponding author upon request.

## Conflicts of Interest

The authors declare that there are no conflicts of interest regarding the publication of this paper.

## Acknowledgments

This work was supported by the National Natural Science Foundation of China (nos. 51875195 and 52075163).

## References

- [1] B. Liu, S. Riemenschneider, and Y. Xu, "Gearbox fault diagnosis using empirical mode decomposition and Hilbert spectrum," *Mechanical Systems and Signal Processing*, vol. 20, no. 3, pp. 718–734, 2006.
- [2] D. Bianchi, E. Mayrhofer, M. Gröschl, G. Betz, and A. Vernes, "Wavelet packet transform for detection of single events in acoustic emission signals," *Mechanical Systems and Signal Processing*, vol. 64–65, pp. 441–451, 2015.
- [3] O. D. Mohammed, M. Rantatalo, J.-O. Aidanpää, and U. Kumar, "Vibration signal analysis for gear fault diagnosis

- with various crack progression scenarios,” *Mechanical Systems and Signal Processing*, vol. 41, no. 1-2, pp. 176–195, 2013.
- [4] J. Rafiee and P. W. Tse, “Use of autocorrelation of wavelet coefficients for fault diagnosis,” *Mechanical Systems and Signal Processing*, vol. 23, no. 5, pp. 1554–1572, 2009.
  - [5] Y. Tian, J. Ma, C. Lu, and Z. Wang, “Rolling bearing fault diagnosis under variable conditions using LMD-SVD and extreme learning machine,” *Mechanism and Machine Theory*, vol. 90, pp. 175–186, 2015.
  - [6] X. Liu, L. Bo, and H. Luo, “Bearing faults diagnostics based on hybrid LS-SVM and EMD method,” *Measurement*, vol. 59, pp. 145–166, 2015.
  - [7] M. Buzzoni, E. Mucchi, G. D’Elia, and G. Dalpiaz, “Diagnosis of localized faults in multistage gearboxes: a vibrational approach by means of automatic EMD-based algorithm,” *Shock and Vibration*, vol. 2017, Article ID 8345704, 22 pages, 2017.
  - [8] J. Rafiee, M. A. Rafiee, and P. W. Tse, “Application of mother wavelet functions for automatic gear and bearing fault diagnosis,” *Expert Systems with Applications*, vol. 37, no. 6, pp. 4568–4579, 2010.
  - [9] X. Hu, S. Peng, and W.-L. Hwang, “EMD revisited: a new understanding of the envelope and resolving the mode-mixing problem in AM-FM signals,” *IEEE Transactions on Signal Processing*, vol. 60, no. 3, pp. 1075–1086, 2011.
  - [10] Y. Li, X. Liang, Y. Yang, M. Xu, and W. Huang, “Early fault diagnosis of rotating machinery by combining differential rational spline-based LMD and K-L divergence,” *IEEE Transactions on Instrumentation and Measurement*, vol. 66, no. 11, pp. 3077–3090, 2017.
  - [11] K. Dragomiretskiy and D. Zosso, “Variational mode decomposition,” *IEEE Transactions on Signal Processing*, vol. 62, no. 3, pp. 531–544, 2013.
  - [12] J. Ding, D. Xiao, and X. Li, “Gear fault diagnosis based on genetic mutation particle swarm optimization VMD and probabilistic neural network algorithm,” *IEEE Access*, vol. 8, pp. 18456–18474, 2020.
  - [13] J. Ding, L. Huang, D. Xiao, and X. Li, “GMPSO-VMD algorithm and its application to rolling bearing fault feature extraction,” *Sensors*, vol. 20, no. 7, 1946 pages, 2020.
  - [14] J. Li, X. Yao, H. Wang, and J. Zhang, “Periodic impulses extraction based on improved adaptive VMD and sparse code shrinkage denoising and its application in rotating machinery fault diagnosis,” *Mechanical Systems and Signal Processing*, vol. 126, pp. 568–589, 2019.
  - [15] X. Yan and M. Jia, “Application of CSA-VMD and optimal scale morphological slice bispectrum in enhancing outer race fault detection of rolling element bearings,” *Mechanical Systems and Signal Processing*, vol. 122, pp. 56–86, 2019.
  - [16] X. Zhang, Q. Miao, H. Zhang, and L. Wang, “A parameter-adaptive VMD method based on grasshopper optimization algorithm to analyze vibration signals from rotating machinery,” *Mechanical Systems and Signal Processing*, vol. 108, pp. 58–72, 2018.
  - [17] Y. Li, X. Wang, Z. Liu, X. Liang, and S. Si, “The entropy algorithm and its variants in the fault diagnosis of rotating machinery: a review,” *IEEE Access*, vol. 6, pp. 66723–66741, 2018.
  - [18] Y. Chen, T. Zhang, Z. Luo, and K. Sun, “A novel rolling bearing fault diagnosis and severity analysis method,” *Applied Sciences*, vol. 9, no. 11, p. 2356, 2019.
  - [19] Y. Chen, T. Zhang, W. Zhao, Z. Luo, and H. Lin, “Rotating machinery fault diagnosis based on improved multiscale Amplitude-aware permutation entropy and multiclass relevance vector machine,” *Sensors*, vol. 19, no. 20, p. 4542, 2019.
  - [20] C. Liu, L. Zhu, and C. Ni, “Chatter detection in milling process based on VMD and energy entropy,” *Mechanical Systems and Signal Processing*, vol. 105, pp. 169–182, 2018.
  - [21] Z. Zhang, H. Li, G. Meng, X. Tu, and C. Cheng, “Chatter detection in milling process based on the energy entropy of VMD and WPD,” *International Journal of Machine Tools and Manufacture*, vol. 108, pp. 106–112, 2016.
  - [22] A. A. Abdoos, P. Khorshidian Mianaei, and M. Rayatpanah Ghadikolaei, “Combined VMD-SVM based feature selection method for classification of power quality events,” *Applied Soft Computing*, vol. 38, pp. 637–646, 2016.
  - [23] W. Deng, H. Liu, J. Xu, H. Zhao, and Y. Song, “An improved quantum-inspired differential evolution algorithm for deep belief network,” *IEEE Transactions on Instrumentation and Measurement*, vol. 69, no. 10, pp. 7319–7327, 2020.
  - [24] G. Qiu, Y. Gu, and Q. Cai, “A deep convolutional neural networks model for intelligent fault diagnosis of a gearbox under different operational conditions,” *Measurement*, vol. 145, pp. 94–107, 2019.
  - [25] J. Lei, C. Liu, and D. Jiang, “Fault diagnosis of wind turbine based on Long Short-term memory networks,” *Renewable Energy*, vol. 133, pp. 422–432, 2019.
  - [26] Z. Chen and W. Li, “Multisensor feature fusion for bearing fault diagnosis using sparse autoencoder and deep belief network,” *IEEE Transactions on Instrumentation and Measurement*, vol. 66, no. 7, pp. 1693–1702, 2017.
  - [27] H. Shao, H. Jiang, Y. Lin, and X. Li, “A novel method for intelligent fault diagnosis of rolling bearings using ensemble deep auto-encoders,” *Mechanical Systems and Signal Processing*, vol. 102, pp. 278–297, 2018.
  - [28] S. Cofre-Martel, P. Kobrich, E. Lopez Droguett, and V. Meruane, “Deep convolutional neural network-based structural damage localization and quantification using transmissibility data,” *Shock and Vibration*, vol. 2019, Article ID 9859281, 27 pages, 2019.
  - [29] J. J. Hopfield, “Neural networks and physical systems with emergent collective computational abilities,” *Proceedings of the National Academy of Sciences*, vol. 79, no. 8, pp. 2554–2558, 1982.
  - [30] D. Xiao, J. Ding, X. Li, and L. Huang, “Gear fault diagnosis based on kurtosis criterion VMD and SOM neural network,” *Applied Sciences*, vol. 9, no. 24, p. 5424, 2019.

## Research Article

# Multisensor Prognostic of RUL Based on EMD-ESN

Jiixin Pei  and Jian Wang

Computer Integrated Manufacturing System Research Center, College of Electronics and Information Engineering, Tongji University, Shanghai 201804, China

Correspondence should be addressed to Jiixin Pei; 1832973@tongji.edu.cn

Received 14 October 2020; Revised 11 November 2020; Accepted 16 November 2020; Published 24 November 2020

Academic Editor: Mohammad Mahdi Abaei

Copyright © 2020 Jiixin Pei and Jian Wang. This is an open access article distributed under the Creative Commons Attribution License, which permits unrestricted use, distribution, and reproduction in any medium, provided the original work is properly cited.

This paper presents a prognostic method for RUL (remaining useful life) prediction based on EMD (empirical mode decomposition)-ESN (echo state network). The combination method adopts EMD to decompose the multisensor time series into a bunch of IMFs (intrinsic mode functions), which are then predicted by ESNs, and the outputs of each ESN are summarized to obtain the final prediction value. The EMD can decompose the original data into simpler portions and during the decomposition process, much noise is filtered out and the subsequent prediction is much easier. The ESN is a relatively new type of RNN (recurrent neural network), which substitutes the hidden layers with a reservoir remaining unchanged during the training phase. The characteristic makes the training time of ESN is much shorter than traditional RNN. The proposed method is applied to the turbofan engine datasets and is compared with LSTM (Long Short-Term Memory) and ESN. Extensive experimental results show that the prediction performance and efficiency are much improved by the proposed method.

## 1. Introduction

Prognostics is an engineering discipline with regard to predictive diagnostics, including calculation of the remaining useful life based on the observed system condition [1]. As machines are getting increasingly complicated, prognostics for complex systems has attracted more significant interest [2]. RUL prediction enables identifying problems at an early stage, which makes it beneficial for industries to make effective maintenance planning and reduce maintenance cost [1, 3]. Research techniques of RUL have been adopted in various industrial objects, including lithium-ion battery [4] and turbofan engine [5].

In general, the RUL prediction methods are typically classified as physics-model based approaches, data-driven approaches, and hybrid approaches, and data-driven methods can be divided into statistical model based approaches and AI approaches further [6, 7]. Among them, approaches based on the physical model [8, 9] generate an explicit mathematical model of the degradation processes of machinery. The modeling process tends to be difficult because in-depth knowledge and rich experiment are required

[7]. Thus, the methods are less used [6]. Compared with physics-model based approaches, data-driven approaches are easier to be implemented. They often extract features reflecting the failure through mining the historical data. Statistical model based approaches such as AR models [10] and random coefficient models [11] describe the degradation process by statistical or stochastic models. The methods can depict the uncertainty of the degradation process and its influence on RUL prediction [6]. However, they are not good at modeling for nonlinear systems, and AI approaches such as ANNs [12, 13], NF systems [14], and SVM [15] can deal with the issue. They operate RUL prediction through feature extracting and data training without building the specific model. In recent years, research about AI approaches for RUL prediction has gained more and more attention. Hybrid approaches combine physics-model based approaches and data-driven approaches to take advantage of different approaches.

RNN (recurrent neural network) is a kind of AI approaches for RUL prediction, and it performs well for forecasting tasks of time series data [16]. But the use of RNN is limited due to the “fading memory” problem caused by

gradient explosion or gradient dispersion. A variant of RNN called LSTM (long short-term memory) was proposed [17, 18]. Lots of research work based on LSTM has been carried out, and good results are acquired [19–22].

Nevertheless, the traditional RNNs possess disadvantages of computational burdens and being time consuming because numerous parameters need to be trained. ESN (echo state networks) can provide a solution to deal with the problem [16]. ESN was first proposed in 2001 [23] and it is a relatively new type of RNN. ESN has a randomly generated reservoir, which remains unchanged during the training phase and only a readout is trained [24]. The characteristic makes ESN consumes much less time for the training process compared with traditional RNN such as LSTM. In-depth research for RUL prediction based on ESN still needs to be carried out [16]. Most of the existing research concentrates on optimization of the architecture and parameters of ESNs to obtain a better prediction result [25, 26].

However, existing research lacks attention to the analysis and mining of the original data. To deal with this, decomposing the raw time series into subsequence is an effective solution [27–30]. Reference [28] proposed an SDA (secondary decomposition algorithm) to decompose the original wind speed data into detailed components twice. The decomposition algorithms include WPD (wavelet packet decomposition) and FEEMD (fast ensemble EMD). Then an Elman neural network performed the prediction. In [29], to mitigate the problem that the model cannot handle environmental factors, a hybrid EMD-based prediction model was proposed for wind speed and solar irradiation forecasts. In [30], for chaotic time series prediction, PE (permutation entropy) was adopted to analyze the complexity of the IMFs decomposed by EEMD (ensemble EMD). The decomposed IMFs with similar complexities were combined, so fewer inputs for prediction were gained. Then, the ESNs performed the prediction and the ultimate results were assembled.

Although the combination of signal decomposition and ESN have performed well for forecasting problems, in recent years, few related studies have been conducted. As far as the authors know, they are not yet applied to RUL prediction. In most cases, the prediction of RUL is based on multisensor data and a large amount of noise needs to be filtered out. Signal decomposition methods can handle noise well exactly. Inspired by this, this paper proposes a novel combination method for RUL prediction based on EMD and ESN. EMD can smooth the noisy data and decompose the time series into a bunch of IMFs, which are then predicted by ESNs. The outputs of the ESNs are summarized as the final RUL prediction results. Besides, data processing methods including GBDT feature selection and Kalman filtering are also adopted. The proposed method is verified through a case study on turbofan engines of aircraft. The relevant data of turbofan engines is collected from multiple sensors under variable operating conditions. The proposed method is compared with ESN and LSTM [19]. The results demonstrate the superiority of our proposed method. The contributions of this paper are as follows: (1) We introduce the idea of signal decomposition to multisensor data processing for

RUL prediction. The adoption of EMD has a good effect on noise disposal, which provides a reference solution for reducing the noise of the RUL prediction problem. (2) We propose a combination method of EMD and ESN for RUL prediction, which provides a new idea for RUL prediction methods based on ESN. (3) We conduct a lot of experiments on C-MAPSS datasets. During the process, some data processing skills such as GBDT feature selection and Kalman filtering are adopted. The results show that our proposed method is well performed and effective for RUL prediction.

The rest of this paper is organized as follows. Section 2 elaborates the methodology and presents our method. Section 3 demonstrates our experimental process. Meanwhile, a comparison of models and results analysis is also given. In Section 4, conclusion and highlights of future work are drawn.

## 2. Methodology

**2.1. Empirical Mode Decomposition.** The EMD [31] is the core component of the Hilbert–Huang transform. It is an adaptive time-frequency analysis method for processing nonlinear and nonstationary time series. EMD can decompose time series into a group of IMFs without analysis in advance. An IMF should satisfy two conditions: (1) Throughout the data segment, the number of the extreme points and that of the zero crossing points should be equal or the difference is no more than 1; (2) The mean of the upper envelope formed by the local maximum points and the lower envelope formed by the local minimum points is zero. The detailed steps of the EMD decomposition process are described below.

- (1) Assume the time series to be analyzed is  $x(t)$ . Extract all the local maxima and minima.
- (2) Fit the maximum value points and minimum value points by cubic spline interpolation, respectively, to form the maximum value envelope  $e \max(t)$  and the minimum value envelope  $e \min(t)$ . The mean value of the extreme envelopes  $m(t)$  can be obtained:

$$m(t) = \frac{(e \max(t) + e \min(t))}{2}. \quad (1)$$

- (3) Subtract the mean value  $m(t)$  of the envelope from the original time series  $x(t)$ , and record the result as  $y1(t)$ .

$$y1(t) = x(t) - m(t). \quad (2)$$

- (4) Determine whether  $y1(t)$  is an IMF component according to the above-mentioned judgement criteria of the two conditions. If  $y1(t)$  does not meet the conditions, treat  $y1(t)$  as the original data and repeat the above steps until  $y1(t)$  satisfies IMF conditions. At this time, take  $c1(t) = y1(t)$  and  $c1(t)$  as the first IMF component of the time series  $x(t)$ .



- (5) Take the remaining data  $r_1(t) = x(t) - c_1(t)$  as the original time series and decompose it for  $k$  times with the same principles as above to obtain the  $k$ -order IMF and a residual. The stopping criterion includes the following: (i) The residual  $r(t)$  is a monotone function; (ii) the  $k$ th IMF or the residual  $r(t)$  is smaller than the specified threshold; (iii) the number of zero crossing points and extrema values differs by 1 at most.
- (6) Finally,  $x(t)$  can be described as follows:

$$\mathbf{x}(t) = \sum_{k=1}^n c_k(t) + r(t), \quad (3)$$

where  $c_k(t)$ ,  $r(t)$  and  $n$  represent the  $k$ th IMF, the residual, and the number of IMFs, respectively.

## 2.2. Echo State Network

**2.2.1. Basic Structure of ESN.** ESN is a relatively new type of RNN, which replaces a reservoir for the hidden layers of RNN [23]. It is able to catch the system's dynamic behaviours and has intrinsic memory properties [16]. ESN uses the reservoir to map input space to feature space, in which neurons connect with each other randomly and sparsely. Input, feedback, and connection in the reservoir matrix are generated at random and remain unchanged during the training process, so the only variable that needs to be trained is the output matrix, which realizes computational savings.

As shown in Figure 1, ESN consists of a  $K$  units' input layer, a  $N$  internal units' reservoir, and a  $M$  units' output layer. The directed arrows represent the weight connections of neurons. The solid arrows indicate required connections, while the dashed arrows denote that connections are possible but not required. At time step  $t$ , variables of the input units are  $\mathbf{u}(t) = (u_1(t), u_2(t), \dots, u_K(t))^T$ , of the internal units are  $\mathbf{x}(t) = (x_1(t), x_2(t), \dots, x_N(t))^T$ , and of the output units are  $\mathbf{y}(t) = (y_1(t), y_2(t), \dots, y_L(t))^T$ . The input weight matrix  $W^{\text{in}} \in R^{N \times K}$  represents the weights from input units to internal units, and the internal weight matrix  $W \in R^{N \times N}$  represents the weights between the internal units and the feedback weight matrix  $W^{\text{back}} \in R^{N \times L}$  represents the weights from the output units to the internal units. Activation functions such as sigmoid function and hyperbolic tangent function are adopted in the reservoir and the output layer. And at time step  $t$  the reservoir state can be acquired as follows:

$$\mathbf{x}(t) = f(W^{\text{in}}\mathbf{u}(t) + W\mathbf{x}(t-1) + W^{\text{back}}\mathbf{y}(t-1)), \quad (4)$$

where  $f = \{f_1, f_2, \dots, f_N\}$  are activation functions of the internal units. The ESN's output equation can be obtained as follows:

$$\mathbf{y}(t) = f^{\text{out}}(W^{\text{inout}}\mathbf{u}(t) + W^{\text{out}}\mathbf{x}(t) + W^{\text{outout}}\mathbf{y}(t-1)), \quad (5)$$

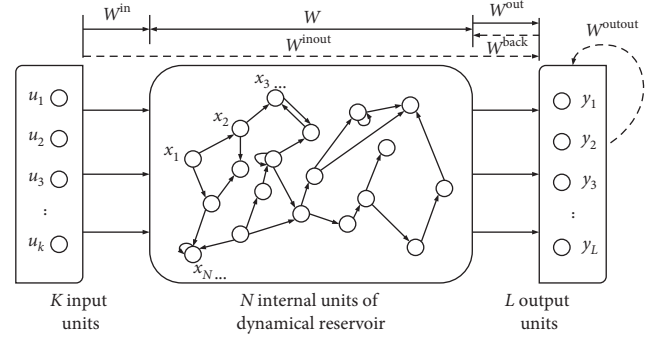


FIGURE 1: Basic structure of ESN.

and if we use  $W^{\text{out-gen}} = \{W^{\text{inout}}, W^{\text{out}}, W^{\text{outout}}\}$  to indicate all the connections to the output neurons, then the above formula can be given as follows:

$$\mathbf{y}(t) = f^{\text{out}}(W^{\text{out-gen}}[\mathbf{u}(t); \mathbf{x}(t); \mathbf{y}(t-1)]), \quad (6)$$

where  $f^{\text{out}} = \{f_1^{\text{out}}, f_2^{\text{out}}, \dots, f_M^{\text{out}}\}$  are also activation functions for the output layer which are often chosen to be linear. Moreover,  $[\mathbf{u}(t); \mathbf{x}(t); \mathbf{y}(t-1)]$  is a concatenation of the input state, internal state, and the output state of the last time step. The dimension of the output weights  $W^{\text{out-gen}}$  is  $M \times (K + N + M)$ .

Thus, we can use  $ESN = \{W^{\text{in}}, W^{\text{inout}}, W^r, W^{\text{out}}, W^{\text{outout}}, W^{\text{back}}\}$  to depict the ESN and the weights  $W^{\text{inout}}$ ,  $W^{\text{outout}}$ , and  $W^{\text{back}}$  are optional. All the weights except the output weights  $W^{\text{out-gen}}$  are initialized randomly and remain unchanged during the training process. Only the weights  $W^{\text{out-gen}}$  need to be trained.

### 2.2.2. Key Parameters of ESN

- (1) Reservoir size ( $N$ ): The reservoir size  $N$  represents the number of neuron units in the reservoir, which is very important and has a great influence on the performance of ESN [32]. If  $N$  is chosen to be too small, the network may not fit the expected output fully, while a too large reservoir may cause data overfitting and calculation consumption. The choice of  $N$  should take the complexity and effectiveness of the network into account to meet specific task requirements.
- (2) Spectral radius ( $\rho(W^r)$  or SR). The spectral radius represents the maximum absolute eigenvalue of the internal weight matrix ( $W$ ) of the reservoir. It decides the memory capacity of the ESN. If it is too small, the previous input has little effect on the present output, and the reservoir has a poor memory. If it is too large, the state of the reservoir may be unstable during the iteration process. It is not sufficient but necessary that the setting  $\rho(W^r) < 1$  can guarantee ESP (echo state property) in most cases [33]. ESP can ensure the network state is uniquely decided by the input history [26].

- (3) Sparsity ( $D$ ): Different from most neuron networks, the neurons in the reservoir are not fully connected and the sparsity denotes the sparse degree of the neurons in the reservoir. In a general way, the  $D$  is selected around 0.1 to guarantee the reservoir has enough dynamic properties [34]. When  $D$  is selected as 1, the neurons in the reservoir is fully connected and the ESN has evolved into a traditional RNN at this time.
- (4) Input scaling ( $\alpha_{W^{\text{in}}}$ ): The input scaling factor  $\alpha_{W^{\text{in}}}$  is a parameter that can realize a scaling transform to the input weight matrix  $W^{\text{in}}$  and it influences the degree of linearity of the responses of the reservoir units [35]. The larger  $\alpha_{W^{\text{in}}}$  is, the more nonlinear the response is. It is usually chosen to be within the interval  $[0, 1]$ .

2.2.3. *Training Steps of ESN.* Assume that a training sample is  $(\mathbf{u}(t), \mathbf{y}(t))$ , which contains  $t$  time steps. The general training steps of ESN are depicted below.

- (1) Initialize the parameters of ESN. The ESN weights  $\{W^{\text{in}}, W^r, W^{\text{out}}\}$  are randomly initialized first. To satisfy the requirement of ESP (echo state property), the  $W^r$  is scaled by the scaling factor  $\alpha_{W^r}$  to meet  $\rho(W^r) < 1$ . The state variables  $\mathbf{x}(0)$  also need to be initialized.
- (2) Update and collect the internal states of the reservoir. The internal states can be updated according to equation (4) driven by input signals  $\mathbf{u}(t)$  and the internal state of the last time step  $\mathbf{x}(t-1)$ . The state variables before the time step  $k_{\text{min}} - 1$  should be abandoned to eliminate the influence of initial states on the network performance, which is called the washout phase. The state variables after  $k_{\text{min}}$  are collected.
- (3) Compute the output weights. The output weights  $W^{\text{out}}$  are computed according to equation (5) to minimize the target function.

2.3. *Combination Model Based on EMD-ESN.* A combination model based on EMD and ESN is adopted in this paper, comprising decomposition of EMD, prediction of the ESNs, and summation of the separate outputs. The process is demonstrated in Figure 2.

First, the raw time series has been denoised to obtain cleaner results, which are then taken as inputs to be decomposed by EMD into IMFs adaptively. The IMFs are arranged from high to low frequency and the complexity of the IMFs is reduced greatly; thus the analysis and modeling of each IMF are much easier.

Second, we use multiple ESNs to train and predict decomposed IMFs. The training steps are illustrated in Section 2.2.3. A sampling window is used to construct samples of the training and testing datasets, which are taken as inputs to train the ESNs. Each ESN gives an output.

Finally, the outputs of the ESNs are assembled to obtain the final prediction result of the RUL.

### 3. Experimental Study

#### 3.1. Experimental Setup

3.1.1. *C-MAPSS Dataset.* The dataset used to support the findings in this paper have been deposited in the "Turbofan Engine Degradation Simulation Data Set," NASA Ames Prognostics Data repository [36], which contains simulated degradation data for turbofan engine [37]. There are 4 sub-datasets in the C-MAPSS dataset denoted as FD001, FD002, FD003, and FD004. Each dataset contains multivariate time series data under different kinds of operational conditions and fault modes. It is also separated into a training set and a testing set, as shown in Table 1. Each row is a snapshot of the run-to-failure records taken within a single time cycle. It contains 26 columns, which represent an engine ID, a current operational cycle number, 3 operational settings, and 21 sensor values, respectively. Each engine unit's initial state is unknown but is considered to be healthy. As the operational cycle number increases, the engine units begin to degrade at some point, which is also unknown. For the training set, the engines run till a failure occurs and the whole snapshots of degradation data can be acquired. While for the test set, the degradation ends sometime prior to a failure. The goal is to predict the number of remaining operational cycles (RUL) for the test set to verify our proposed method.

#### 3.1.2. Data Preprocessing

(1) *Sensor Data Selection and Normalization.* There are 21 sensor measurements contained in the C-MAPSS dataset. However, not all variables are closely related to the RUL prediction. We analyze the correlation between sensor data and the RUL values to select important features using GBDT (gradient boost decision tree). GBDT is a kind of ensemble learning algorithm with the decision tree as its basic estimator. It performs well when used for feature selection and can output the relative importance of the features, which is shown in Figure 3. The results are ranked according to relevance from high to low, and the top 10 sensor measurements are selected as the data to be analyzed next.

As different ranges of sensor values are generated, min-max normalization has been used to normalize the original data and limit it within the interval  $[0, 1]$ .

$$x_{i,j}'(t) = \frac{x_{i,j}(t) - \min(\mathbf{x}_{i,j})}{\max(\mathbf{x}_{i,j}) - \min(\mathbf{x}_{i,j})}, \quad (7)$$

where  $x_{i,j}(t)$  is the original sensor measurement of the  $j$ th sensor of the unit  $i$ .  $\min(\mathbf{x}_{i,j})$  and  $\max(\mathbf{x}_{i,j})$  represent the minimum value and the maximum value of the unit  $i$ .  $x_{i,j}'(t)$  is the normalized value.

(2) *Samples Constructed through Time Window.* In order to construct training samples of the ESNs, a time window is used, sliding along the processed sensor data. As shown in

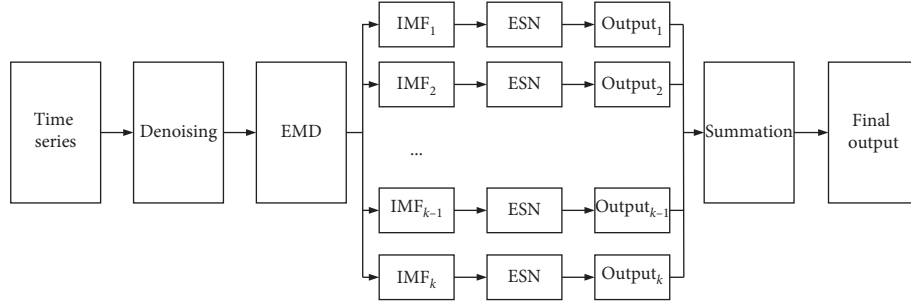


FIGURE 2: Flowchart of the combination model based on EMD-ESN.

TABLE 1: Information of the C-MAPSS dataset.

C-MAPSS data set	FD001	FD002	FD003	FD004
Engine units for training	100	260	100	249
Engine units for testing	100	259	100	248
Operating conditions	1	6	1	6
Fault modes	1	1	2	2

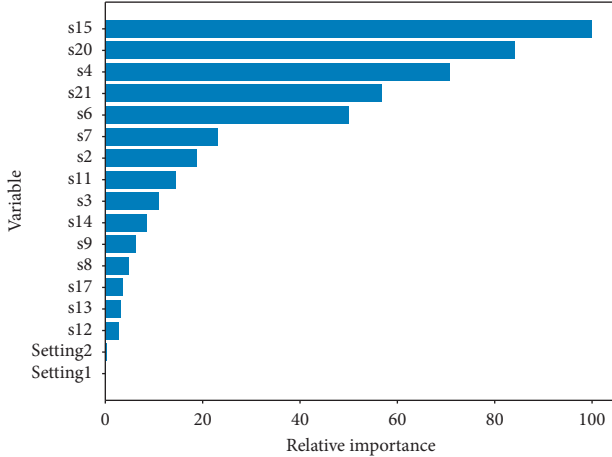


FIGURE 3: Relative importance ranking of the features in train\_FD001 by GBDT.

Figure 4, the length of the time window is time\_step. Each time the time window slides forward for one time-unit, an overlap exists in the two adjacent samples. The RUL value of the last time step is taken as the label of the training sample. Assume that the maximum life cycle of the equipment is  $L$  and the length of the time window is  $l$ , then the number of training samples we can obtain is  $L - l + 1$ .

**3.1.3. Performance Metrics.** To evaluate the performance of our proposed method, a score function and RMSE are used at the same time in this paper. Equation (8) denotes the definition of the scoring function.

$$(8) \quad \begin{cases} \sum_{i=1}^n (e^{-(h_i/13)} - 1), & \text{when } h_i < 0, \\ \sum_{i=1}^n (e^{-(h_i/10)} - 1), & \text{when } h_i \geq 0, \end{cases}$$

where  $n$  is the total number of the testing data samples, and  $h_i = \overline{\text{RUL}}_i - \text{RUL}_i$  (for the  $i_{\text{th}}$  data point estimated RUL - true RUL). More penalty is given to overestimation than early predictions by the function since in a real industrial scene, late maintenance may result in more severe consequences than untimely maintenance.

Root Mean Square Error (RMSE) is defined as equation (9), which is a widely used evaluation metric for RUL estimation. RMSE gives an equal penalty to both early and late predictions. The difference between the scoring function and the RMSE function can be seen in Figure 5.

$$(9) \quad \text{RMSE} = \sqrt{\frac{1}{n} \sum_{i=1}^n h_i^2}$$

**3.1.4. RUL Target Function.** In practical prognostic applications, the accurate RUL values of the turbofan engines are unknown, which is different from our simulation experiment data as it contains the specific RUL value of each cycle [22]. In a system, the degradation of the equipment for the initial period of time is negligible until it runs for a certain time. So, the initial state of the engines is often taken as healthy and a piecewise linear RUL target function is adopted for the prediction. As shown in Figure 6, the maximum RUL value is limited to a constant value of 130 cycles [19, 38], which represents that we neglect degradation in the initial cycles and the linear decline of the RUL value starts from the time cycle of the number 130.

**3.1.5. Prognostic Procedure.** The prognostic procedure can be depicted in Figure 7. First, the raw data is preprocessed including Kalman filtering, data normalization, and sensor data selection to obtain cleaner data. Then, the processed data is selected through time window sliding and training samples are constructed. Next, the time series is decomposed by EMD and multiple IMFs and a RES are obtained, which are then trained by ESNs of the same number. Finally, the output of each ESN is added up to get the final prediction result.

## 3.2. Experimental Procedure and Performance Analysis

**3.2.1. Experimental Procedure and Comparison.** In this section, we take FD001 dataset as an example to demonstrate

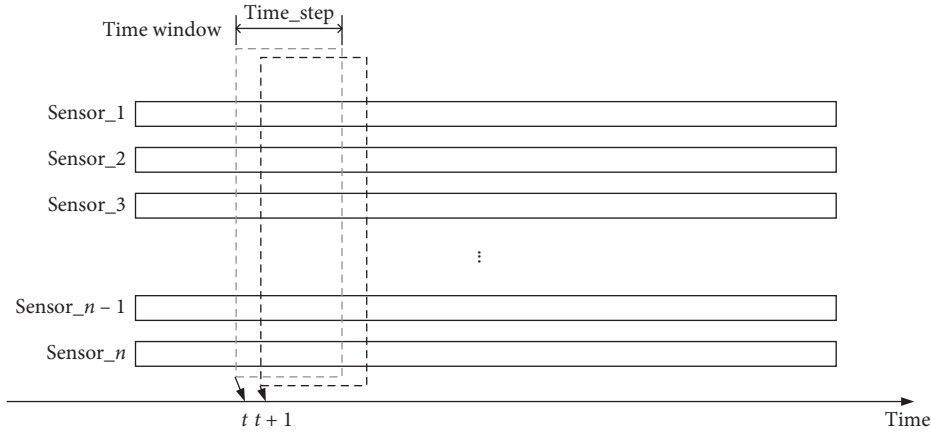


FIGURE 4: Training samples constructing through a time window.

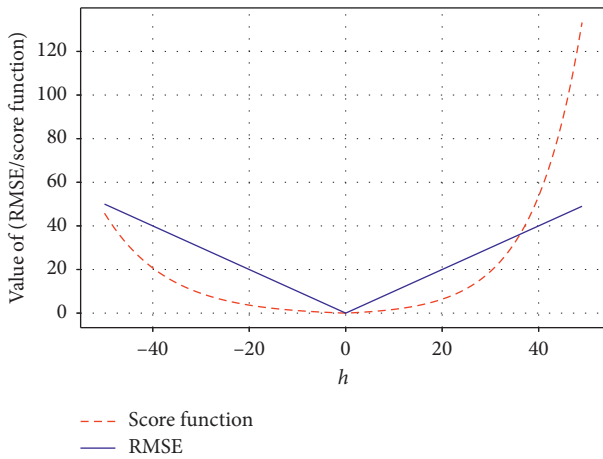


FIGURE 5: Comparison of the scoring function and RMSE.

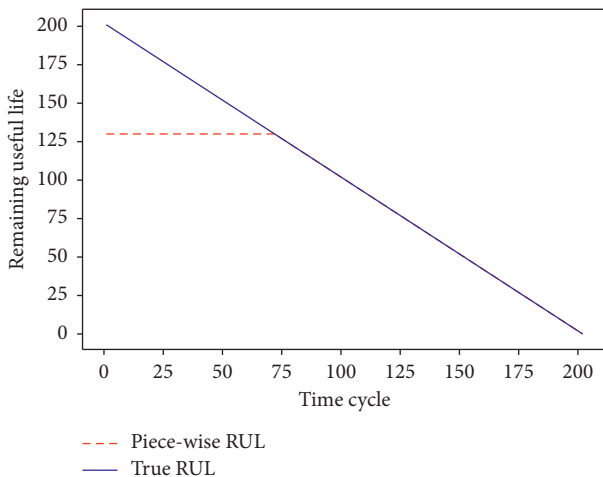


FIGURE 6: Piecewise RUL of C-MAPSS data set (the maximum RUL is 130 time cycles).

the experimental procedure. Then, the proposed method is employed on the C-MAPSS data set and is compared with LSTM [17] and basic ESN. Finally, a results analysis is given.

(1) *The Time Window Length Selection Experiment.* An experiment is carried out to select the most appropriate length of the time window to construct training samples. As we can see in Figure 8, the corresponding relations between the time step and RMSE are shown. As the time step increases, the trend of RMSE is generally downward. This can explain that to a certain degree, the more historical data training samples take, the more accurate the prediction is. The minimum cycles of the test dataset are only 31, so we choose 30 as the length of the time window in this paper. Besides, when the length grows more than 30, the decline of RMSE is not that much. In some research based on the C-MAPSS data set, the length of the time window is also chosen to be no more than 30 [19, 21, 22, 25, 26].

(2) *The EMD Decomposition.* After the process of feature extraction by GBDT and sampling by the time window, the 10 sensor measurements are then decomposed by EMD. The decomposition result of the training set of FD001 is shown in Figure 9. There are 4 IMFs and a RES generated, which have simpler information each and can be synthesized into the original time series. The decomposition results are taken as the input of the ESNs next. Much noise can be filtered out during the decomposition process, which is beneficial for prediction improvement.

(3) *The ESN Training Experiment.* As depicted in Sections 2.2.2 and 2.2.3, to train ESN, we need to set some parameters, i.e., the reservoir size  $N$  which influences dynamics of the system, the spectral radius  $SR$  which decides the ESP (echo state property) of the reservoir, the sparsity  $D$  to represent the connection degree of the neurons, and the input scaling  $\alpha_{W_{in}}$  to scale the input signal. Besides, in this paper, the regularization coefficient  $\lambda$  is used to prevent overfitting. With the grid search strategy, the parameters of the ESN are set as the values in Table 2.

The training process of the ESN can be divided into two subprocesses, which includes preliminary training and weights calculation. The preliminary training process is for the purpose to eliminate the effects of the initial network state on the training process. The weights calculation process

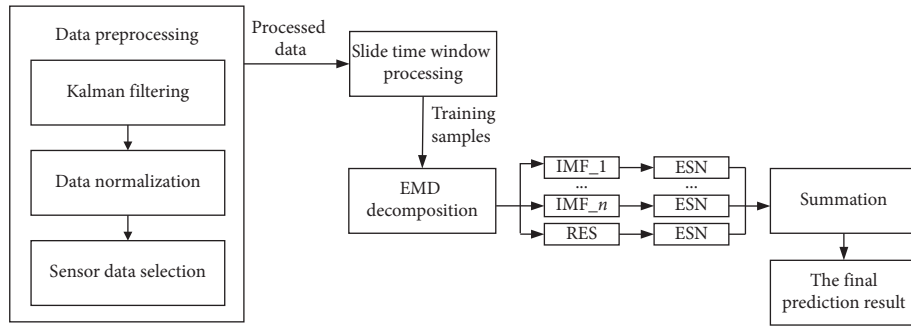


FIGURE 7: Flow chart of the prognostic procedure.

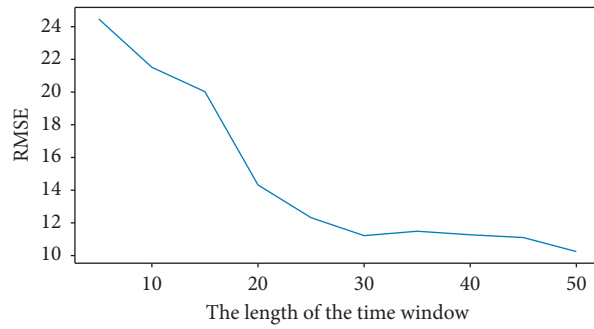


FIGURE 8: Influence of different time steps on the prediction accuracy in train\_FD001.

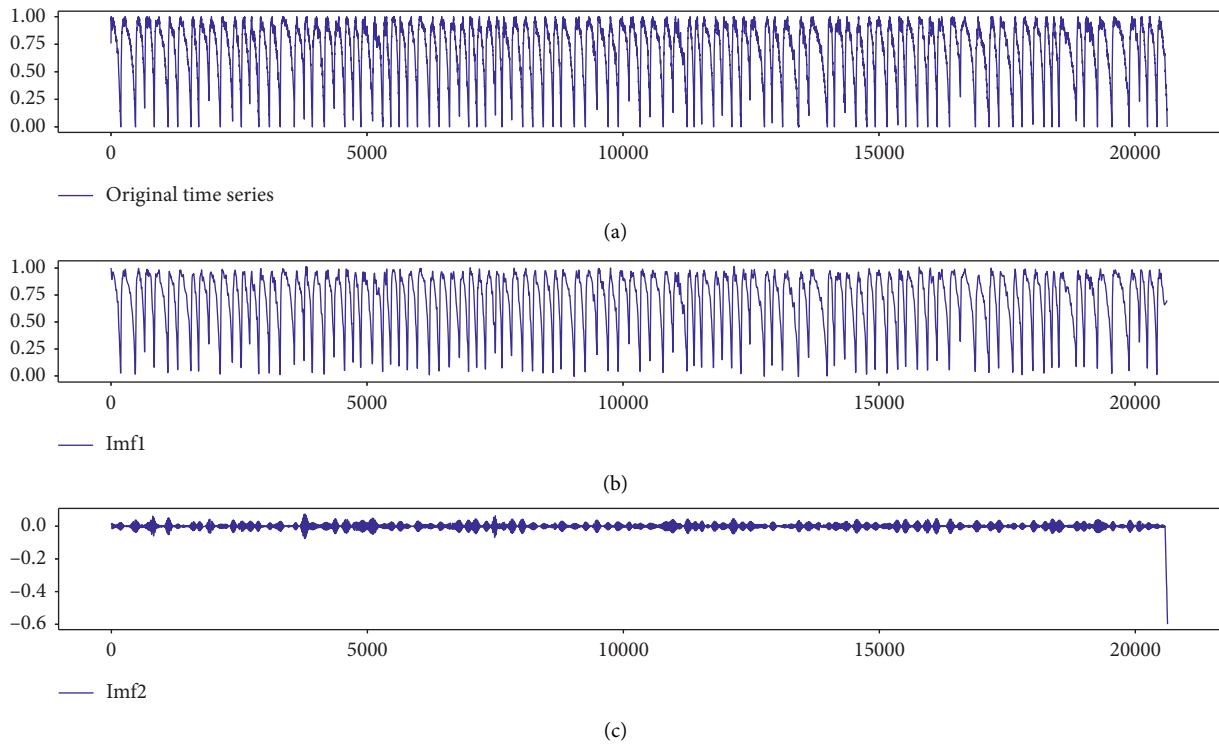


FIGURE 9: Continued.

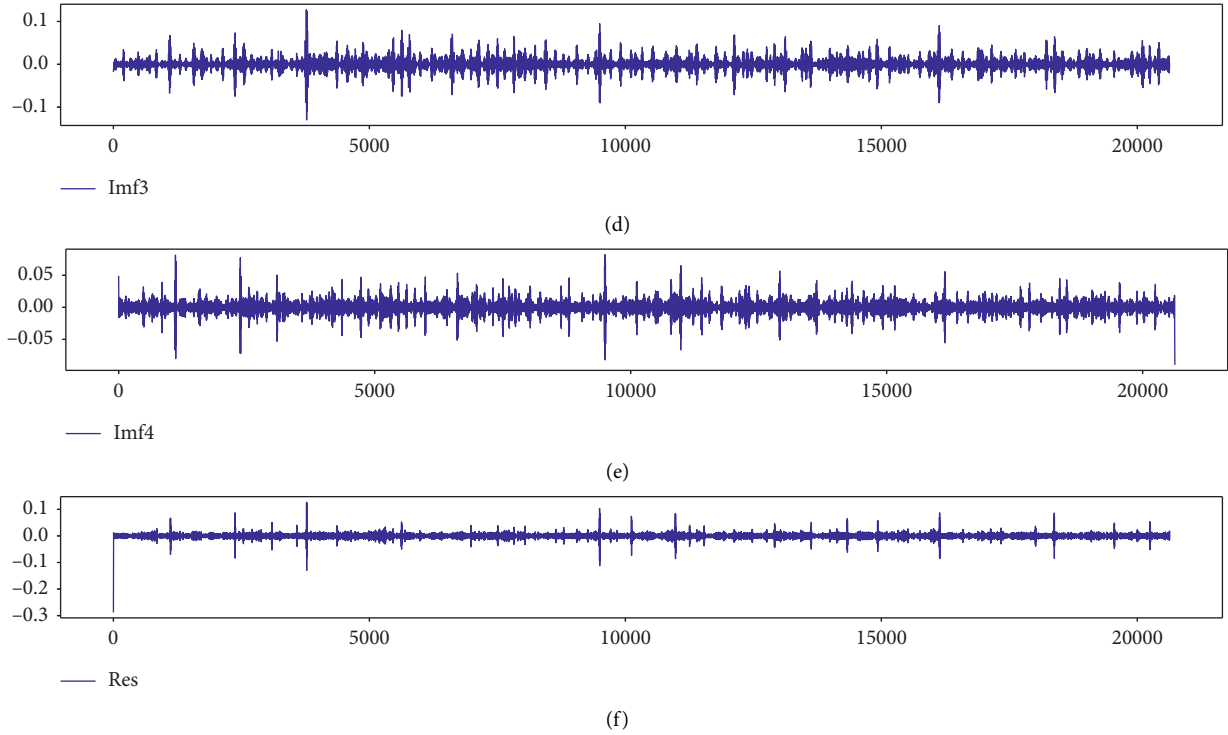


FIGURE 9: Decomposition results of the processed data in train\_FD001.

TABLE 2: Parameter setting of the ESN.

Optimal parameter	Value
Reservoir size $N$	0.9
Spectral radius SR	500
Sparsity $D$	0.2
Input scaling $\alpha_{W^{in}}$	0.05
Regularization coefficient $\lambda$	0.0001

is to calculate the  $W^{\text{out}}$  illustrated in Section 2.2.3, which is taken as a linear regression process. The learning algorithm adopted in this paper is RR (Ridge Regression). The hyperbolic tangent function is chosen as the activation function in this paper, which can be expressed as equation (10). The response curve is demonstrated in Figure 10. The activation can make the network have good nonlinearity.

$$f(x) = \frac{e^x - e^{-x}}{e^x + e^{-x}}. \quad (10)$$

The overall prediction results are shown in Figures 11 and 12, which demonstrate the prediction of ESN and EMD-ESN, respectively. As we can see in the figures, the models of ESN and EMD-ESN have both acquired good results. However, the prediction accuracy is enhanced by EMD-ESN. The circumstances of overpredicting have also been reduced, which is encouraged in the PHM (prognostics and health management) applications because delay maintenance may cause major damage and cost. Besides, it can be discovered that when the actual RUL values are relatively small, an overprediction situation is more likely to happen.

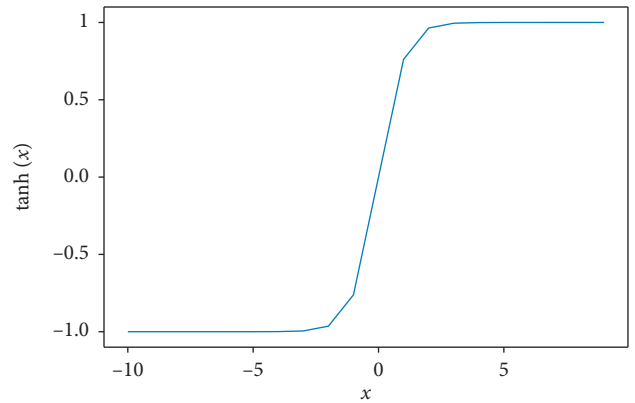


FIGURE 10: The response curve of the activation function.

One of the reasons for the problem may be that the amount of historical data is small.

**3.2.2. Results Comparison and Analysis.** In the experiment, the prediction performance and efficiency of EMD-ESN, LSTM, and ESN are compared. The experimental results and analysis are discussed below.

*(1) Results Comparison of Prediction Performance.* The results of the prediction performance of different models are revealed in Table 3. The performance metrics include Score and RMSE, which are depicted in Section 3.1.3. The length of the time window is 15 for LSTM and is 30 for ESN and EMD-ESN. Although more historical training data often

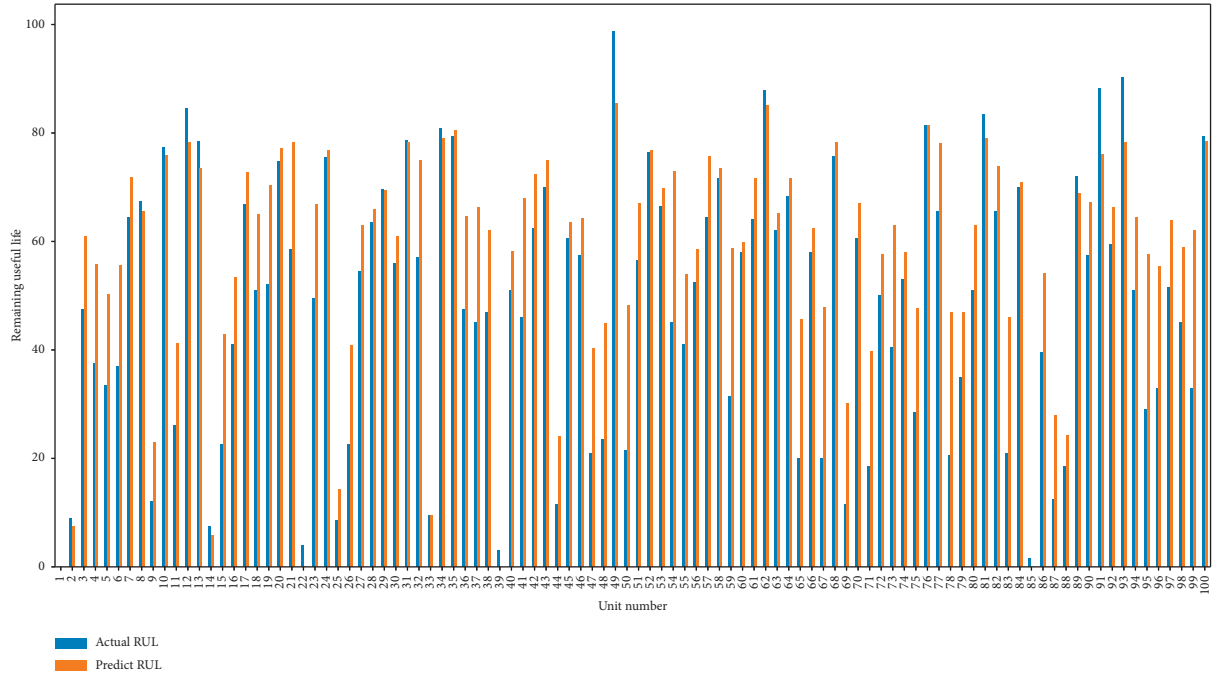


FIGURE 11: The prediction results of ESN for 100 units in test\_FD001.

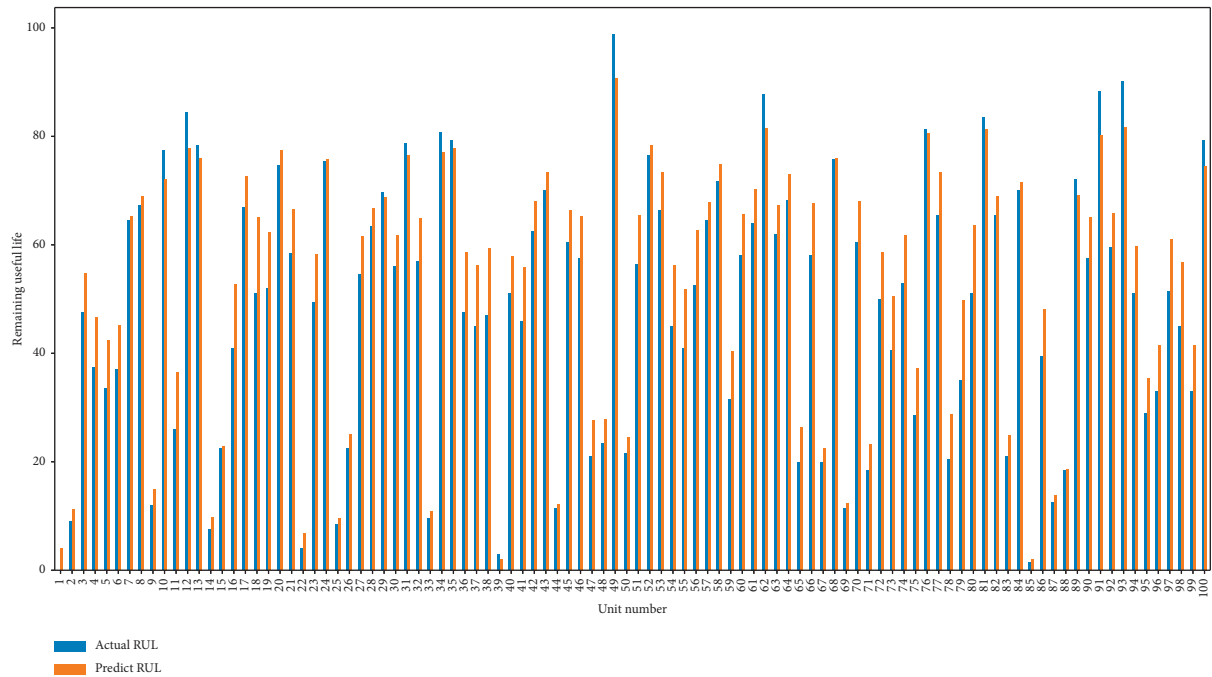


FIGURE 12: The prediction results of EMD-ESN for 100 units in test\_FD001.

TABLE 3: Prediction comparison on C-MAPSS data set. The IMP over LSTM represents an improvement of EMD-ESN over LSTM ( $IMP = 1 - EMD - (ESN/LSTM)$ ), while the IMP over ESN represents improvement of EMD-ESN over ESN ( $IMP = 1 - EMD - (ESN/ESN)$ ).

Data set	FD001		FD002		FD003		FD004	
	Score	RMSE	Score	RMSE	Score	RMSE	Score	RMSE
LSTM [21]	338	16.14	4450	24.49	852	16.18	5550	28.17
ESN	359	13.92	748	13.33	4971	23.72	2912	16.88
EMD-ESN	<b>184</b>	<b>10.63</b>	<b>293</b>	<b>8.85</b>	<b>299</b>	<b>11.54</b>	<b>525</b>	<b>9.87</b>
IMP over LSTM (%)	45.56	34.14	93.41	63.86	64.91	28.68	90.54	64.96
IMP over ESN (%)	48.75	23.64	60.83	33.61	93.99	51.35	81.97	41.53



TABLE 4: Training time comparison on C-MAPSS data set.

Data set	FD001 (s)	FD002 (s)	FD003 (s)	FD004 (s)
LSTM [21]	6540.53	17159.43	7649.63	15494.50
ESN	34.58	105.80	47.84	91.57
EMD-ESN	419.40	1318.06	508.97	1262.64

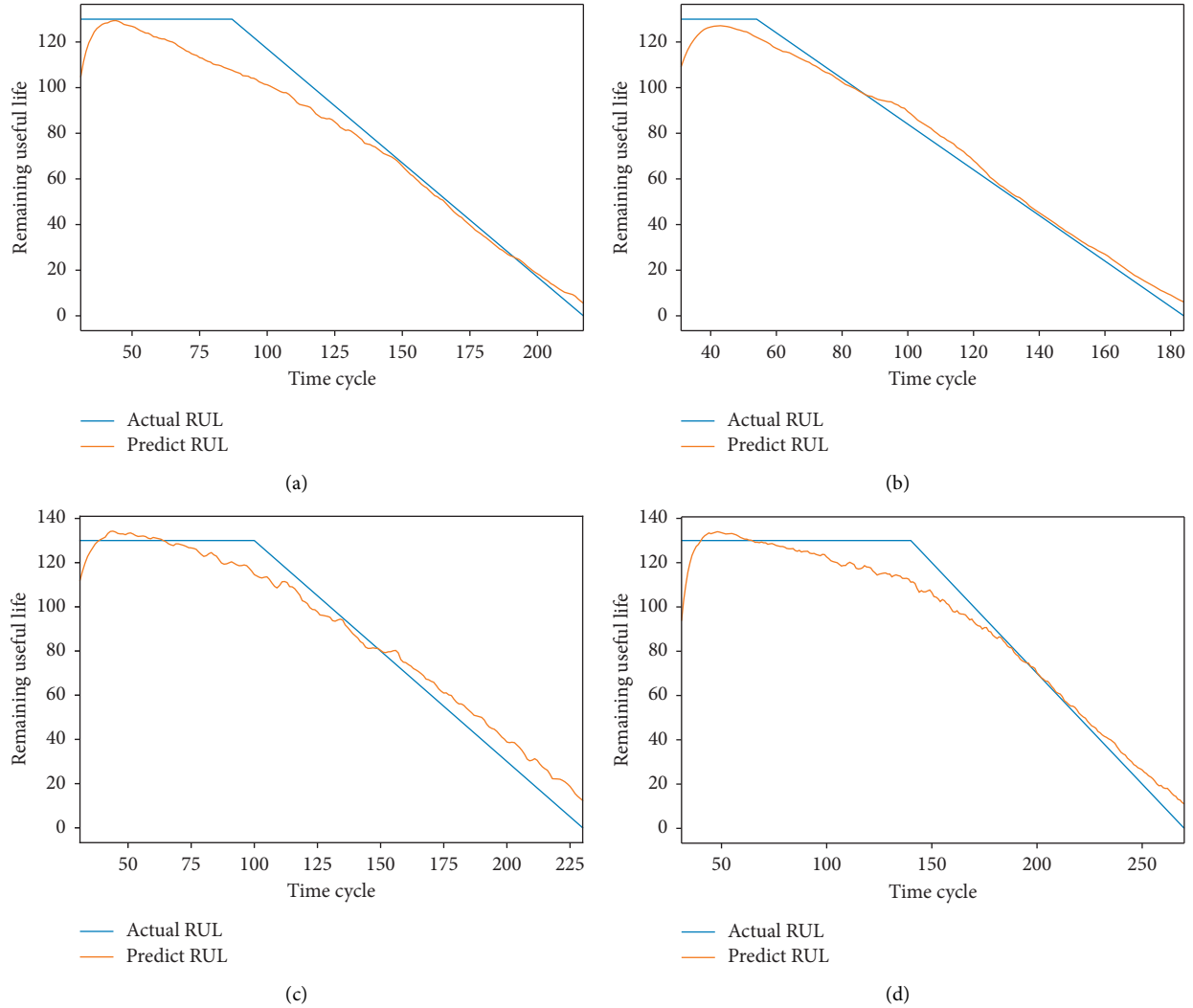


FIGURE 13: RUL prediction for engine unit examples of C-MAPSS dataset. (a) The example is unit 12 in test\_FD001. (b) The example is unit 7 in test\_FD002. (c) The example is unit 9 in test\_FD003. (d) The example is unit 12 in test\_FD004.

lead to improvement of results, we get a significant gain in prediction result of our proposed method. As we can see in Table 3, the EMD-ESN method proposed in this paper performs best on the four C-MAPSS datasets, whether it is for Score or RMSE. For Score, IMP over LSTM of our proposed method is up to 93.41% on FD002 and IMP over ESN is up to 93.99% on FD003. For RMSE, IMP over LSTM of our proposed method is up to 64.96% on FD004 and IMP over ESN is up to 51.35% on FD003. We can conclude that the proposed method can improve the prediction effect to a large extent. When we take Score as the performance metrics, the improvement effect is particularly obvious.

For RMSE, the ESN has also performed better than the LSTM on all the datasets. However, for Score the LSTM performs better than the ESN on FD001 and FD003. The situation demonstrates that overpredicting tends to be generated by the ESN, especially for FD001 and FD003, which contain just 1 operational condition. Different from the ESN, our proposed method has improved the overpredicting situation, which can also be seen by comparing Figure 12 with Figure 11. In Figure 12, the situations of overprediction are less than those in Figure 11, obviously. Besides, there is a substantial improvement for the EMD-ESN on FD004, which is the most complicated dataset

containing 6 operating conditions and 2 fault modes. This all shows that the EMD-ESN can filter out redundant signals or noise, in which EMD plays a crucial role. This inspires us that the signal decomposition technology can be adopted in the RUL prediction to deal with noise.

(2) *Results Comparison of Prediction Efficiency.* In addition to results comparison of prediction performance, the training time comparison is also performed, and the results are demonstrated in Table 4. As we can see in Table 4, the training time of the ESN and the EMD-ESN are significantly saved compared with the LSTM, which means fewer computing resources are required. Although the EMD-ESN still takes more training time than the ESN, which consumes a certain time for the EMD decomposition process, the prediction improvement is also considered, especially for data with much noise. This shows the necessity to adopt EMD to decompose the raw sensor data.

(3) *Sample Examples of RUL Prediction.* In Figure 13, the RUL prediction of a sample engine unit for each dataset is illustrated. We can see that the prediction for the four examples all perform well, with an unobvious trend for overpredicting. It can also be seen that for each unit, the preceding period prediction is generally not as good as the following period prediction. This can be explained by the fact that with the increase of the training data, the accuracy is becoming higher.

In this section, the prediction performance and efficiency are compared between LSTM, ESN, and the proposed EMD-ESN, and result analysis is performed. Through experiments, the superiority of our proposed method is verified.

## 4. Conclusions

Prognostic of RUL contributes to timely maintenance and less cost consuming. In this paper, we propose a combination method of EMD and ESN to predict the RUL. The proposed EMD-ESN method is performed on the turbofan engine multisensor time series, which demonstrates the validity, accuracy, and effectiveness of our method. The EMD decomposes the raw time series to obtain portions with simpler information, which can be easily trained by the ESN further. The output of each ESN is summarized to get the final prediction value. Compared with the LSTM and the basic ESN method, the prediction effect of the EMD-ESN method is greatly improved, especially for data with much noise. Besides, the computing time is largely reduced.

However, there is still a lot of research to be conducted and some of the directions are as follows:

- (1) Although the adoption of EMD improves the prediction effect, it also consumes more time. It is necessary to study how to improve prediction accuracy and save computing resources at the same time.
- (2) EMD is one of the signal processing methods in the time and frequency domain, and there are many other relative methods such as wavelet packet

decomposition. The adoption of relative methods into noise data processing is also worthy of further study.

## Data Availability

The dataset used to support the findings in this paper have been deposited in the “Turbofan Engine Degradation Simulation Data Set,” NASA Ames Prognostics Data repository, which contains simulated degradation data for turbofan engine developed by NASA. The dataset can be found through the link <https://ti.arc.nasa.gov/tech/dash/groups/pcoe/prognostic-data-repository/>.

## Conflicts of Interest

The authors declare that there are no conflicts of interest regarding the publication of this article.

## Acknowledgments

This research was funded by a major project of the National Natural Science Foundation of China, “Operation Optimization of Intelligent Factories for High-end Equipment Manufacturing under the Internet and Big Data Environment” (Project no. 71690230/71690234).

## References

- [1] J. Z. Sikorska, M. Hodkiewicz, and L. Ma, “Prognostic modelling options for remaining useful life estimation by industry,” *Mechanical Systems and Signal Processing*, vol. 25, no. 5, pp. 1803–1836, 2011.
- [2] M. S. Kan, A. C. C. Tan, and J. Mathew, “A review on prognostic techniques for non-stationary and nonlinear rotating systems,” *Mechanical Systems and Signal Processing*, vol. 62–63, pp. 1–20, 2015.
- [3] M. Compare, L. Bellani, and E. Zio, “Availability model of a PHM-equipped component,” *IEEE Transactions on Reliability*, vol. 66, no. 2, pp. 487–501, 2017.
- [4] Y. Zhang, R. Xiong, H. He, and M. G. Pecht, “Lithium-ion battery remaining useful life prediction with box-cox transformation and Monte Carlo simulation,” *IEEE Transactions on Industrial Electronics*, vol. 66, no. 2, pp. 1585–1597, 2019.
- [5] L. Yongxiang, S. Jianming, W. Gong, and Z. Mengying, “An ensemble model for engineered systems prognostics combining health index synthesis approach and particle filtering,” *Quality and Reliability Engineering International*, vol. 33, no. 8, pp. 2711–2725, 2017.
- [6] Y. Lei, N. Li, L. Guo, N. Li, T. Yan, and J. Lin, “Machinery health prognostics: a systematic review from data acquisition to RUL prediction,” *Mechanical Systems and Signal Processing*, vol. 104, pp. 799–834, 2018.
- [7] M. S. K. Kopuru, S. Rahimi, and K. Baghaei, “Recent approaches in prognostics: state of the art,” in *Proceedings of the International Conference on Artificial Intelligence (ICAI)*, pp. 358–365, Xuzhou, China, August 2019.
- [8] C. H. Oppenheimer and K. A. Loparo, “Physically based diagnosis and prognosis of cracked rotor shafts,” in *Component and Systems Diagnostics, Prognostics, and Health Management II*, P. K. Willett and T. Kirubarajan, Eds., pp. 122–132, SPIE, Bellingham, WA, USA, 2002.

- [9] J. Sun, H. Zuo, W. Wang, and M. G. Pecht, "Prognostics uncertainty reduction by fusing on-line monitoring data based on a state-space-based degradation model," *Mechanical Systems and Signal Processing*, vol. 45, no. 2, pp. 396–407, 2014.
- [10] Y. Qian, R. Yan, and S. Hu, "Bearing degradation evaluation using recurrence quantification analysis and kalman filter," *IEEE Transactions on Instrumentation and Measurement*, vol. 63, no. 11, pp. 2599–2610, 2014.
- [11] R. Zhou, N. Gebraeel, and N. Serban, "Degradation modeling and monitoring of truncated degradation signals," *IIE Transactions*, vol. 44, no. 9, pp. 793–803, 2012.
- [12] L. Xiao, X. Chen, X. Zhang, and M. Liu, "A novel approach for bearing remaining useful life estimation under neither failure nor suspension histories condition," *Journal of Intelligent Manufacturing*, vol. 28, no. 8, pp. 1893–1914, 2017.
- [13] F. O. Heimes, "Recurrent neural networks for remaining useful life estimation," in *Proceedings of the 2008 International Conference on Prognostics and Health Management*, pp. 1–6, IEEE, Denver, CO, USA, October 2008.
- [14] D. Zurita, J. A. Carino, M. Delgado et al., "Distributed neuro-fuzzy feature forecasting approach for condition monitoring," in *Proceedings of the 2014 IEEE Emerging Technology and Factory Automation (ETFA)*, pp. 1–8, IEEE, Barcelona, Spain, September 2014.
- [15] X. Si, T. Li, Q. Zhang, and X. Hu, "An optimal condition-based replacement method for systems with observed degradation signals," *IEEE Transactions on Reliability*, vol. 67, no. 3, pp. 1281–1293, 2018.
- [16] M. Rigamonti, P. Baraldi, E. Zio, I. Roychoudhury, K. Goebel, and S. Poll, "Ensemble of optimized echo state networks for remaining useful life prediction," *Neurocomputing*, vol. 281, pp. 121–138, 2018.
- [17] J. Zhang, P. Wang, R. Yan, and R. X. Gao, "Long short-term memory for machine remaining life prediction," *Journal of Manufacturing Systems*, vol. 48, pp. 78–86, 2018.
- [18] S. J. Hochreiter and J. Schmidhuber, "Long short-term memory," *Neural Computation*, vol. 9, no. 8, pp. 1735–1780, 1997.
- [19] S. Zheng, K. Ristovski, A. Farahat, and C. Gupta, "Long short-term memory network for remaining useful life estimation," in *Proceedings of the 2017 IEEE International Conference on Prognostics and Health Management (ICPHM)*, pp. 88–95, IEEE, Dallas, TX, USA, June 2017.
- [20] H. Miao, B. Li, C. Sun, and J. Liu, "Joint learning of degradation assessment and RUL prediction for aeroengines via dual-task deep LSTM networks," *IEEE Transactions on Industrial Informatics*, vol. 15, no. 9, pp. 5023–5032, 2019.
- [21] C.-G. Huang, H.-Z. Huang, and Y.-F. Li, "A bidirectional LSTM prognostics method under multiple operational conditions," *IEEE Transactions on Industrial Electronics*, vol. 66, no. 11, pp. 8792–8802, 2019.
- [22] A. Al-Dulaimi, S. Zabihi, A. Asif, and A. Mohammadi, "A multimodal and hybrid deep neural network model for remaining useful life estimation," *Computers in Industry*, vol. 108, pp. 186–196, 2019.
- [23] H. Jaeger, "The "echo state" approach to analysing and training recurrent neural networks," vol. 148, German National Research Center for Information Technology, Sankt Augustin, Germany, 2001, Technical Report GMD Report 148.
- [24] M. Lukoševičius and H. Jaeger, "Reservoir computing approaches to recurrent neural network training," *Computer Science Review*, vol. 3, no. 3, pp. 127–149, 2009.
- [25] C. Liu, R. Yao, and L. e. a. Zhang, "Attention based echo state network: A novel approach for fault prognosis," in *Proceedings of the 2019 11th International Conference on Machine Learning and Computing*, pp. 489–493, Zhuhai, China, February 2019.
- [26] S. Zhong, X. Xie, L. Lin, and F. Wang, "Genetic algorithm optimized double-reservoir echo state network for multi-regime time series prediction," *Neurocomputing*, vol. 238, pp. 191–204, 2017.
- [27] Z. Tan, J. Zhang, J. Wang, and J. Xu, "Day-ahead electricity price forecasting using wavelet transform combined with ARIMA and GARCH models," *Applied Energy*, vol. 87, no. 11, pp. 3606–3610, 2010.
- [28] H. Liu, H.-q. Tian, X.-f. Liang, and Y.-f. Li, "Wind speed forecasting approach using secondary decomposition algorithm and Elman neural networks," *Applied Energy*, vol. 157, pp. 183–194, 2015.
- [29] Y. Wang and L. Wu, "On practical challenges of decomposition-based hybrid forecasting algorithms for wind speed and solar irradiation," *Energy*, vol. 112, pp. 208–220, 2016.
- [30] X. Xu and W. Ren, "A combination model based on EEMD-PE and echo state network for chaotic time series prediction," in *Proceedings of the 2019 Eleventh International Conference on Advanced Computational Intelligence (ICACI)*, pp. 290–295, Guilin, China, June 2019.
- [31] N. E. Huang, Z. Shen, S. R. Long et al., "The empirical mode decomposition and the Hilbert spectrum for nonlinear and non-stationary time series analysis," *Proceedings of the Royal Society of London. Series A: Mathematical, Physical and Engineering Sciences*, vol. 454, no. 1971, pp. 903–995, 1998.
- [32] J. Qiao, S. Li, and W. Li, "Mutual information based weight initialization method for sigmoidal feedforward neural networks," *Neurocomputing*, vol. 207, pp. 676–683, 2016.
- [33] M. Lukosevicius, "A practical guide to applying echo state networks," in *Neural Networks: Tricks of the Trade*, pp. 659–686, Springer, Berlin, Germany, 2012.
- [34] H. Jaeger, M. Lukoševičius, D. Popovici, and U. Siewert, "Optimization and applications of echo state networks with leaky-integrator neurons," *Neural Networks*, vol. 20, no. 3, pp. 335–352, 2007.
- [35] A. Bala, I. Ismail, R. Ibrahim, and S. M. Sait, "Applications of metaheuristics in reservoir computing techniques: a review," *IEEE Access*, vol. 6, pp. 58012–58029, 2018.
- [36] A. Saxena and K. Goebel, "Turbofan engine degradation simulation data set," *NASA Ames Prognostics Data Repository*, <http://ti.arc.nasa.gov/project/prognostic-data-repository>, NASA Ames Research Center, Moffett Field, CA, USA, 2008, <http://ti.arc.nasa.gov/project/prognostic-data-repository>.
- [37] A. Saxena, K. Goebel, D. Simon, and N. H. W. Eklund, "Damage propagation modeling for aircraft engine run-to-failure simulation," in *Proceedings of the IEEE International Conference on Prognostics and Health Management*, pp. 1–9, Denver, CO, USA, October 2008.
- [38] F. O. Heimes, "Recurrent neural networks for remaining useful life estimation," in *Proceedings of the 2008 International Conference on Prognostics and Health Management*, pp. 1–6, IEEE, Denver, CO, USA, October 2008.

## Research Article

# A Generalized Chart-Based Decision-Making Tool for Optimal Preventive Maintenance Time under Perfect Renewal Process Modeling

Pablo Viveros Gunckel <sup>1</sup>, Fredy Kristjanpoller <sup>1</sup> and René Tapia Peñaloza<sup>2</sup>

<sup>1</sup>Department of Industrial Engineering, Universidad Técnica Federico Santa María, Av. España 1680, Valparaíso, Chile

<sup>2</sup>RelPro SpA, Santiago, Chile

Correspondence should be addressed to Pablo Viveros Gunckel; pablo.viveros@usm.cl

Received 2 July 2020; Revised 31 July 2020; Accepted 4 August 2020; Published 24 September 2020

Academic Editor: Gianpaolo Di Bona

Copyright © 2020 Pablo Viveros Gunckel et al. This is an open access article distributed under the Creative Commons Attribution License, which permits unrestricted use, distribution, and reproduction in any medium, provided the original work is properly cited.

The most commonly used probabilistic model in reliability studies is the Perfect Renewal Process (PRP), which is characterized by the condition or type of maintenance represented: once the maintenance activities are executed, the equipment is restored to its original condition, leaving it “as good as new.” It is widely used since it represents an optimistic state when an item is replaced, assuming a perfect operational condition of the item after the maintenance. Some models have been developed for determining optimum preventive maintenance (PM) based on different criteria, and almost all aimed at PRP reliability modeling. The contribution of this paper is to analyze a model for determining the optimal preventive maintenance policy for a long time run under PRP and developing a general and chart-based tool for the problem, making it easier to solve the day-to-day practice and operation of equipment. As a result, a generalized chart was developed to support maintenance decisions through the elaboration of an original isometric table and complemented with a step-by-step methodology to determine the optimum time in which the preventive maintenance activities must be implemented. In most cases, these types of maintenance activities will consider a replacement activity.

## 1. Introduction

Preventive maintenance is primarily intended to avoid high costs incurred due to unplanned maintenance activities, which usually causes higher downtimes, direct costs, and most times catastrophic determining events for business continuity.

Because of the need for planning PM activities at the industry level, a direct requirement emerges in consequence: knowing when to perform these activities. Since the PM has considerable importance in safety-critical processes, where the occurrence of a failure has a high impact, most of the developed models are intended to replace the equipment [1–3]. In this sense, most of the policies are based on constant age replacement of equipment, i.e., constant wear time after the equipment entry into operation; this occurs because all devices are under the same condition when they enter as new. Considering that, in the industry, the amount

of equipment that only has replacement as a solution for the failure is frequently high, the operators and engineers related to this equipment have to do a lot of exhaustive calculations to find the best policies of replacement. Most of those aforementioned operations, which are also cited in this paper, involve at least calculating nonclosed integrals by Riemann sum.

Given the above considerations, this research focuses on analyzing an optimization model with constant age PM on repairable systems and getting a simple way to approach the procedures involved in this optimization process.

In the maintenance management context, a repairable system can be defined as “a system that after failing to develop an activity can be restored properly functioning satisfactorily by some method” [4].

Depending on the type of maintenance that is given to the equipment, it is possible to find 5 cases [5,6]:

- (a) Perfect maintenance: maintenance operation restores the equipment to a status of “as good as new.”
- (b) Minimum maintenance: maintenance operation restores the equipment to a status of “as bad as old.”
- (c) Imperfect maintenance: maintenance operation restores the equipment to a status of “worse than new but better than old.”
- (d) More than perfect maintenance: maintenance operation restores the equipment to a status of “better than new.”
- (e) Destructive maintenance: maintenance operation restores the equipment to a status of “worse than old.”

Cases (d) and (e) have little presence in reality [6]; almost all correspond to specific events in the equipment life and are highly unlikely to present a series of repairs to such standard.

In case (a), the most widely used model that fits precisely the described scenario is the Perfect Renewal Process (PRP) [6,7]; in case (b) a Nonhomogenous Poisson Process (NHPP) [6,7] is used, among others. In the case of (c), various models of failure processes, including variants of generalized geometric processes (for details, see [8]), have been developed; if, besides, the effect of the repair is considered to be limited due to a constant value, then the general repair model is obtained and applied for this particular case [9]; in the same way, the Generalized Renewal Process (GRP) model developed by Kijima and Sumita [10] has been used.

The current intense international competition, the need for faster innovation, and the structural organizational changes in response to new information and manufacturing technologies are still surprising [11]. In response to this phenomenon, the increasing importance of effective maintenance planning is fueled by increasing automation of processes, so that a substantial part of the total costs of industrial assets is today directly or indirectly related to maintenance [12].

In this sense, maintenance personnel need simple and general methods for the design of maintenance programs and optimization policies [13]. Also, the decision-making tools are needed to give quick but precise answers, simplifying an intricate application of the theory, capable of offering standardized values and ideally easy to read, execute, and interpret.

Considering the motivations established above, the main contribution of this research is the elaboration of a practical tool for obtaining fast and reliable information for the decision-making process in maintenance management, by developing a generalized chart-based tool to obtain optimal preventive maintenance times in single-unit systems. Based on the knowledge gathered from the literature review, there are no references related to the development and use of chart-based tools that allow a practical approach to obtain optimal preventive maintenance times.

Besides, it is possible to realize that the models developed for equipment replacement can only be used for elements maintained under Perfect Renewal Process modeling, considering that their condition is “as good as new” once they begin its operational functions.

The research is structured as follows: Section 2 states the problem and its necessity in the industry, Section 3 presents the state of the art related to the PRP modeling and the chosen long-run cost minimization model. Section 4 develops the generalized chart-based proposal solution for the problem, starting with a mathematical analysis of the problem and ends with presenting the results. Finally, Section 5 presents the discussion, potentialities, and conclusions.

## 2. Problem Statement and Motivation

Specialized literature reveals that the industry continues to demand methodologies, approaches, and tools to better understand machine inefficiencies [14]. Specifically, in the maintenance management area, the continuous development of technical systems and the increasing dependence on equipment have generated an increasing interest in effective maintenance activities [15]. In this sense, it becomes necessary not only to determine the maintenance activity to be executed but also to optimize the execution intervals of said activities and correctly model the random behavior of the failures.

This approach is targeted at the traditional Perfect Renewal Process (PRP), which is a complement to the existent solution procedures and is also easy to understand when searching and getting the optimal PM time value. Although this stochastic process for the random modeling of failures is elementary, it is the starting point for the elaboration and conceptualization of more sophisticated, but also more complex, models.

According to [16], if the purpose of maintenance models is to increase the knowledge of the data, this knowledge should be organized so that the end-user, maintenance personnel, can use it. Current models for getting the optimal time of a PM activity imply exhaustive calculation to get solutions, mainly because of the evaluation of the objective function to be minimized. This means that when it is required to establish the optimization procedure for the equipment, the computation operations of these values can become expensive in terms of time and resources used for this task. Something that also must be considered is the fact that the nature of the problem is completely analytical, requiring an advanced domain of calculus and engineering skills by the user to face and solve the problem.

Considering the previous observations, the motivation that guides this research is to find a practical solution to be used quickly, which ideally uses graphical support to find a quick convergence process for an optimal solution.

## 3. State of the Art

*3.1. Literature Review.* Maintenance management has become increasingly relevant within business management, becoming one of its essential functions and also one of the critical aspects within the operational phase of asset management given the current conditions and needs of a highly competitive market and the increasing automation of its processes. In this context, maintenance optimization



consists of the development and analysis of mathematical models to optimize maintenance policies [15]; this process is, therefore, essential for the decision-making process in asset management.

In this sense, the correct modeling of the failure process is relevant, as well as the different units or components of the system on which the maintenance activities will be carried out. A wide variety of failure process models have been developed and extended over the past three decades addressing different characteristics of failure processes, namely, geometric processes [17], renovation processes [10], virtual age models [18], arithmetic models of intensity reduction (ARI), and arithmetic reduction of age (ARA) [19], among others. To determine the different extensions and generalizations that have been made, Wu et al. [8] elaborate a review of the extensions of the geometric processes, from which it follows that the general repair models are derived from a particular case of the generalized geometric processes.

Regarding the relevant investigations carried out in recent years, the research developed by Mullor et al. [20] considers establishing the failure distribution experimentally, disaggregating a specific and independent model for each component of the equipment, and also associating an imperfect maintenance model with each case. In other words, the model developed in said research considers multiple failure modes depending on the different components that integrate the equipment, addressing the implicit assumption that modeling considers a unique degradation process.

To address this assumption in turn, [21] develops a multi-dependent system degradation process modeled by a copula function and influenced by the environment, using finite analysis for performance evaluation of life cycle cost. While these studies address single-unit systems, [22] proposes a new failure process model for a series component system. For this problem, a distinction is made between the real system, the mathematical model, and the system made up of virtual components.

The previous research works address maintenance activities considering that the failure is self-announcing. The research carried out by Liu et al. [23] considers addressing condition-based maintenance (CBM) policy, and therefore the failure or condition of the equipment can only be detected under the inspection, which is referred to as a soft failure. The problem addressed considers both a system and a sensor in a degraded state, so the traditional maintenance policy without considering this fact may be operating in a suboptimal state.

The investigations detailed above are based on the development and application of stochastic processes and often multiple-objective or cost optimization models, with all the complexity that this involves. Based on the classifications used in the literature of the field, the proposed research is framed on the development of a practical tool to obtain optimal maintenance preventive maintenance intervals for single-unit systems and thus a single degradation process, considering perfect maintenance for preventive maintenance activities and minimal maintenance for corrective

maintenance actions. Considering the above, said interval is calculated based on the optimization of the expected cost in the long term for said activities.

*3.2. Maintenance Tools for Decision Making.* Related to the problem previously stated, other graphical tools for supporting decision making in the area of operational reliability have been developed.

One of the classic management tools for decision making is Pareto diagram. Although this tool is widely used in management, this diagram is not only used to prioritize risk in quality control but also to get Pareto-efficient borders to optimize maintenance costs. In this sense, this tool allows considering the impact of costs from spare parts to downtime and outages [24]. Since the available resources are always scarce and considering the increasing search for integrating different areas within the organization, the search for a Pareto-efficient solution can even be carried out to address a multicriteria objective function [25].

The GAMM (Graphical Analysis for Maintenance Management) is a method and maintenance management decision-making tool to visualize and analyze equipment dependability data in a graphical form [26]. One of the advantages of this method is that it supports decision making in the overall maintenance management, through the visualization and graphic analysis of data; for the application of the method, a relatively simple database is enough to generate the graphic support of this tool, consisting in scatter diagrams, bubble charts, and graphs to measure the correlation between each of the equipment reviews and the existing level of equipment reliability before these [27].

The Graphical Analysis for Operation Management (GAOM) is a maintenance and operation management tool that is also built from an integrated database but considers three main types of information: maintenance interventions, production, and time. All this information is processed together with values of the key performance indicators for the subsequent development of an integrated and exhaustive graphic analysis of the decision-making process [28].

Reviewing the scientific literature, we found that the use of generalized chart-based tools is applied in a wide variety of research fields (see, e.g., [29–32]). This reveals the existing potential and effective utilization of this type of instruments, which can be exploited in the field of maintenance management.

*3.3. Perfect Renewal Process.* The modeling under the Perfect Renewal Process is characterized by considering the perfect operational condition of the equipment (AGAN) after maintenance activity execution. This means that the maintenance activity was fully effective in the rejuvenation process of the equipment such that it returns the equipment to its original condition [6, 7, 10].

A complete renovation implies that the time between failures or any unit for which reliability is calculated has no trend over the total time and is independent and identically distributed (i.i.d.) throughout the entire planning horizon.

The PRP modeling is the simplest of all, but at the same time it is the one with the greatest limitations in terms of its implementation, not faithfully representing the behavior of most mechanical and electrical equipment. However, PRP modeling is ideal for items that cannot be repaired, considering that after failing there is no way to restore the functionality of these items, and therefore they must be replaced. Thus, whenever a failure occurs, the item is replaced by a new one, describing exactly the operational scenario of PRP. In this model, the failure rate is characterized by the following expression:

$$\lambda(t | t \geq T) = \frac{f(t - T)}{1 - F(t - T)}. \quad (1)$$

Here,  $f(t)$  corresponds to the p.d.f. of the operating times,  $\lambda(T)$  the failure rate at the elapsed time  $T$  since the start of the operation, and  $t_i$  is the  $i$ -th operation time.

In the case applied to the 2-parameter Weibull distribution, the basic expressions are

$$\begin{aligned} F(t) &= 1 - e^{-(t/\alpha)^\beta}, \\ R(t) &= e^{-(t/\alpha)^\beta}, \\ f(t) &= \frac{\beta}{\alpha} \left(\frac{t}{\alpha}\right)^{\beta-1} e^{-(t/\alpha)^\beta}. \end{aligned} \quad (2)$$

A graphical representation of how failures occur under this modeling is shown in Figure 1, which seeks to represent the independence in the occurrence time of the failures.

Through the use of the inverse function, it is possible to generate a random time value with the following expression:

$$t_i = \alpha \sqrt[\beta]{-\ln(u)}, \quad (3)$$

where  $t_i$  represents the time between failures and  $u$  a uniformly random variable in the  $[0, 1]$  interval.

**3.4. Optimal Preventive Maintenance in PRP.** The Wang and Christer model [33] is the most widely accepted and is based on the minimization of the expected cost in the long run. For this analysis, it is required to consider two possibilities:

- (a) The equipment fails before performing PM
- (b) The equipment survives until it has performed the maintenance activity

Since under modeling PRP, times are identically and independently distributed, and the p.d.f. of the times between failures is the same for all cases, which is also the main difference from NHPP and GRP repairable models. This feature makes the probability of occurrence for both the first and second cases the same over time, so there is a single optimum time in which the PM activity is performed.

The occurrence of each of these scenarios implies incurring certain maintenance operations, which have a particular cost and time associated with each case. Namely, in case of no failing before PM (case (b)), the equipment works continuously up to an arbitrary interval  $t_p$ , executing

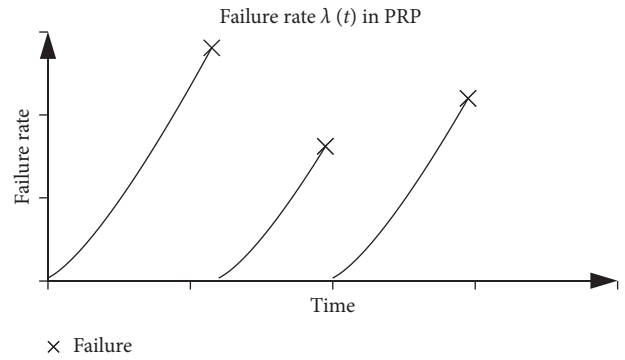


FIGURE 1: Failure rate in PRP.

only the PM activity immediately after this event. The above can be represented mathematically by establishing that the random variable related to the time of occurrence of the failure  $t_f$  takes a greater value than the moment of execution of the PM activity  $t_p$ . Meanwhile, in case (a), the occurrence of the early failure does not allow the preventive maintenance activity to be executed at instant  $t_p$ , being necessary to carry out repair tasks at the instant of time  $t_f$ , in which the failure occurs. Mathematically speaking, time becomes a random variable called  $t_f$  and is represented by the truncated distribution of the times between failures, bounded above by value  $t_p$ . Figure 2 provides a summary of the previously stated cases. Additionally, the probability associated with each case is clearly shown in Figure 3.

Since in case (b) the operating time is  $t_p$ , for case (a) the expected time of operation is given by

$$E[t | t < t_p] = \frac{\int_0^{t_p} (t \cdot f(t)) dt}{F(t_p)}. \quad (4)$$

The model also considers a differentiated cost for each of the two cases, where the cost of case (a) is usually larger than case (b), being an unplanned task. This defines  $C_c$  presented to the cost of case (a) (corrective cost) and  $C_p$  for case (b) (preventive cost).

Considering that each of the cases has different lengths, the model suggests minimizing the cost per time rate ( $[\$/t]$ ).

For a certain  $t_p$ , the expected cost of  $C$  is given by the following expression:

$$E[C] = \underbrace{F(t_p) \cdot C_c}_{\text{Case (a)}} + \underbrace{R(t_p) \cdot C_p}_{\text{Case (b)}}. \quad (5)$$

Besides, the expected duration after each maintenance activity is

$$E[t] = \underbrace{F(t_p) \cdot \left( \frac{\int_0^{t_p} (t \cdot f(t)) dt}{f(t_p)} \right)}_{\text{Case (a)}} + \underbrace{R(t_p) \cdot t_p}_{\text{Case (b)}}. \quad (6)$$

$$E[t] = \underbrace{\int_0^{t_p} (t \cdot f(t)) dt}_{\text{Case (a)}} + \underbrace{R(t) \cdot t_p}_{\text{Case (b)}}. \quad (7)$$



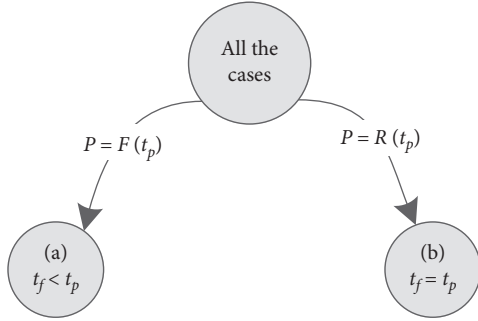


FIGURE 2: Cases representation.

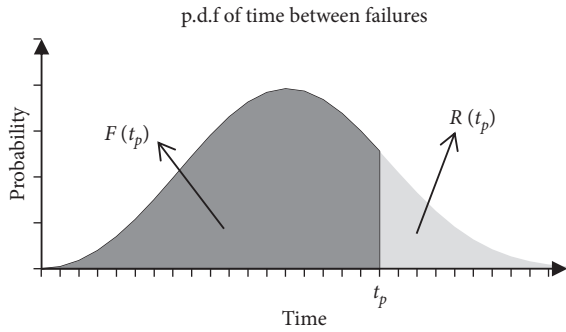


FIGURE 3: p.d.f. of time between failures.

Thus, the expected cost per unit of time can be expressed as

$$E\left[\frac{dC_t(t_p)}{dt}\right] = \frac{F(t_p) \cdot C_c + R(t_p) \cdot C_p}{\int_0^{t_p} (t \cdot f(t)) dt + R(t_p) \cdot t_p} \quad (8)$$

#### 4. Research Proposal

To develop the methodology, firstly it is required to take the model from the previous point to tangible terms and simplify the number of parameters included. In the case described by two-parameter Weibull distribution, the expected cost per unit of time corresponds to

$$E\left[\frac{dC_t(t_p)}{dt}\right] = \frac{\left(1 - e^{-(t_p/\alpha)^\beta}\right) \cdot C_c + e^{-(t_p/\alpha)^\beta} \cdot C_p}{\underbrace{\int_0^{t_p} \left(t \cdot \frac{\beta}{\alpha} (t/\alpha)^{\beta-1} e^{-(t/\alpha)^\beta}\right) dt}_k + e^{-(t_p/\alpha)^\beta} \cdot t_p} \quad (9)$$

Here, the  $k$  variable corresponds to

$$k = \int_0^{t_p} \left(t \cdot \frac{\beta}{\alpha} \left(\frac{t}{\alpha}\right)^{\beta-1} e^{-(t/\alpha)^\beta}\right) dt. \quad (10)$$

By changing the variables for the defined  $k$  part,

$$\left(\frac{t^\beta}{\alpha^\beta}\right) = u,$$

$$(\alpha^\beta u)^{(1/\beta)} = t, \quad (11)$$

$$\frac{(\alpha^\beta u)^{(1/\beta)}}{\beta u} du = dt.$$

Replacing the integration limits,

$$t = t_p \longrightarrow u = \left(\frac{t_p}{\alpha}\right)^\beta, \quad (12)$$

$$t = 0 \longrightarrow u = 0,$$

and considering that  $(t/\alpha) = u^{(1/\beta)}$ ,

$$\begin{aligned} k &= \int_0^{(t_p/\alpha)^\beta} (\alpha^\beta u)^{(1/\beta)} \cdot \left(\frac{\beta}{\alpha}\right) u^{(1-1/\beta)} e^{-u} \cdot \frac{(\alpha^\beta u)^{(1/\beta)}}{\beta u} du, \\ k &= \int_0^{(t_p/\alpha)^\beta} (\alpha^\beta u)^{(1/\beta)} \cdot \left(\frac{\beta}{\alpha}\right) u^{(1-1/\beta)} e^{-u} \cdot \frac{(\alpha^\beta u)^{(1/\beta)}}{\beta u} du \\ &= \int_0^{(t_p/\alpha)^\beta} \alpha u^{(1/\beta)} \cdot \left(\frac{\beta}{\alpha}\right) u u^{(-1/\beta)} e^{-u} \cdot \frac{\alpha u^{(1/\beta)}}{\beta u} du. \end{aligned} \quad (13)$$

Thus,  $k$  satisfies that

$$\begin{aligned} k &= \alpha \int_0^{(t_p/\alpha)^\beta} u^{(1/\beta)} e^{-u} du \\ &= \alpha \underbrace{\int_0^{(t_p/\alpha)^\beta} u^{(1/\beta+1)-1} e^{-u} du}_{\gamma(1/\beta+1, (t_p/\alpha)^\beta)} \end{aligned} \quad (14)$$

$$k = \alpha \cdot \gamma\left(1/\beta + 1, \left(\frac{t_p}{\alpha}\right)^\beta\right),$$

where the  $\gamma(a, x)$  function represents the lower incomplete gamma function:

$$\gamma(a, x) = \int_0^x u^{(a-1)} du. \quad (15)$$

This leads to formulating expression (8) as follows:

$$E\left[\frac{dC_t(t_p)}{dt}\right] = \frac{\left(1 - e^{-(t_p/\alpha)^\beta}\right) \cdot C_c + e^{-(t_p/\alpha)^\beta} \cdot C_p}{\alpha \cdot \gamma\left(\left(1 + 1/\beta\right), (t_p/\alpha)^\beta\right) + e^{-(t_p/\alpha)^\beta} \cdot t_p} \quad (16)$$

Then, the objective is to minimize the long-run expected cost; i.e.,

$$\text{Min}_{t_p \in \mathbb{R}^+} : \frac{\left(1 - e^{-(t_p/\alpha)^\beta}\right) \cdot C_c + e^{-(t_p/\alpha)^\beta} \cdot C_p}{\alpha \cdot \gamma\left(\left(\frac{1+1}{\beta}\right), (t_p/\alpha)^\beta\right) + e^{-(t_p/\alpha)^\beta} \cdot t_p}. \quad (17)$$

Before continuing, it is important to consider that the value of  $t_p$  is determined by  $C_c, C_p, \beta$ , and  $\alpha$ , and it is possible to simplify the expression stated in (17) by using the rate between  $C_c$  and  $C_p$  and using a single value for  $\alpha$  that only impacts the size of  $t_p$ . It is clear that  $\alpha$  and  $t_p$  have a direct proportionality. In other words, for the ratio between costs for each different  $\beta$ , there is a  $t_p$  which is directly proportional to  $\alpha$ . Considering that it is possible to formulate a change of variable

$$t'_p = \left(\frac{t_p}{\alpha}\right), \quad (18)$$

this further simplifies the denominator, since it represents the expected duration.

At this point, the rate

$$p = \left(\frac{C_p}{C_c}\right), \quad (19)$$

is defined, with the purpose of diminishing the variables involved in the objective function stated in (17). Finally, the function depends only on  $t'_p$  and  $p$ , stated as follows:

$$\text{Min}_{t'_p \in \mathbb{R}^+} : \frac{\left(1 - e^{-(t'_p)^\beta}\right) \cdot C_c + e^{-(t'_p)^\beta} \cdot p C_p}{\alpha \cdot \gamma\left(\left(\frac{1+1}{\beta}\right), (t'_p)^\beta\right) + e^{-(t'_p)^\beta} \cdot t'_p}. \quad (20)$$

It is also important to note that, using the lower incomplete gamma function, it is possible to rewrite it as

$$\gamma(a, x) = P(a, x) \cdot \Gamma(a). \quad (21)$$

Here,  $P(a, x)$  is the cumulative distribution function of a gamma distribution probability with a scale parameter equal to 1 and a shape parameter equal to  $a$ . This change greatly improves the possibility of reaching a better solution, given that most calculation software has already defined the function approximations for the probability distribution function of gamma and the gamma function itself. Then, the equivalence between the variables is

$$\begin{aligned} a &= 1 + \left(\frac{1}{\beta}\right), \\ x &= (t'_p)^\beta. \end{aligned} \quad (22)$$

Then, by changing the corresponding variables

$$\gamma\left(\left(\frac{1+1}{\beta}\right), (t'_p)^\beta\right) = P\left(\left(\frac{1+1}{\beta}\right), (t'_p)^\beta\right) \cdot \Gamma\left(\frac{1+1}{\beta}\right), \quad (23)$$

and applying all the mentioned changes, expression (17) is equal to

$$\text{Min}_{t'_p \in \mathbb{R}^+} : \frac{C_c}{\alpha} \cdot \frac{1 - e^{-(t'_p)^\beta} \cdot (1-p)}{P\left(\left(\frac{1+1}{\beta}\right), (t'_p)^\beta\right) \cdot \Gamma\left(\frac{1+1}{\beta}\right) + e^{-(t'_p)^\beta} \cdot t'_p}, \quad (24)$$

which is equivalent to solving the following expression:

$$\text{Min}_{t'_p \in \mathbb{R}^+} : \frac{1 - e^{-(t'_p)^\beta} \cdot (1-p)}{P\left(\left(\frac{1+1}{\beta}\right), (t'_p)^\beta\right) \cdot \Gamma\left(\frac{1+1}{\beta}\right) + e^{-(t'_p)^\beta} \cdot t'_p}. \quad (25)$$

**4.1. Constant Failure Rate Analysis.** First, an analysis is made for the value of  $\beta = 1$ , with a value  $p = 0$ , so the preventive cost is zero, an extreme case value applied to expression (8):

$$E\left[\frac{dC_t(t_p)}{dt}\right] = \frac{\left(1 - e^{-(t_p/\alpha)^\beta}\right) \cdot C_c + e^{-(t_p/\alpha)^\beta} \cdot C_p}{\alpha \cdot \gamma\left(\left(\frac{1+1}{\beta}\right), (t_p/\alpha)^\beta\right) + e^{-(t_p/\alpha)^\beta} \cdot t_p}. \quad (26)$$

By simplifying

$$\begin{aligned} \alpha &= 1, \\ p &= \left(\frac{C_p}{C_c}\right) = 0, \\ \beta &= 1, \end{aligned} \quad (27)$$

and replacing the values

$$E\left[\frac{dC_t(t_p)}{dt}\right] = C_c \frac{(1 - e^{-t_p})}{\gamma(2, t_p) + e^{-t_p} \cdot t_p}, \quad (28)$$

evidently the expected cost minimization for a given time value does not depend on  $C_c$ ; this is a scale parameter for the problem. Then, the problem becomes

$$\text{Min}_{t_p \in \mathbb{R}^+} : \frac{(1 - e^{-t_p})}{\gamma(2, t_p) + e^{-t_p} \cdot t_p}. \quad (29)$$

However,

$$\gamma(2, t) + e^{-t} \cdot t = \underbrace{\int_0^t s^{2-1} e^{-s} ds}_{w} + e^{-t} \cdot t. \quad (30)$$

Taking the indefinite integral of the  $w$  part

$$w = \int s^{2-1} e^{-s} ds, \quad (31)$$

it is possible to develop the integral by parts  $\int u dv = uv - \int v du$ , making the changes of variables

$$\begin{aligned} u &= s, \\ dv &= e^{-s} ds, \\ du &= ds, \\ v &= -e^{-s}. \end{aligned} \quad (32)$$

This leads to

$$w = -e^{-s}s + \int e^{-s} ds = (-e^{-s}s - e^{-s} + C), \quad (33)$$

in the definite form

$$\int_0^t s^{2-1} e^{-s} ds = -e^{-s}s - e^{-s} \Big|_0^t = -e^{-t}(t+1) + 1. \quad (34)$$

So

$$\begin{aligned} \gamma(2, t) + e^{-t} \cdot t &= \int_0^t s^{2-1} e^{-s} ds + e^{-1} \cdot t \\ &= -e^{-t}(t+1) + 1 + (e^{-t} \cdot t) \\ &= 1 - e^{-t}. \end{aligned} \quad (35)$$

Therefore, expression (29) is equal to

$$\frac{(1 - e^{-t_p})}{\gamma(2, t_p) + e^{-t_p} \times t_p} = \frac{(1 - e^{-t_p})}{1 - e^{-t_p}} = 1 \Big|_{\forall t_p > 0}. \quad (36)$$

The latter demonstrates and verifies that it is indifferent to the time when PM is performed: the cost will be the same. With this result, it is possible to establish that if the PM cost is not null but less than the cost of corrective maintenance, it will never be desirable to carry out a PM activity, so it is better to wait for the occurrence of the failure since it will decrease the cost per operating time. This because it has just been proven that a PM cost of zero is indifferent to when PM is executed.

**4.2. Nonconstant Failure Rate Analysis.** Again, we start from expression (8) as:

$$E \left[ \frac{dC_t(t_p)}{dt} \right] = \frac{\left(1 - e^{-(t_p/\alpha)^\beta}\right) \cdot C_c + e^{-(t_p/\alpha)^\beta} \cdot C_p}{\alpha \cdot \gamma\left(\left((1+1)/\beta\right), (t_p/\alpha)^\beta\right) + e^{-(t_p/\alpha)^\beta} \cdot t_p}. \quad (37)$$

We consider a special case, where

$$\begin{aligned} \alpha &= 1, \\ p &= \left(\frac{C_p}{C_c}\right) = 0. \end{aligned} \quad (38)$$

Then, we replace the values in expression (8):

$$E \left[ \frac{dC_t(t_p)}{dt} \right] = C_c \frac{1 - e^{-t_p^\beta}}{\gamma\left(\left((1+1)/\beta\right), t_p^\beta\right) + e^{-t_p^\beta} \cdot t_p}. \quad (39)$$

Based on the above, the value of  $t_p$  that satisfies the slightest expected cost per unit of time is the same as the solution of the following expression:

$$\text{Min}_{t_p \in \mathbb{R}^+} : \frac{1 - e^{-t_p^\beta}}{\gamma\left(\left((1+1)/\beta\right), t_p^\beta\right) + e^{-t_p^\beta} \cdot t_p}. \quad (40)$$

To mathematically analyze this problem is quite complex, mainly due to an iterative integration problem. In this sense, it is interesting to note that if the shape parameter of the Weibull distribution tends to zero, then

$$\lim_{\beta \rightarrow 0} \gamma\left(\left(\frac{1+1}{\beta}\right), t_p^\beta\right) = 0. \quad (41)$$

Therefore, the minimization of the objective function expression becomes trivial, considering an expected cost that tends to a null value. This means that maintenance activities are avoided since, for  $\beta \in [0, 1]$ , they are unproductive. This situation could be resolved by a search algorithm in space  $\beta > 1$ , which estimates that the best way to solve the situation is to develop an algorithm to find the optimal time directly for the original function and obtain a graphical tool with the results of this algorithm. The development of this tool is presented in the next section.

**4.3. Development of the Generalized Charts.** Considering the defined requirements of the problem in the above sections, it has been justified that a graphical tool is really necessary. The problem has been simplified, and it is now possible to generalize the problem considering  $\beta$ ,  $p$ , and  $\alpha$ . This amount of variables tells us that it could be possible to plot all the solutions of the problems on a chart, which is the challenge of this section.

**4.3.1. Search Algorithm.** With regard to the function already defined, it must be remembered that the parameters that alter the problem are  $\beta$  and  $p$ , given that  $\alpha$  is a scale parameter that is extracted and generalized with value 1. In other words, without loss of generality, it is possible to use for this purpose the expression in (25) considering that  $t_p = t'_p$ . Once these optimal values for this standard  $t_p$  value are obtained, then it is enough to only scale the value from the estimation of the shape parameter  $\alpha$  to obtain the practical optimal PM time value. Establishing the previous observations, we have developed an algorithm for finding optimal PM time for different values of  $\beta$  and  $p$ .

The time exploring ranges from  $t = 0$  to  $t = 10^{-5}\alpha$ . With  $\alpha = 1$ , the initial value is  $t = 10^{-5}$  time units. The maximum scan time is given by the value of  $t$  that contains the  $(1 - \delta)$  cases for the probability distribution function,  $t = F^{-1}(1 - \delta)$ . Then,  $\delta$  would be the percentage of the highest values of  $t$  that are not being considered for the analysis. Thus,  $t_{e\max}$  value as the maximum exploring time remains as

$$t_{e\max} = F^{-1}(1 - \delta) = \alpha \sqrt[\beta]{-\ln(\delta)}. \quad (42)$$

This expression is represented in Figure 4.

As expected,  $\delta$  should have a small value for the sample to be valid. In this research case, 99.9% of the cases have been explored, which implies a value of  $\delta = 0.001$ . The steps in the value of  $t$  are also defined, which defines the resolution of the search. Also, certain steps numbers,  $n_1$  and  $n_2$ , are defined, each one with a different space search as shown in Figure 5.

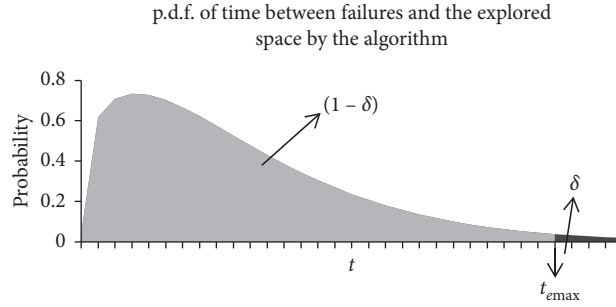


FIGURE 4: Explored space in the c.d.f. by the algorithm.

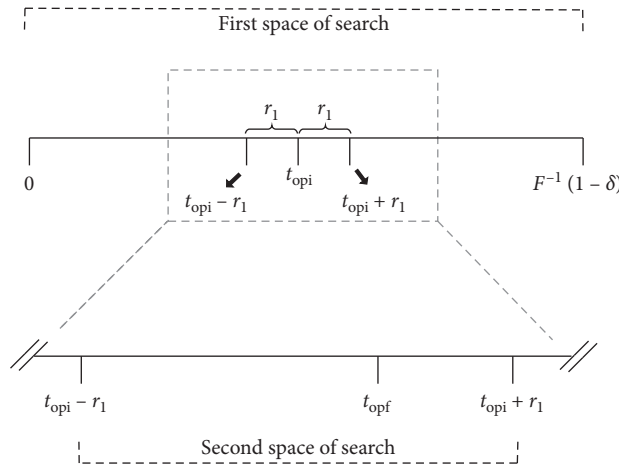


FIGURE 5: Search algorithm.

As shown in the previous illustration, the first search space is defined at interval  $[0, F^{-1}(1 - \delta)]$ . This space is explored by a number of discrete steps  $n_1$ , which is given by

$$n_1 = \frac{F^{-1}(1 - \delta)}{r_1}, \quad (43)$$

where  $r_1$  corresponds to the range for each consultation of a new value for the objective function. The second search space has new  $n_2$  and  $r_2$ , corresponding to the number of values to be explored and the of value the range between each observation. A value of  $n_1 = n_2 = 10^3$  was used for this study, with a final resolution of a rate close to  $10^{-6}$ .

It is important to note that this algorithm is tunable in terms of the size of sample spaces and the number of assessments in space in order to reduce the total number of assessments and for overall better resolution. For this publication, this is not very significant and could be studied in another case where the objective is to optimize the optimization algorithm.

Once an optimal value is found in the first search space and  $t_{opti}$  value is obtained, we proceed to define the second search space corresponding to segment  $[t_{opti} - r_1, t_{opti} + r_1]$ . This range is again explored in  $n_2$  equidistant points. Within this range, it is shown that the lowest value of the objective function value is defined as the smallest  $t_{opt}$  found in the second search space as the optimal value for preventive

intervention to the original  $\alpha$  value, which for simplification has been  $\alpha = 1$ . This  $t_{opt}$  has been denominated standard optimal time to PM.

**4.3.2. Results of Algorithm for PRP.** The previous algorithm has been run for different values of  $\beta$  and  $p$  as indicated in 4.3.1. A 3D-chart representation of several solutions has been obtained and presented in Figure 6.

The chart in Figure 6 has been modified, so that areas where the optimal value of PM time gives inconsistent results, such as an undefined value or a value greater than the MTBF, are not considered. Besides, the grid used for the graph is reduced with respect to the resolution of the generalized chart to improve the visualization. Although this figure represents a first approach prior to obtaining generalized charts, important conclusions were obtained from the result:

- 1 There is a clearly defined area where it is convenient to perform PM on modeling PRP.
- 2 There is no time for PM for values of  $\beta < 1$ . It is not convenient to perform PM, independently of the ratio between the cost and the cost preventive correction,  $p$ .

Under the criterion, preventive activity is not performed within 0.1% of the highest times; the results have shown that, in in 99.91% of cases, the optimal values for a given  $\beta$  and  $p$

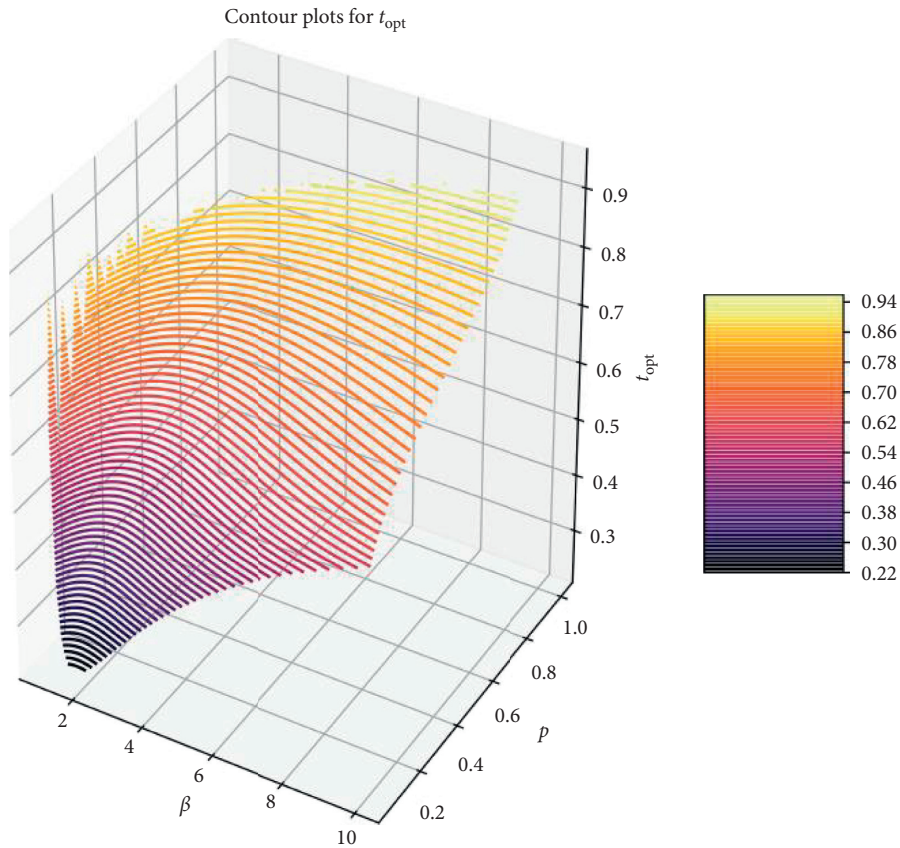


FIGURE 6: Optimal preventive time for PRP modeling.

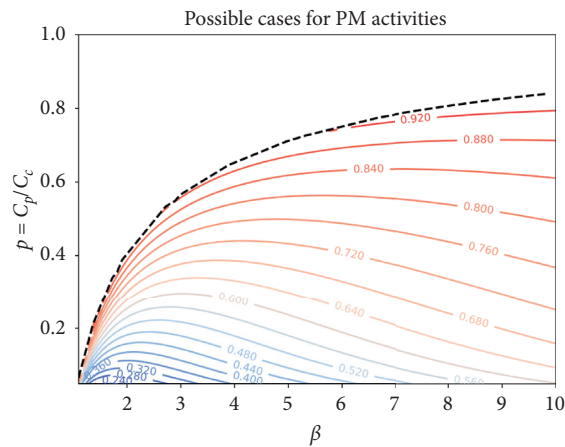


FIGURE 7: Limit possibilities for preventive maintenance under PRP modeling.

are within the search range, previously established by the  $\delta$  variable. The results are then consistent with the assumptions used.

In Figure 7, the boundary zone to run optimal PM is also presented. The entire area under the dashed curve corresponds to the pair of values for  $p$  and  $\beta$ , in which it is convenient to implement the PM policy in a fixed time, which is considered throughout this work. The area above

the curve corresponds to the possibilities where it is not convenient to have a policy of fixed-time PM.

Finally, a generalized chart has been developed as a result of this research, which is shown schematically in Figure 8 and presented in detail in the appendix. Since the most common values for the beta parameter are  $\beta \in (1, 2]$ , the generalized charts for this range are incorporated in detail in Appendix A, using a 0.01 step for each adjustment. For

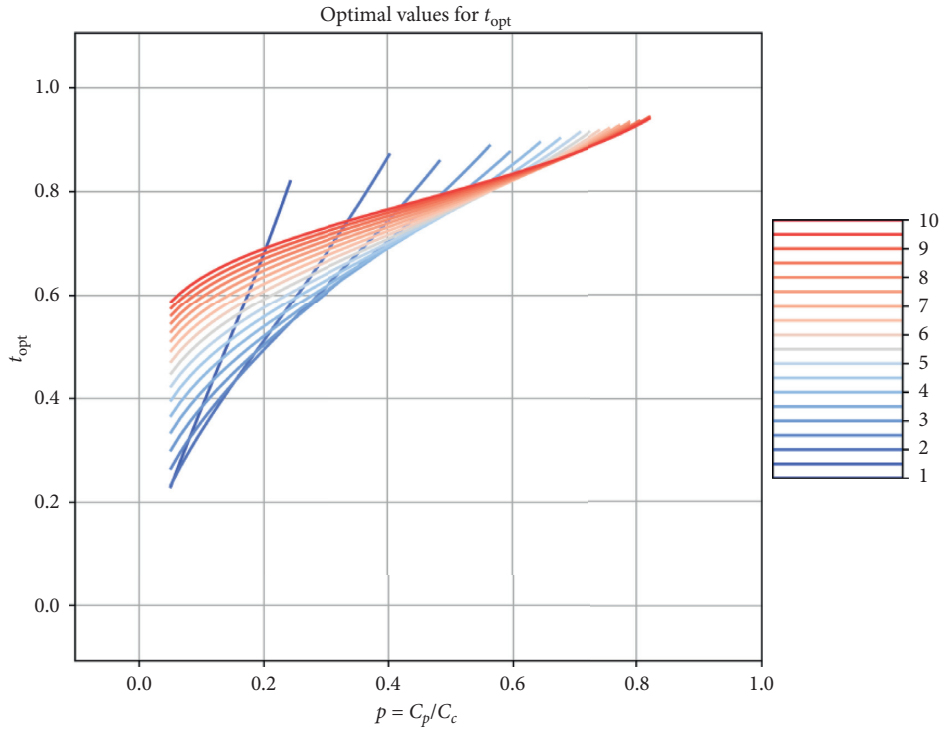


FIGURE 8: Chart representation for optimal values searching.

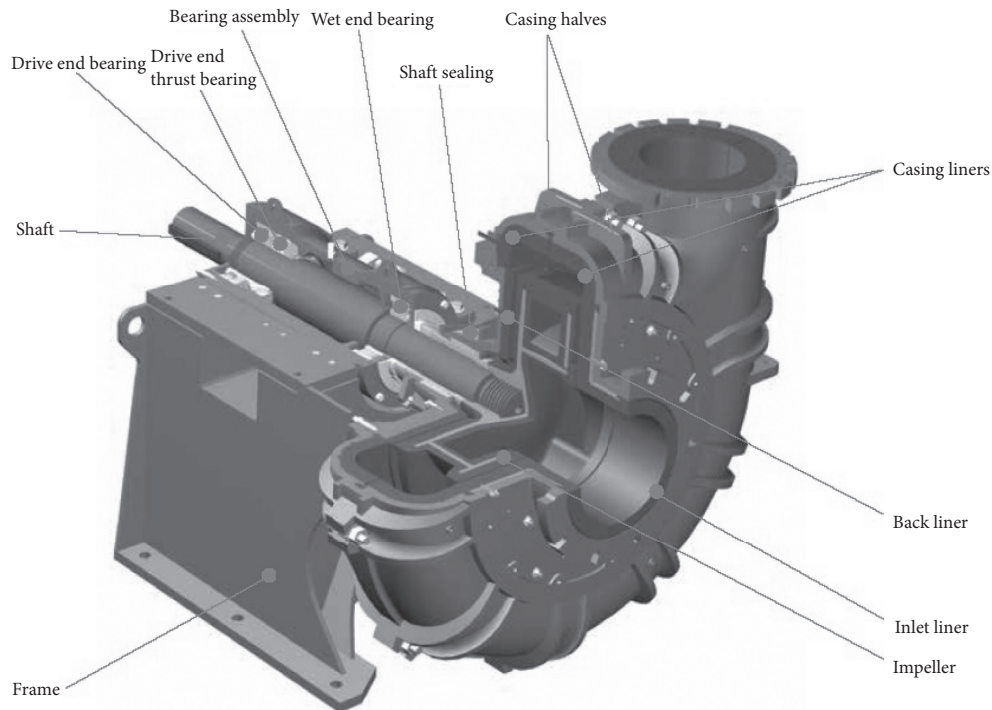


FIGURE 9: General scheme of slurry pumps.

general purposes, generalized charts for  $\beta \in (1, 5]$  are also incorporated in Appendix B considering a step of 0.05 for each  $\beta$  value.

This chart contains a generalization of the optimization for different parameter values. In other words, to obtain the

optimal time of replacement for a 2-parameter Weibull distributed lifetime of an item, first, the  $p$  parameter is needed, i.e., the relation between PM cost and corrective maintenance cost. Then, it is necessary to find the corresponding curve for the  $\beta$  value of the distribution. Once the



TABLE 1: Times between failures for slurry pump P1 in hours.

No. of failures	Time between failures (h)	No. of failures	Time between failures (h)
1	434.09	16	375.05
2	226.04	17	496.48
3	266.67	18	649.41
4	681.33	19	540.68
5	1127.85	20	491.59
6	634.69	21	947.31
7	474.84	22	718.78
8	38.72	23	953.63
9	31.89	24	182.2
10	711.52	25	391.55
11	726.9	26	327.71
12	574.15	27	986.04
13	1043.54	28	352.53
14	336.54	29	631.86
15	771.23	30	680.52

TABLE 2: Corrective maintenance cost for each failure in USD.

No. of failures	Cost of the failure (USD)	No. of failures	Cost of the failure (USD)
1	1132.71	16	847.8
2	972.75	17	1049.03
3	853.58	18	474.86
4	789.41	19	1740.39
5	836.97	20	1041.64
6	994.39	21	898.1
7	1274.33	22	594.43
8	528	23	1539.22
9	847.06	24	1496.3
10	1140.66	25	1375.55
11	1010.95	26	748.04
12	468.01	27	877.48
13	1045.29	28	793.51
14	1493.85	29	430.25
15	1320.56	30	1375.03

intersection is located, it is necessary to scroll horizontally to the left to find the corresponding  $t_{opt}$  value. This  $t$  value is generalized considering  $\alpha = 1$ , and then the  $t_p$  optimal value will be  $t_p = \alpha \cdot t_{opt}$ . If there is no intersection between the  $p$  parameter and the  $\beta$  corresponding curve, it is not convenient to perform a PM activity.

## 5. Case Study

**5.1. Description of the Process.** The case study and application of the proposed methodology are focused on one of the slurry pumps (P1) of a mining process, which is essential for the continuity of the process (critical) and is exposed to a high-stress job, especially by the transfer characteristics of highly abrasive and corrosive flow, high solids content, and strong acidity.

A slurry pump is a rugged heavy-duty pump intended for aggressive or abrasive slurry solutions typically found in the mining industry with particles of various sizes. These pumps increase the pressure of a liquid and solid particle mixture (commonly called slurry) through centrifugal force (a rotating impeller) and convert electrical energy into slurry potential and kinetic energy. In Figure 9, a general scheme of the pump is presented.

**5.2. The Proposed Methodology.** In the following are presented the steps of the proposed methodology, as well as the historical collection of failure data to obtain the required parameters, applied in the case study mentioned. (Table 1)

### Step 1 Trend test

Slurry pump P1 has registered the following 30 times between failures, measured in hours and presented in order of occurrence.

First of all, as the literature [34] proposes, it is required to evaluate a trend test; the most commonly used is the Laplace Trend Test [34, 35], which gives a test statistic  $z$  that has to be compared with the standard normal distribution because it fits approximately to  $n$  standard normal random variable. The  $z$  value is calculated by

$$z = \frac{(\sum_{i=1}^n t_i/n) - (t_o/2)}{t_o \sqrt{1/12n}}. \quad (44)$$

Here,  $t_o$  is the total elapsed time,  $n$  is the number of times, and  $t_i$  is the total elapsed time to element  $i$ .

And the null  $H_0$  and alternative  $H_a$  hypotheses consider the following:

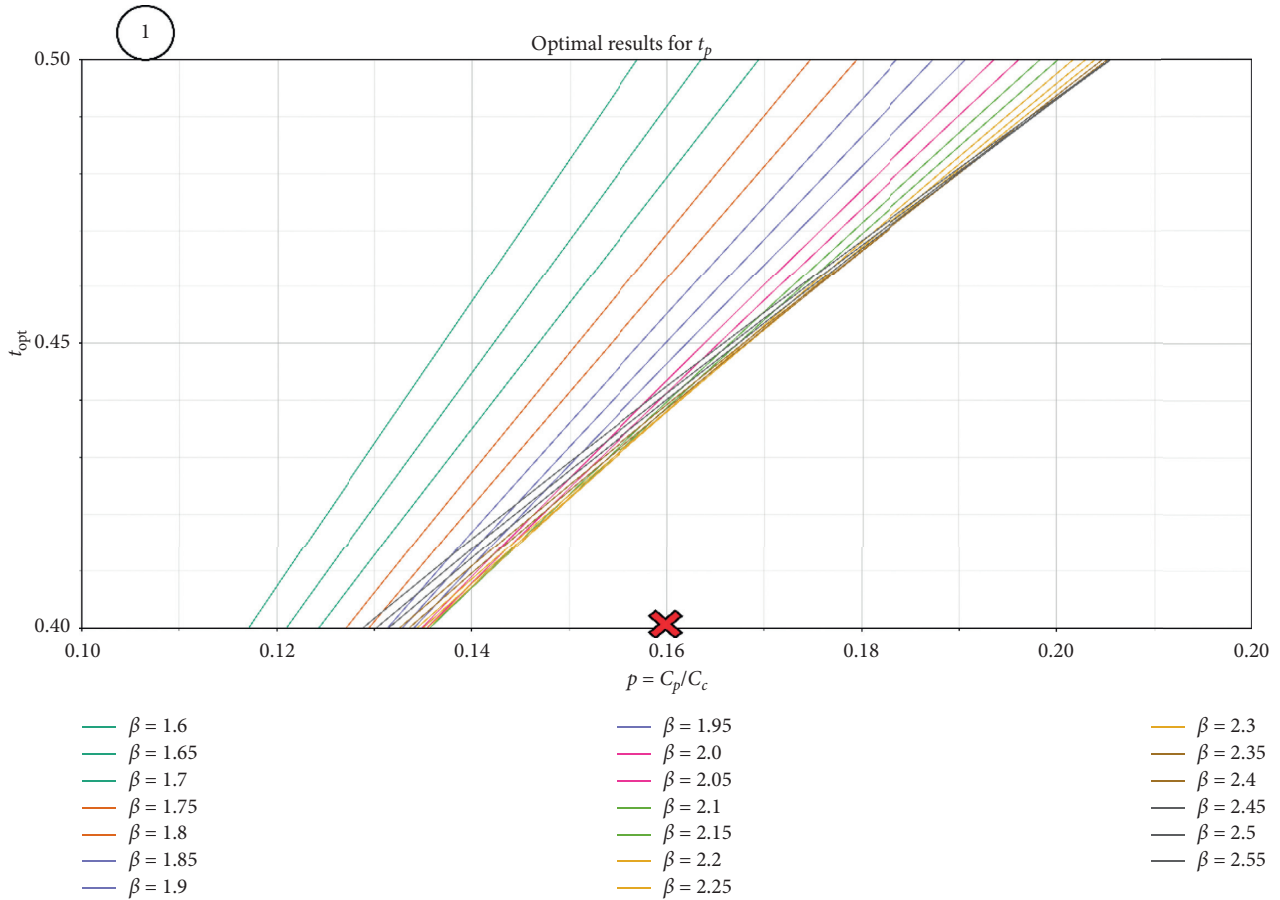


FIGURE 10: Step 1 for use of the proposed chart.

$H_0$ : no trend ( $z = 0$ ).

$H_a$ : deteriorating trend ( $z > 0$ ).

$H_a$ : improving trend ( $z < 0$ ).

Evaluating the expression gives a value of  $z = -0.0953$ . From the standard normal tables with a significance level of 0.10, the critical value is equal to 1.645. If the  $z$  value satisfies  $-1.645 < z < 1.645$ , then we would fail to reject the hypothesis of no trend. Since  $z = -0.0953$ , then is not possible to say that a trend exists, so PRP modeling is applicable.

Step 2 Distribution fitting

Once PRP modeling is properly justified it is necessary to adjust the parameters for the 2-Weibull distributions for this modeling. The most traditional method is to estimate the parameters maximizing the likelihood. The likelihood function is expressed through the joint probability as

$$P(x_i \text{ in } [x_i, x_i + dx], \quad \forall i \in \{1, \dots, n\}) = \prod_{i=1}^n f(x_i; \theta),$$

$$L(\theta) = \prod_{i=1}^n f(x_i; \theta), \tag{45}$$

where  $\theta$  corresponds to the vector of parameters of the distribution related to  $f(t)$  and  $x_i$  corresponds to the  $i$ -th realization of the sample. As the desired maximum is the likelihood between data and a p.d.f.:  $f(t | \theta)$ , the values of the vector  $\theta$  have to be adjusted with the objective function to meet that maximum. Conceptually, it is to find the parameters that adjust better to a sample  $x_1, \dots, x_n$  so that the likelihood of the values provided in a random sampling is maximum:  $P(x_i \text{ in } [x_i, x_i + dx], \forall i \in \{1, \dots, n\})$ .

Then, the parameters  $\theta$  for this case  $\{\alpha, \beta\}$  that provide maximum likelihood are those that meet [36, 37]

$$\hat{\alpha} = \left( \frac{\sum_{i=1}^n (t_i)^\beta}{n} \right)^{(1/\beta)} \tag{46}$$

$$\left( \frac{\sum_{i=1}^n (t_i)^\beta \ln(t_i)}{\sum_{i=1}^n (t_i)^\beta} \right) - \left( \frac{1}{\hat{\beta}} \right) = \left( \frac{1}{n} \right) \sum_{i=1}^n \ln(t_i). \tag{47}$$

Here,  $t_i$  is the observed time between successive failures and  $n$  is the total number of failures.

Solving the above equations, the estimators are  $\hat{\alpha} = 632.04$  and  $\hat{\beta} = 1.99$ .

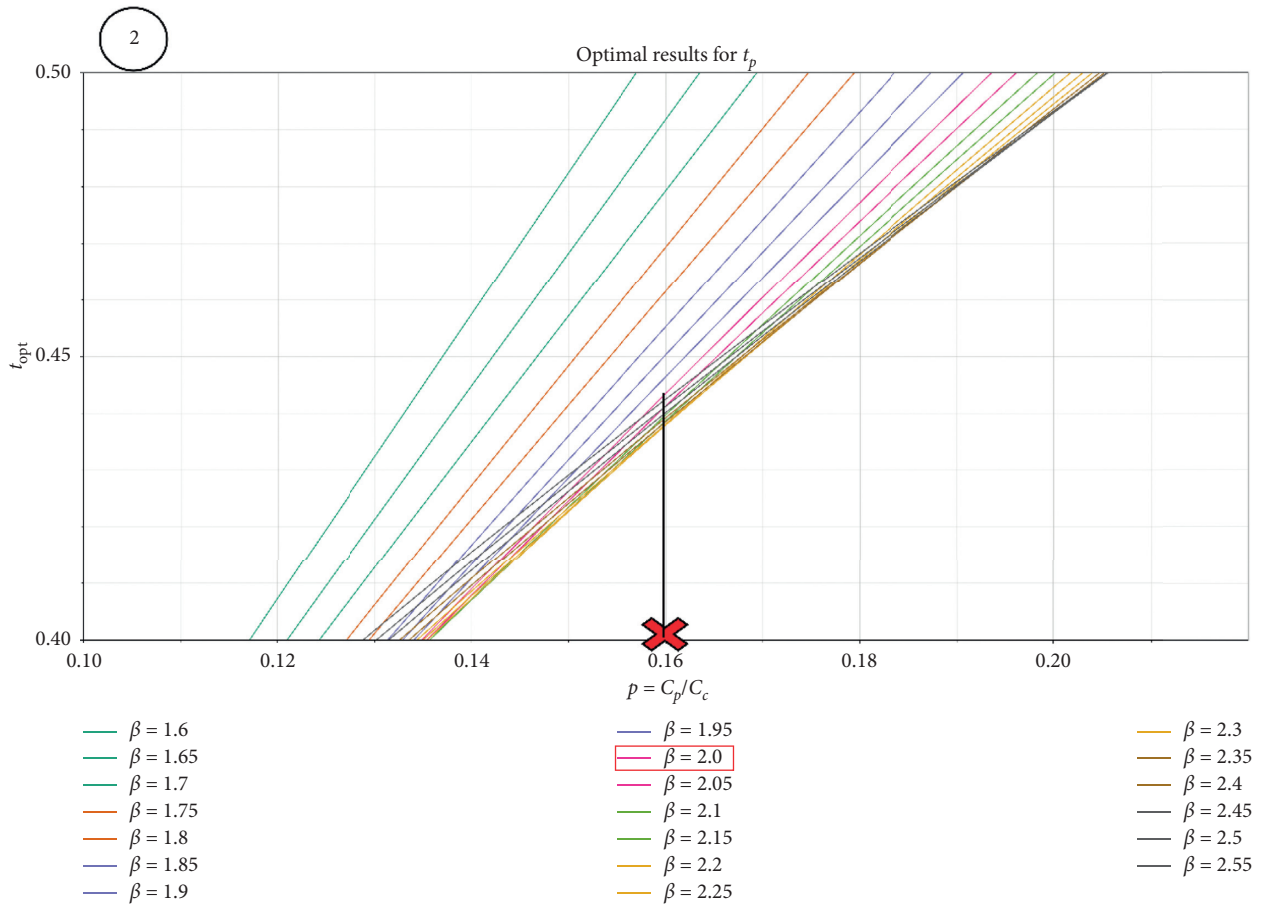


FIGURE 11: Step 2 for use of the proposed chart.

Step 3 Calculating the cost related parameter

In relation to the cost for the historical failure data, the costs of the corrective interventions have been collected in Table 2, expressed in (USD).

The average corrective cost is 999.67 (USD), and it is known that the preventive activity has a cost of 160 (USD), so the value of  $p$  is given by

$$p = \frac{c_0(\text{USD})}{999.67(\text{USD})} \approx 0.16. \tag{48}$$

Step 4 Chart use

This step is composed of substeps. In this stage, the proposed chart in the appendix is needed. The substeps are the following:

- (1) With the value of  $p$ , go to the abscissae axis, in this case 0.16.
- (2) Find the corresponding  $\beta$  value: In this case, we consider  $1.99 \approx 2$ . Follow the corresponding line for the value of  $p$  in vertical sense up to the intersection with the corresponding  $\beta$  curve.
- (3) Once the intersection is found, move horizontally to the left and find the standard  $t_{\text{opt}}$  value.

- (4) Calculate the optimal  $t_p$  time with the product between the standard  $t_{\text{opt}}$  value and  $\alpha$ .

The steps are schematically represented in Figures 10–12.

Following Step 4, we find that the optimal  $t_p$  value when performing the preventive activity is at  $t_p = 0.443 \cdot \alpha = 279.99(h)$ . Then, the PM policy is ready to be implemented. Notice that, for other values of  $\beta$ , an interpolation could be useful between the curves.

6. Discussion

It is interesting to analyze how the solution changes with altering one of the parameters of the problem. Sensitizing this to the shape parameter  $\beta$ , for different values of  $p$ , a chart has been developed and shown in Figure 13.

The unplotted area reveals the fact that it is not convenient to perform PM activities.

In the case of sensitizing the values of the standard optimal PM time  $t$  for different values for the scale parameter  $\alpha$ , considering the same  $\beta$  and  $p$  values, we find that there is a direct relation, and this has been shown in Section 4.

From the results, it can be stated that if there are two kinds of equipment, Equipment A and Equipment B, both with the same  $\beta$  and  $p$  values, Equipment A with scale parameter  $\alpha_A$ , and Equipment B with scale parameter  $\alpha_B$ ,

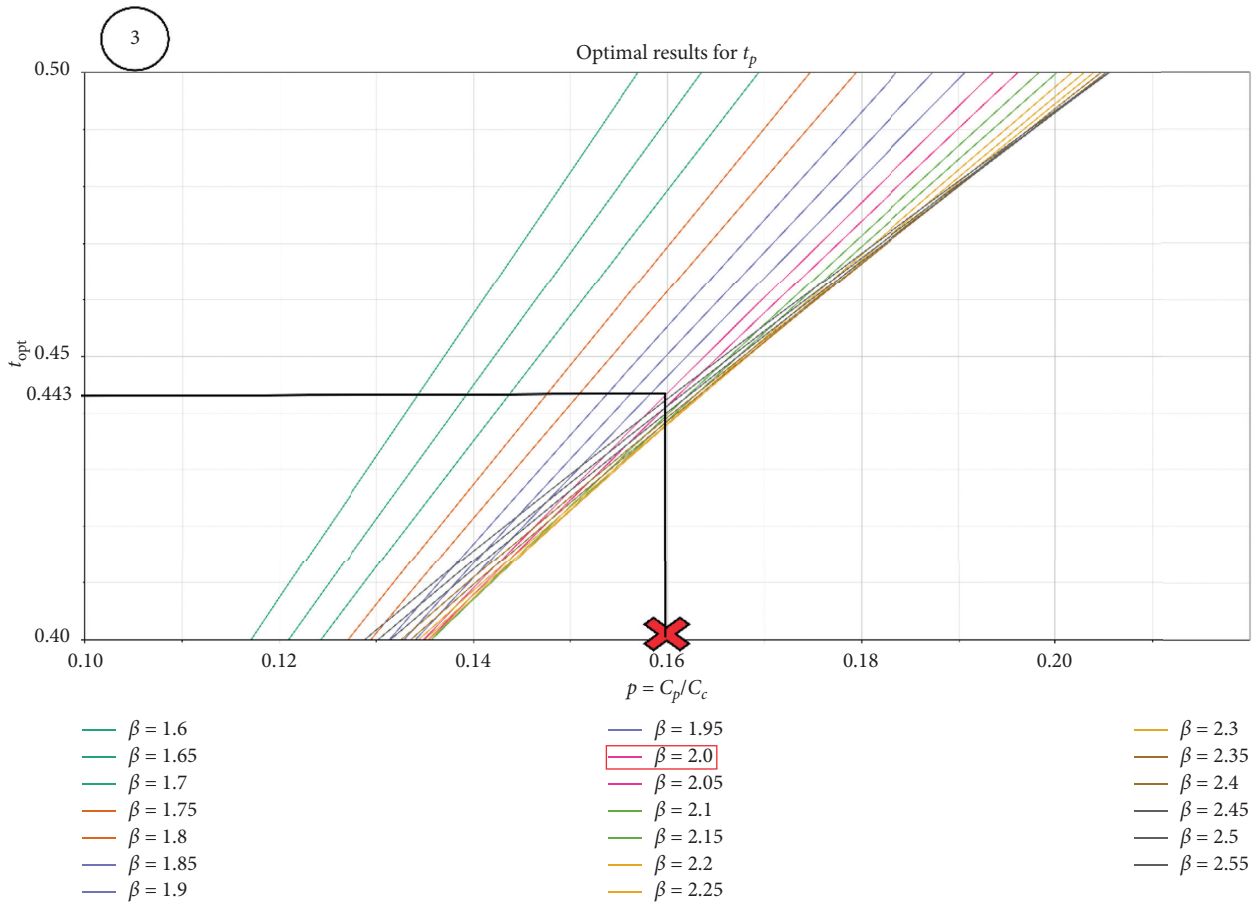


FIGURE 12: Step 3 for use of the proposed chart.

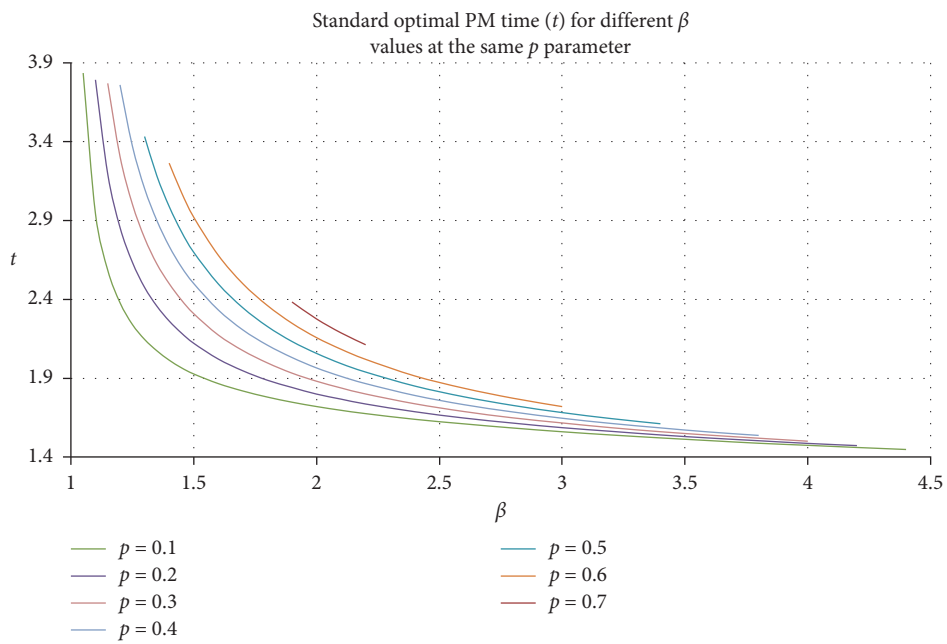


FIGURE 13: Sensitizing the standard optimal PM time ( $t$ ) to different values of  $\beta$ , for different values of  $p$ .

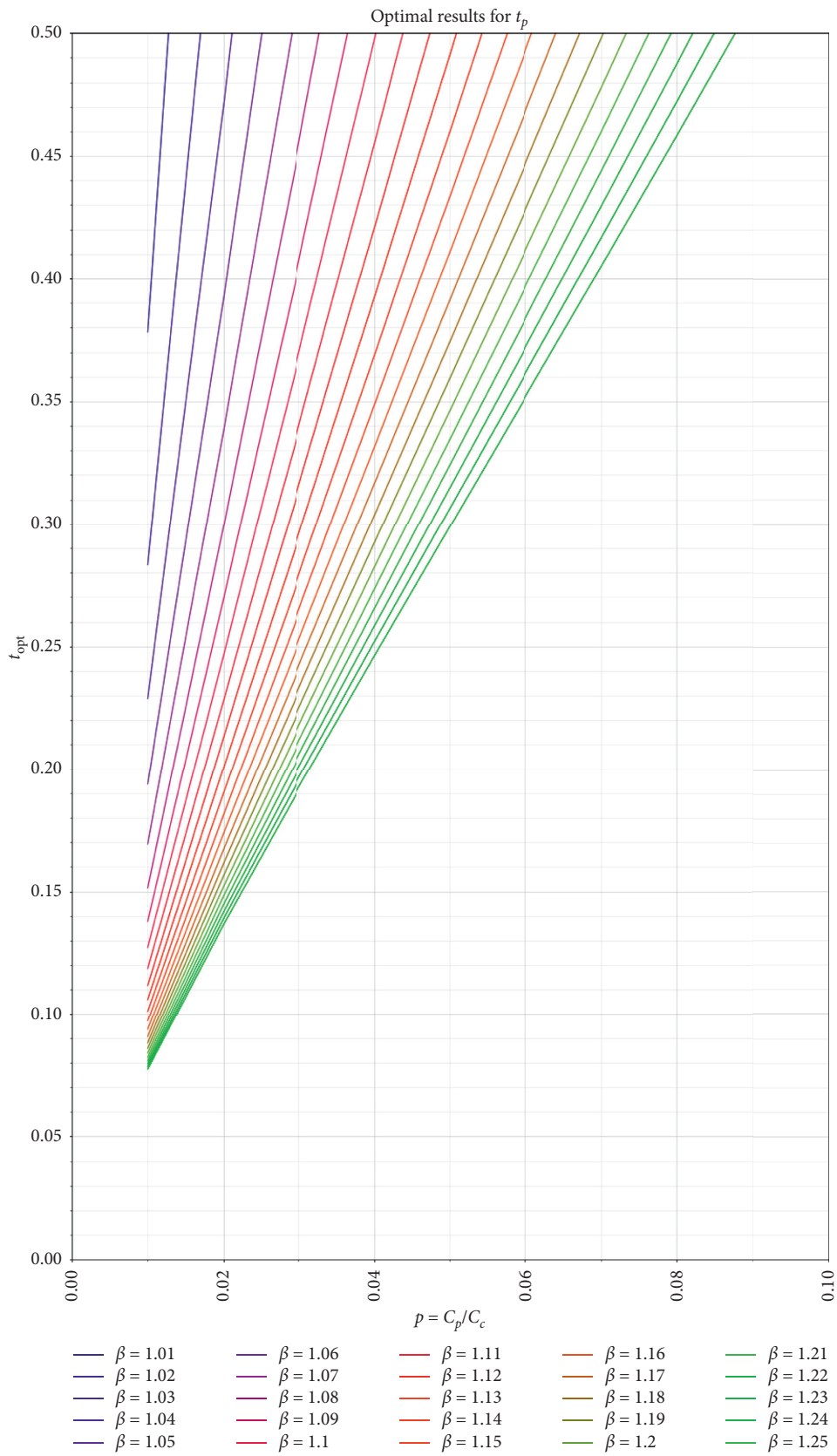


FIGURE 14: Optimal values for  $\beta \in [1.01, 1.25]$  (part 1).

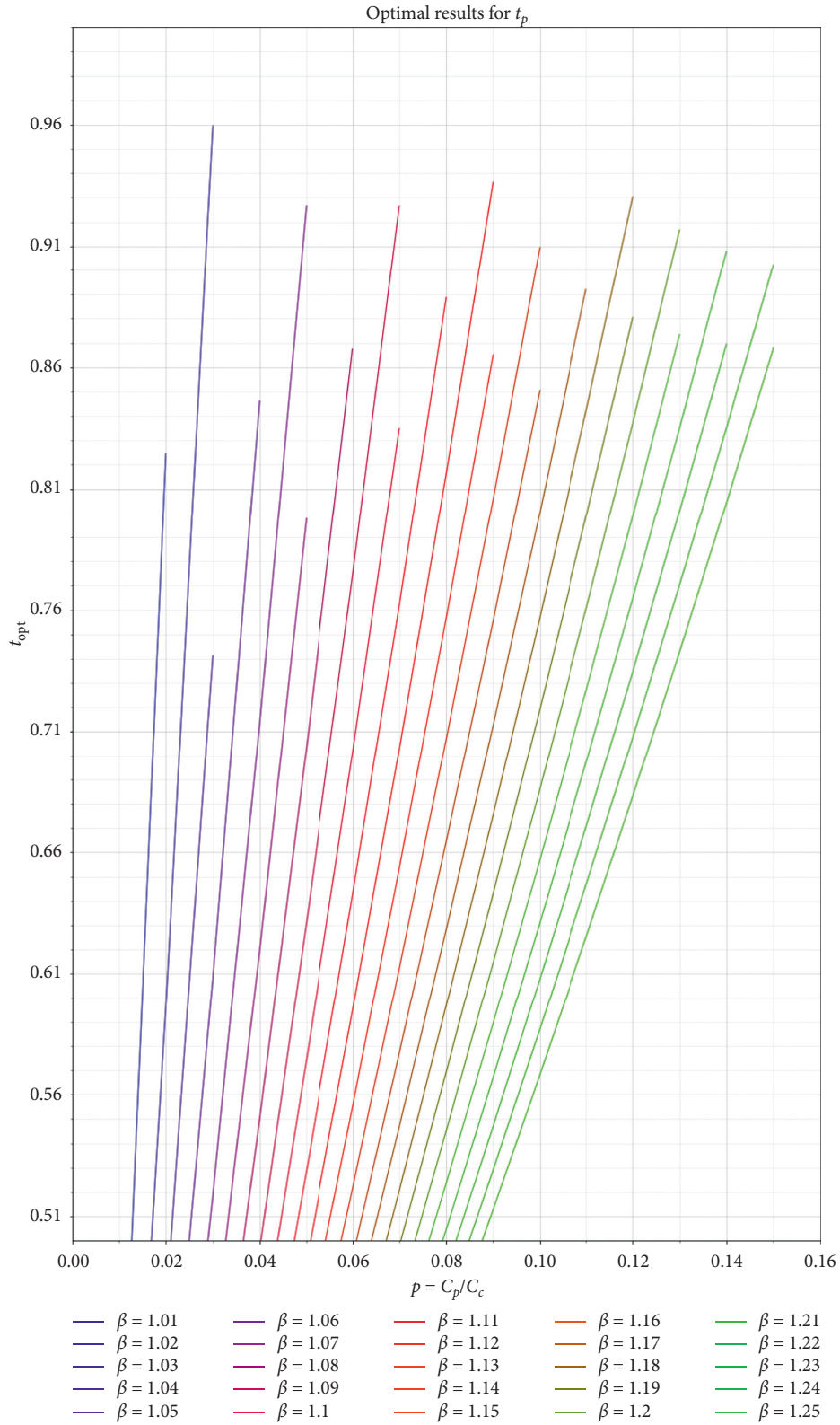


FIGURE 15: Optimal values for  $\beta \in [1.01, 1.25]$  (part 2).



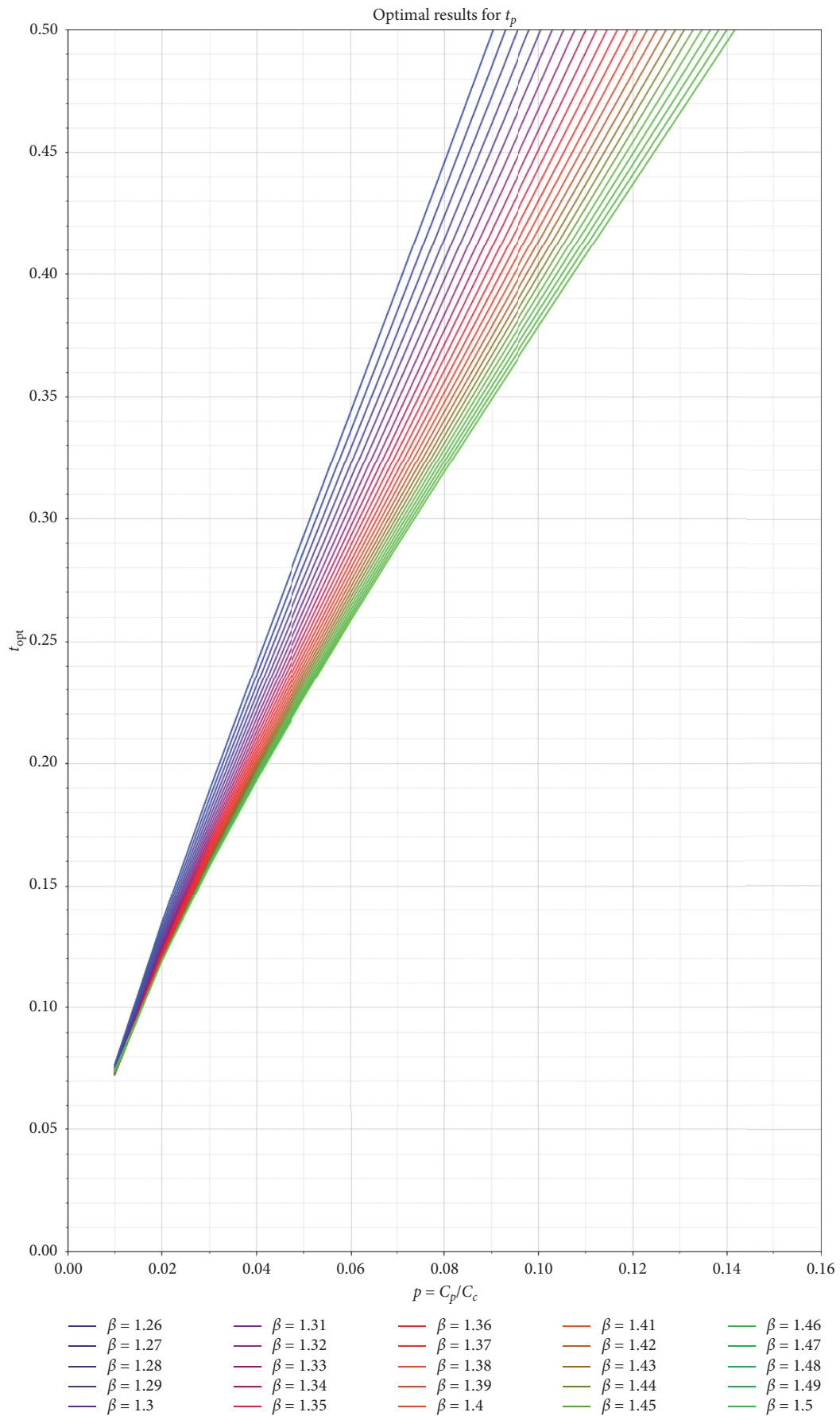


FIGURE 16: Optimal values for  $\beta \in [1.26, 1.5]$  (part 1).

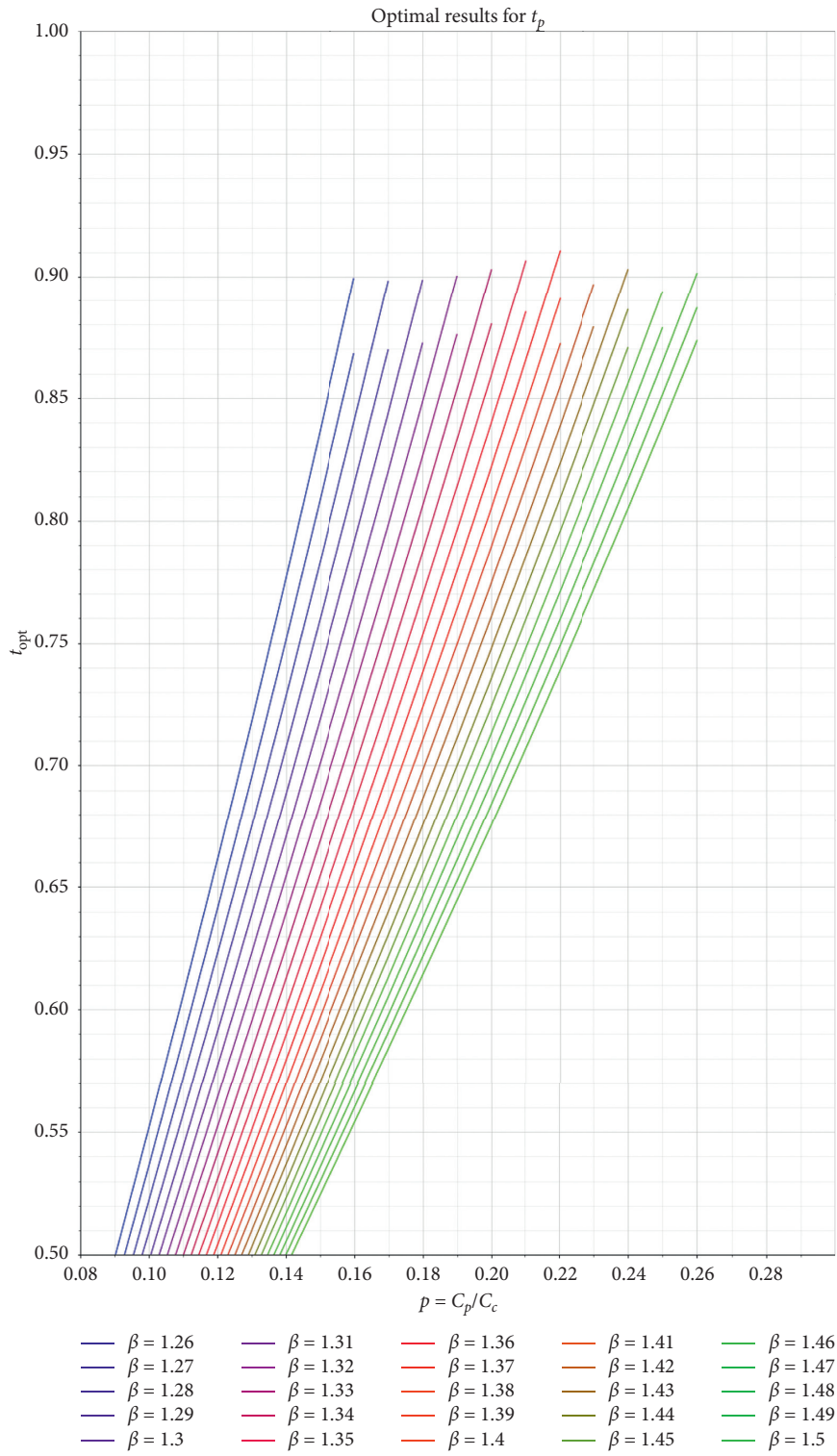


FIGURE 17: Optimal values for  $\beta \in [1.26, 1.5]$  (part 2).

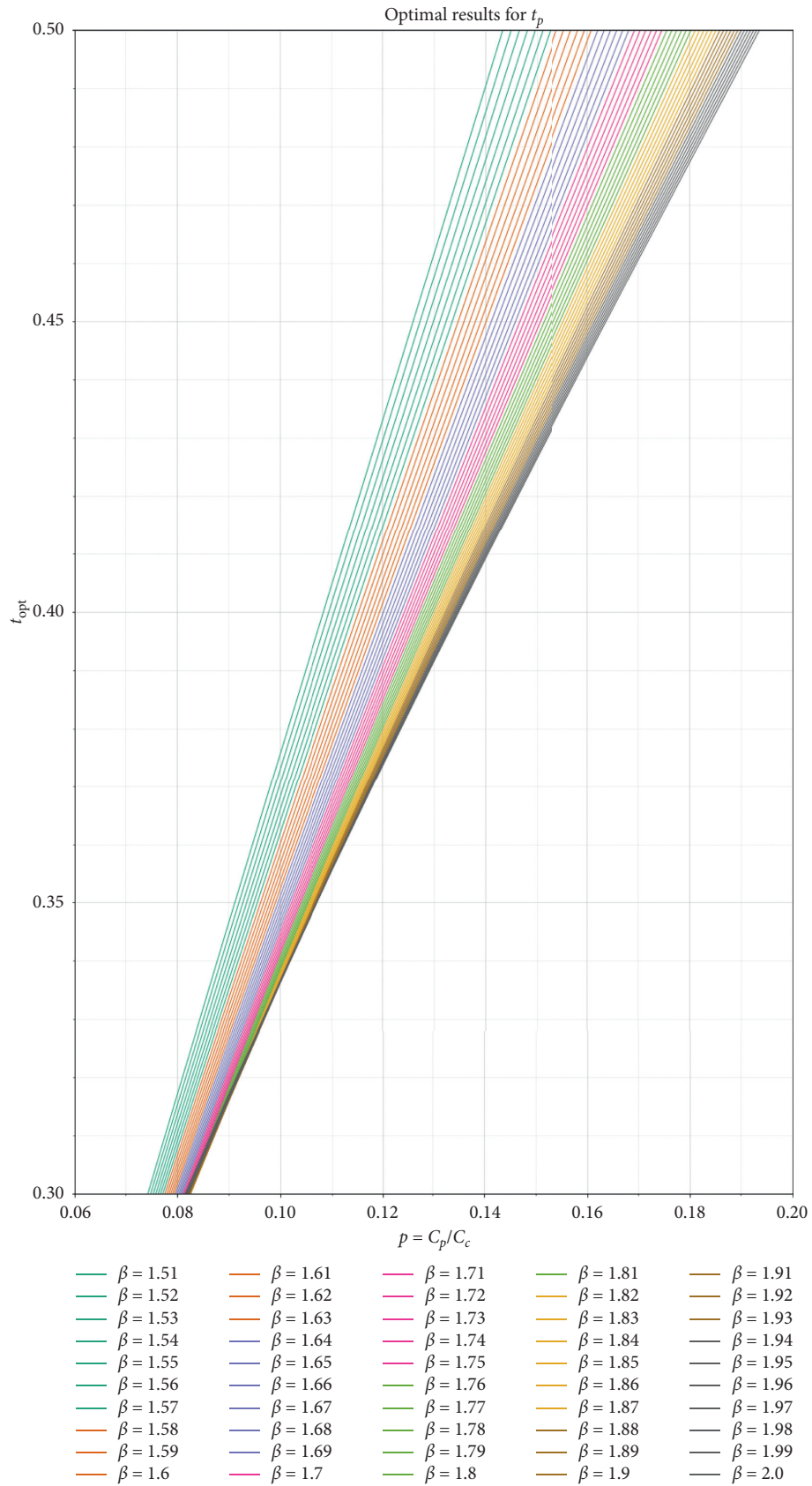


FIGURE 18: Optimal values for  $\beta \in [1.51, 2.00]$  (part 1).

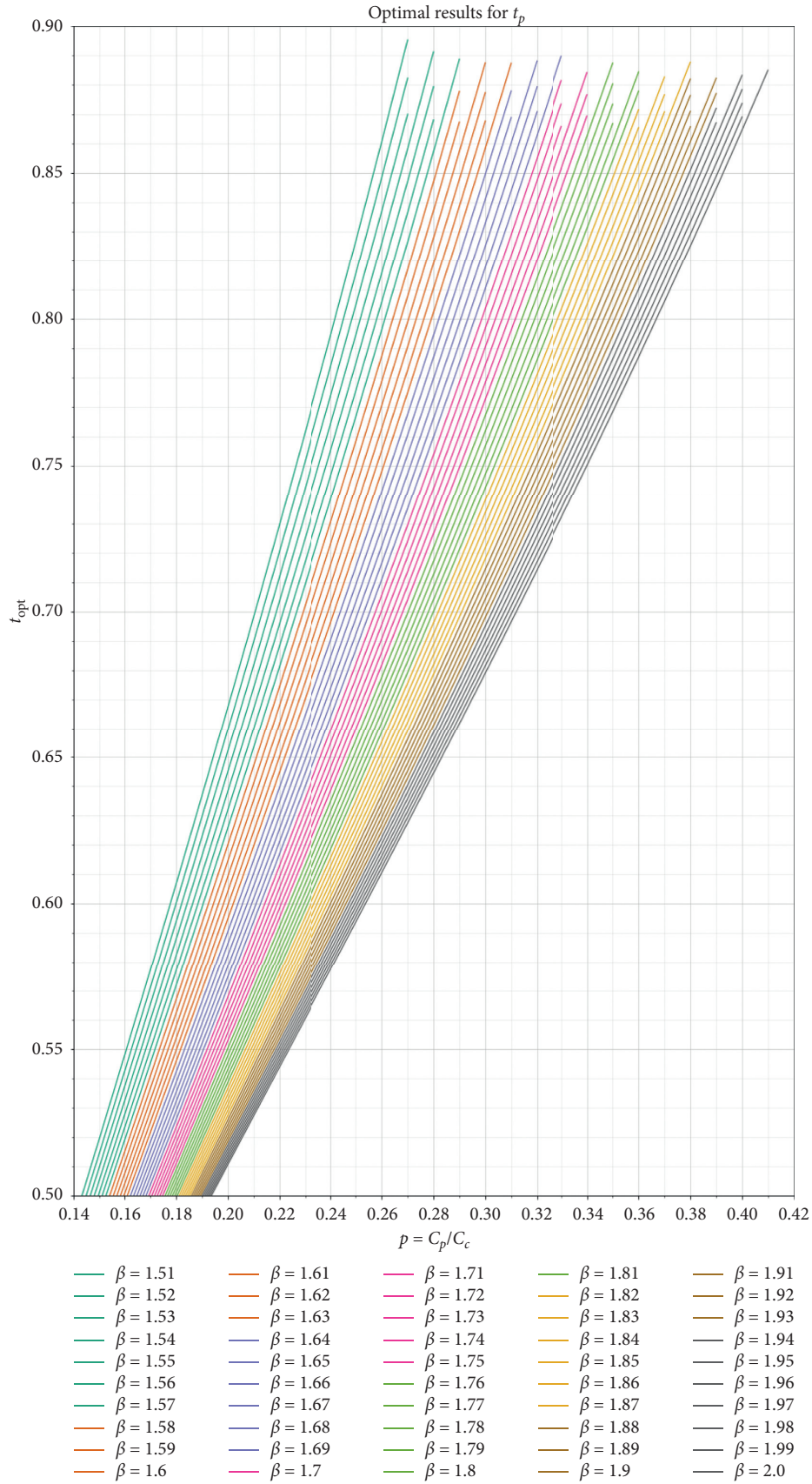


FIGURE 19: Optimal values for  $\beta \in [1.51, 2.00]$  (part 2).

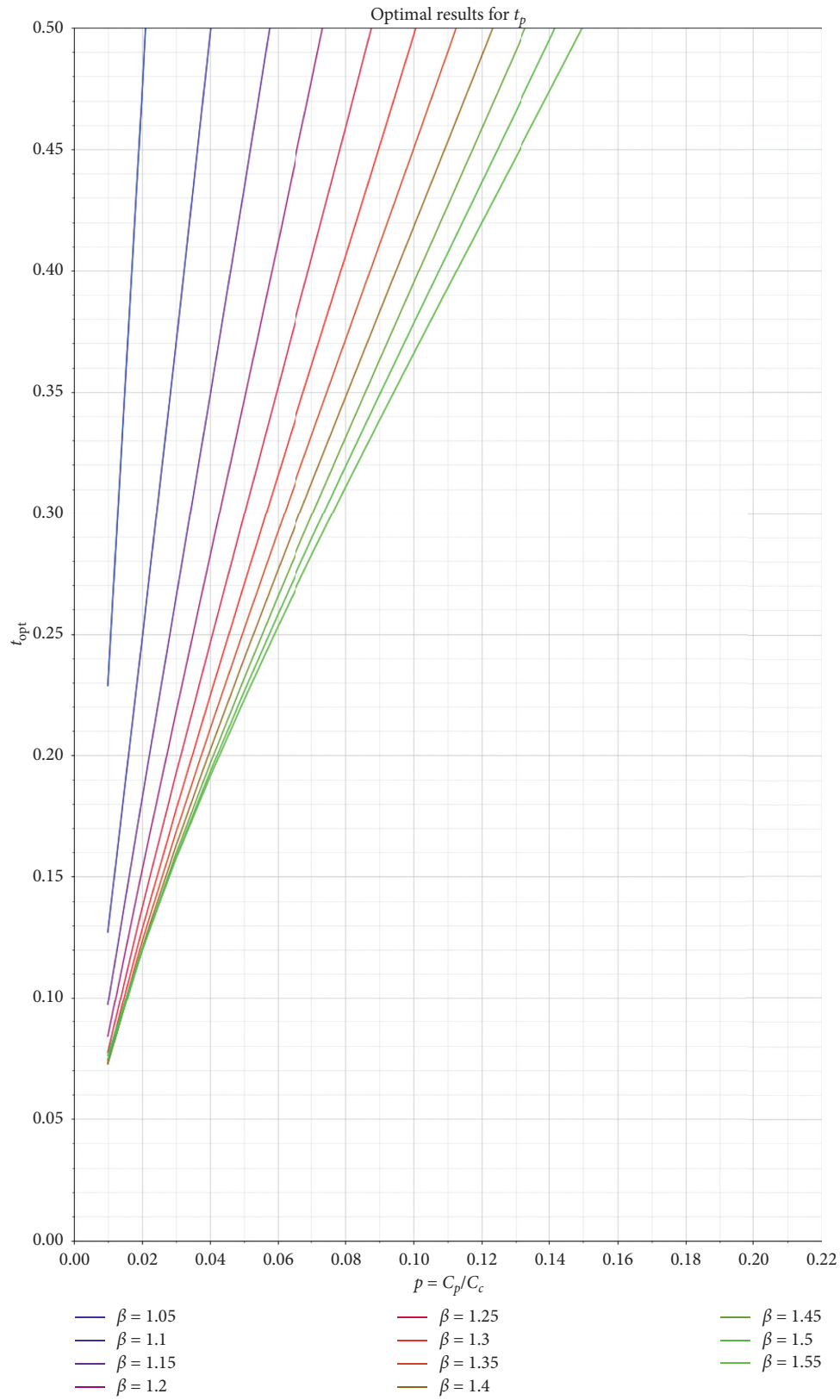


FIGURE 20: Optimal values for  $\beta \in [1.05, 1.55]$  (part 1).

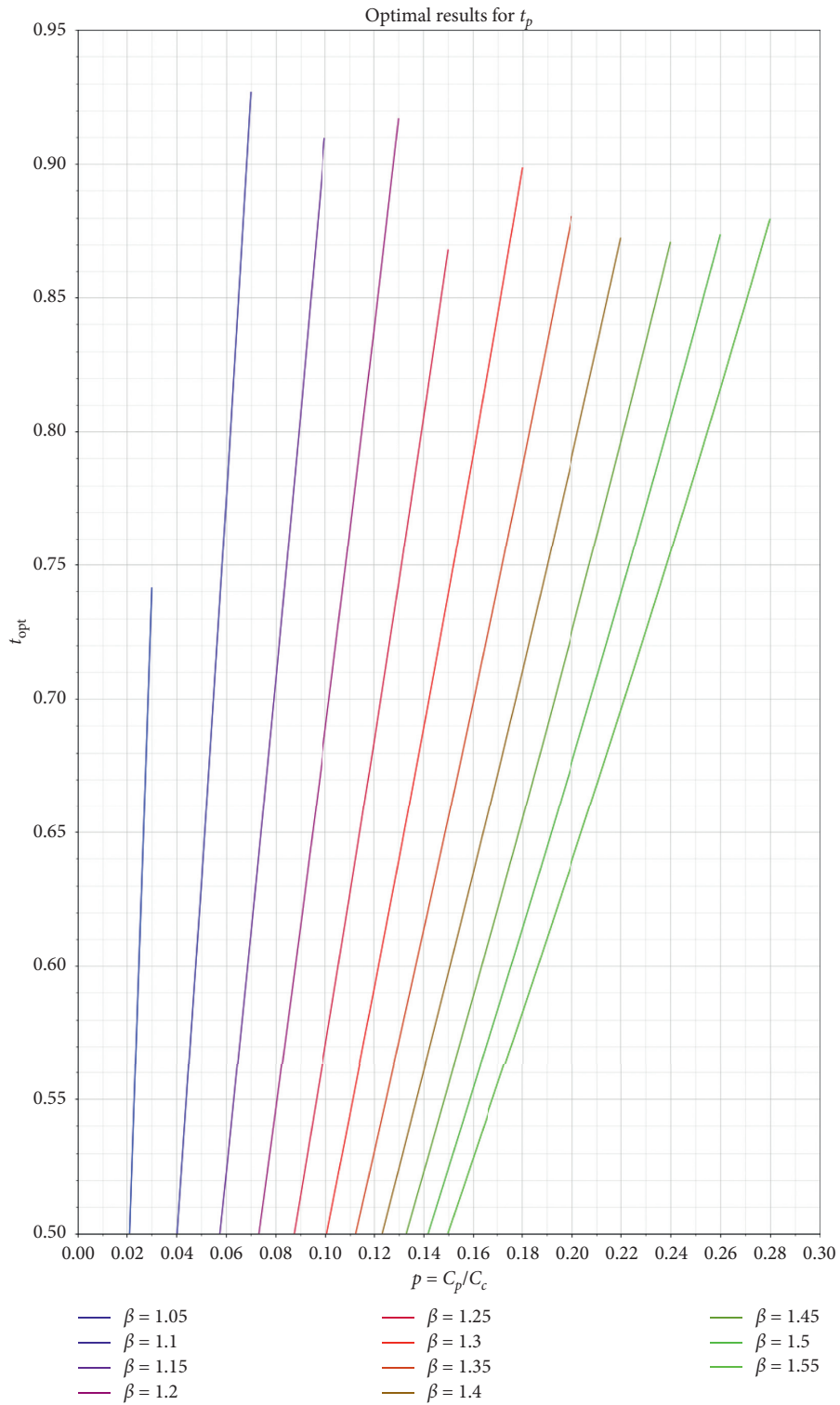


FIGURE 21: Optimal values for  $\beta \in [1.05, 1.55]$  (part 2).



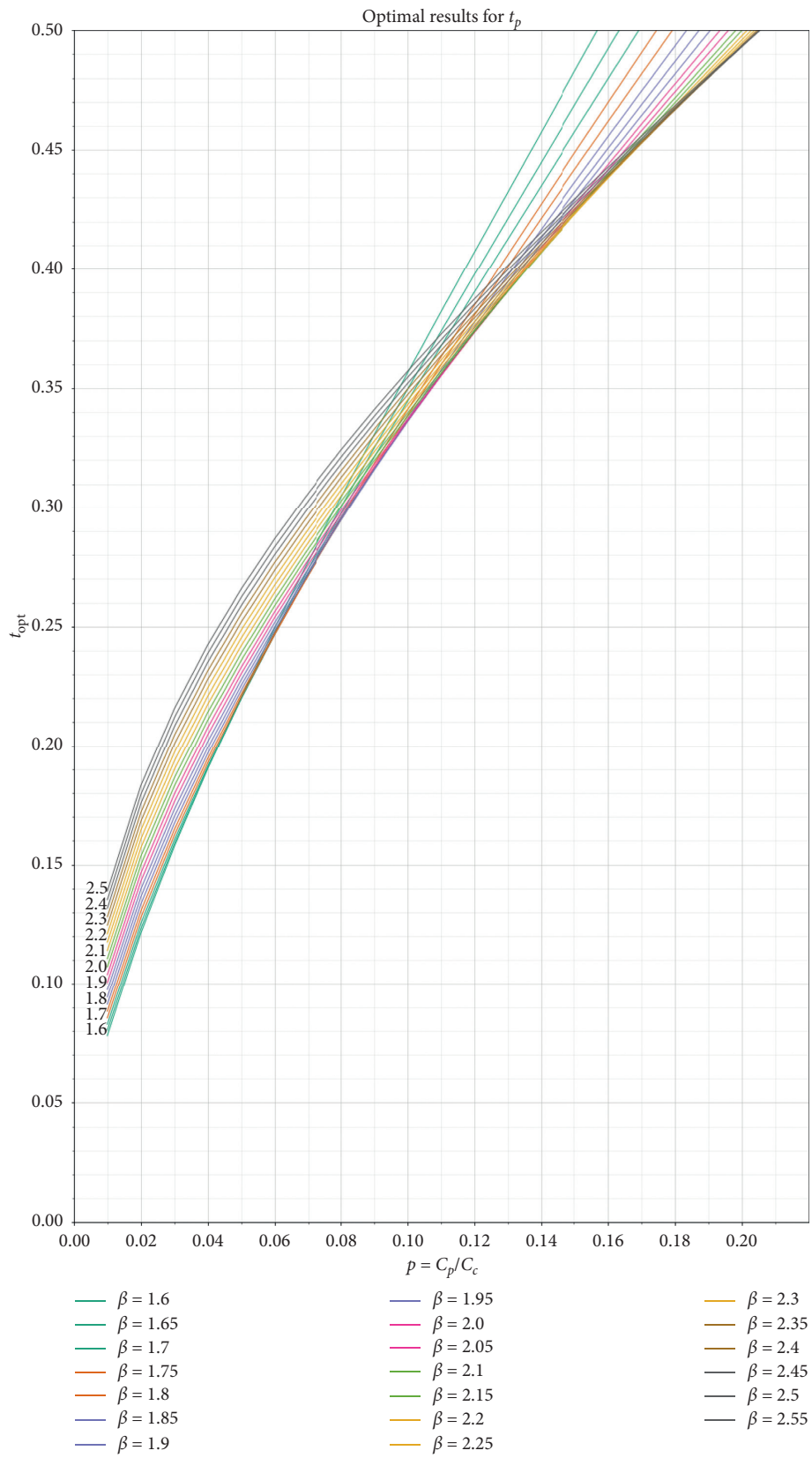


FIGURE 22: Optimal values for  $\beta \in [1.6, 2.55]$  (part 1).

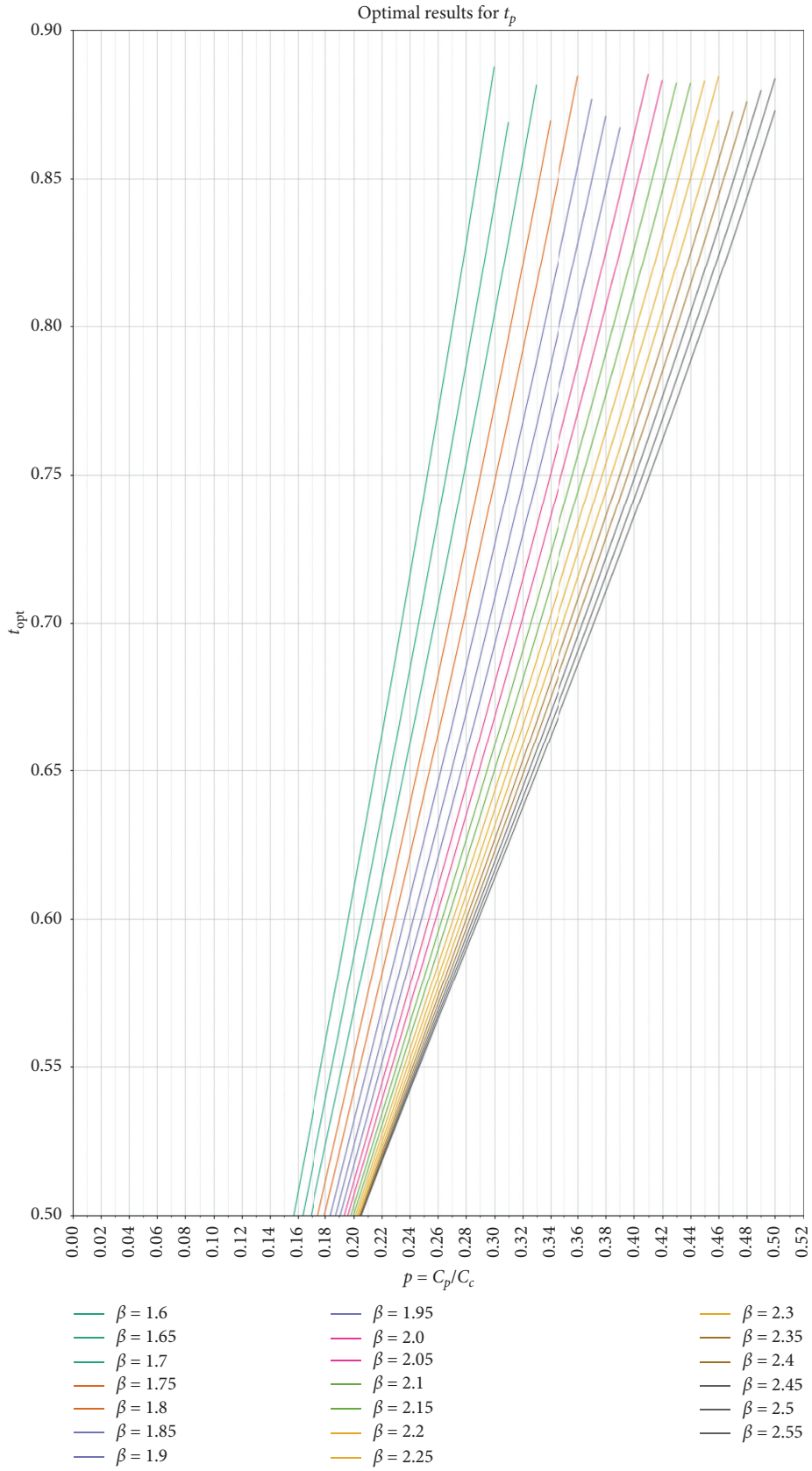


FIGURE 23: Optimal values for  $\beta \in [1.6, 2.55]$  (part 2).

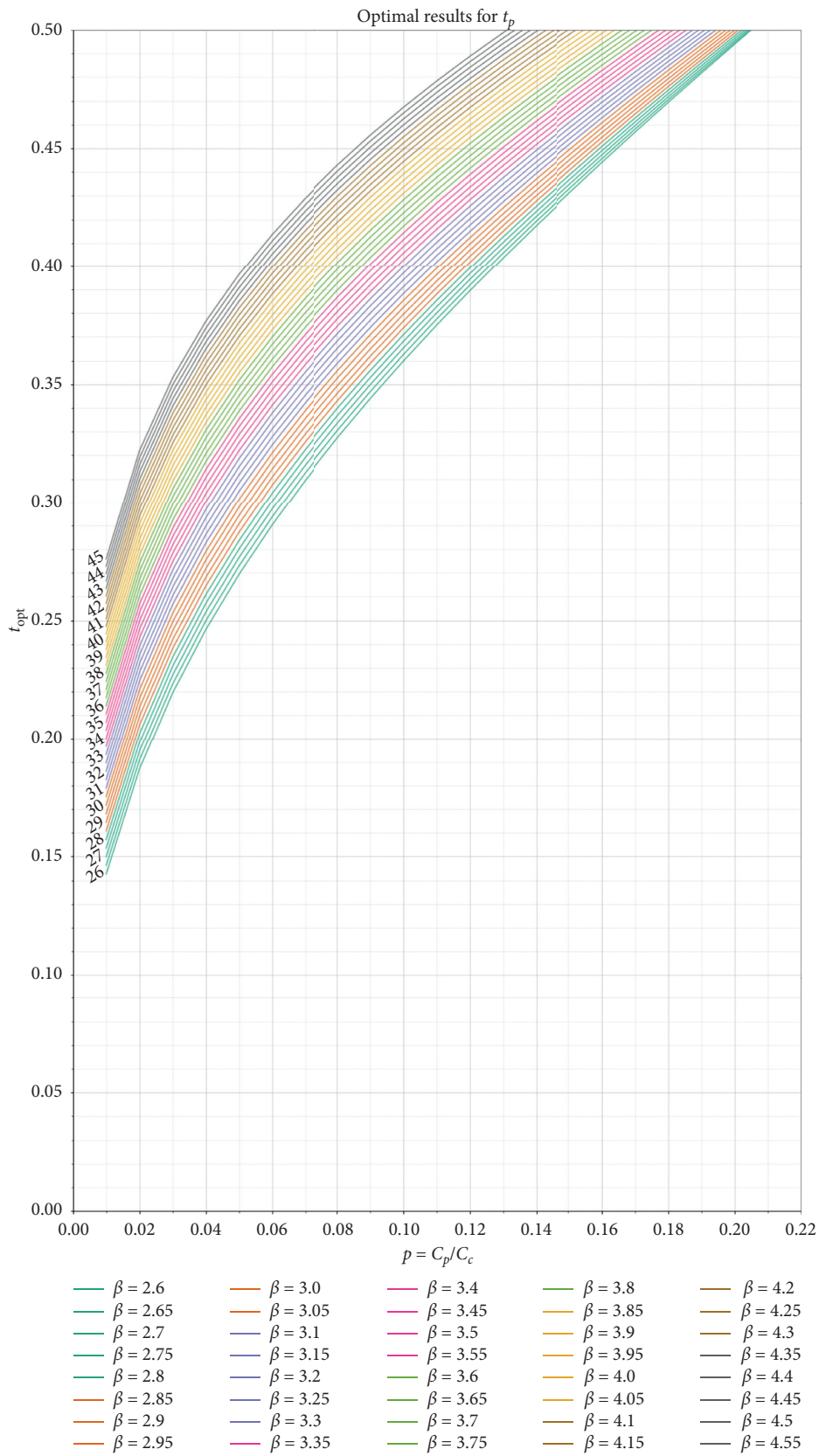


FIGURE 24: Optimal values for  $\beta \in [2.6, 4.55]$  (part 1).

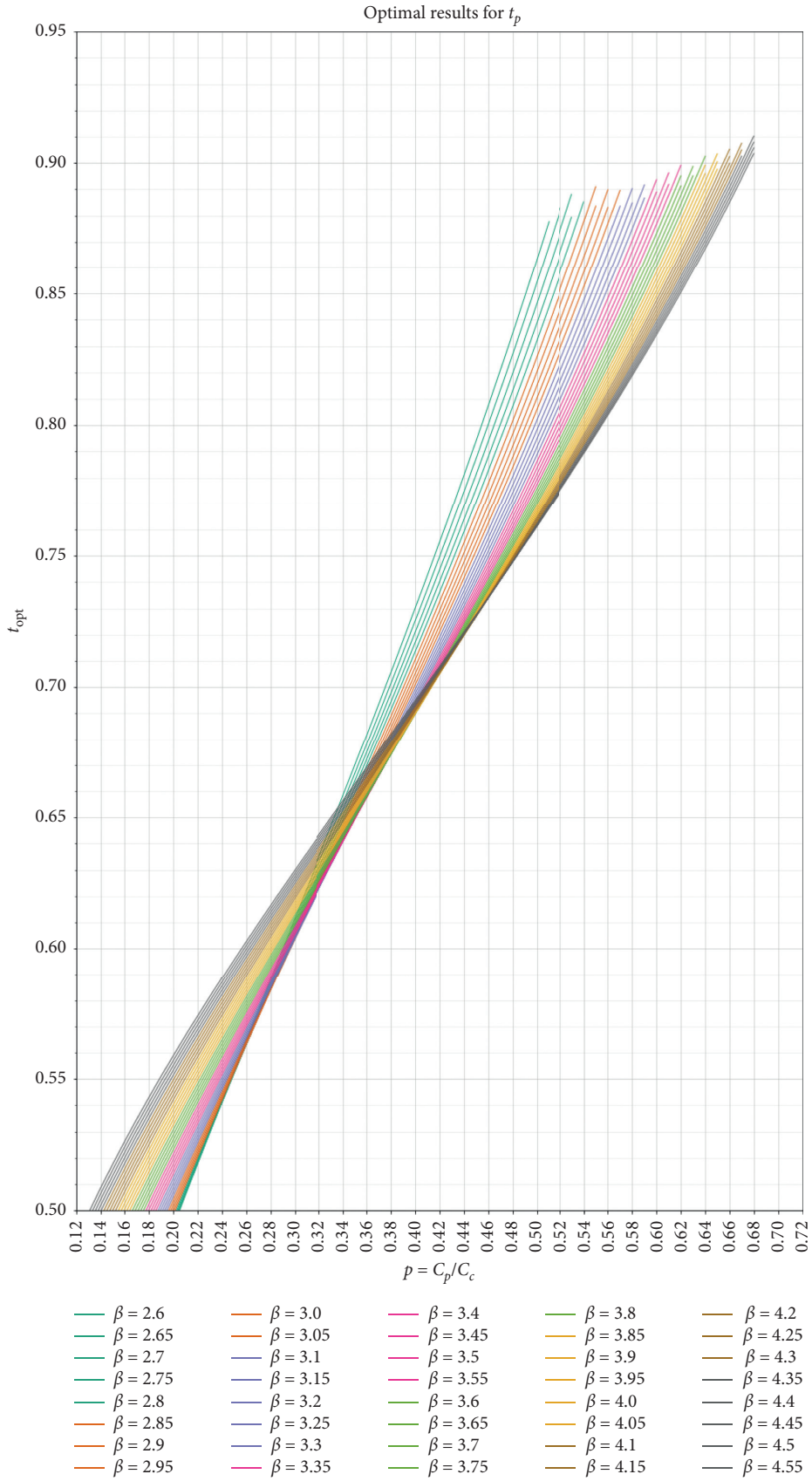


FIGURE 25: Optimal values for  $\beta \in [2.6, 4.55]$  (part 2).

and the optimal  $t_p$  for Equipment A is  $t_{p,A}$ , then the optimal  $t_p$  for Equipment B is  $t_{p,B} = (\alpha_A/\alpha_B) \cdot t_{p,A}$ .

## 7. Conclusion

From the present research, it is possible to conclude that, under PRP modeling and minimal long-run cost of maintenance in items, there is a boundary zone of possible combinations of  $p$  and  $\beta$  parameters in which it is convenient to perform this kind of activity.

Moreover, it has been shown from the solution for the optimization problem that a general solution could be obtainable by a chart that contains enough information to get the optimal PM time for those combinations of  $p$  and  $\beta$  parameters, for which it is convenient to perform PM under PRP modeling. The solution to the problem is provided in the appendix.

This solution has enormous potential because the tasks of the person in charge related to the determination of the policies of preventive maintenance or replacement are reduced drastically. Now, this person does not need the analytical skills and deep understanding of the mathematical problem that could cause considerable errors. This method indeed dramatically reduces the possibility of making calculation mistakes.

Nowadays, increasing competitiveness is a requirement in the industry; this research is a contribution in terms of expediting processes and accelerated insertion of good policy implementation as the optimal preventive maintenance, and also in terms of education of reliability.

Future research based on the elaboration of this type of instrument can be extended in general to other types of maintenance currently addressed in the literature, such as the consideration of imperfect maintenance, and, in turn, this tool can be applied and adapted for different models of failure processes that consider these characteristics, for example, NHPP and GRP models. Regarding the latter, the challenge will be to correctly manipulate and reduce the number of parameters that models include. Another area of future research addresses the development and implementation of generalized chart-based tools for maintenance models that consider a delay time stage, including in this way monitoring information on the equipment that conforms to the system to be analyzed.

## Appendix

### A. Optimal Results for PM Standard Time ( $\beta \in (1, 2]$ )

Figures 14–19 show optimal results for PM standard time ( $\beta \in (1, 2]$ ).

### B. Optimal Results for PM Standard Time $\beta \in [1.05, 4.55]$

Figures 20–25 show optimal results for PM standard time  $\beta \in [1.05, 4.55]$ .

## Data Availability

No data were used to support this study.

## Conflicts of Interest

The authors declare that they have no conflicts of interest regarding the publication of this paper.

## References

- [1] G. Ji, W. Wu, B. Zhang, and H. Sun, "A renewal-process-based component outage model considering the effects of aging and maintenance," *International Journal of Electrical Power & Energy Systems*, vol. 44, no. 1, pp. 52–59, 2013.
- [2] J. H. Park, W. Chang, and C. H. Lie, "Stress-reducing preventive maintenance model for a unit under stressful environment," *Reliability Engineering & System Safety*, vol. 108, pp. 42–48, 2012.
- [3] Y.-H. Chien, S.-H. Sheu, and Z. G. Zhang, "Optimal maintenance policy for a system subject to damage in a discrete time process," *Reliability Engineering & System Safety*, vol. 103, pp. 1–10, 2012.
- [4] H. Wang, "A survey of maintenance policies of deteriorating systems," *European Journal of Operational Research*, vol. 139, no. 3, pp. 469–489, 2002.
- [5] J. M. van Noortwijk, "A survey of the application of gamma processes in maintenance," *Reliability Engineering & System Safety*, vol. 94, no. 1, pp. 2–21, 2009.
- [6] M. Yañez, F. Joglar, and M. Modarres, "Generalized renewal process for analysis of repairable systems with limited failure experience," *Reliability Engineering & System Safety*, vol. 77, no. 2, 2002.
- [7] B. Veber, M. Nagode, and M. Fajdiga, "Generalized renewal process for repairable systems based on finite Weibull mixtures," *Reliability Engineering & System Safety*, vol. 93, no. 10, pp. 1461–1472, 2008.
- [8] D. Wu, R. Peng, and S. Wu, "A review of the extensions of the geometric process, applications, and challenges," *Quality and Reliability Engineering International*, vol. 36, no. 2, pp. 436–446, 2020.
- [9] M. S. Filkestein, "A scale model of general repair," *Microelectronics Reliability*, vol. 33, no. 1, pp. 41–44, 1993.
- [10] M. Kijima and U. Sumita, "A useful generalization of renewal theory: counting processes governed by non-negative Markovian increments," *Journal of Applied Probability*, vol. 23, no. 01, pp. 71–88, 1986.
- [11] P. Veen-Dirks, "Management control and the production environment: a review," *International Journal of Production Economics*, vol. 93–94, pp. 263–272, 2005.
- [12] E. Zio and M. Compare, "Evaluating maintenance policies by quantitative modeling and analysis," *Reliability Engineering & System Safety*, vol. 109, pp. 53–65, 2013.
- [13] V. Legát, F. Mošna, Z. Aleš, and V. Jurča, "Preventive maintenance models—higher operational reliability," *Eksploatacja I Niezawodność—Maintenance and Reliability*, vol. 19, no. 1, pp. 134–141, 2017.
- [14] G. May, I. Barletta, B. Stahl, and M. Taisch, "Energy management in production: a novel method to develop key performance indicators for improving energy efficiency," *Applied Energy*, vol. 149, pp. 46–61, 2015.
- [15] B. de Jonge and P. A. Scarf, "A review on maintenance optimization," *European Journal of Operational Research*, vol. 285, no. 3, pp. 805–824, 2020.



- [16] D. Galar, A. Gustafson, B. Tormos, and I. Berges, "Maintenance Decision Making based on different types of data fusion," *Eksplotacja I Niezawodność-Maintenance and Reliability*, vol. 14, no. 2, pp. 135–144, 2012.
- [17] Y. Lam, "Geometric processes and replacement problem," *Acta Mathematicae Applicatae Sinica*, vol. 4, pp. 366–377, 1988.
- [18] M. Kijima, "Some results for repairable systems with general repair," *Journal of Applied Probability*, vol. 26, no. 1, pp. 89–102, 1989.
- [19] L. Doyen and O. Gaudoin, "Classes of imperfect repair models based on reduction of failure intensity or virtual age," *Reliability Engineering & System Safety*, vol. 84, no. 1, pp. 45–56, 2004.
- [20] R. Mullor, J. Mulero, and M. Trottini, "A modelling approach to optimal imperfect maintenance of repairable equipment with multiple failure modes," *Computers & Industrial Engineering*, vol. 128, pp. 24–31, 2019.
- [21] B. Liu, X. Zhao, G. Liu, and Y. Liu, "Life cycle cost analysis considering multiple dependent degradation processes and environmental influence," *Reliability Engineering & System Safety*, vol. 197, Article ID 106784, 2020.
- [22] S. Wu, "A failure process model with the exponential smoothing of intensity functions," *European Journal of Operational Research*, vol. 275, no. 2, pp. 502–513, 2019.
- [23] B. Liu, P. Do, B. Iung, and M. Xie, "Stochastic filtering approach for condition-based maintenance considering sensor degradation," *IEEE Transactions on Automation Science and Engineering*, vol. 17, no. 1, pp. 177–190, 2020.
- [24] A. Certa, G. Galante, T. Lupo, and G. Passannanti, "Determination of Pareto frontier in multi-objective maintenance optimization," *Reliability Engineering & System Safety*, vol. 96, no. 7, pp. 861–867, 2011.
- [25] A. Cakirgil, E. Yücel, and G. Kuyzu, "An integrated solution approach for multi-objective, multi-skill workforce scheduling and routing problems," *Computers & Operations Research*, vol. 118, 2020.
- [26] L. Barberá, A. Crespo, P. Viveros, and A. Arata, "The graphical analysis for maintenance management method: a quantitative graphical analysis to support maintenance management decision making," *Quality and Reliability Engineering International*, vol. 29, no. 1, pp. 77–87, 2013.
- [27] L. Barberá, A. Crespo, P. Viveros, and R. Stegmaier, "A case study of GAMM (graphical analysis for maintenance management) in the mining industry," *Reliability Engineering & System Safety*, vol. 121, pp. 113–120, 2014.
- [28] P. Viveros, A. Crespo, L. Barberá, and J. P. Gonzalez, "Graphical analysis for operation management: a graphical method to support operation decision making," *Quality and Reliability Engineering International*, vol. 32, no. 7, pp. 2299–2311, 2015.
- [29] I. V. Klumpar, "Generalised sensitivity charts," *Engineering Costs and Production Economics*, vol. 8, no. 1-2, pp. 55–115, 1984.
- [30] P. Li, J. Van Lew, W. Karaki, C. Chan, J. Stephens, and Q. Wang, "Generalized charts of energy storage effectiveness for thermocline heat storage tank design and calibration," *Solar Energy*, vol. 85, no. 9, pp. 2130–2143, 2011.
- [31] A. L. Mohamadein, "Generalised chart, load angle, and stability limit in induction motors," *Electric Machines & Power Systems*, vol. 3, no. 1, pp. 65–74, 1978.
- [32] R. Privat, E. Moine, B. Sirjean, R. Gani, and J.-N. Jaubert, "Application of the corresponding-state law to the parametrization of statistical associating fluid theory (SAFT)-type models: generation and use of "generalized charts"" *Industrial & Engineering Chemistry Research*, vol. 58, no. 21, pp. 9127–9139, 2019.
- [33] W. Wang and A. H. Christer, "Towards a general condition based maintenance model for a stochastic dynamic system," *Journal of the Operational Research Society*, vol. 51, no. 2, pp. 145–155, 2000.
- [34] O. Gaudoin, "Optimal properties of the Laplace trend test for soft-reliability models," *IEEE Transactions on Reliability*, vol. 41, no. 4, pp. 525–532, 1992.
- [35] A. L. Goel and K.-Z. Yang, "Software reliability and readiness assessment based on the non-homogeneous Poisson process," *Advances in Computers*, vol. 45, pp. 197–267, 1997.
- [36] C. E. Ebeling, *An Introduction to Reliability and Maintainability Engineering*, McGraw-Hill, New York, NY, USA, 1997.
- [37] M. Modarres, M. Kaminskiy, and V. Kritsov, *Reliability Engineering and Risk Analysis*, Marcel Dekker, New York, NY, USA, 1999.